INTERNATIONAL JOURNAL OF CIRCUITS, SYSTEMS AND SIGNAL PROCESSING
DOI: 10.46300/9106.2022.16.85 Volume 16, 2022

Design and Performance analysis of hybrid energy harvesting and WSN application for more life time and high throughput

[1]Shiva Kumar V., [2]Rajashree V. Biradar, [3]V. C. Patil
[1]Dept. of CSE,RYMEC, Ballari, Karnataka, India,
[2]Dept. of CSE, BITM, Ballari,Karnataka, India
[3]Dept. of ECE Ballari,Karnataka, India
[1]shiva.vadla@gmail.com, [2]rajashreebiradar@yahoo.com and [3]patilvc@rediffmail.com

Received: June 29, 2021. Revised: December 8, 2021. Accepted: January 16, 2022. Published: January 17, 2022.

Abstract— **the technology of wireless sensor-actuator networks (WSANs) is widely employed in the applications of IoT due to its wireless nature and it does not involve any wired structure. The wireless systems that are battery-driven can easily reconfigure the existing devices and sensors efficiently in the manufacturing units without employing any cable for power operation as well as for communication. The wireless sensor-actuator networks that are based on IEEE 802.15.4 consumes significantly less power. These networks are designed and built cost-effectively by considering the capacity of battery and expense so that they can be employed for many applications. The application of a typical wireless Autonomous Scheduling and Distributed Graph Routing (DDSR) has illustrated the reliability of employing its basic approaches for almost ten years and it consists of the accurate plot for routing and time-slotted channel hopping therefore ensuring accurate low-power wireless communication in the processing site. Officially declared by the controversial statements associated with the government of Greek experiences fourth industrialization. There is a huge requirement for sensor nodes link via WSAN in the industrial site. Also, reduced computational complexity is one of the drawbacks faced by the existing standards of WSAN which is caused because of their highly centralized traffic management systems and thereby significantly improves the consistency and accessibility of network operations at the expense of optimization. This research work enables the study of efficient Wireless DGR network management and also introduces an alternative for DDSR by enabling the sensor nodes to determine their data traffic routes for the transmission of data. When compared to the above two physical routing protocols, the proposed technique can drastically improve the performance of a network, throughput, and energy consumption under various aspects. Energy harvesting (EH) plays a significant role in the implementation of large IoT devices. The requirement for subsequent employment of power sources is eliminated by the efficient approach of Energy Harvesting and thereby providing a relatively close- perpetual working environment for the network. The structural concept of routing protocols that are designed for the IoT applications which are based on the wireless sensor has been transformed into "energy-harvesting-aware" from the concept of "energy-aware" because of the development in the Energy harvesting techniques. The main objective of the research work is to propose a routing protocol that is energy-harvesting-aware for the various network of IoT in case of acoustic sources of energy. A novel algorithm for routing called Autonomous Scheduling and Distributed Graph Routing (DDSR) has been developed and significantly improved by incorporating a new "energy back-off" factor. The proposed algorithm when integrated with various techniques of energy harvesting enhances the longevity of nodes, quality of service of a network under increased differential traffic, and factors influencing the accessibility of energy. The research work analyses the performance of the system for various constraints of energy harvesting. When compared to previous routing protocols the proposed algorithm achieves very good energy efficiency in the network of distributed IoT by fulfilling the requirements of QoS.**

Keywords—: Routing Algorithm, WSN, Wireless network, DDSR, QoS, IoT, WSAN, DGR and Scheduling algorithm.

I. Introduction

Development in the technology of senor has paved the way for the design of low powered and relatively small, sensors that are well furnished with programming ability, efficiency in detecting various parameters, and competency in communication that are wireless. Since the sensor technology is cost-effective, the network incorporates several hundreds of sensors and thus improving the efficiency, area availability, and data precision. In obscure and undeveloped areas, the networks of the wireless sensor provide necessary information or data regarding common ecological factors, remote systems, and so on. When compared to wired communication, the network of wireless sensor offers many advantages like simplicity in designing a network (minimizing initial cost overhead), high speed (a network with relatively small sensors can be allocated over a wide area), fault tolerance (malfunctioning of one node do not impact on the network functioning), self-oriented (the reconfiguring ability of node itself) and some of the intrinsic problems faced by wireless sensors are limited bandwidth, data transmission that is error-free, interference-free and so on. Since cell-phones are the most widely used wireless nodes they use only specific batteries to draw the energy and do not require any constant supply of power. Therefore, this reduces the total energy accessible to the nodes. Furthermore, these wireless nodes find it hard to replace both the sensor nodes and battery packs in few areas, therefore, it is essential to maximize the durability of networks by placing a set of new nodes that can recharge the entire area [1]. A pre-defined implementation is required to identify the nodes that are not working and preferentially substitute them by reducing a few network benefits. An optimum sensor system must possess *location responsiveness and addressing that is based on the attribute*. One more essential aspect of sensors is that it should respond instantly to significant environmental variations such as an application that are based on time. The receiver must be given information regarding other remaining nodes that possess small delay and thus ensuring efficient utilization of bandwidth in the wireless media. As a result, data-centric protocols that have data accumulation efficiency, consistently allocating power dissipation, reduced energy to maintain network durability, and eliminating the constraint of a single node (excluding BS) are essential for the wireless sensor networks. As discussed in the previous paper [4] the conventional network protocols are not applicable for wireless communication that is described for MANETs. Recently, a data transmission protocol which is energy efficient named LEACH has been presented [2], and based on the data obtained by BS, the hierarchical clustering is achieved. However, to minimize energy, the cluster-head (CH) and many nodes are frequently varied by the BS. The cluster head receives data from the sensors, analyses, and then transmits to BS. The consumption of energy is evenly allocated by arbitrarily rotating the CH if not the cluster head that is nearer to BS will not allow data to be transmitted and power dissipation compels them to perish quickly when compared to other nodes. Constant re-clustering is done by the BS to allow another active node to function as cluster head when one of the CH because for some reason is unable to interact with its node members or with the BS. The information regarding how a node is established and on what basis the cluster head must be chosen is addressed in [3].

The common drawback noticed was how to resolve the queries of the users and in what way the required data is routed. The majority of the existing protocols acknowledge that a sensor collects the information regularly from the system and when a query arrives the protocol reacts to it. In LEACH [2] the cluster head receives the information continuously, and after the process of clustering, the BS receives the information to store the data. In sensor networks, particularly the applications which are based on time are not focused specifically. The sensor networks must specify the final users to dynamically deal with energy proficiency, precision, and time taken for responding. In this work, we mainly aim at advancing a routing protocol that is efficient and a detailed request managing process that satisfies the above requirements.

The major issue faced in decentralized IoT is the propagation of cost-effective data which is illustrated by many research work [6]. Several research works have been accomplished in the area of data network aggregation [7], without any compression loss and with compression loss [8] (the main concern is to improve the efficiency of energy by minimizing the total bits to be transmitted), as well as enhancement of various objects present in the wireless communication [9]. Particularly, the specific level of compression, quality of signal trading, and quality of service are allowable for a long-lasting network in several applications of the internet of things. In this research work, we visualize the networks of IoT that inevitably switch their activity to various sources, their positions, rate of transmission (i.e. encoding of source), distribution flow systems, and quality of service required by the application. Therefore, we propose the application to overcome the drawbacks of distributed learning techniques, reviewing source compression, and distribution flow issues. In general, we collectively describe the issues related to lossy data compression at the input side and a successful routing path is established towards the data distribution center of the Internet of things (the gateway of the Internet of things is also known as a sink). This helps in analyzing the basic difference between the efficiency of the distortion rate at the inputs and outlay required for transmitting the necessary data and addressing the issues of distribution flow. The primary objective is to interpret exactly how much computation has to be carried out near the input with the help of a few lossy data compression algorithms. Thus the compressed data is processed successfully and communicated via a plot of a network by collectively handling compression and routing. Make sure that the compression is intrinsically combined with the efficiency of interconnected network constraints, their destinations, total inputs and their locations, and the communication node's potency. While identifying the drawbacks, we arrived at the concept of possessing transmission overheads in contrast to the interference of signal and thereby enabling the study of an ideal cost-distortion area (allocative efficiency) of a network.

The main difference between the existing and the proposed work is that no hard-coded protocol standards are used to ensure the quality of source compression and process the data collected. However, these responses generally arrive as alternatives for the process of distributed learning which contains the iterative transmission process among the local signals and the nodes [5]. The nodes do not possess any information regarding the entire network process or status of network standardization, and also they have no idea regarding the detailed structure of the network. Instead, local communications enable the design of a distributed system to integrate the process of optimization worldwide. An initial data centralized system is introduced in the research work of [10]. Several research works have been carried out in the field of distributed WSNs namely source encoding, forwarding, and enhancement techniques for multi-objective. Few research works are concerned with encoding of data at the input [11], and some works enable the accumulation of data at the arbitrator nodes while forwarding the data to the destination node. The paths for routing can be predetermined by the advanced computation [12] or determined with the help of a functional approximation process that requires accumulation and data forwarding network [11]. Since the system implements encoding at the input, the researchers of are concerned with combined data encoding and collection of data by consuming the energy computed for data encryption in contrast to the energy utilized for the communication. The strategy discussed above is analogous to the proposed one and the primary distinction is that the paths for routing and encoding standards at the inputs are simultaneously determined and are executed as the process of deep learning. The drawbacks of combined routing and encoding are introduced by employing the theory of Lyapunov optimization in [13]. On the other hand, the path for routing is already defined and is not implemented with the encoding procedures. The research work of explores a conceptual framework for data collection networks along with data encoding techniques, where every individual node pre-processes the data collected before delivering the information to the local network. The proposed work mainly concentrates on the cost-effective encoding and transmission scheduling for the network with a single hop and considering encoding and communication expenses under a rescheduling limit.

Many research works utilizes spatial correlation for data accumulation example [13]. These works mainly concentrate on the information generated from the temporally correlated inputs and forwards the same information to the destination. Encoding inevitably leads to in-network accumulation, and researches are conducted to explore the difference between routing and accumulation. The issue of routing was not considered by the analysis of the distributed method for compressive sensing, for example, illustrated in [10]. For the multi-objective enhancement, there exist several research works. For example, [8], [9], mainly concentrates on various issues of the target. The combined optimization and routing are not taken into account even though the main aim is energy reduction. In [12] the proposed algorithm corresponds to the compression of the data source in the initial section of the research work, further routing is carried out by employing a flow-based model. We implement a heterogeneous network where the input nodes possess various detection and transmission abilities, however, it is impossible to accumulate the data flow from various sources. The network of multimedia sensors presents a few examples of these types of the network [2]. In the current research work, we propose a combined optimization method for routing and encoding. The proposed algorithm relies on ADMM resulting in a completely allocated system.

A heterogeneous distributed-edge framework has been specifically formed by many public and private networks by offering support to the application of the Internet of Things. The network operators present a Network Function Virtualization (NFV) that distinguishes the operations of the network from specific hardware by operating the features in an adaptable software such as Virtual Network Functions (VNFs) that is operated on specific hardware [14]. The network providers are offered a unique chance that is associated with Software-Defined Networking (SDN), to set up the architecture to satisfy the requirements of a specified application [15]. Recently in fundamental cloud conditions, the research works mainly concentrates on the drawbacks of Network Function Virtualization. One of the disadvantages involved in cloud computing is end-to-end dormancy which is due to the impact of the physical gap between the cloud service providers and a heterogeneous distributed-edge framework that has been specifically formed by many public and private networks by offering support to the application of Internet of Things. The network operators present a Network Function Virtualization (NFV) that distinguishes the operations of the network from specific hardware by operating the features in an adaptable software such as Virtual Network Functions (VNFs) that is operated on specific hardware [16]. The network providers are offered a unique chance that is associated with Software-Defined Networking (SDN), to set up the architecture to satisfy the requirements of a specified application [17]. One of the disadvantages involved in cloud computing is end-to-end dormancy which is due to the impact of the physical gap between the cloud service providers and an efficient technique is developed for the ideal decision making policy and enhance the advantages for a long period. The level of accuracy and recurring is minimized by combining the efficiently handling feature of deep learning with reinforcement learning which is having decision-making capacity [19]. Deep learning is considered as one of the key technology in achieving self-adjusted SFC enhancement because of the benefits of self and virtual learning. Cloud computing that is generally associated with Software-Defined Networking and Network Function Virtualization are employed in various application of IoT to guarantee the efficiency of the service provider. A security framework which is based on cloud computing is introduced in [20] is employed to safeguard the Software-Defined vehicular applications of IoT. The blockchain nodes examine the real-time applications of the Internet of Things so that suspicious traffic and its behavior are updated by the blockchain and thus assuring data

security and cost optimization. The attack of distributed denial of service (DDoS) has a significant effect on the exponential increase in the suspicious devices in the IoT applications. The model of decentralized secure DDoS collaboration solution (Cochain-SC) [21] was introduced by Z. Abou et al. to overcome the above issue by employing smart convention to the model. The main advantage of the Cochain-SC is that the blockchain enables privacy and cost-effective distributed collaboration among various Software-Defined Networking to reduce the attacks. P. K. Sharma et al. introduced a new Software-Defined-cloud architecture consisting of three layers [18] which are based on blockchain to overcome the drawback of security for outsourcing data and hence creating trust between consumer and the service providers. The request services and public set up is examined by the device layer. The distributed resources and enabling data operation are analyzed by a cloud layer. The computational resources are carried to the edge of the IoT network which is based on blockchain and Software-Defined Networking in the fog layer. The architecture of the distributed cloud which is based on the blockchain overcomes the drawback of privacy and decentralization. A unique structure combined with SDN that is used for the application of IoT is introduced by M. Pourvahab et al. in [21]. To assure secure synchronization between various SDN controllers for a network H. Tang et al. in [20] addressed a consensus protocol that is based on the blockchain for Software-Defined Industrial Internet. Blockchains are widely used in many distributed applications because of their service trustworthy, cost-effective, and transparent nature [14].

II. REALTED WORK

The most widely considered technique in the research work of wireless mesh and sensor networks is Routing. The routing protocol that directs any routing path in the network of the wireless sensor to an individual or many defined base stations is termed as CTP [7]. Some of the applications of CTP are research, training, and an industrial process. The development of RPL [8] has been ensured by the perception of CTP. High efficiency is not achieved by the routing protocols such as CTP and RPL which is based on the tree because it is unable to generate the data set routes described in the wireless HART. Since packet loss is the main issue of these two protocols they are not applicable for the basic applications of industries. Therefore, to overcome the above problem, a multipath routing protocol is introduced (example, [11]–[15]) which improves the efficiency between the sender node and receiver node by enabling cluster-head disjoint or connection-disjoint. However, the energy utilization and load in the traffic are maintained between different network nodes by the introduction of routing protocol which is based on multipath RPL (example, [16]–[20]). When compared to other protocols, the data set routing mentioned in Wireless HART ensures high efficiency by considering the significant level of routing latency for the network of TSCH.

The application of a typical wireless HART has illustrated the reliability of employing its basic approaches for almost ten years and ensuring accurate low-power wireless communication in the processing site. A set of algorithms were proposed by Han *et al.* [21] and Wu *et al.* [22] to generate the data set path in a unified manner whereas, with the application of the Bellman-Ford algorithm, Modekurthy et al. introduced the generation of data set paths in a distributed manner [23]. In contrast to these techniques, a basic distributed routing protocol that is based on RPL is designed to produce and work with the data set paths. The overall solution for the network is obtained by designing a strategy of transmission scheduling which is operated just above the designed protocol. The analysis of transmission scheduling is considered as the prime concern for the applications of Wireless HART networks which are based on time [24]–[27]. The above-discussed scheduling methods are unified alternatives that are intended to operate on a data-centric network manager with data set routing operation. Also, researches have been made for the development of RPL networks with distributed scheduling [10], [27]–[32]. Consider an example of Orchestra in RPL networks where the nodes can determine their schedules which are introduced by Duquennoy et al. [10]. To ensure the proper utilization of IPv6 which facilitates load above the IEEE 802.15.4e TSCH networks is regulated by the operating group of 6TiSCH developed by IETF [9]. On the other hand, the experimental results of our analysis illustrated that the network operating with RPL experiences more recovery time and reduced efficiency when node malfunction and external interference take place. Synchronous transmissions [22]–[27] are considered as one more area of research. But for handling the synchronous transmission there is a necessity for a unified node in this transmission.

N. Michelusi et al. [28] presented an algorithm for Energy-opportunistic Weighted Minimum Energy (E-WME) concerned with the routing techniques of "energy-harvesting-aware" and thereby determining the individual sensor node overhead by employing the rate of energy harvesting and the energy available. A routing algorithm for Randomized Minimum Path Recovery Time (R-MPRT) is introduced in the research work of [28]. Therefore, the cost measured for a system can be expressed as the amount of energy consumed by the packet processing node (also known as energy packet) to the rate of energy harvesting. By considering the specified cost metric, the best optimal path to the destination is determined by the node. Further, the destination receives the data packet through a low-cost connection from the source node. An algorithm for R-MPRT is introduced by Hasenfratz et al. in [29] which is developed by making use of the energy remaining at the node rather than using the energy harvesting rate to attain an optimal solution. The decision of routing is considered depending on the cost measurements that consist of energy consumption and harvested energy ruined because of overloads which are explained in [13]. The algorithm for Distributed Energy Harvesting Aware Routing (DEHAR) is presented in [30] this algorithm determines the best optimal path to reach the destination by employing the energy available at every individual node and hop counts of the node. The perception of the Energy harvesting algorithm employs a local charge for every individual node that is constantly

rationalized and is inversely related to the energy available at the node.

A Routing Protocol for Energy Harvesting Aware Ad-hoc On-Demand Distance Vector (AODV-EHA) is introduced by Gong et al. in [31]. The algorithm of AODV-EHA deals with wireless sensor networks by acquiring the benefits of the previous Ad-hoc On-Demand Distance Vector protocols. This algorithm calculates the best optimal path with low-cost transmission by making use of efficient energy harvesting techniques. The protocol required for smart energy harvesting routing (SEHR) is presented in [32]. The algorithm of SEHR initially considers the energy accessibility at the node, expected rate of energy, and approximate the energy collected from the renewable sources (for example solar and radiofrequency) during the process of selecting the path. A routing protocol for energy-harvesting-aware that is based on the topology control scheme is introduced in [33]. Therefore, to speed up the topology of the network, the energy-harvesting-aware protocol uses the method of game-theoretical to evaluate the status of energy and extracting capacity of every individual node. The power consumption of the node is collectively evaluated by itself or by the adjacent node energy resources and further examines the energy produced and extracted at every individual node with various time intervals. Although routing algorithms that are discussed above minimizes the energy consumed and increases the durability of nodes but still these algorithms possess some drawbacks. The feature of energy harvesting introduced in [10] and [12] will not consider the actual amount of energy extracted. The concept proposed in [12] and [18] employs perpetual replacement rates for all the nodes present within the network. Therefore, almost all existing algorithms are unable to interact with the probabilistic feature of the resources that renewable because of the inadequate extraction of energy. One more drawback is the implementation of a single energy source to obtain energy. It is indicated that renewable energy sources are supported by peak/off-peak intervals, climatic changes, seasons, and day and night rotations. Thus in real-time, the application of a single energy source may not be feasible to increase the longevity of the node. As a result, a novel routing algorithm for energy-harvesting aware [34] is developed by considering various types of energy extracting algorithms. In the case of the stratified environment, the overall data is incapable of adjusting to the differences in the energy status of the sensor nodes (for example the remaining, utilized, and collected energy levels). Thus, it is required to create tables for routing by making use of local data in a decentralized manner for the applications of the Internet of things [35]. The framework of efficient routing which is known as directed diffusion is presented by C. Intanagonwiwat. et. al [38] and is utilized for the networks of the sensor. This framework illustrates the concept of data-centric along with the application of data input transmission and encoding. The algorithm of hierarchical clustering mainly focuses on distributed activity, the requirements for communication that are asymmetric, and energy consumption in the networks of the sensor is addressed by Estrin et. al [36]. Jiang et. al in [39] introduced a routing protocol for the networks of mobile ad-hoc and is termed as a cluster-based routing protocol (CBRP). The nodes of a network are split into non-overlapping and interesting nodes that in a decentralized manner with a two-hop diameter. On the other hand, the CBRP protocol is not appropriate for the sensor networks that are energy limited. LEACH is a hierarchical clustering algorithm presented by Heinzelman et. al [37].

III. PROPOSED METHODOLOGY OF WSN FOR EFFECTIVE SCHEDULING AND ROUTING

The technique of energy harvesting is considered as one of the viable strategies that are based on physical-layer security. This technique protects data from surveillance without necessitating upper-layer data encryption as well as significantly enhances the performance of wireless networks. On the other hand, this strategy introduces many difficulties because the opposing parties can listen to the confidential data that is being transmitted between the sender as well as the recipient through a relay. As a result, for energy harvesting, the signal's transmission power must be sufficiently high but to prevent eavesdropping, the transmission power must be low. Multi-hop multipath wireless networks make this much more complex. The shortest path selection protocol, best path selection protocol, as well as random path selection protocol, are the three protocols introduced in this research work. In the context of unauthorized parties as well as hardware failure, these protocols help in improving the security of multi-hop multipath randomize-and-forward cooperative wireless sensor networks where the source, as well as relay nodes, can harvest energy from the signal for transmitting data. Additionally, accurate closed-form expressions as well as the asymptotic outage probability for every protocol is been developed for various eavesdropping attacks. The theoretical outcomes are validated by the simulation results.

Particularly when considering a large number of nodes, the conventional battery charging or replacing for wireless devices is difficult as well as environmentally harmful. As a result, unique approaches that are based on renewable energy sources must be developed to reduce large power consumption. One of the simple, as well as ecologically beneficial techniques, is wireless energy harvesting which is used for extending the life of networks by harvesting energy from radio-frequency (RF), and by using specialized devices the signals are converted into power. The signal produced in the same or different networks could be used to extract this RF energy. On the other hand, solar-powered dedicated transmitters can be used if the harvested energy value is insufficient. Therefore, we can achieve a better result by combining zero-energy network operation as well as ease in wireless device charging. Furthermore, a thorough analysis must be carried out to ensure that good communication performance. The impacts of wireless energy harvesting from cooperative network transmissions on probability coverage as well as network durability are described. We examine the probability of connectivity using battery-less nodes that are driven by customized RF energy transmitters in the subsequent part of the research work. As shown in Fig. 2, by harvesting power from the RF transmissions of other wireless devices, or in

some situations where power transmitters are placed especially for this function is feasible to extend the lifetime of low-power, wireless devices via WEH. On the other hand, the WEH-enabled devices' communication efficiency must also be examined. The primary SWIPT-enabled WEH methods are explained in this section and are shown in Fig. 2.3. This technique can be classified as context-aware or context-unaware.

The performance of RF-to-DC conversion is a significant hardware constraint that affects the energy harvester. The RF energy that is converted into DC power is not lossless. To accommodate for these impairments, the efficiency of RF-to-DC conversion as shown in Fig. 2.4, describes the energy receiver's potential which is highly reliant on the power received. Generally, the conversion efficiency improves linearly as well as in concave form for low input power values as well as for higher power values respectively. In prior research works, the performance of RF-to-DC conversion was assumed to be constant as well as was independent of the instantaneous amplitude irrespective of the received RF signal. Due to small changes in the received power, the above condition may work for randomly placed low-density networks i.e., for intensity 0.05 Devices/m2, but it is not feasible for denser networks with > 0.05 Devices/m2. As a result, the performance of RF-to-DC conversion characteristics must be taken into account while developing upcoming WEH systems. In wireless, routing protocol has become a major role in terms of power consumption, packet delivery ratio and transmission of packet and its packet scheduling, but in the development in wireless communication, there are new protocols such as Collection Tree Protocol (CTP) for better improvement in latency and throughput and Routing Protocol for Low Loss Network and Power (RPL^{2}NP) which is based on IPv6 IEEE standard discussed in [7-9]. These two advanced protocols is replacement of routing centralization and scheduling algorithms in WSAN's in industry. These protocols are combined together by considering the the advantages of both and it is named as Autonomous Scheduling and Distributed Graph Routing (DDSR) which will take care of automatic routing and transmission of packet between source and destination in a disturbed mode. The following are the main contribution of this research work.

1. Development of low power and low lossy networks routing protocol with help of RPL^{2}NP which will operates on graph routing and scheduling through minimum latency and high throughput.
2. Design of two scheduling approaches to compute automatic transmission based on the routing graph. The first approach is to find minimised distance between source and destination for end-to-end latency and eliminates the conflicts between other packet and it is to minimize the traffic in real world scenario.
3. The proposed RPL^{2}NP is an oriented distance based routing protocol for development of low power IPv6 network. The working principles of RPL^{2}NP is as follows.

The scheduling of packet and transmission is totally based on Internet Access Point (IAP) and each node has rank and its rank allocation is purely based on distance to the destination using cost function i.e excepted transmission count (ETC) and then packet is forwarded towards route to neighbor node. The generation of routes by RPL^{2}NP are not in graph route initially because every node has only one preferred "head" in the whole network to use many head's, suppose those head's equally preferred and have same or identical rank in the network then there are choice to get collapse or interference occurring within the network and it leads to lose of packet. To overcome this issue, the modified RPL^{2}NP routing network assigns two preferred head's to each node at a time as default routes and forms the routing graph in the network as per following specifications.

Directed Routing Graph (DRG): it forms the routing among all nodes without co-exists which are wanted communicate with other for packet transmission. This routing i.e all selected links for routing orient toward the neighbor or terminates at the destination or access points for ensuring that data or messages should delivered safely to the destination without any co-exist in the graph. The proposed Directed Routing Graph is more efficient routing algorithm compared with AODV, DSR and OLSR protocols for minimization of delay and congestions and based results obtained the DRG protocol has more throughput and high efficient as shown Table.1.

Best head and second best head selection: This selection alterative solution for avoiding of co-exists or interfering of packet, in the network has best head and second head, the best head is to locates on the main path from node to access point with shortest distance from destination node and second head has another best shortest distance path from the same destination node to serve as backup routing so that packet delivery ratio can be increased.

Allocation of Rank: Every node has a rank and all access points allocates their own rank, initially it is '1' and based on the best head's, the initially assigned rank is updated by increasing by '1'.

Weighted ETC: The cost function of weighted (ETC_w) is the node to measure the distance from the access point by using two routings based on equation (1)

$$ETC_w = W_1 * ETC_{acc} + W_2 * ETC_{accs} \quad \text{----------(1)}$$

Where ETC_{acc} is the distance accounted ETC from access point with help of best head. ETC_{accs} is the distance accounted ETC from access point with help of second head. W_1 and W_2 are two best heads weighted and these are given in equations (2) and (3).

$$W_1 = 1 - \left(1 - \frac{1}{ETC_{bh}}\right)^2 \quad \text{----------(2)}$$

$$W_2 = 1 - \left(\frac{1}{ETC_{bh}}\right)^2 \quad \text{----------(3)}$$

Where ETC_{bh} represents ETC between the source node and its best head. As per standard wireless communication discussed in [5], the transmission of first packet through best head and the retransmission of second packet through second best head which is backup route. So W_1 is probability of successfully delivered packet at time of first two transmission attempts, W_2 is probability of unsuccessful attempts fail. All the nodes present in the network are broadcast their own ranks periodically to join into transmission mode and based on it, the ranks are allocated. After allocation of ranks as best head and second head, "Joined callback message" sends to the selected

best head and second best head and also it informs bout the selection to all other nodes.

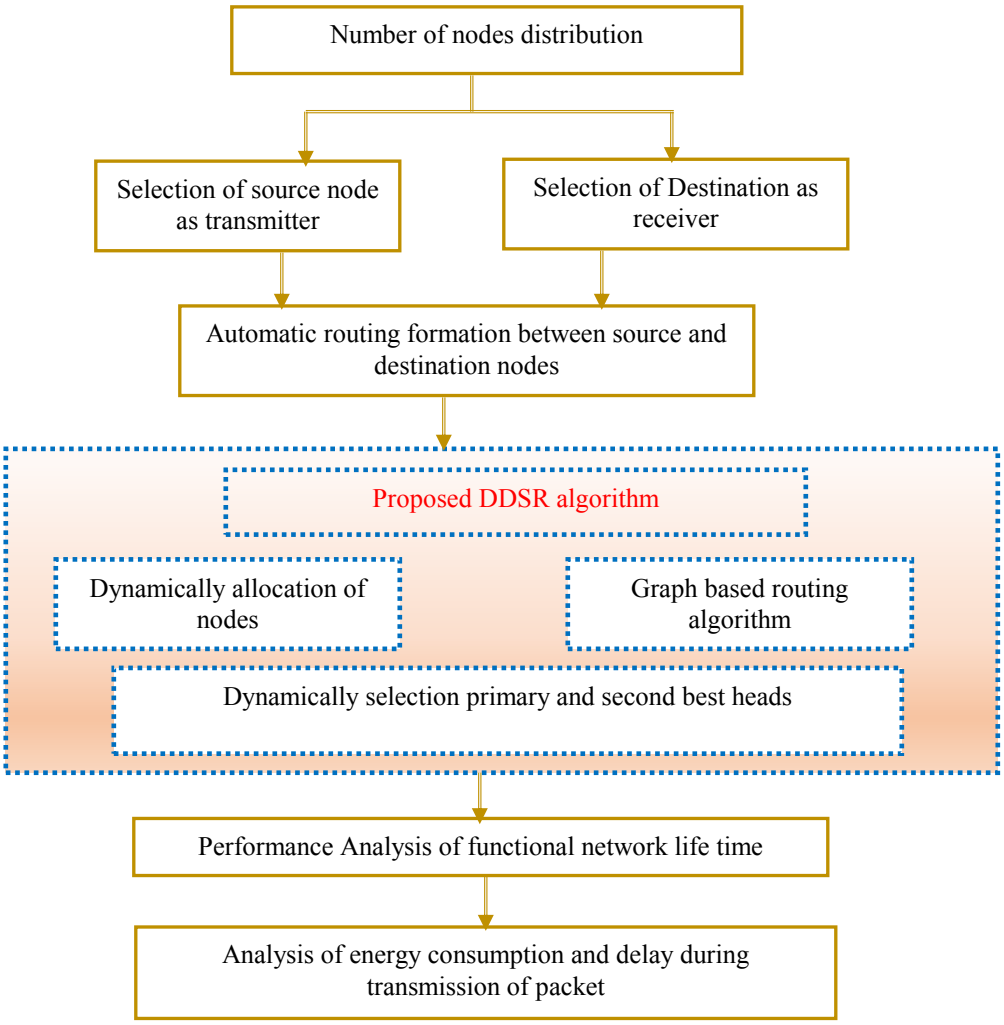

Fig.1. Working Flow diagram of Proposed Dynamically Routing using DDSR for low energy consumption and high throughput

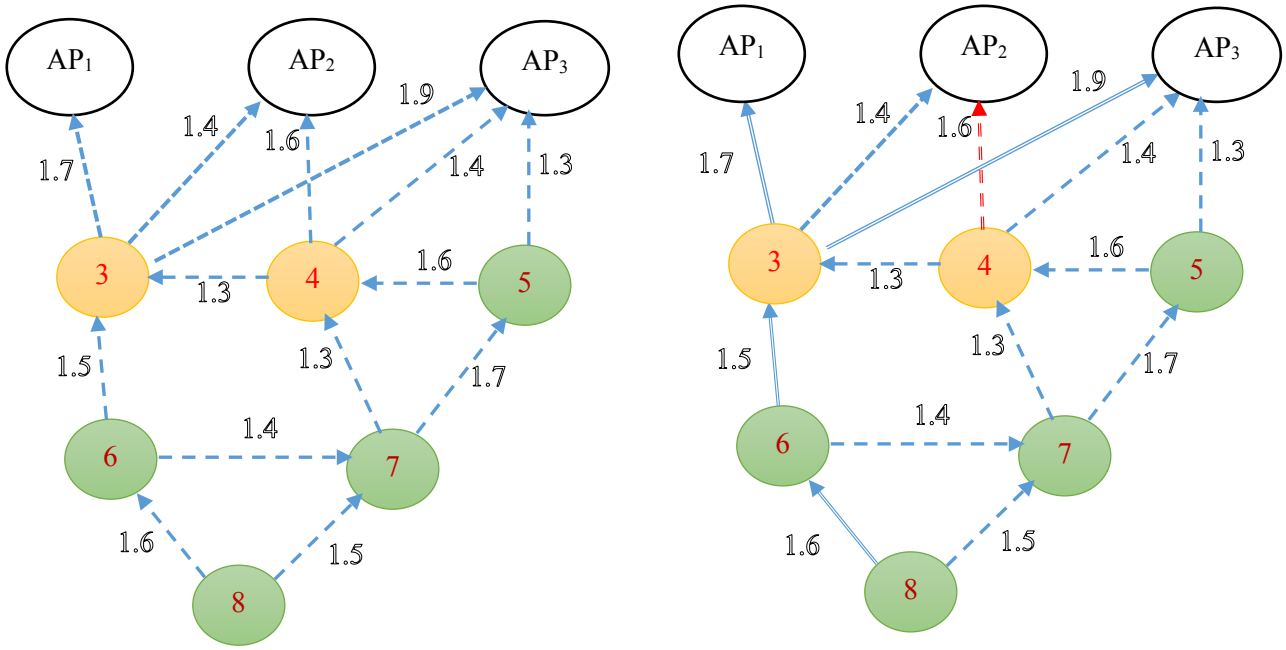

Fig.2. Proposed created network topology for three access points and six field nodes and their transmission paths and directions. (a) Created network topology (b) Routing Graph and best and second head's.

Algorithm 1: Dynamically Distributed & Schedule Routing (DDSR)

Input : R_{id}, N_{id}
Output : Updated router table (R_{table})
Initialization : R_{table}=NULL,
$ETC_w(N_{id}) = Rank(N_{id}) = \infty$

Condition 1: if N_{id}= R_{id} then
//////Initialize the access point
Compute Rank=1 and ETC_w=0;
Broadcast about join-in messages;
end
Condition 2:if Rank(N_{id})=∞ & ~ N_{id}= R_{id} then
//////Allow receiver to receive the first join-in message from i
Compute $ETC_{acc}(N_{id}, i)$=ETC(N_{id},i)+ETC_w (i);
Compute sender message as its bes head;
Compute ETC_{min} =$ETC_{acc}(N_{id},i)$;
Compute Rank (N_{id})=Rank (i)+1;
Transmit joined message callback;
end
Condition 3: if Rank(~N_{id})=∞ & ~ N_{id} = R_{id} then
//////Receiver, receivers the non first messafe join-in from I
Compute ETC_{acc} (N_{id},i)=ETC (N_{id} , i)+ETC_w (i);
If ETC_{acc} (N_{id},i)<ETC_{min} then
Compute it as best head as the second best head;
Compute sender message as best head;
Compute ETC_{min} =ETC_{acc} (N_{id},i);
Compute Rank(N_{id}) –Rank(i)+1;
Transmit as joined callback message;
end
Condition 4: if ETC_{acc} (N_{id}, S_{bh})>ETC_{acc} (N_{id}, i)>=ETC_{min} and Rank(i)<Rank(N_{id}) then
Compute sender, sends message as second best head;
Transmit joined message as joinback;
end
$ETC_w(N_{id})$=W_1*$ETC_{acc}(N_{id}, S_{bh})$+$W_2$*$ETC_{acc}(N_{id}, S_{bh})$;
Broadcast message as join-in;
end
Condition 5:if Receive joined message callback then
Update the router table R_{table} and sender message is added as sub router;
end

The proposed distributed graph shown in algorithm 1 and it start with access point to form the routing graph and it routes towards the access pint. Before network starts, the graph initialize the rank to 1 and ETC_w to 0, therefore, the network starts broadcasting join-in message. The remaining nodes computes their rank and ETC_w to infinity. Suppose any node receives the join-in messages from any another nodes, it opts its best head and second head purely based on accounted ETC routing table values and then it compute its rank by raising its best heads rank by 1. After updating of heads ranks, the node starts broadcasting join-in message to another nodes. The ETC initialization between any two nodes are decided purely based on Strength of Received Signals (SRS). In this work, we have set SRS_{min}=-75dBm and SRS_{max}=-90dBm, when SRS value is more than -90dBm, then ETC is set to 1 otherwise ETC is set to 5, and the ETC can scaled randomly netween 1 and 5. In case, there is transmission error occurs between range 1 and 5, it can be measured by using equation (4).

$$ETC = ETC_{old} * \beta + q * (1 - x) \text{----------(4)}$$

Where ETC_{old} is the ETC value applied before maximum error occurs, q is error coeeficients and β is weight factor between 0 and 1. The Fig.2. shows the data paths examples for packet transmissions that has three Access Point (AP) and six field nodes. The dash lins shows the ETC values with links. Whenever network starts the packet transmission, the three AP_1, AP_2 and AP_3 are starts broadcasting their ETC_w values and ranks to neighbour nodes. #3 selcts AP_3 as its best head and AP_1 as its second best head, the selection of head's are based on ETC_{acc} values because ETC_{acc}(3, AP_3) is greater than ETC_{acc}(3, AP_1). Similary #4 selects AP_2 as its best head and AP_3 as second best head since ETC_{acc}(4, AP_2) is greater than ETC_{acc}(4, AP_3). Therefore the rank of both #3 and #4 are 2 and these are starts broadcasting their rasnks as join-in measssage to neighbours as shown in Fig.3. To avoid loops, the #3 and #4 are not selected th link between #4 and #5. Based on connectivity among selected heads and neighbour nodes, the routing graph is generated and it is shown in Fig.1. The solid lines are denoted the major path (primary) i.e $\#8 \rightarrow \#6 \rightarrow \#3 \rightarrow \#AP_1$ and the dash lines denotes the backup routes ($\#8 \rightarrow \#7, \#7 \rightarrow \#4, \#4 \rightarrow \#3, \#3 \rightarrow AP_1$ *and* $\#5 \rightarrow AP_3$).

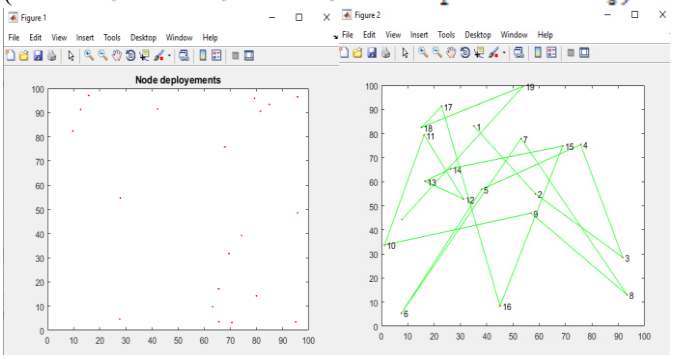

(a) *(b)*

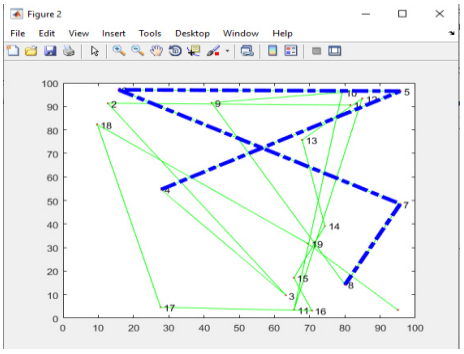

(c)

Fig.3. Proposed Wireless Sensor Network, nodes deployment and path establishment between source node and destination node. (a) 20 Nodes deployment (b) Connection establishment among all nodes (c) Path establishment between source and destination nodes.

Slots allocation for application as shown in Fig.1.: There is choice of attempting multiple transmission through scheduling for each and every packet with help of major path and backup path. Therefore, the transmission and reception of packet or schedule are purely depending on their unique id which is assigned to each and every node. All these id's are generated as integer byte and stored in LUT and mapped as MAC address. The allocation of slots (s) is given in equation (5).

$$s = N * (Node_{id} - M_{AP}) - N + \beta \text{----------(5)}$$

Where N is no of attempts for transmission for each packet, M_{AP} is no of access points, $Node_{id}$ is neighbour node id from routing table and β is s[th] slot in the application for β^{th} transmission attempts. To increase throughput of the DDSR in WSN, the hybrid WSN which includes Dijkstra algorithm, minimum tree spanning and localized minimum spanning are incorporated for finding of shortest path between source and destination. In these hybrid algorithms mainly depending on message and node id's which are based on locally best decision of each and every node and it has its own information and this will be shared with neighborhood to find the shortest path in the graph in terms of best and second head's. By reducing of distance among the source and destination nodes, the throughput drastically increased and minimized the number dead nodes as shown Fig.5. With help of Dijkastra algorithm, the problem of maximum distance between source and destination are minimized and step by step process is shown in algorithm 2.

Algorithm 2: Shortest path identification between source and destination nodes

Step 1: Parameters initialization

Iteration number=0, distance=any number in positive infinity and data set[i]=0, where i=0,1,2,3……..n-m).

Notations: r_n=radius of transmission

sv= starting of the node

n_r=node relay

r_n=Receiver node

Step 2: When cos(e)[sv] [i[<r then data set[i]=1,(i=0,1,2,3……m)

Compute cos[i][j] for distance between source node (i) and destination node (j)

Step 3: If data set[r_n]=1 then

Compue distance=cos(e)[sv][**r_n**]

else

go to step 4

Stept 4: All values of i are belongs to {data set [i]=1}, n_r [i]=1, data set[j]=1 when j also belongs to {cos(e)[n_r[j]<k} for all values og j=0,1,2,3……n)

else

record the distance that falls in data set**[r_n]=1 and compue the distance between nodes is cos(e)[sv]** $n_r[0]<\sum_{j=0}^{i-1} \cos(e)\,[sv]\,[nr[(j+1)\cos(e)[nr(i(sv))]$

end

3.1. Measurement of Energy in WSN

After establishment of paths among the heads and other field nodes, the energy is measured per packet transmission as per following specifications and ploted the obtained energy for without DDSR and with DDSR.

Sinks: sink.x=1.5*WIDTH and sink.y=0.5*HEIGHT

Number of Nodes in base station area is n=20

Probability of a node is p=0.2

Battery capacity is Eo=0.1, ETX=50*0.000000001,ERX=50*0.000000001

Transmission energy Efs=10*0.000000000001 and Emp=0.0013*0.000000000001.

Data Propagation Energy is EDA=5*0.000000001

Thresholod for transmiting data to SINK are h=100 and s=2

IV. RESULTS AND DISCUSSION

The Fig.5. Shows the performance analysis between different paramedics and their optimization shown in Fig.4. The DDSR able to minimized the end to end delay during the transmission of packets from source node to destination node, Fig.5.(a) shows the optimization of delay between proposed DDSR algorithm and existing algorithm, the red color shows the end to end delay for existing algorithm and yellow color shows the proposed algorithm delay and it is concluded that the delay of proposed communication for packet transmission is optimized 14% compared to existing work. The Fig.6 (b) shows the number of packets lost during the packets transmission and due to effective scheduling and formation routing table, the losses are able to minimize and compared to existing results shown in [12].

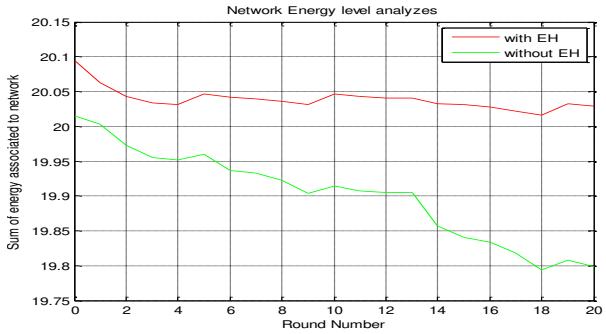

Fig.4. Energy consumption per round per packet transmission between with DDSR-EH and without DDSR-EH.

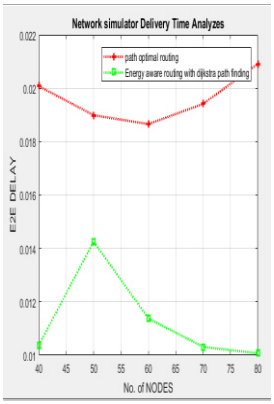

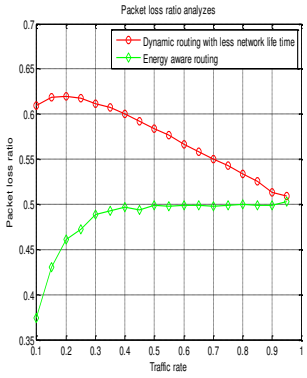

(a)

(b)

Fig.5. Performance analysis of End-to-End delay, packet loss ration with and without of dynamic routing (a) End-to-End delay (b) Without dynamic routing and with dynamic routing.

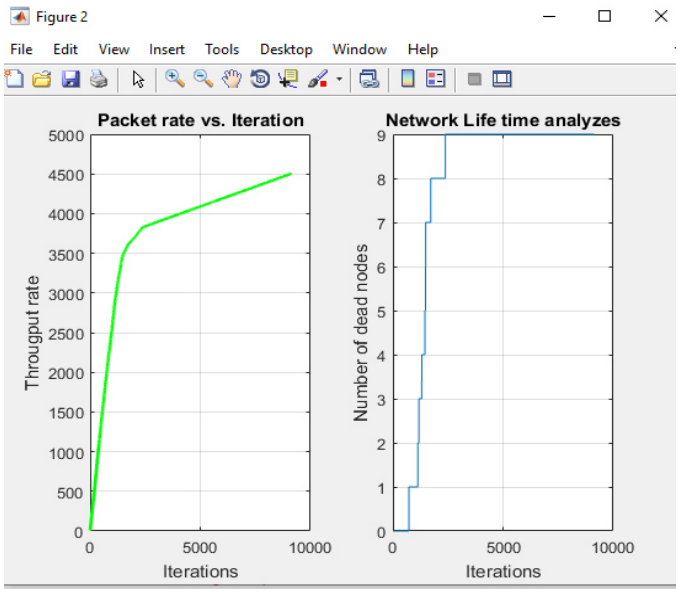

Fig.6. Performance analysis of throughput and number of dead nodes w.r.t life time of network of DDSR during transmission of packets.

In proposed system, DDSR as feasible design flow to model the energy hravesting thorugh both solar and RF fading channel. An energy received and storage by the receiver antenna under different noisy channel like Rayleigh fading enviornment is simulated in MATLAB 2017a using communication system toolbox. The modeled channel is accessed with help of command i.e energy_channel= rayleighchan(T_s, D_m) where T_s is sampling frequency of 1000Hz and D_m is doppler maximum shift of 25Hz and its correspondings to rayleigh fading channel as shown in Fig.7. The received signal power harvested by a RF rectifer with minimum loss efficiency and its energy harvesting at time t is given by

$$H_e(t) = \int_0^1 P_r(\tau)\, d\tau$$

Where P_r received power at given timeτ. $The\ \{H_e(t)$, t >0$\}$ is the energy harvested during process of observing RF signals. The Rayleigh RF channel$\{H_e(t)$, t >0$\}$ has been modeled help of homogeneous to fulfill the following basic properties:

1. $P(H_e(0) = 0) = 1$
2. Increasing the $H_e(A+s) - H_e(A)$
3. An energy harvested in a given interval of magnitude (A), $H_e(A+s) - H_e(A)$ is the distribution process with parameter αA and β along with density.

$f_{H_{e(A)}(y)} = \frac{\beta^{\alpha A}}{\Gamma(\alpha A)} y^{A\alpha-1} e^{-\beta y}$ for y>0 where $\overline{P_r} = \frac{\alpha}{\beta}$ is the mean received signal power

The harvested energy of mean and its variance in an interval of magnitude A is given by

$$\in [H_e(A)] = \overline{P_r} A \ and \ var\left(H_e(A)\right) = \alpha^{-1} A \overline{P_r^2}$$

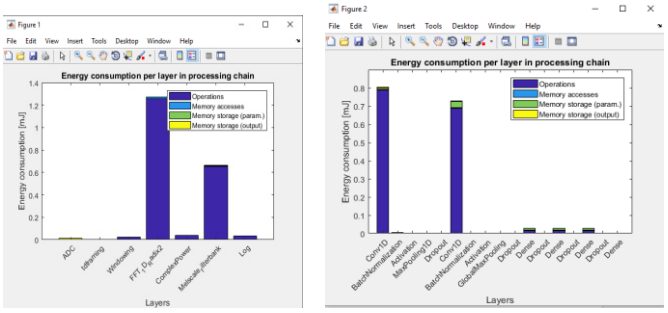

Fig.7 Energy saved through RF and Solar and consumed during the process DDSR.

The first thing that must be considered when harvesting energy is the source of the energy particularly where the energy source is located and the amount of energy available. When considering radio frequency (RF) energy there are many different options including radio, digital TV, cell phones, and Wi-Fi. To choose from. The power density and availability of the RF energy was considered in the tables below. Table 1 shows the power density in a given range for a 50 Kw AM radio station which usually operates between 420 KHz – 1350 KHz. Table 2 covers the power density and range for 95 W stations which operate at 628 MHz to 862 MHz and 1520 MHz to 2110 MHz.

Table 1. Power density available for a 50 kW AM radio station.

50 kW AM Radio Station	
Distance	Power Density Available
5 Km	159 μW/m^2
10 Km	40 μW/m^2

Table 2. Power density available for a 100 W GSM base station.

95W Base Station	
Distance	Power Density available
100 m	800 μW/m^2
500 m	32 μW/m^2
1000 m	8 μW/m^2

V. CONCLUSION

The contribution of this paper is on improvising of current WSAN and WSN networks for wireless communications and increasing od their scalability through effective routing and scheduling to enhance visibility and predictability of wireless network operation in WSN. This paper decentralizes the organization the board in Wireless DDSR and presents the primary circulated diagram steering and self-governing booking arrangement that permits the field gadgets to process their own chart courses and transmission plans. The Figures show the synopsis of contrasts among existing directing and booking calculations like DiGS/DiGS-CD contrasted with proposed Wireless DDSR. Test results from two physical testbeds and a huge scope recreation show our answer gives a huge enhancement for network dependability, dormancy, energy proficiency, and disappointment resilience under elements, basic properties for modern applications, over cutting edge at the expense of somewhat higher force utilization and longer organization instatement. In this paper, we have likewise explored the issues of energy proficiency and QoS in a consolidated way for heterogeneous WSN networks within the sight of three energy the executive's methods: to address the issues of varieties of traffic burden and energy accessibility conditions. We have then built up an "energy ease off" instrument, to be coordinated into WSN sensors for DDSR. The DDSR calculation can be executed in any IEEE 02.15.4 standard-based WSN applications with the least alterations. Reproduction results have exhibited that our proposed calculation essentially improves energy effectiveness while fulfilling the QoS prerequisites. The outcomes likewise show that the organization of the crossbreed setup with different fuel sources is an effective, compelling and pragmatic answer for at the same time improves the energy-proficient and QoS issues just as to expand the lifetime of gadgets in heterogeneous WSN networks. We examined the accessibility of a WPSN over various routing algorithms such as unicast, broadcast as well as fading scenarios in this research work. The computation of connectivity probability for every event is carried out mathematically by taking into account the probability of nodes that are active and further evaluated using Monte Carlo simulations. In addition, we examined various routing algorithms by considering battery-powered as well as battery-less nodes that harvest RF energy from PBs, also considering the conditions in which a WPSN is associated. We intend to continue this study in three different ways in future research work: i) using the variable performance of RF-to-DC conversion in the framework that offers more precise as well as genuine outcomes; ii) obtaining the best alternatives analytically by offering the highest connectivity, and the last way is to analyze PBs energy consumption and thereby determining the optimal parameters for an energy-efficient WPSN.

REFERENCES

[1] Arati Manjeshwar,et.al, “APTEEN: A Hybrid Protocol for Efficient Routing and Comprehensive Information Retrieval in Wireless Sensor Networks”, 1530-2075/02,, IEEE, 2002.

[2] W. Heinzelman, A. Chandrakasan, and H. Balakrishnan, “uAMPS ns Code Extensions”. http://wwwmtl.mit.edu/research/icsystems/uamps/ leach.

[3] W. B. Heinzelman. “Application-Specific Protocol Architectures for Wireless Networks”. PhD thesis, Massachusetts Institute of Technology, June 2000.

[4] A. Manjeshwar and D. P. Agrawal. TEEN: A Routing Protocol for Enhanced Efficiency in Wireless Sensor Networks.In 1st International Workshop on Parallel and Distributed Computing Issues in Wireless Networks and Mobile Computing, April 2001.

[5] Michele Rossi,et.al, “Distributed Learning Algorithms for Optimal Data Routing in IoT Networks”, IEEE Transactions on Signal And Information Processing Over Networks, 2373-776X, 10.1109/TSIPN.2020.2975369, VOL. 6, 2020.

[6] N. A. Pantazis, A. Spiridonos, S. A. Nikolidakis, and D. D. Vergados, "Energy-proficient directing conventions in remote sensor networks:Asurvey," IEEE Commun. Surv. Tut., vol. 15, no. 2, pp. 551–591, May 2013.

[7] D. Zordan, B. Martinez, I. Villajosana, and M. Rossi, "On the exhibition of lossy pressure plans for energy compelled sensor organizing," ACM Trans. Sensor Netw., vol. 11, no. 1, pp. 1–34, Nov. 2014.

[8] N. Cao, E. Masazade, and P. K. Varshney, "A multiobjective improvement based sensor choice strategy for target following in remote sensor organizations," in Proc. sixteenth Int. Conf. Inf. Combination, 2013, pp. 974–980.

[9] M. Centenaro, M. Rossi, and M. Zorzi, "Joint improvement of lossy pressure and transport in remote sensor organizations," in Proc. IEEE Globecom Workshops, Washington, DC, USA, Dec. 2016, pp. 1–6.

[10] P. Giselsson and S. Boyd, "Direct intermingling and metric determination for Douglas–Rachford parting and ADMM," IEEE Trans. Autom. Control, vol. 62, no. 2, pp. 532–544, Feb. 2017.

[11] A. Biason, C. Pielli, A. Zanella, and M. Zorzi, "Access control for IoT hubs with energy and constancy requirements," IEEE Trans. Remote Commun., vol. 17, no. 5, pp. 3242–3257, May 2018.

[12] F. Iutzeler, P. Bianchi, P. Ciblat, and W. Hachem, "Unequivocal union pace of a conveyed rotating course technique for multipliers," IEEE Trans. Autom. Control, vol. 61, no. 4, pp. 892–904, Apr. 2016.

[13] S. Javaid, H. Fahim, Z. Hamid, and F. B. Hussain, "Traffic-mindful blockage control (TACC) forwirelessmultimedia sensor organizations," Multimedia Tools Appl., vol. 77, no. 4, pp. 4433–4452, Feb. 2018.

[14] Shaoyong Guo,at.al, "Confided in Cloud-Edge Network Resource Management: DRL-driven Service Function Chain Orchestration for IoT", IEEE Internet of Things Journal, DOI 10.1109/JIOT.2019.2951593, 2327-4662 (c) 2019 IEEE.

[15] H. Hawilo, M. Jammal, and A. Shami, "Organization work virtualizationaware orchestrator for administration

work affixing position in the cloud," IEEE Journal on Selected Areas in Communications, vol. 37, no. 3, pp. 643–655, March 2019.

[16] M. M. Tajiki, S. Salsano, L. Chiaraviglio, M. Shojafar, and B. Akbari, "Joint energy productive and qos-mindful way allotment and vnf position for administration work tying," IEEE Transactions on Network and Service Management, vol. 16, no. 1, pp. 374–388, March 2019.

[17] Junyang Shi.et.al, "Distributed Graph Routing and Scheduling for Industrial Wireless sensor-actuator Networks", 1063-6692, 2019 IEEE, IEEE/ACM TRANSACTIONS ON NETWORKING, VOL. 27, NO. 4, AUGUST 2019.

[18] L. Gu, D. Zeng, S. Tao, S. Guo, H. Jin, A. Y. Zomaya, and W. Zhuang, "Decency mindful powerful rate control and stream planning for network utility boost in network administration chain," IEEE Journal on Selected Areas in Communications, vol. 37, no. 5, pp. 1059–1071, May 2019.

[19] X. Chen, Z. Zhu, J. Guo, S. Kang, R. Proietti, A. Castro, and S. J. B. Yoo, "Utilizing blended system gaming to acknowledge motivation driven vnf administration chain provisioning in representative based flexible optical interdatacenter networks," IEEE/OSA Journal of Optical Communications and Networking, vol. 10, no. 2, pp. A232–A240, Feb 2018.

[20] C. Mouradian, S. Kianpisheh, M. Abu-Lebdeh, F. Ebrahimnezhad, N. T. Jahromi, and R. H. Glitho, "Application segment arrangement in nfvbased cross breed cloud/mist frameworks with portable haze hubs," IEEE Journal on Selected Areas in Communications, vol. 37, no. 5, pp. 1130–1143, May 2019.

[21] Z. Chen, S. Zhang, C. Wang, Z. Qian, M. Xiao, J. Wu, and I. Jawhar, "A tale calculation for nfv chain arrangement in edge figuring conditions," in 2018 IEEE Global Communications Conference (GLOBECOM), Dec 2018, pp. 1–6.

[22] Thien Duc Nguyen.et.al, "A Distributed Energy-Harvesting-Aware Routing Algorithm for Heterogeneous IoT Networks", DOI 10.1109/TGCN.2018.2839593, IEEE, IEEE Transactions on GREEN Communications and Networking, 2473-2400, 2018 IEEE

[23] P. K. Sharma, M. Chen, and J. H. Park, "A product characterized haze hub based disseminated blockchain cloud engineering for iot," IEEE Access, vol. 6, pp. 115–124, 2018.

[24] F. Ferrari, M. Zimmerling, L. Mottola, and L. Thiele, "Low-power remote transport," in Proc. SenSys, 2012, pp. 1–14.

[25] F. Ferrari, M. Zimmerling, L. Thiele, and O. Saukh, "Productive organization flooding and time synchronization with polished," in Proc. SenSys, Apr. 2011, pp. 73–84.

[26] O. Landsiedel, F. Ferrari, and M. Zimmerling, "Mayhem: Versatile and productive all-to-all information sharing and in-network preparing at scale," in Proc. SenSys, 2013, p. 1.

[27] M. Doddavenkatappa, M. C. Chan, and B. Leong, "Sprinkle: Fast information dispersal with useful impedance in remote sensor organizations," in Proc. NSDI, 2013, pp. 269–282

[28] M. Doddavenkatappa and M. C. Chan, "P3: A functional parcel pipeline utilizing simultaneous transmissions for remote sensor organizations," in Proc. IPSN, 2014, pp. 203–214.

[29] N. Michelusi and M. Zorzi, "Optimal adaptive random multiaccess in energy harvesting wireless sensor networks," IEEE Trans. Commun., vol. 63, no. 4, pp. 1355–1372, Apr 2015.

[30] T. D. Nguyen, J. Y. Khan, and D. T. Ngo, "An adaptive MAC protocol for RF energy harvesting wireless sensor networks," in Proc. of GLOBECOM'16, 2016.

[31] D. Hasenfratz, A. Meier, C. Moser, J. J. Chen, and L. Thiele, "Examination, correlation, and enhancement of directing conventions for energy reaping remote sensor organizations," in Proc. of SUTC'10, Jun 2010, pp. 19–26.

[32] G. Martinez, S. Li, and C. Zhou, "Wastage-mindful steering in energy harvesting Remote Sensor Networks," IEEE Sensors J., vol. 14, no. 9, pp. 2967–2974, Sep 2014.

[33] P. Gong, Q. Xu, and T. M. Chen, "Energy collecting mindful directing convention for remote sensor organizations," in Proc. of CSNDSP'14, Jul 2014, pp. 171–176.

[34] J. Bai, M. Fan, J. Yang, Y. Sun, and C. Phillips, "Keen energy collecting steering convention for WSN based E-wellbeing frameworks," in Proc. of the 2015 Workshop on Pervasive Wireless Healthcare (MobileHealth '15), 2015, pp. 23–28.

[35] Q. Tan, W. An, Y. Han, Y. Liu, S. Ci, F.- M. Shao, and H. Tang, "Energy collecting mindful geography control with power transformation in remote sensor organizations," Ad Hoc Networks, vol. 27, pp. 44 – 56, 2015.

[36] T. He, K. W. Jawline, and S. Soh, "On remote force move and max stream in battery-powered remote sensor organizations," vol. 4, pp. 4155–4167, Aug 2016.

[37] N. Michelusi and M. Zorzi, "Optimal adaptive random multi-access in energy harvesting wireless sensor networks," IEEE Trans. Commun., vol. 63, no. 4, pp. 1355–1372, Apr 2015.

[38] D. Estrin, R. Govindan, J. Heidemann, and S. Kumar. "Next Century Challenges: Scalable Coordination inWireless Networks". In Proceedings of the fifth Annual ACM/IEEE International Gathering on Mobile Computing and Networking (MOBICOM), pages 263–270, 1999.

[39] W. Heinzelman, A. Chandrakasan, and H. Balakrishnan. "Energy-Efficient Communication Protocols for Wireless Microsensor Networks". In Proceedings of Hawaiian International Gathering on Systems Science, January 2000.

[40] C. Intanagonwiwat, R. Govindan, and D. Estrin. "Coordinated Dissemination: A Scalable and Robust Communication Worldview for Sensor Networks ". In Proceedings of the sixth Annual ACM/IEEE International

Conference on Mobile Figuring and Networking(MOBICOM), pages 56–67, August 2000.

[41] M. Jiang, J. Li, and Y. C. Tay. "Bunch Based Routing Protocol". Web Draft, 1999.

[42] Josef Börcsök.et.al, "Safe Position Detection Based on Safety System-on-Chip (SSoC) for Wireless IoT Application", INTERNATIONAL JOURNAL OF CIRCUITS, SYSTEMS AND SIGNAL PROCESSING, DOI: 10.46300/9106.2020.14.132, ISSN: 1998-4464,Volume 14, 2020.

[43] Michael H.et.al, "Investigation of a Safety Parameter Observer for Wireless Communication", INTERNATIONAL JOURNAL OF CIRCUITS, SYSTEMS AND SIGNAL PROCESSING, DOI: 10.46300/9106.2020.14.128, ISSN: 1998-4464, Volume 14, 2020.

[44] Aymen Zreikat, "Performance Evaluation of 5G/WiFi-6 Coexistence", INTERNATIONAL JOURNAL OF CIRCUITS, SYSTEMS AND SIGNAL PROCESSING, DOI: 10.46300/9106.2020.14.116, ISSN: 1998-4464, Volume 14, 2020

International Journal of Engineering Trends and Technology
ISSN: 2231 – 5381 /doi:10.14445/22315381/IJETT-V69I9P208

Volume 69 Issue 9, 56-65, September, 2021

Original Article

Adaptive Scheduling Technique Based Operating System for Wireless Sensor Networks and Internet of Things

Anita Patil[1,*] and Rajashree.V.Biradar[2]

[1]*Department of CSE, Ballari Institute of Technology and Management, Bellary-583104, Karnataka, India*
[2]*Department of CSE, Ballari Institute of Technology and Management, Bellary-583104, Karnataka, India*

[1]anitha.bijapur@gmail.com, [2]rajashreebiradar@yahoo.com

Abstract - *Wireless Sensor Network (WSN) has significance in various fields, including home and industry automation, medical instrumentation, military surveillance, etc. Though the battery-dependent and resource-constrained tiny sensor nodes challenge the design of the operating system (OS) very critically, there are many OS that exists for WSN and IoT. However, the available operating systems have their own advantages and disadvantages for various WSN applications. Among those, TinyOS is the widely used, highly documented, and most suitable OS for low power devices. Conversely, having only First Come First Serve (FCFS) scheduler is the major limitation of TinyOS that hinders the application developers from using this. The necessity of other schedulers is justified in the motivation part of the paper. Thus, to overcome this problem, the new adaptive scheduling algorithm proposed in this paper provides a choice for FCFS, Priority, and Round Robin schedulers. Moreover, the priority scheduler itself can represent the schedulers SJF, EDF, and any application requirement-based prioritizing scheduler. Accordingly, the application developer can adapt any scheduler for the application. This changing order of tasks' execution also benefits the overall system performance by giving reduced average waiting for time (AWT) and average turnaround time (ATT), resulting from inefficient utilization of resources and better throughput.*

Keywords - *IOT operating systems, TinyOS Scheduling techniques, Wireless Sensor Network, WSN Applications, WSN operating systems.*

I. INTRODUCTION

Wireless Sensor Network (WSN), being a very special type of network, has many applications in different fields of technology and also is the basis for advanced technologies like IoT. The main specialties of this network are communicating wirelessly and sensing the surrounding environment with the help of tiny sensor nodes. These 2 features are tremendously advantageous as WSN applications also cover the fields where the physical presence of the human being is either impossible or not feasible. Here is an example of industrial automation where in some sort of industry, the working environment temperature may be too high, and there may be life-threatening hazardous operating processes, etc., because of which the physical presence of human beings at that place is not feasible. Another example is medical instrumentation, where the tiny instruments of medical diagnosis may need to pass through human body organs. Like this, there are numerous applications where sensor nodes are working on behalf of the human being. Moreover, wired communication is not at all practical in the densely deployed numerous sensor nodes in the application area [1]. But this wireless communication and the tiny-sized nature of the sensor nodes themselves challenge the design of the Operating System (OS) very critically. Despite that, there are many OS exist for WSN as of today. Some of them are application-specific, some are hardware-specific, etc. For e.g., RTOS (real-time operating system) is meant for real-time applications, raspbian is for the only raspberry pi platform, RIOT (Real-time OS for IoT) is a real-time OS for IoT, and so on. Thus, none of them is general purpose. Such many issues make the operating system of WSN itself a research issue.

Basically, there are many research issues in WSN, including operating systems of WSN, uninterrupted support for diversified numerous applications of WSN [2, 3], energy efficiency, routing in WSN, and so on. The novel work presented in this paper is for the OSs of WSN and IoT. By the way, WSN being the backbone support of IoT technology, share the same set of OSs with IoT [4, 5, 9]. The comparative analysis of some popular OSs: TinyOS, Contiki, RIOT, freeRTOS, MANTIS, and SOS concludes that TinyOS is the open-source, most robust, innovative, traditional, highly documented, and widely used OS. Moreover, this is the most suitable OS for low power devices, which is the main concern for energy efficiency [6, 7, 8, 13]. Being energy efficient means a lot as the densely deployed and resource-constrained tiny nodes have to survive for longer in application fields to achieve their

purpose [19]. Because the unattended and battery-dependent life span of the nodes decides the effectiveness of the application. For example, the battery life of the mica2 mote while running the blink application in different OS, namely TinyOS, MANTIS OS, and SOS, are respectively 22.49 days, 7.84 days, and 7.73 days (approximately) [10].

Ultimately, TinyOS is the OS for resource-constrained, low-power tiny devices being used in various applications of both WSN and IoT [11, 12, 13]. Though with this major concern towards energy efficiency [12] and less memory footprint (less than 400 bytes), TinyOS has the disadvantage in scheduling, as it has only a First Come First Serve (FCFS) scheduler [14, 15, 16, 17]. In FCFS, the tasks get processed based on their arrival order that can be appropriate for some kind of applications or at some situation only. Although this is one of the best scheduling algorithms, it can't fulfill the requirements of all types of tasks and applications. Thus, having only the FCFS scheduling technique affects other parameters also as not supporting real-time applications, reduced performance of some tasks, inefficient usage of resources, etc. Instead, if the operating system is flexible in scheduling by having multiple schedulers like priority scheduler, round-robin scheduler, the shortest job first scheduler, etc., then it is more beneficial for the tasks, applications, as well as resource utilization. In this direction, we have surveyed [18] the recent literature for other possible scheduling algorithms for TinyOS. Then, came to the conclusion of designing and integrating the new adaptive scheduling algorithm that allows the application developer to adapt a suitable scheduler from the list of FCFS scheduler, Priority scheduler, and Round Robin scheduler.

In this regard, the first section of this paper introduces WSN applications' requirements and TinyOS along with FCFS scheduling, and then the second section articulates the compulsion of other types of schedulers, thereby conveying the scope of this novel work. The new adaptive scheduling algorithm implementation is explored in the 3rd section, followed by the results and discussion in the 4th section.

II. MOTIVATION

In this technological era, where every field of life is evolved by technologies like WSN, IoT, robotics, artificial intelligence, and machine learning, etc. Consequently, the daily life needs are getting fulfilled through one or the other hardware appliance, which in turn run by software technology. An operating system is a basis for such appliances along with application-specific software. Specifically, OS of WSN and IoT are very challenging as they have to reside in limited memory, then control and coordinate the constrained resources of the tiny sensor node [5, 19]. Moreover, WSN and IoT cover a wide range of distinct fields with the applications like seismic detection, military surveillance, wildlife study, underwater study, medical instrumentation, industrial automation, etc. The varying requirements of such diversified applications resulted in the number of OSs with specific features, like real-time application supporting OS, platform-specific OS, energy-efficient OS, etc. This causes the application developer to study all these OS in detail while selecting a suitable one for new application development. This makes the application developer invest the time and put more effort, along with the intended application designing. Thus, here is the necessity of surveying the existing OS, then improvise the best OS among them as a generalized OS that can be a default selection to cover a wider range of applications.

Based on the requirements of diversified WSN applications [2, 3], the sensor node can have multiple tasks like light sensing, sound sensing, vibration sensing, temperature sensing, data processing, communicating to the base station, etc. For example, in wildlife study, if the application is for capturing the images of wild animals, monitoring the surrounding environment, and recording the video of any event occurrence like wandering of an animal, fighting of animals, or the activities of an animal when it is alone, then different sensors like light sensing, sound sensing, temperature sensing, etc., need to function like the tasks. At the same time, other tasks include processing the gathered data from different sensors, aggregating the data, and communicating to the base station. Thus, when there are multiple tasks involved in an application, then definitely the order of their processing will have an impact on the application result.

As already said, the event-driven TinyOS has one and only FCFS scheduler that processes the tasks in the order of their occurrences as a natural practice, but the parallel and continuous tasks may need a change in their processing order in some situations. For instance, in wildlife study applications, if the temperature exceeds the defined threshold limit, then temperature sensing, processing this sensed data, and communicating this processed data to the base station must be given the highest priorities compared to all other tasks. Thereby predicting the forest fire, the fire accident can be prevented. For such an application priority scheduler is beneficial. In some applications where scheduling is done using SJF scheduler, there the average waiting time (AWT) and the average turnaround time (ATT) of all tasks will be lesser satisfying all tasks as well as the application. Moreover, such scheduling improves the overall system performance by utilizing all the resources efficiently [19]. While in some applications giving equal opportunity to each task in each round may be the requirement. Such type of scheduling is the responsibility of the round-robin scheduler (RR). At the same time, the RR scheduler gives the least possible response time to each one of the tasks giving an illusion of interactive task processing. Actually, this is also the better option for TinyOS as it is not having real-time application support. Like this, there are different

options for scheduling a single processor among multiple tasks, and those have to get streamlined in this new adaptive scheduling algorithm. This is the main motivation behind this novel work.

On the other hand, authors in [20] say that there are abundant applications of WSN and IoT, for which specialized OSs are needed, but a slow reaction of OS researchers is an alarm for the urgency of more research in this area. However, in reality, OS developers/researchers are rare due to the fact that it is a highly specialized field with a very slow curve and tolerance for change. This is one more motivating point for this research. In this direction, authors in [8] did a detailed survey in 2016. As per the survey, TinyOS alone is in 60% usage, and the remaining all OS together is in 40% usage [8]. The same is depicted below Figure1.

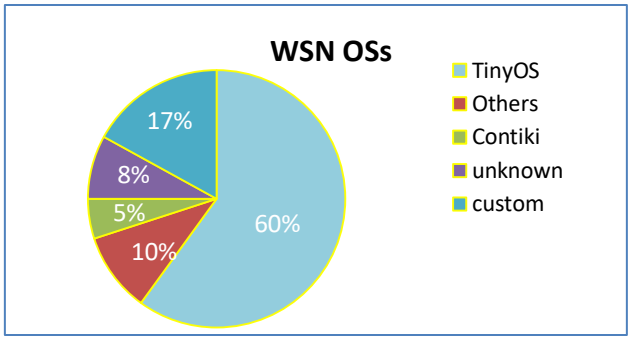

Fig. 1Usage of different OSs (adapted from[8])

In this situation where TinyOS itself is covering more than 50% of the WSN and IoT applications, then here is the necessity of research in TinyOS to nullify its disadvantages.

The detailed study of TinyOSreveals the advantages and disadvantages that motivated us to proceed further in the field of processor scheduling among multiple tasks of the application. Further, the detailed survey on "Scheduling Techniques for TinyOS" [18] in 2016 concludes that there is the possibility of designing and implementing a new algorithm that can retain the existing FCFS scheduler and also provide other important schedulers.

In fact, the TinyOS developers themselves provided the document in the "docs" folder of TinyOS documentation to encourage researchers to design and integrate new schedulers in TinyOS. The document is available as TinyOS Enhancement Proposal-106 (TEP-106).

- 2.55*1.24*0.24 inches, within which 10kb RAM, 48kb flash memory, 2*AA batteries, 8MHz MSP430 microcontroller, 3 sensors, and 3 LEDs, etc., objects are soldered, which all together weighs 23 grams(excluding batteries weight)[23,25].

Thus, there are many motivating factors behind this empirical work of the new adaptive scheduling algorithm that retains the existing FCFS scheduler and also provides 2 more schedulers in choice.

III. IMPLEMENTATION

The main work has the flow as shown in the flowchart of Figure-2. Here, the job queue is nothing but the flash memory of the sensor node. For example, Telosb node has 48kb flash memory and 10kb RAM. For better utilization of the main resources in the node, which is input-output devices and processor (herein TinyOS, processor or CPU is nothing but MSP430 microcontroller), the good combination of I/O (Input/Output) bound tasks and processor bound tasks are to be placed on RAM. If these tasks don't need any fashion of execution, then the pre-existing FCFS scheduler itself can schedule the processor based on their arrival order; else, the appropriate one from the new adaptive scheduling algorithm schedules the processor. This new adaptive scheduling algorithm provides the choice for FCFS, Priority, and Round Robin (RR) schedulers.

The new adaptive scheduling algorithm implemented in this novel work is named AdaptiveSchedulerC.nc. As the name itself indicates, this scheduler allows an application developer to adapt any of the schedulers as per requirement. Adaptive scheduling algorithm provides choice among 1, 2, and 3 for FCFS, Priority, and Round Robin schedulers, respectively. The application developer has to enter the choice taken in the header file named SchedulerSelection.h. If the priority scheduler is the choice taken, then the priorities for tasks also must be entered in the SchedulerSelection. Header file itself.

This newly designed and developed adaptive scheduling algorithm implementation is carried out as follows.

- Here in this work, tinyos-2.1.2 is installed in Ubuntu 18.04. It can be installed in the Windows system also. TinyOS has a footprint of fewer than 400 bytes, which is the core or base code of OS that has to fit in node memory along with the compiled code of the application and other required software.

- Telosb has MSP430 microcontroller. Hence, the emulator used here is MSPSim [21, 22].

- In the emulator, Telosb is the platform [14, 24] used, which is one of the suitable sensor boards for TinyOS. Like any sensor node, the size of Telosb is also tiny i.e
- The language nesC [26] is used to code an Adaptive scheduling algorithm.
- The interfaces Scheduler, TaskBasic, and McuSleep of the "tos" folder are redefined to implement the new Adaptive scheduling algorithm.

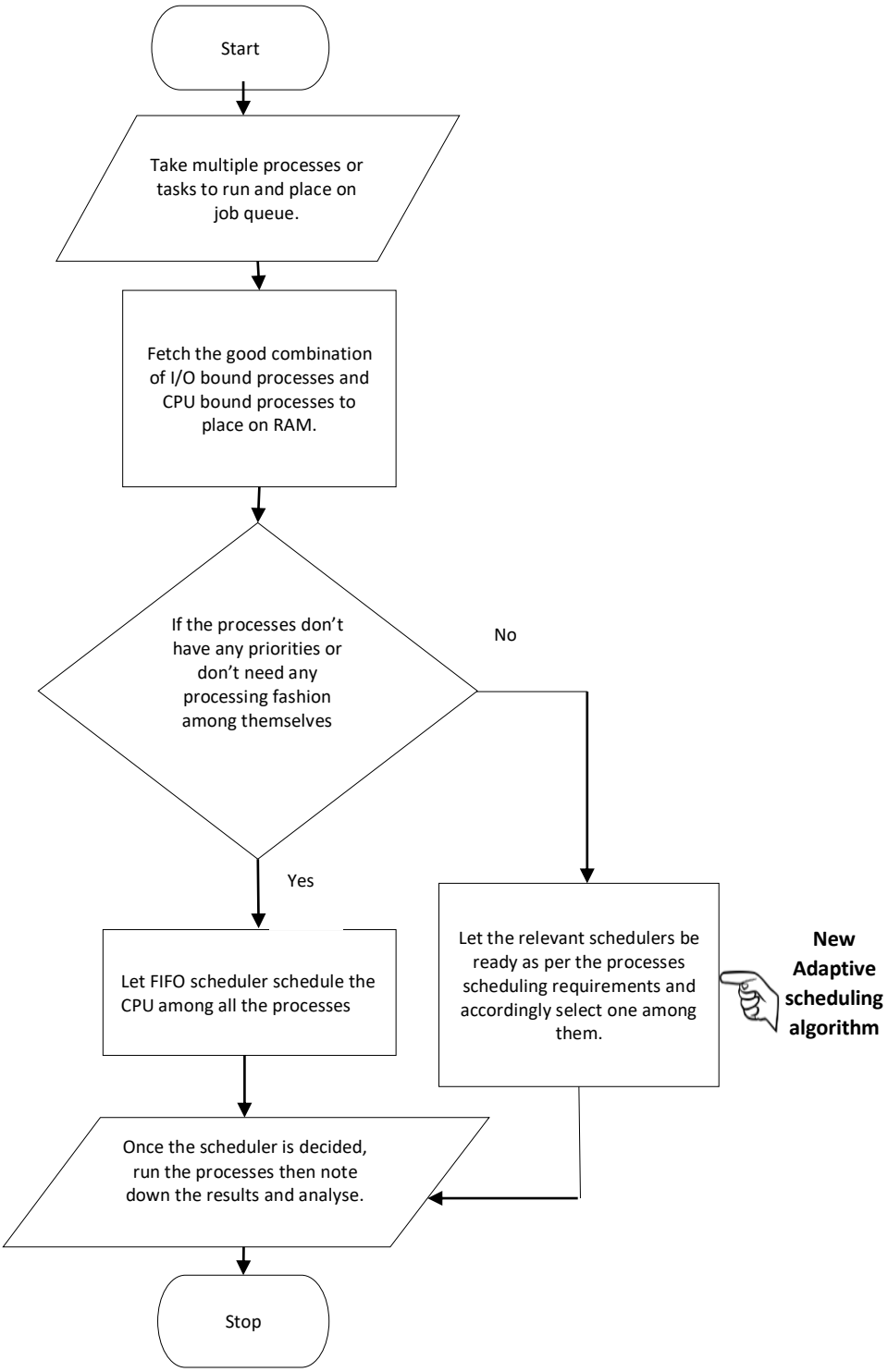

Figure 2. Workflow

The below figure, Fig 3, shows the partial hierarchy of TinyOS-2.1.2 with the newly added schedulers.

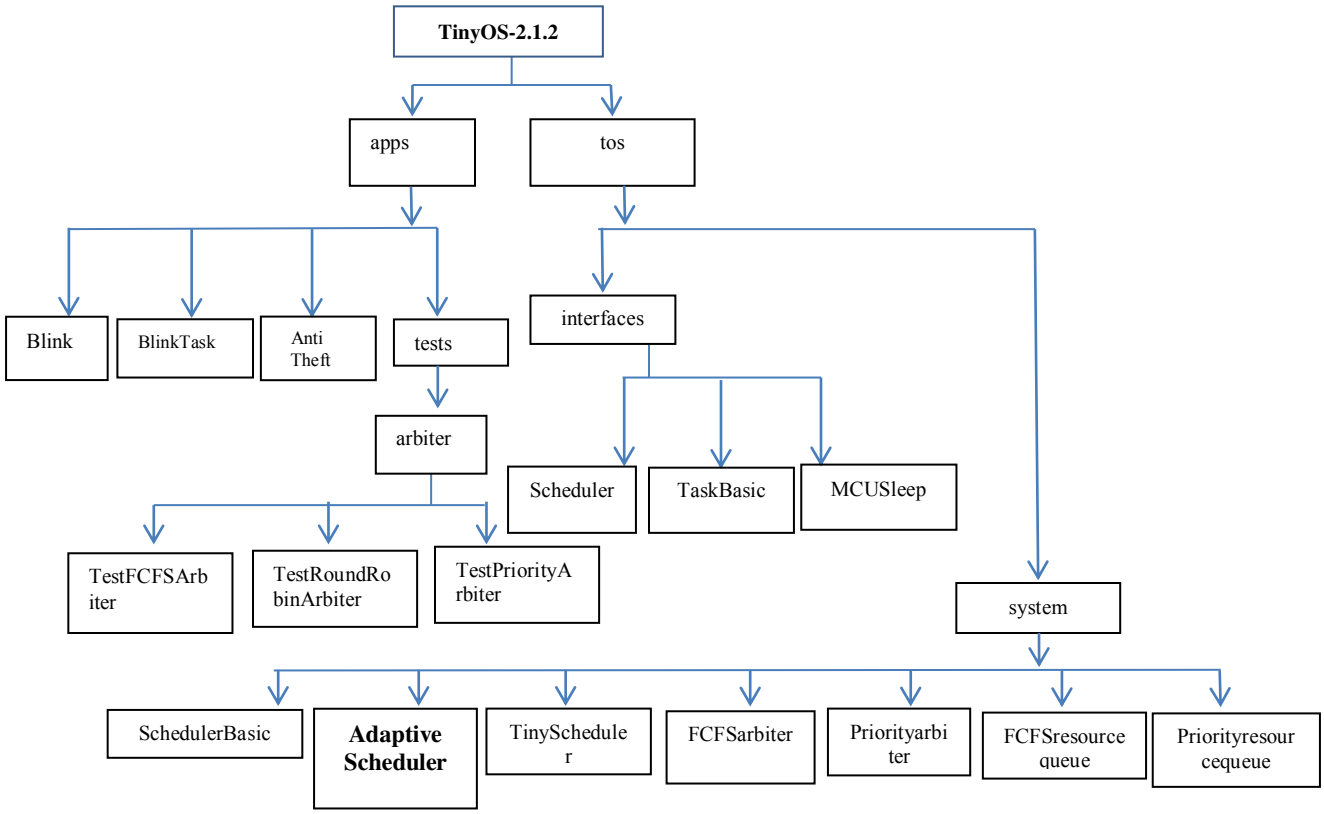

Fig. 3 Partial hierarchy of TinyOS-2.1.2

Basically, in TinyOS-2.1.2, at the different hierarchy, there are many folders like tos (core OS), app (example applications), docs (documentation), system, interfaces, lib, platforms, etc. [27]. In the docs folder, there are around 40 TEPs (TinyOS Enhancement Proposals) [28], TEP-106 says about scheduler in TinyOS. The folder "tos" contains the core of the operating system, which is dispersed in different sub-folders like system, interfaces, tools, platforms, etc. As shown in Fig-3, the new Adaptive scheduling algorithm is implemented in /tos/system/AdaptiveschedulerP.nc, with the help of the interfaces namely Scheduler, TaskBasic, and McuSleep of **tos** folder.

IV. RESULTS AND DISCUSSION

The results of FCFS, Priority, and RR Schedulers are shown respectively in Figure-4 to Figure-6 below.

Each snapshot shows:

• **Application code editor: -** To see the tasks posting order.

• **Control UI:-** The user interface to control the node, like stop and run the execution.

• **Mote GUI:-**GUI with blinking LEDs, sensors, MSP430 microcontroller, etc.

• **Serial mon for MSPsim:-**To sees the order of execution with some printf statements, as there are only 3 LEDs and the number of tasks may exceed 3. Moreover, taking the results from these printf statements is easier than monitoring the blinking LEDs.

All these 3 schedulers are tested for the same application. To read the results of tasks' execution order, the colors-Red1, Green1, Blue1, and Pink1 are displayed inside the tasks test0, test1, test2, and test3, respectively. In task2, the searching function is written to observe the task processing that also executes correctly. As shown in the code editor of the below screenshots, for all three schedulers, the application is the same that posts the tasks with the order test3, test2, test0, test1.

As shown in the below screenshot of Fig-4, the FCFS scheduler schedules the processor to the tasks in the same order of their posting, i.e., First Come First Serve, resulting in the display statements for PINK1, BLUE1, RED1, GREEN1 at MSPSim's serial monitor.

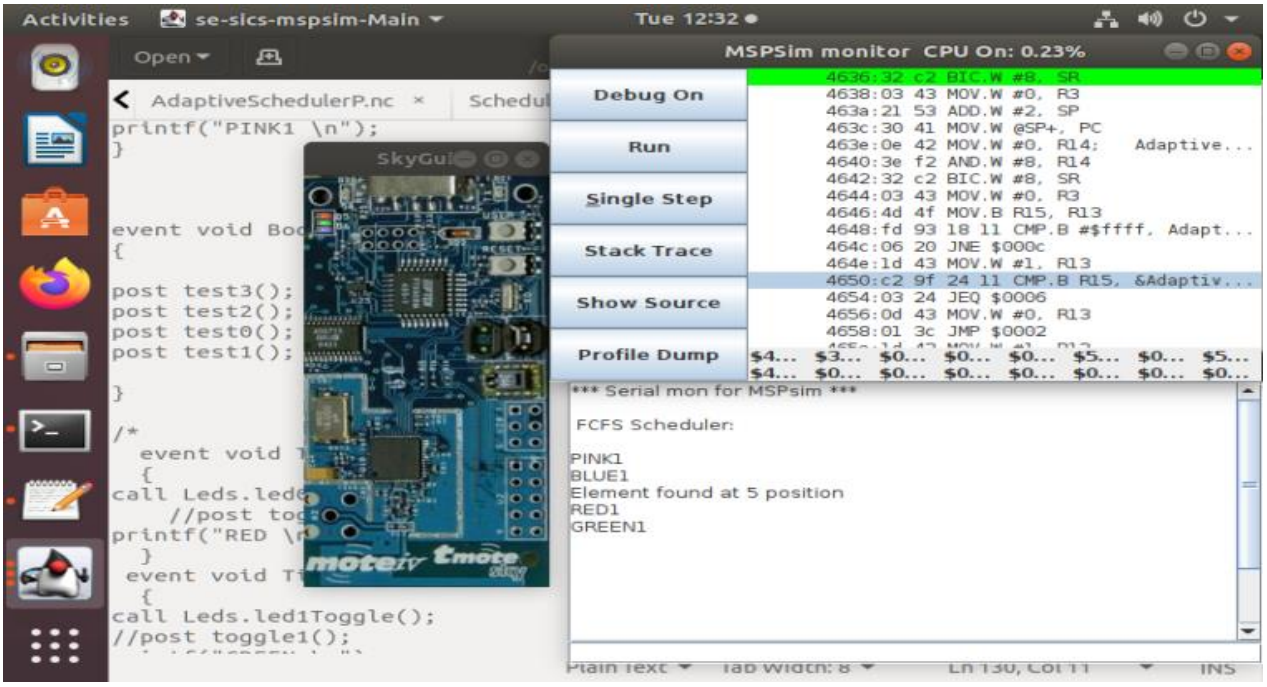

Fig. 4 FCFS scheduler

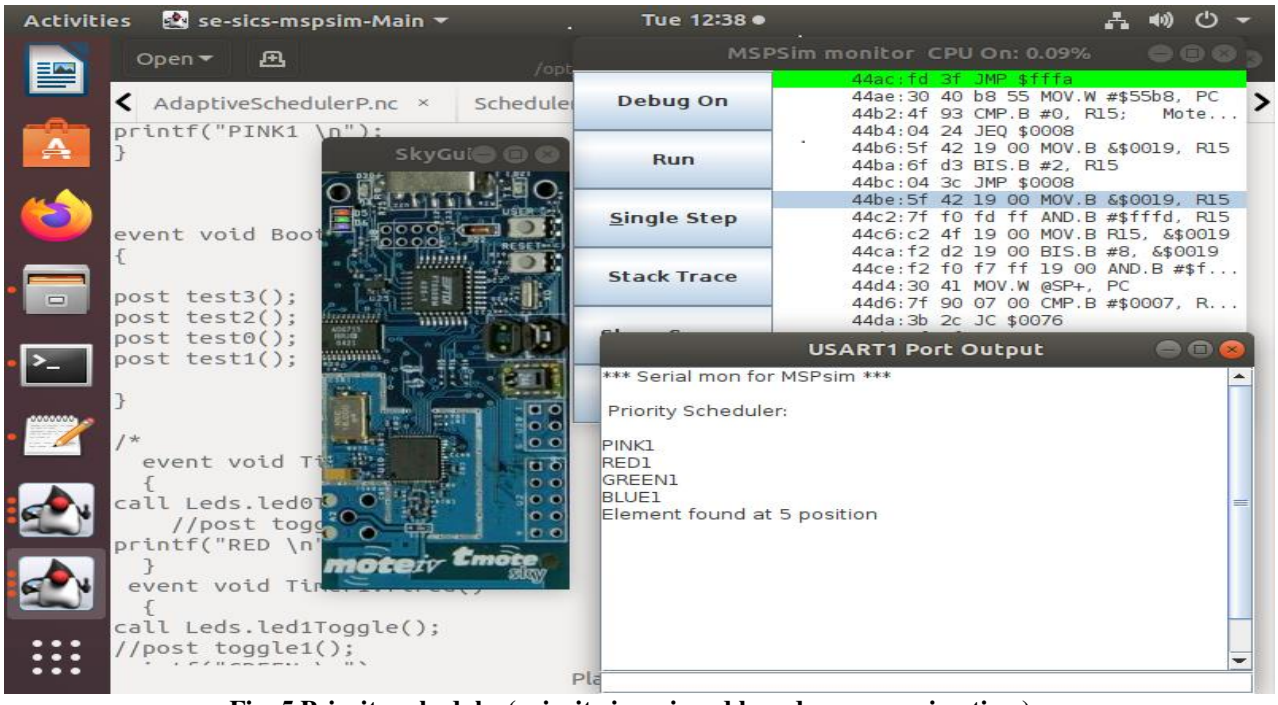

Fig. 5 Priority scheduler(priority is assigned based on processing time)

As shown in the above screenshot of Fig-5, the priority scheduler schedules the processor to the tasks as per priorities assigned to them in SchedulerSelection.h. The largest number indicates the highest priority. With this notion, priorities assigned are 4→test3, 3→test0, 2→test1 and 1→test2 resulting in display statements forPINK1, RED1, GREEN1, BLUE1 at serial monitor of MSPsim.

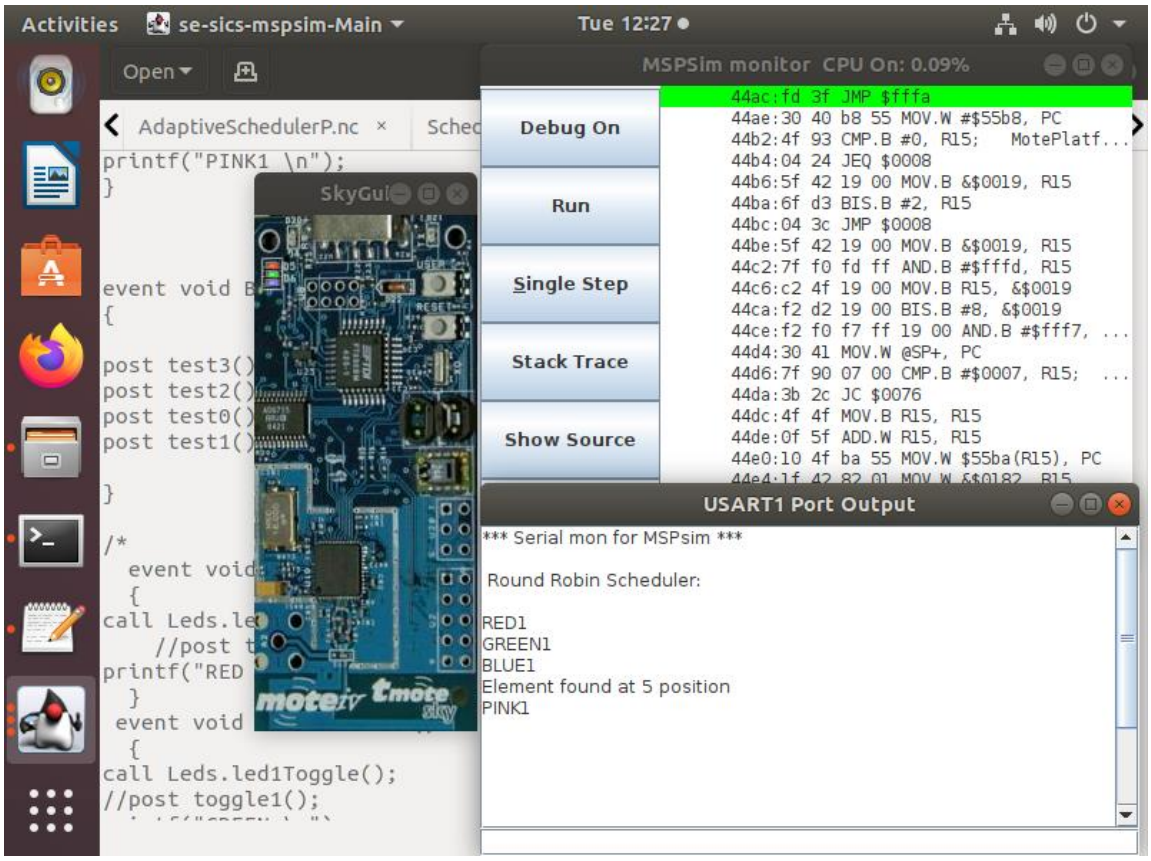

Fig. 6 Round Robin (RR) scheduler

The above snapshot of figure-6 shows RR scheduler results. In RR scheduling, at every round, every task will get a chance to get processed by the processor. It schedules the processor to the tasks in the order of their IDs generated during their definition coding in the application program. In the given program, the tasks are defined in the order test0, test1, test2, test3, and hence, the IDs generated are 0,1,2,3, respectively. Accordingly, the displays are for RED1, GREEN1, BLUE1, PINK1.

Like this, an adaptive scheduling algorithm permits the application developer to adapt the necessary scheduler for the application. This change in task order not only satisfies the tasks but also improves the overall performance of the system with the best utilization of all the resources.

Resource utilization or scheduling algorithm performance can be measured in terms of Average Waiting Time (AWT) and Average Turnaround Time (ATT) of tasks. The lesser the AWT and ATT are, the better the performance [29]. The below-shown tables and graphs of all 3 figures illustrate a theoretical example that runs 4 tasks with the depicted arrival times and processing times. The performance analysis of FCFS scheduling, Priority scheduling, and RR scheduling are respectively explored by figures 7, 8, and 9. Tables display the arrival time, processing time, waiting time, and turnaround time for each one of the tasks along with AWT and ATT. The same is depicted in their respective graphs.

Tasks	Arrival timeless	Processing time msec	Waiting Time msec	Turnaround Time msec
Task 1	0	2	0	2
Task 2	1	4	1	5
Task 3	2	1	4	5
Task 4	3	3	4	7
			AWT= 2.25 msec	ATT= 4.75 msec

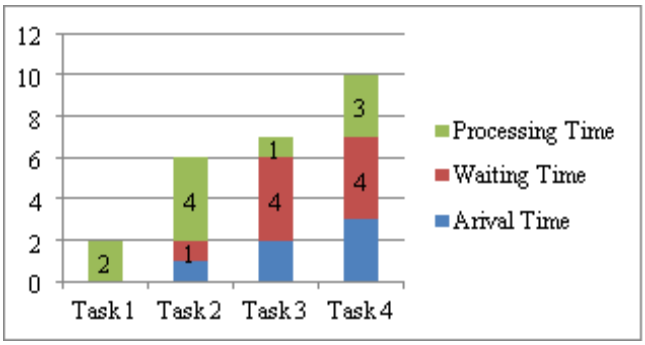

Fig. 7 Performance analyses in FCFS scheduling

Tasks	Arrival time msec	Processing time msec	Waiting Time msec	Turnaround Time msec
Task 1	0	2	0	2
Task 2	1	4	5	9
Task 3	2	1	0	1
Task 4	3	3	0	3
			AWT= 1.25 msec	ATT= 3.75 msec

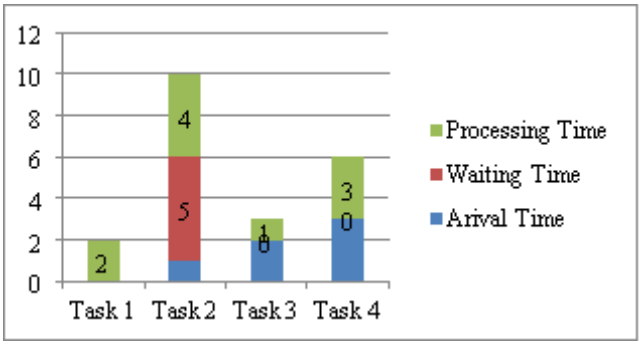

Fig. 8 Performance analysis in Priority scheduling (priority is assigned based on processing time)

Tasks	Arrival time msec	Processing time msec	Waiting Time msec	Turnaround Time msec
Task 1	0	2	3	5
Task 2	1	4	5	9
Task 3	2	1	0	1
Task 4	3	3	3	6
			AWT= 2.75 msec	ATT= 5.25 msec

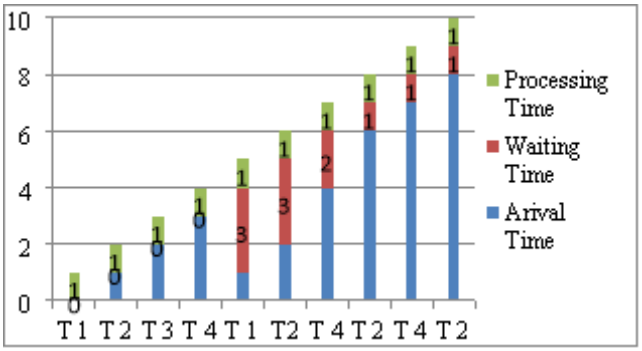

Fig. 9 Performance analyses in RR scheduling

In the RR scheduling graph, the tasks' names are taken as T1, T2, T3, and T4 instead of Task1, Task2, Task3, and Task4, so that they can fit in the chart area. In priority scheduling, the priorities assigned to the tasks Task1, Task2, Task3, and Task4 are respectively 2, 4, 1, and 3. In this example, priority is based on the processing time of the tasks. The task with the least processing time gets the highest priority, and here in this example, the smallest number represents the highest priority. Though, instead of Task3 of priority 1, task Task1 gets executed first.

The reason is, at 0thmsec, only Task1 arrived and start getting processed. Since it is the non-preemptive priority scheduling, Task1 gets completely executed without preempting in between, even when high-priority tasks arrive. By the end of Task1 execution, the remaining all 3 tasks arrive. Then scheduling continues based on their priorities, i.e., Task3, Task4, and Task2. Thus priority assignment can be done based on any criteria such as Early Deadline First (EDF), foreground tasks first, interactive tasks first, etc.

The comparative analysis of the performance of all 3 scheduling algorithms is explored in below Table-1 and the graph of Fig-10**.** The resultant AWT shows that the priority scheduler is the best with nearly half of the AWT of FCFS, whereas the AWT of RR is more than both FCFS and priority scheduling, but important here is that the order of tasks processing is as per the requirement of RR scheduler. Correspondingly ATT also has the same influence, which is, ATT of priority scheduler is least, and that of RR is more than both priority and FCFS schedulers.

Table.1 Performance analysis of FCFS, Priority, and RR scheduling algorithms.

Tasks	Arrival time msec	Processing time msec	AWT FCFS msec	AWT Priority msec	AWT RR msec	ATT FCFS msec	ATT Priority msec	ATT RR msec
Task 1	0	2	0	0	3	2	2	5
Task 2	1	4	1	5	5	5	9	9
Task 3	2	1	4	0	0	5	1	1
Task 4	3	3	4	0	3	7	3	6
			AWT= 2.25 msec	AWT= 1.25 msec	AWT= 2.75 msec	ATT= 4.75 msec	ATT= 3.75 msec	ATT= 5.25 msec

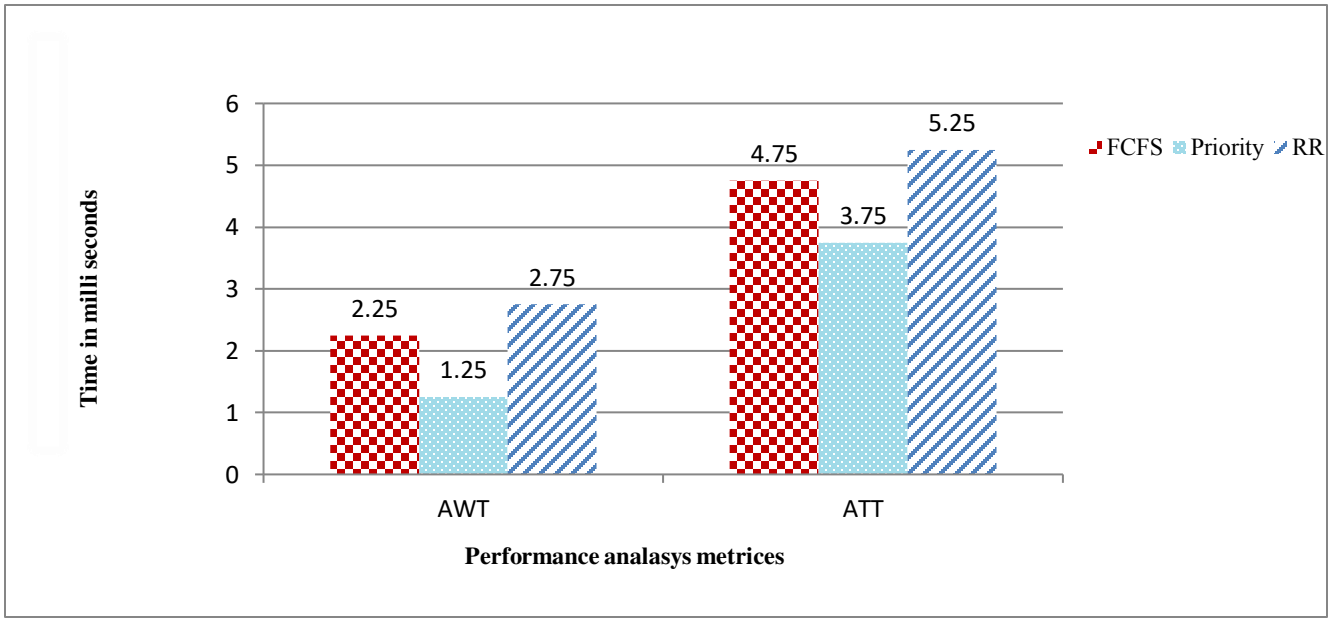

Fig. 10 Performance analysis of FCFS, Priority, and RR scheduling algorithms.

V. CONCLUSION

For decades many researchers working on energy efficiency in WSN declare that tinyOS is the best OS for resource-constrained and low-power tiny devices being used in WSN and IoT applications. Even knowing this fact, application developers hesitate to use this OS as it has only an FCFS scheduler that can't support the diversified applications whose needs may be either SJF or RR or any other scheduling. Nonetheless, now the Adaptive scheduling algorithm proposed in this paper provides choice for FCFS, Priority, and RR schedulers, thereby inspiring the application developer to use TinyOS to get the benefit of energy efficiency nature. At the same time, the priority scheduler itself can represent the schedulers SJF and EDF by assigning priorities to the tasks based on different lengths and different deadlines, respectively. As well, an application developer can assign the priorities based on the criteria such as interactive tasks first, foreground jobs first, likewise to fulfill the application requirement. This change in the order of tasks' execution also benefits the overall system performance by giving reduced AWT and reduced ATT resulting inefficient utilization of limited resources and better throughput of the overall system.

REFERENCES

[1] AkhilendraPratap Singh, Ashish Kr Luhach, Xiao-ZhiGao, Sandeep Kumar and DiptenduSinha Roy. Evolution of wireless sensor network design from technology-centric to user-centric: An architectural perspective, International Journal of Distributed Sensor Networks, 16(8) (2020) DOI: 10.1177/1550147720949138

[2] Ahmad Ali [1,*], Yu Ming [1], SagnikChakraborty[2] and SaimaIram[2]. Review-A Comprehensive Survey on Real-Time Applications of WSN, Future Internet, 9(77) (2017) ; doi:10.3390/fi9040077 www.mdpi.com/journal/futureinternet

[3] DionisisKandris, Christos Nakas, DimitriosVomvas and GrigoriosKoulouras.Applications of Wireless Sensor Networks: An Up-to-Date Survey- Review. Appl. Syst. Innov. 3(14)(2020) doi:10.3390/asi3010014 www.mdpi.com/journal/asi

[4] Rebin B Khoshnaw[1], Dana FarhadDoghramachi, Mazin S. Al-Hakeem.A Review on Internet of Things Operating Systems, Platforms, and Applications. Conference Paper · DOI:10.23918/iec2017.06 February (2017)

[5] ZoranCekerevac, Zdenek Dvorak, Tamara Pecnik.Top seven IoT operating systems in mid-2020. MEST Journal DOI 10.12709/mest.08.08.02.06 Published: July 8(2) (2020) 47-68

[6] AdiMallikarjuna Reddy V AVU Phani Kumar, D Janakiram, and G Ashok Kumar.Operating Systems for Wireless Sensor Networks: A Survey Technical Report. May 3, (2007) 1-30

[7] Nahla S. Abdel Azeem 1, Ibrahim Tarrad 2, Anar Abdel Hady 3,4, M. I. Youssef 2, and Sherine M. Abd El-kader 3,*.Shared Sensor Networks Fundamentals, Challenges, Opportunities, Virtualization Techniques, Comparative Analysis, Novel Architecture, and Taxonomy. Journal of Sensor and Actuator Networks. (2019), doi:10.3390/jsan8020029

[8] Muhammad Amjad, Muhammad Sharif, Muhammad Khalil Afzal, and Sung Won Kim.TinyOS-New Trends, ComparativeViews, and Supported Sensing Applications: A Review. IEEE SENSORS JOURNAL, 16(9) (2016).

[9] Hugo Landaluce, Laura Arjona, AsierPerallos, Francisco Falcone, Ignacio Angulo and Florian Muralter.A Review of IoT Sensing Applications and Challenges Using RFID and Wireless Sensor Networks. Sensors 2020, 20, 2495; doi: 10.3390/s20092495 available at www.mdpi.com/journal/sensors

[10] Michael Healy, Thomas Newe, ElfedLewis.Power Management in Operating Systems for Wireless Sensor Nodes. SAS 2007 - IEEE Sensors Applications Symposium San Diego, California USA, (2007) 6-8.

[11] DolvaraGunatilak -Based on tutorial by Mo Sha, RahavDor.TinyOS Tutorial. CSE521S, Spring 2017, CPSL, Cyber-Physical System Laboratory. (2017)

[12] Yousaf Bin Zikria 1, Sung Won Kim 1,*, Oliver Hahm 2, Muhammad Khalil Afzal 3, and Mohammed Y. Aalsalem 4. Internet of Things (IoT) Operating Systems Management: Opportunities, Challenges, and Solution. Sensors, 19(2019) 1793; doi:10.3390/s19081793 www.mdpi.com/journal/sensors

[13] Dang Huynh-Van, Ngan Le-Thi-Chau, Khoa Ngo-Khanh, Quan LE-TRUNG.Towards an Integration of AES Cryptography into Deluge Dissemination Protocol for Securing IoTs Reconfiguration. 2019 IEEE-RIVF International Conference on Computing and Communication Technologies (RIVF).

[14] Cíntia B. Margi, Bruno T. de Oliveira, Gustavo T. de Sousa, Marcos A. SimplicioJr, Paulo S. L. M. Barreto, Tereza C. M. B. Carvalho, Mats Näslund, Richard Gold,Ericsson.Impact of Operating Systems on Wireless Sensor Networks (Security) Applications and Testbeds. IEEE, 978-1-4244-7116-4/10/$26.00 ©2010 IEEE 2010

[15] Piergiuseppe Di Marco, Ericsson Research, Lecture 2 Introduction to Programming WSNs. Principles of Wireless Sensor Networks, https://www.kth.se/social/course/EL2745/, September 1, 2015

[16] Martin Perner.TinyOS Part 1. 182.694 Microcontroller VU, SS 2017

[17] Martin Perner.TinyOS Part 2. 182.694 Microcontroller VU, SS 2017

[18] Anita Patil (1), Dr. Rajashree.V.Biradar (2).Scheduling Techniques for TinyOS: A Review. International Conference on Computational Systems and Information Systems for Sustainable Solutions, 978-1-5090-1022-6/16/$31.00 ©2016 IEEE, (2016) 188-193.

[19] Elhadi M. Shakshuki, Stephen Isiuwe. Resource Management Approach to an Efficient Wireless Sensor Network. 9th International Conference on Emerging Ubiquitous Systems and Pervasive NetworksEUSPN 2018 Procedia Computer Science 141 (2018) 190–198.

[20] Salahuddin M. ElKazak, Cairo University, Masters in Computer Engineering.GEN600 Final Technical Report: Research in the Internet of Things Operating Systems (IoT OS's). Research in IoT OS's, GEN600: Final Technical Report

[21] TinyOS homepage(accessed 2021) available at : http://tinyos.stanford.edu/tinyos-wiki/index.php/MSPSim

[22] Anita Patil, Dr.Rajashree.V.Biradar.Programming the Sensor Nodes in WSN. International Journal of Engineering and Advanced Technology (IJEAT), ISSN: 2249–8958, Volume-8, Issue-2S, December 2018

[23] Wikipedia information about Sensor nodes (accessed 2021), available at https://en.wikipedia.org/wiki/List_of_wireless_sensor_nodes

[24] Ram Prasadh Narayanan[1*], ThazathVeedu Sarath[2], VelloraVeetil Vineeth[3].Survey on Motes Used in Wireless Sensor Networks: Performance & Parametric Analysis. Wireless Sensor Network, 2016, 8, 51-60 Published Online April 2016 in SciRes.http://www.scirp.org/journal/wsn. 2016

[25] Walter Tiberti, DajanaCassioli, Antinisca Di Marco, Luigi Pomante and Marco Santic.A Model-Based Approach for Adaptable Middleware Evolution in WSN Platforms. Journal of Sensor and Actuator Networks. 2021, doi : 10.3390/jsan10010020 https://www.mdpi.com/journal/jsan

[26] Wikipedia information about NesC (accessed 2021), available at https://en.wikipedia.org/wiki/NesC

[27] TinyOS supporting document (accessed 2021), available at https://github.com

[28] TinyOS homepage (accessed 2021) for TEPs, available at: http://tinyos.stanford.edu/tinyos-wiki/index.php/TEPs

[29] Naji A. Majedkan[1],[*], Abdulraheem J. Ahmed[2], Lailan M. Haji[3], (2020).CPU Scheduling Techniques: A Review on Novel Approaches Strategy and Performance Assessment. Journal of Applied Science and Technology Trends 01(02) (2020) 48 –55, doi: 10.38094/jastt1215.

Effective ANN Model based on Neuro-Evolution Mechanism for Realistic Software Estimates in the Early Phase of Software Development

Ravi Kumar B N[1]
Dept. of Computer Science and Engineering
BMS Institute of Technology and Management
Bangalore, India

Dr. Yeresime Suresh[2]
Dept. of Computer Science and Engineering
Ballari Institute of Technology and Management
Ballari, India

***Abstract*—There is no doubt that the software industry is one of the fastest-growing sectors on the planet today. As the cost of the entire development process continues to rise, an effective mechanism is needed to estimate the required development cost to control better the cost overrun problem and make the final software product more competitive. However, in the early stages of planning, the project managers have difficulty estimating the realistic value of the effort and cost required to execute development activities. Software evaluation prior to development can minimize risk and upsurge project success rates. Many techniques have been suggested and employed for cost estimation. However, computations based on several of these techniques show that the estimation of development effort and cost vary, which may cause problems for software industries in allocating overall resources costs. The proposed research study proposes the artificial neural network (ANN) based Neural-Evolution technique to provide more realistic software estimates in the early stages of development. The proposed model uses the advantages of the topology augmentation using an evolutionary algorithm to automate and achieve optimality in ANN construction and training. Based on the results and performance analysis, it is observed that software effort prediction using the proposed approach is more accurate and better than other existing approaches.**

***Keywords*—Software cost estimation; COCOMO-II; neuro-evolution; artificial neural network; genetic algorithm**

I. Introduction

The software industry is undoubtedly one of the greatest innovations in the modern world [1]. The software development process broadly requires various discrete actions such as understanding the client requirements, analysis, preparing the user requirement specification, technical requirement specification, software requirement specification, and hardware requirement specification in the initial stages [2]. Further actions architecture design of the software, design of the modules, coding, integration, testing, and debugging. The overall development cost estimation depends on the individual cost and efforts required for each of the actions involved in the SDP. However, estimating the cost in software development has been a challenge facing researchers and professionals in software engineering over the past few years. The purpose of cost estimation is to help with decisions made during the development of a software project. Many factors affect the accuracy of cost estimation. If the cost is underestimated, the project may be delayed, lack implemented features, or not be completed. On the other hand, an overestimated cost can lead to higher software costs, a waste of resources, and even loss of opportunities for competing markets [3]. These factors can have negative consequences for the project, the development organization, and the customers. Thus, the quality of estimates can affect the quality of the software project.

Many software cost estimation models have been developed and improved, which can be categorized into algorithmic and non-algorithmic models [4]. In algorithmic cost model (ACM), typically a mathematical model or expressions are formulated using factors like i) source line of codes (SLOC), ii) risk calculation, and iii) skill levels obtained from the historical records; however, it fails to enumerate many vital factors including i) complexities, ii) reliability and experiences of the projects and due to this, it leads to the imprecise estimation. The constructive cost model- COCOMO is the most popular method in this category [5]. Further, it has evolved as COCOMO-II and has been widely used to design software cost predictors with various strategies considering basic cost indicators like lines of codes (LOC) and the function points [6-7]. The non-algorithmic approach is basically concerned with soft-computing approaches that overcome the limitations of the algorithmic model. The soft-computing approaches handle a better approximation of the solutions of the complex problems where many nonlinear and uncertain parameters are involved. Table I highlights the comparison of algorithmic and non-algorithmic models. Specifically, the existing approaches for the estimation, such as COCOMO and iii) function point-based model, all lack providing desirable accuracy as they ignore many of the critical drivers. So, these methods limit their applicability in the real-time scenario. In order to address these challenges, the soft-computing approaches are being extensively attracted the focus of the researchers by including approaches either individual or by hybrid techniques like- swarm optimization, fuzzy logic, genetic algorithm, machine learning, and neural network [8-10]. The advantage of the soft-computing approach is that it approximates the solutions created by the mess due to nonlinear factors that are uncertain and imprecise. In recent years, neural networks have gained prominence in software development. However, the literature presents several studies on applying neural networks and machine learning techniques

to estimate cost [11-12]. However, there is no consensus on which method best predicts software costs. The neural network architecture involves different configuration and hyperparameters such as layers, neuron nodes, transfer function, and learning parameters (weights and biases). Generally, the design of the learning model is specific to the particular data set and problem context. If the same model is introduced with a different dataset, it may not perform similarly. Therefore, the parameters mentioned above affect network performance. However, the evolution of models that produce good results in different environments is still a driving force for current research work. This paper suggests a unique approach to software development cost estimation based on Neuro-evolution. The proposed Neuro-evolution approach implements a mechanism of artificial intelligence (AI) that employs an evolutionary algorithm to generate optimal Artificial Neural Network (ANN) architecture. Further, the constructed ANN model in the proposed work is trained to adopt characteristics of software attributes using the previous dataset to produce accurate software estimates.

TABLE I. ANALYSIS OF ALGORITHMIC AND NON-ALGORITHMIC TECHNIQUES

Techniques	*Category*	*Advantages*	*Limitations*
Analogy	Non-Algorithmic	Independent of new resources	Dependent on past information & huge data requirement.
Expert-based		Highly responsive and fast process	Biased outcome
Bottom-Up		Stable	Inaccurate timings & needs huge data
Top-Down		Faster & low cost	less stable outcome & decisions
COCOMO	Algorithmic	Flexible analysis, input modification, & clear outcomes	Inaccurate estimates & practically infeasible
Function Point		Tool independent	Not good enough
Neural Network	Machine learning	Precise predictive estimates	Highly dependent on the dataset and no standard rule for implementation

The ANN model constructed is a feedforward neural network utilizing backpropagation learning mechanisms. The entire configuration and learning parameter is realized with the evolutionary algorithm, particularly a genetic algorithm (GA) implemented via the Neuro-evolution concept. The proposed study aims to achieve:

- A unique ANN model with an optimal selection of its parameters, including the size of hidden layers, number of neuron units at each layer, and transfer functions, from the given interval (linear, Relu, and sigmoid).
- The stable training process of the constructed ANN model that supports large training data samples.
- Self-adjustment in the weight and biases in an optimal manner from the training samples.
- Enhanced generalization in the training phase and efficient identification of dependencies of the predicted values from the input observations.
- Higher accuracy in the prediction to achieve realistic estimates of the cost required for the software development compared to the existing techniques.

The remaining sections of this paper are organized in the following manner: Section-II presents the review of the literature in the context of software cost and effort estimations; Section III discusses the material and methodology adopted in the proposed work; Section IV presents the system design and implementation procedure adopted in the proposed system; Section V presents the outcome and discusses the performance of the proposed system concerning its scope and effectiveness compared to the existing approaches, and finally, the entire contribution of the proposed work is summarized in Section VI.

II. RELATED WORK

Currently, the literature consists of several types of techniques and schemes for software cost estimation and prediction. This section discusses some of the recent research works carried in the context of enhancing prediction of the cost required for software development.

A. Algorithmic Approaches

The algorithmic approaches are concerned with mathematical models or expressions for cost predictions. To date, various methods have been suggested based on the algorithmic approaches. Work carried out by Kumawat, and Sharma [13] focuses on estimating the size metric for computing the cost required for the software project development (SPD). The authors have used the function point analysis (FPA) technique to compute cost estimates. The work of Khan et al. [14] suggested a cost estimation model by customizing features of the COCOMO-II that integrates additional cost drivers for computing the estimates of actual cost and effort required for SDP. Similarly, the study of Keil et al. [15] has introduced a different version of COCOMO-II to fit in the context of global software development (GSD). Two additional cost drivers are added in this version of cost drivers concerning collaboration and communication among different sites. The researchers in the above-discussed literature have tried to provide a significant contribution. All the factors are determined and devised based on the literature analysis and researchers' knowledge. However, there is a lack of empirical support, effective benchmarking, and validation of the scope of the suggested schemes. The authors in the study of Menzies et al. [16] have introduced a tool that encompasses case studies and previous experience to reduce the execution time, the effort required, and the number of defects in the project's development. Their results were obtained from small data sets, and they recommend conducting other tests where large volumes of information are handled. They do not explicitly use control indicators from other areas of knowledge, for example, to measure human and logistical resources. In the existing literature, few extensions to COCOMO were suggested, including dynamic multistage models to meet the analytical needs of prototyping SPD models. These models consider the

dynamics of varying requirements, system design, and other strategies, but all lack desirable accuracy as they ignore many critical drivers. So, these methods limit their applicability with varied IDEs models, languages, and tools.

B. Non-Algorithmic Approaches

The non-algorithmic approach generally implies the soft-computing techniques that handle ambiguity and nonlinearity in the cost estimation techniques. The previous section discusses the conventional approaches regarding software cost and effort estimation. However, software project requirements constantly change over time, which also causes the estimates of cost and effort to change. The researchers realized the need for soft computing approaches that include machine learning techniques, fuzzy logic, and various metaheuristic method. This section discusses the existing soft computing approaches for software effort and cost estimation to analyze the current research trend. Nandal and Sangwan [17] a hybrid Bat and Grautational algorithm is used to estimate the effort of software, whereas fuzzy regression models are used to overcome the problem of imprecise in the dataset for the prediction software effort (Nassif et al. [18]). All these approaches provide a good solution but at the cost of huge computational complexity. The application of evolutionary algorithms like GA is used in the study of Zaidi et al. [19] and Reena et al. [20] to optimize the coefficients of different estimation models in the presence of nonlinear data. The approach of intelligent techniques like the neural network deals with the complexities and uncertainty in the software effort estimation is presented in Venkataiah et al. [21] [22]. Few recent research studies have also focused on applying the hybrid approach in the SPD process. The joint approach of nature-inspired algorithm and ML is adopted by authors in [23-25] to compute the estimates of effort in project development. The work of Singh et al. [26] evaluated different ML techniques in the software effort estimation. The outcome reported in this study showed better performance achieved by LR in terms of error percentage analysis. A neural network approach [27-28] has also been widely accepted in software cost estimation. In the work of Choetkiertikul et al. [29], a long short-term memory (LSTM) and recurrent highway network (RHN) are employed to estimate the effort required for completing user stories or issues. Also, Bayesian Network is used to estimate the work time required in the SPD process [30].

C. Motivation of the Research

A wide range of schemes and techniques have been described in the literature for predicting SPD's costs. The recent literature has been observed more focused on applying metaheuristic techniques, neural networks, and machine learning algorithms. Building a model based on the dataset is difficult due to the complexity and nonlinearity involved in the data attributes. Also, the learning model's design is affected by a variety of factors concerned with network parameters, data modeling, and feature engineering. Apart from this, the factors that determine the connectivity among nodes are complicated to analyze before the training phase to develop an ideal network. Generally, the building and training of the learning model involves a lot of human effort and is specific to the particular context, which is a significant concern as software attributes vary over time. However, even small changes in parameters can dramatically alter the result of the trained model.

A unique model with accurate estimation is presented based on the neuro-evaluation augmenting topology to evolve with an optimized ANN architecture to address and overcome these problems. This type of approach for the cost estimation problem has not yet been applied to the software cost estimation problem. The proposed study aims to explore the effectiveness of augmenting the topology mechanism to automate the construction and training of the ANN model that generates better solutions.

III. Materials and Methodology

The material used for evaluating the proposed model is the COCOMO dataset. The methodology used for designing and developing the proposed ANN model for cost estimation is based on the Neuro-evolution AI technique, which constructs an optimal ANN model using a genetic algorithm. This section briefly highlights the dataset and methodology adopted in the proposed system.

A. Dataset

The COCOMO (Constructive Cost Model) is a widely known software estimation model introduced by Barry Boehm [31]. This model utilizes an approach of statistical correlation between software attributes and lines of the code. In other words, it basically adopts regression analysis with the responsible parameters that are representative of the estimates of the cost required in software development. In the current research work, the study uses the COCOMO NASA-2 dataset publicly accessible at the promise software engineering repository. This dataset consists of a total of 24 vital cost attributes from 93NASA projects.

B. Artificial Neural Network

In recent years, ANN has received wide attention to address complex nonlinear problems in various fields such as computer vision, image processing, natural language processing, and many more. ANN can be viewed as a function approximator that takes an input from observation state and maps to the output state (decision), such that: $f(x) \rightarrow y$. Typically, the function approximators consist of neurons, often referred to as cells or units, composed of summation and activation functions. The typical function of ANN cell is described in Fig. 1 as follows:

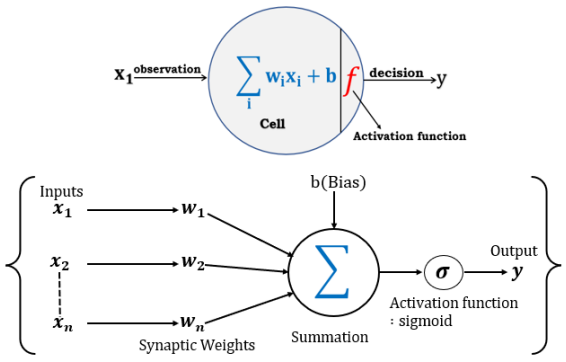

Fig. 1. Typical Function of ANN Cell.

In Fig. 1, the architecture of the basic ANN cell is described where x is the n input such that:$x \in [x_1, x_2, x_3 \cdots x_n]$, w indicates synaptic weight, such that: $w \in [w_1, w_2, w_3 \cdots w_n]$. Each weight 'w' are associated with input sample $'x'$ both together served as input to the cell function, where all x is multiplied with w and are summed with biased (b) using summation function as described as follows:

$$x \cdot w = (x_1 \times w_1) + (x_2 \times w_2) + \cdots + (x_n \times w_n) \quad (1)$$

Equation 25 describes the dot product of vector x and vector w, and their summation is given in equation 26 as follows:

$$\sum = x \cdot w \quad (2)$$

The weights'w_i' can be considered as a strength of the association between cells, and it also decides how much influence the given input will have on the cell's output. Another essential component of the ANN cell is the offset value added to the summation of dot product $x \cdot w$. This offset value is often called a bias that allows shifting the phenomenon of the nonlinear activation function to produce the expected result correctly to the output state. Moreover, the w and b are also often called learning parameters of the ANN model; the relationship between w and b can be numerically represented as follows:

$$(x \cdot w) + b \quad (3)$$

Equation 3 is then passed to the nonlinear function, which is generally a sigmoid function that enables nonlinearity in the ANN cell as numerically represented as follows:

$$y = \sigma(x \cdot w) + b \quad (4)$$

Where y denotes the output of the cell and nonlinear σ sigmoid function. Sigmoid or Logistic: takes a real-valued input and returns output in the range [0,1]. The ANN cells are arranged into several layers, typically classified as input layers, hidden layers and output layers all interconnected to each other.

Usually, the topological structure of the artificial neural network is selected based on empirical analysis, and the learning parameters are determined using the training process, which is related to the trial-and-error process. Therefore, developing an ANN model is not a big problem. However, training ANN models to accomplish certain tasks is a real challenge. In this regard, Neuro-Evolution can be an effective mechanism for determining the optimal topology of neural networks and learning parameters (weights and biases) to construct an ideal ANN model.

C. Neuro-Evolution of Augmenting Topologies

Neuro-Evolution of Augmenting Topology (NEAT) is a neuroevolutionary AI technology that deals with topology augmentation to automate the construction and training of ANN models using evolutionary algorithms (EA) [32]. The EA in NEAT is a kind of genetic algorithm (selection, crossover, and mutation), which allows the evolution of ANN units, learning parameters (weight and biases), and structure, trying to determine stability between the fitness of the obtained solution and assortment. Fig. 2 shows a sample visualization of the topology construction of ANN using the NEAT algorithm.

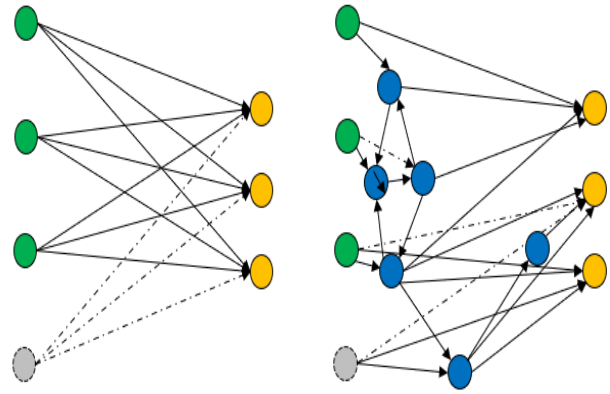

(a) Initial Architecture of AN (b) Augmented Topologies of ANN.

Fig. 2. Topology Construction of ANN using NEAT.

In the above Fig. 2, visualization of initial topology (a) and final topology construction of ANN model (b) after several iterations is shown using NEAT. The flow process of topology augmentation in the construction and training of the ANN model is shown in Fig. 3.

The mechanism of topology augmentation for the optimal ANN model requires the initialization of variables concerning network hyperparameter and loss function. The initialization of hyperparameter variables (such as learning rate and the number of neurons) is crucial to determine the training performance of the network during the crossover and mutation process of EA. On the other hand, the loss function determines the optimality of the neuron genes (bias) and synapse genes (weight) in the learning phase. The loss function in NEAT is also regarded as a fitness function, and a set of neuron genes and synapse genes are called genomes.

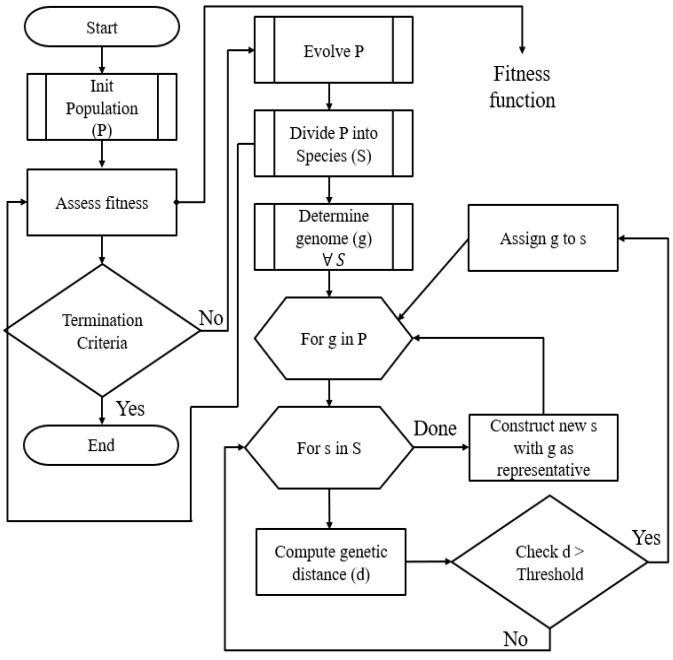

Fig. 3. Flow Process of Topology Augmentation using NEAT.

The algorithm generates a genome considering single input and output layer during the initialization of an initial set of solution candidates (population). Therefore, in the first generation, the genomes only vary in weights and biases but not network topology. After assessing the fitness value of each genome, the algorithm stops if the termination criterion is met. Otherwise, it generates a new set of solution candidates by executing crossovers phase y between genomes and then performs mutations in the subsequent offspring. All these processes are carried out randomly, and prior to computing the fitness of neuron genes and synapse genes, i.e., optimality of weight and biases, the algorithm splits the set of solution candidates into species (a particular class with the common characteristics) based on the computation of the genetic distance between each set of neuron weight and biases. The computation of the genetic distance is carried out using the following numerical equation:

$$d = d_b + d_w \tag{5}$$

The above equation 6 represents the computation of distance (d) based on the summation of neuron (d_b i.e., bias) and synapse (d_w i.e., weight). The computation of the d_b and d_w are shown in equations 6 and 7 as follows:

$$d_b = c_n \times \frac{\Delta_b}{\max(B(g_1),B(g_2))} \tag{6}$$

$$d_w = c_s \times \frac{\Delta_w}{\max(W(g_1),W(g_2))} \tag{7}$$

Where c_n and c_s are the user-defined variables for fine-tuning the model parameters.

IV. Proposed Cost Estimation Model

This section discusses the proposed cost estimation implementation procedure based on the ANN model determined using the NEAT algorithm discussed in the previous section. In the proposed study, the cost estimation problem is being studied as a regression problem rather than an optimization problem to predict kilo line of code (KLOC). The proposed cost estimation model design involves three core modules; namely, i) data exploration module ii) data preprocessing, and iii) design of ANN Model.

A. Dataset Exploration

In the current study, the data is available on the NASA website. The data is downloaded by sending an HTTP GET request to the respective URLs. When the request is sent, the data can be retrieved in the form of an a.arff file. However, this is not readable readily by our system. Hence, the data is sub-set from the 'Arff file', which contains 10 parts, including {Title, Past Usage, Relevant Information, Number of instances, Number of attributes, Attribute information, Missing attributes, Class distribution, Data}. The sub-set extracts only the Data. The Data Store stores the data in the form of a simple CSV file. Each column is separated by a (delimiter), and a new line character separates each sample. Many data science platforms can read and process this format, including pandas used in the current study. The data imported into the numerical computing environment (NCE) describes 124 entries ranging from the index number 0 to 123 with 24 columns. The dataset consists of 24 variables with type numeric and two categorical variables. The memory taken to upload the data is more than 25 KB. Table II presents a statistical description of all the 25 predictors and an output KLOC. The closer shows that the counts of all the parameters are identical to the number of samples, which indicates there are no missing values. The differential between the consecutive pair between {0, 25%}, {25%, 50%}, {50%, 75%} and {75%, 100%} sometimes are not less than standard deviation (σ) that means there is the presence of outliers in the data, as well if RMSE and MAE of the model have a difference more than mean KLOC then outliers need to be corrected. Another important observation on the dataset is that certain parameters show a specific correlation with the effort. The correlations are either negative correlation or positive correlation. In positively correlated parameters, the effort decreases with a decrease in the parameter's values, whereas, in negatively correlated parameters, the effort decreases if the parameters increase. The positively correlated parameters are the cost drivers (CD) ∈ {acap, pcap}, and negatively correlated parameters such that CD ∈ {rely, Cplx, data, time, stor, sced}. Further, on the analysis of co-efficient using linear regression analysis, it is found that reduced reusability (ruse) and 'site' have a higher multiplier effect on cost/effort compared to other CDs, as evident in Fig. 4. It is clear that the correlation of data points with the actual effort is highly non-uniform in nature. Therefore, a custom feature engineering process for the proposed ANN-based CEM is being carried out.

B. Preprocessing

In this section, the preprocessing operation is carried out from the perspective of the feature engineering task and the extraction of suitable input for the proposed learning model. The core module in this stage contains i) correlation analysis and ii) dataset normalization. In the correlation analysis, the relationships between various variables are analyzed using a mathematical approach that helps find correlations between various cost drivers. The formula for correlation is shown in the equation as follows:

$$r_{x,y} = \frac{\sum(x_i - x').(y_i - y')}{\sqrt{\sum(x_i - x')^2.\sum(y_i - y')^2}} \tag{8}$$

Where, x_i and y_i denotes cost drivers, x' and y' are means values of the cost drivers and $r_{x,y}$ is the correlation factor between x and y that ranges from -1 to +1. As it can be observed from the formula if $x \propto y$, which means that $x = ky$, then the following outcome is achieved when the same is substituted in equation 9.

$$r_{x,y} = \frac{\sum(x_i - x').k(x_i - x')}{\sqrt{\sum(x_i - x')^2.k^2\sum(x_i - x')^2}} \tag{9}$$

$$r_{x,y} = \frac{\sum k(x_i - x')^2}{k\sqrt{(\sum(x_i - x')^2)^2}} \tag{10}$$

$$r_{x,y} = \frac{k\sum(x_i - x')^2}{k\sum(x_i - x')^2} \tag{11}$$

$$r_{x,y} = 1 \tag{12}$$

The above equation 12 proves that when the two cost drivers are proportional, the correlation between them is one. Similarly, when one cost driver reduces and another cost driver

increases, in other words, x=k-ly, then the correlation is said to be -1 and considered as an ideal scenario when there is a perfect linear relationship between two CDs. However, a zero correlation refers to total randomness and no relation between two CDs. The correlation plot for among CDs is given in Fig. 5. It can be analyzed that there is a strong correlation between the 'prec', 'flex', 'resl' and 'team'. As it can be observed that except for exponential CDs such that {'prec', 'flex, 'resl', 'team' and 'pmat'} all other CDs have (>10%) correlation. Hence, all variable turns out to be significant while building an ANN model.

TABLE II. DESCRIPTIVE STATISTICS

Cost Drivers	count	mean	std	min	25%	50%	75%	max
ACT_EFFORT	124.0	563.334677	1029.227941	6.00	71.50	239.500	581.750	8211.00
prec	124.0	3.110000	1.292409	0.00	2.48	2.480	4.9600	4.960000
flex	124.0	2.618952	1.041618	0.00	103	2.030	4.0500	5.070000
resl	124.0	3.688871	1.403707	0.00	2.83	2.830	5.6500	6.010000
team	124.0	1.837097	1.094185	0.00	1.10	1.100	3.2900	4.660000
pmat	124.0	5.602984	1.288265	2.84	4.68	4.680	6.2400	7.800000
relay	124.0	1.078522	0.103427	0.85	1.00	1.100	1.1000	1.740000
Cplx	124.0	1.189892	0.163256	0.87	1.17	1.170	1.2125	1.740000
Data	124.0	1.014919	0.117179	0.90	0.90	1.000	1.1400	1.280000
Ruse	124.0	0.996935	0.014605	0.95	1.00	1.000	1.0000	1.070000
Time	124.0	1.124516	0.184476	1.00	1.00	1.000	1.2900	1.630000
Stor	124.0	1.107097	0.163149	1.00	1.00	1.000	1.1700	1.460000
Pvol	124.0	0.927406	0.095456	0.87	0.87	0.870	1.0000	1.150000
Acap	124.0	0.880276	0.101079	0.71	0.85	0.850	1.0000	1.016667
Pcap	124.0	0.918817	0.085625	0.76	0.88	0.895	1.0000	1.000000
pcon	124.0	1.000544	0.035766	0.81	1.00	1.000	1.0000	1.205000
Apex	124.0	0.925712	0.083496	0.81	0.88	0.880	1.0000	1.220000
Plex	124.0	1.004590	0.080974	0.91	0.91	1.000	1.0000	1.190000
ltex	124.0	0.966781	0.089415	0.91	0.91	0.910	1.0000	1.200000
Tool	124.0	1.115847	0.078542	0.83	1.09	1.170	1.1700	1.170000
Sced	124.0	1.043065	0.063760	1.00	1.00	1.000	1.1400	1.140000
Site	124.0	0.925040	0.017623	0.86	0.93	0.930	0.9300	0.947500
docu	124.0	1.024940	0.057830	0.91	1.00	1.000	1.1100	1.230000
Physical Delivered KLOC	124.0	103.443901	141.455891	0.00	20.00	51.900	131.7500	980.000000

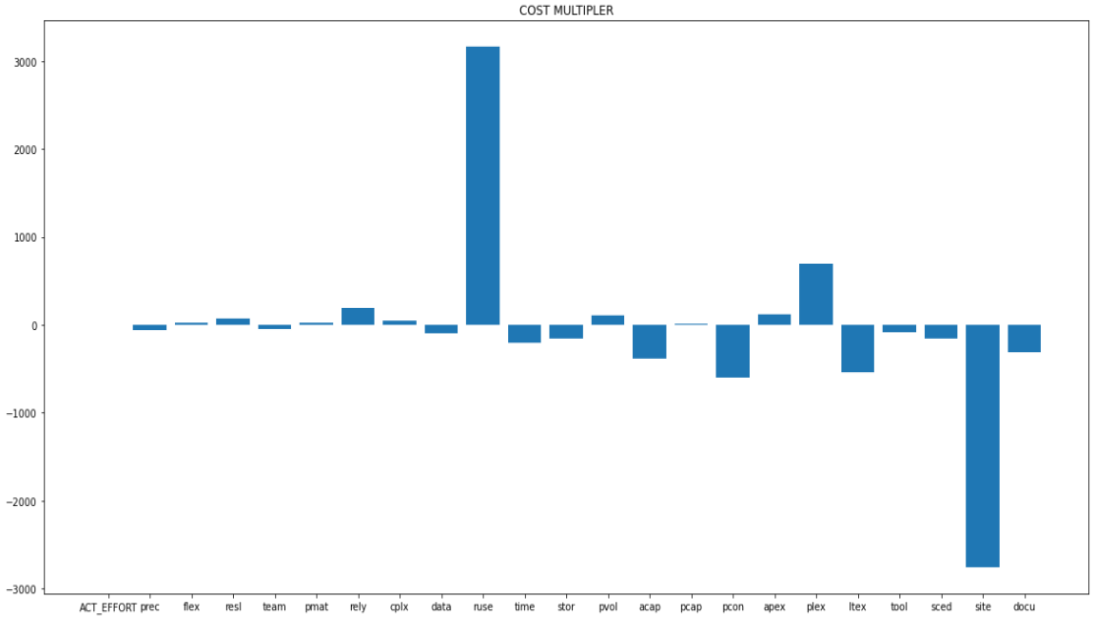

Fig. 4. Representation of Cost Multiplier.

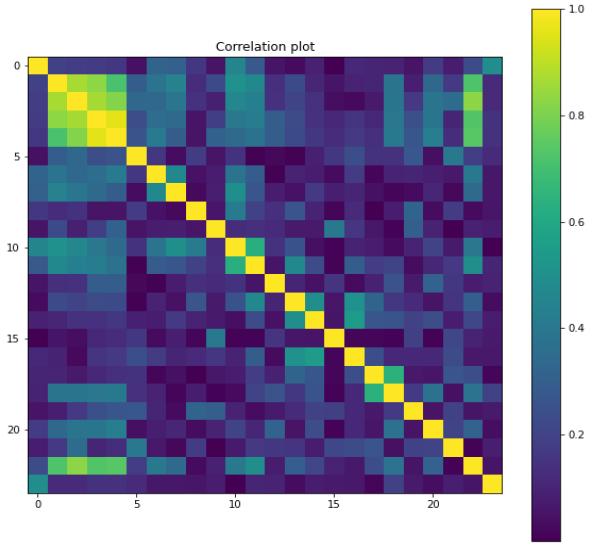

Fig. 5. Correlation Plot among CDs and KLOC.

In order to provide an input to a learning model, the input data is required to be in a vector form. Feature vectorization refers to converting a row of values into a usable vector. In this phase of implementation, the data is normalized with the help of the Min-Max scaling method. Further, each row is transposed and fed to neural networks. The typical formula for data normalization for feature vectors is numerically expressed in equation 13.

$$x' = \frac{x - min(x)}{max(x) - min(x)} \quad (13)$$

Where, x is the input data, i.e., original CDs feature samples, which is normalized using min and max function and rescaled in the range of [0,1], and x' normalized CDs feature samples which are further fed to the proposed learning model.

C. Design of the Proposed ANN Model

This section discusses the ANN model design and its implementation procedure with the support of the algorithmic steps. The implementation procedure utilizes the NEAT library of python executed in the Anaconda distribution. The dataset is split into training and testing sets, where 80% of the dataset is kept for the model training, and 20% of the dataset is kept for model testing. The design configuration of the proposed ANN model is carried out using neural evolution mechanisms, where the features from the input observation are considered for determining weights and biases. In this process, the optimality of the ANN architecture is determined through topology augmentation using a genetic algorithm. The configuration parameters considered in the ANN construction consist of hidden layers, neurons unit at each hidden layer, and a set of transfer functions. The proposed study considers three transfer functions: linear, Relu, and nonlinear sigmoid. On the other hand, mean square error (MSE) is considered a fitness function. Since the proposed study has considered MSE, the fitness evaluation is carried out based the less error. Therefore, the inverse roulette selection (IRS) technique is considered for the proportionate fitness selection. The core configuration and training process of ANN construction using topology augmentation is shown in Fig. 6. The topology augmentation begins with the initialization of population (a set of candidate solutions), basically a pool of random neural networks. The process iterates several times, which is also called a generation where the algorithm chooses the optimal ANN based on the fitness value, which is then further cross overed according to the selection/decision process.

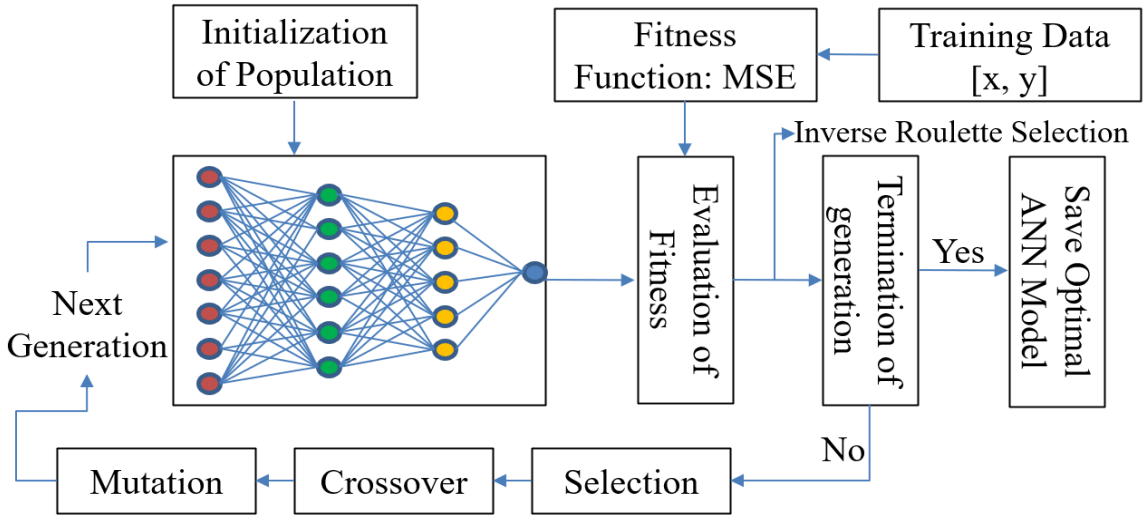

Fig. 6. Generation of Optimal ANN Model using Neuro-evolution Technique.

Afterward, a new ANN model is generated, and after mutation, an evolved version of the ANN model is further carried out for the training process. All these processes continue until the termination criteria are met. This termination criterion is based on the specified number of generations, wherein each generation, the trained model is evaluated and selected according to the prediction performance. The implementation steps for the above-discussed procedure are mentioned as follows:

Algorithm:1 Neuro evolution training

Step 1. Create population pool

In this step, the population pool is generated, a set of random neural networks with random layers and neurons and random activation functions. Inputs to the algorithm are given in the form of a finite number of layers and neurons and, at the same time, a set of activation functions. The activation functions allowed are, Sigmoid, Linear, and relu.

Step 2. Evaluate fitness of the population

The MSE fitness function measures the fitness of the population. The MSE of the input data is considered with the output in the training set.

Step 3. Select the fittest individual to reproduce

The inverse Russian roulette process selects the individuals for the repopulation pool. The lower the fitness function value, the higher the probability of the selection. The following equation decides the probability of selection.

$$P_i = 1 - \frac{MSE_i}{\sum_{i=1}^{n} MSE_i} \quad (14)$$

Step 4. Repopulate using copies of the fittest network

Most fit individuals among the population are selected and used for further processing. The crossover of these individuals is made here, and also mutation is applied according to the mutation probability.

Step 5. Introduce normally distributed mutations to the network weights

The neural networks are finalized in this step, and the newly formed networks are introduced to the population pool.

V. Result and Performance Analysis

This section discusses the performance metrics followed by outcome analysis to justify the scope and effectiveness of the proposed system.

A. Neuro Evolution Model Parameters

The design and development of the proposed system are done using python programming language and execution on Anaconda. The parameters considered for executing proposed neuroevolutionary technique for obtaining optimal ANN model is mentioned in Table III.

The parameter namely population size is the total number of offspring (networks) present in each generation and total number of generations is number of times the fitness is measured. In 15% of the cases a new neuron is added to the network. In 10% of the cases an existing neuron is deleted from the network. Addition and deletion of neurons happen within a single generation. Either relu, sigmoid or linear activation functions are chosen. Initial bias is assigned according to the normal distribution. Maximum value of weights and bias are set to 30 however the minimum weight is set to 0 in order avoid negative values. At the same time, minimum bias is set to -5 in order to cancel out certain values.

Mutation probability is 5%. This is necessary to display the stochastic nature of the system. After successful execution of the neuro-evolution training, the proposed algorithm returns optimal ANN model discussed in Table IV.

The architecture of the obtained ANN model is shown in Fig. 7. After evolution through several iteration, the neuro-evolution algorithm provides optimal number of layers and number of neurons unit at each layer as mentioned in Table IV.

TABLE III. Neuro-evolution Hyperparameters

Parameters	Values
Population size	200
Number of generations	100
Probability of adding a new neuron	0.15
Probability of deleting a neuron	0.1
Activation function	Sigmoid, Relu, Linear
Initial bias	according to normal distribution
Mutation probability	0.5
Minimum neuron bias	-5
Maximum neuron bias	30
Minimum weight	0
Maximum weight	30
Weight mutation probability	0.5

TABLE IV. Configuration Description of Obtained Optimal ANN Model

Layer	Number of neurons	Trainable parameters
Layer 1 (input)	24	N/A
Layer 2	10	(24*10) + 10 = 250
Layer 3	5	(10 * 5) + 5 = 55
Layer 4 (output)	1	(5 * 1) + 1 = 7
Loss Function (MSE)	-	-
Activation Function (Relu)	-	-
	Total neurons: 40	Total trainable parameters: 312

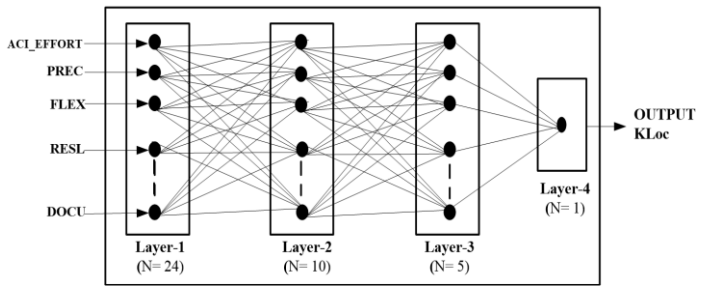

Fig. 7. Architecture of Optimal ANN Model.

B. Performance Metrics

1) MMRE (Mean Magnitude of Relative Error): The MMRE performance metric is the most common basis for the assessment of the effort estimation process. The matric MMRE is computed for the given dataset of software projects whose estimated efforts are compared with their actual efforts. The estimation process with minimum MMRE is considered to be the most accurate. The formula for calculating MMRE is given as Eq. 15.

$$\text{MMRE} = \frac{1}{\text{N}} \cdot \sum_{\text{i=1}}^{\text{n}} \frac{\lfloor (\text{y} - \text{y}\prime) \rfloor}{\text{y}} \quad (15)$$

Where, y is the actual effort, and y' denotes estimated work effort for project pi, and N is the total project (PI) under consideration. Mathematically, MMRE gives an average percentage of error between y and y'.

2) MSE (Mean Squared Error): MSE is being calculated in proposed implementations to analyze the performance of proposed methods over other LR and SVR. MSE is more critical function while building better models while optimizing the learning model. The formula for calculating MSE is given as Eq. 16.

$$\text{MSE} = \frac{1}{\text{n}} \sum_{\text{i=1}}^{\text{n}} (\text{y} - \text{y}')^2 \quad (16)$$

Where y is the actual effort, and y' denotes estimated work effort for project pi, and N is the total number of the project under consideration.

3) RMSE (Root Mean Square Error): Since the unit of MSE is squared, RMSE is the square root of MSE used since the unit of MSE is Nl^2 where Nl is the number of lines of code in the project. Though MSE is significant for optimizing the model, it would make no sense to human beings. Hence, the study considers $\text{RMSE} = \sqrt{\text{MSE}}$. Since the unit of RMSE is Nl, it can be assumed that the most probable range for y can be $\text{y} = \text{y}' \pm \text{RMSE}$. The computation of RMSE can be numerically represented as follows in eq. 17:

$$\text{RMSE} = \sqrt{\frac{1}{\text{n}} \sum_{\text{i=1}}^{\text{n}} (\text{y} - \text{y}')^2} \quad (17)$$

4) MAE (Mean Absolute Error): This is similar to MMRE, representing average absolute error instead of providing average percentage error. In MAE abs function is used to remove the error from simple error, and the average is calculated. Due to this, some of the extreme points, like outliers, will provide less significance; hence this measure is less sensitive to outliers. MAE can be numerically represented as follows in eq. 18:

$$\text{MAE} = \frac{1}{\text{N}} \cdot \sum_{\text{i=1}}^{\text{n}} \lfloor (\text{y} - \text{y}') \rfloor \quad (18)$$

Since the unit of MAE and output (actual cost) is the same, MAE represents total cost overrun or underrun.

5) Pred: PRED is the de facto standard for cost model accuracy measurement. It is called the percentage of predictions falling within the K% of the actual known value. The formula for PRED calculation is shown in equation 19:

$$\text{PRED} = \frac{1}{\text{n}} \sum_{\text{i=1}}^{\text{n}} \left| \frac{\text{EstimationEffort} - \text{ActualEffort}}{\text{Actual Effort}} \right| \text{K \%} \quad (19)$$

Where k% is the percentage error between AE and EE, PRED represents the percentage of a number of projects whose cost overrun or underrun is below 25% in some researches 30%.

C. Outcome Analysis

This section discusses the outcome obtained for the proposed system based on the comparative analysis. The proposed study implements two machine learning algorithms for the comparative analysis such as Linear regression (LR) and supports vector regression (SVR). In order to compare ANN with LR and SVR, the performance metrics MSE, RMSE, and MAE are considered. To justify the scope of the proposed optimal ANN model, the study also considers performance analysis with similar existing approaches such as estimation technique based on fuzzy-genetic [33] and based Dolphin optimization technique [34], Bat optimization [34], and combined Dolphin-BAT [34], the performance metric PRED and MMRE is used. The quantitative outcome obtained for the proposed system and its comparison is shown in Table V.

As it can be observed in Table V, that LR, SVR is associated with 151% and 128% errors, respectively, which means the predicted/estimated value could be more than twice as big as the actual value; therefore, making LR and SVR unfit for real-world implementations. However, even the most basic benchmarked algorithms (GA) are giving 29.9% error which is below 30%, which is an acceptable cost overrun ratio for software projects in general. It is also far below 77%, which is the average cost overrun ratio of the NASA project from which the dataset is collected. The overall numerical outcome shows the proposed ANN's effectiveness regarding the cost overrun ratio. Performance analysis regarding MAE is shown in Table VI.

TABLE V. QUANTITATIVE OBSERVATION IN TERMS OF MMRE

Methods	Performance Metrics
LR	1.510457
SVR	1.281522
GA	0.299469
BAT	0.1698
DOLPHIN	0.1665
DOLPHIN-BAT	0.14576
ANN	0.113518

TABLE VI. QUANTITATIVE OBSERVATION IN TERMS OF MAE

Methods	Performance Metrics
LR	119.266357
SVR	81.872095
ANN	22.151230

The performance metric MAE is used to calculate the performance of proposed methods over other LR and SVR. Since the unit of MAE is in Nl, the MAE value 22.15 obtained for ANN represents a number of lines of codes in the projects that may vary by 22,151 lines in ANN. An average developer writes 250 lines of production code per week (40 hours of working per week). An extra 22151 lines represent 88 weeks of work (3520-man hours). Considering that an average developer in the USA earns approximately $34 per hour, the total cost overrun might come to $119,680. In the cases of LR and SVR, the cost overrun is quite more than ANN, which is impractical for real-time implementation? The performance of the learning models implemented in this study regarding MSE is shown in Table VII.

The metric MSE is being considered in proposed implementations to assess the performance of the proposed ANN over other LR and SVR. MSE represents the overall training of the algorithm as it is used for optimization. Even though the MSE does not directly represent the algorithm's performance, it does represent the quality and level of training given to the algorithm. Lower MSE represents higher knowledge of the algorithm. More trainable parameters can store more knowledge among them. The MSE score is higher in both LR and SVR as they contain fewer trainable parameters than ANN. The quantified outcome indicates that ANN is less associated with error compared to LR and SVR. Therefore, it can be concluded that SVR and LR are subjected issue of underfitting. The performance analysis in terms of RMSE is mentioned in Table VIII.

Similarly, the metric RMSE is considered to evaluate the training performance of the learning models. The RMSE also helps to understand the requirement re-training model by the preprocessing step. From the quantified outcome, the proposed ANN scored 39.33 % RMSE and 22.15% MAE from Table VI, i.e., a difference of 17.18 % compared to mean KLOC of all projects, i.e., 103.44. This indicates minor variation with 16%-17%, which is within the acceptable limit of 20 %. The performance analysis regarding PRED is shown in Table IX.

PRED represents the ratio of projects which has less than a threshold percentage of cost overrun. Hence, this performance measurement is more practical than the other metrics since it represents the number of projects that will fall below the acceptable cost overrun ratio. In most of the studies, the threshold is set to 30%. In this study, 25% of the threshold value is considered to perform comparative analysis. From Table IX, it can be observed that the proposed model ANN achieved a higher PRED value, i.e., 68.91, compared to other ML methods and existing approaches. Bat, Dolphin, hybrid Dolphin-Bat, and the proposed ANN are more practical to implement as they have PRED value much higher than GA. But among them, the proposed ANN method has the highest PRED value, which indicates its suitability and scope in the real-world system. The following analysis mentions the overall improvement (%) of ANN concerning MMRE in Fig. 8 and PRED in Fig. 9 over other implemented ML models and existing approaches.

TABLE VII. QUANTITATIVE OBSERVATION IN TERMS OF MSE

Methods	Performance Metrics
LR	42545.810081
SVR	29240.145478
ANN	1547.247493

TABLE VIII. QUANTITATIVE OBSERVATION IN TERMS OF RMSE

Methods	Performance Metrics
LR	206.266357
SVR	170.997501
ANN	39.335067

TABLE IX. QUANTITATIVE OBSERVATION IN TERMS OF PRED

Methods	Performance Metrics
LR	2.335234
SVR	5.297425
GA	11.66
BAT	61.66
DOLPHIN	61.66
DOLPHIN-BAT	66.66
ANN	68.91522

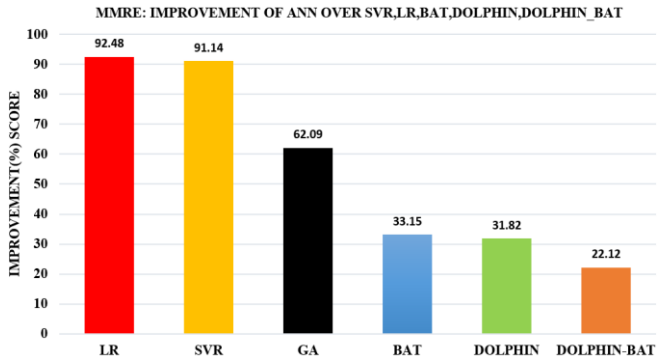

Fig. 8. MMRE Improvement (%) of ANN over SVR, LR and existing Methods.

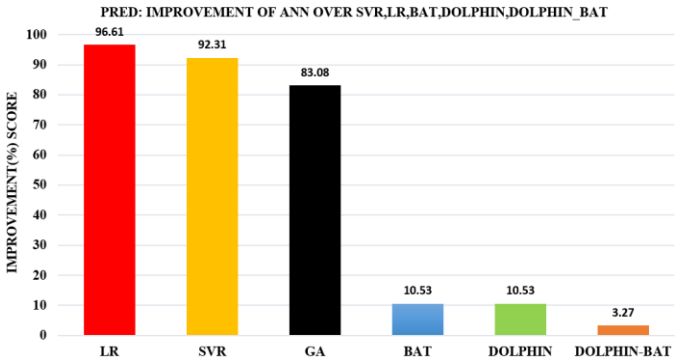

Fig. 9. PRED Improvements (%) of ANN over SVR, LR and Existing Methods.

The analysis from Fig. 8 shows ANN has achieved 92.4% improvement over LR, 91.14% improvement over SVR, and 62.09%, 33.15%, 31.82%, 22.12% over Fuzzy-GA, BAT, Dolphin, and Dolphin-Bat, respectively. The analysis from Fig. 9 shows that ANN has achieved 96.91% improvement over LR, 92.31% improvement over SVR, and 83.08%, 10.53%, 10.53%, 3.27% over Fuzzy-GA, BAT, Dolphin, and Dolphin-Bat, respectively. Hence, it can be seen that the proposed offers a good result regarding software cost estimates. The overall analysis shows effectiveness of the proposed neuro-evolution algorithm towards devising suitable learning model for achieving realistic estimates of the cost required in the initial stage of the software development process. Hence, the proposed research work suggested a technically-efficient method acquainted with recent trends and technologies to benefit real-world applications.

VI. Conclusion

The development of software projects involves various phases like initial planning, risk assessment, effort, and cost estimation. Among these, cost estimation is the key concern in the software industry. The conventional approaches do not provide accurate estimation due to the lack of precise system and cost drivers modeling. In this paper, the study has presented a novel and unique approach to predict realistic estimates of the cost needed to develop a software project. The proposed study applied a mechanism of neural evolution in conjunction with evolutionary technique, namely genetic algorithm top construct ANN, which predicts actual estimates of the cost required to develop a software. The application of neural evolution in ANN modeling proves its effectiveness and scope that it can compete with the existing techniques in terms of realistic estimates of the cost and effort. Once developed and trained, the proposed ANN can estimate the development costs in real-time as it computes cost estimates based on the responsible attributes required in the development of the software. The execution complexity grows linearly with the problem context and size of data samples. Based on the result analysis, it is observed that the proposed ANN is producing better results than other previously proposed algorithms and other machine learning models being implemented. The existing works adopted global optimization algorithms that require huge computing resources due to recursive operation in parallel. However, the proposed ANN model is constructed optimally using the mechanism of augmenting topology, and it better adopts generalization of the feature from the input observations, therefore, providing accurate estimates of the cost compared to the existing approaches.

References

[1] Alt, R., Leimeister, J.M., Priemuth, T. et al. Software-Defined Business. Bus Inf Syst Eng 62, 609–621 (2020).

[2] Trendowicz, A., 2013. Software Cost Estimation, Benchmarking, and Risk Assessment: The Software Decision-Makers' Guide to Predictable Software Development. Springer Science & Business Media.

[3] Mittas, N. and Angelis, L., 2013, September. Overestimation and underestimation of software cost models: Evaluation by visualization. In 2013 39th Euromicro Conference on Software Engineering and Advanced Applications (pp. 317-324). IEEE.

[4] Khan, B., Khan, W., Arshad, M. and Jan, N., 2020. Software Cost Estimation: Algorithmic and Non-Algorithmic Approaches. International Journal of Data Science and Advanced Analytics (ISSN 2563-4429), 2(2), pp.1-5.

[5] Kaushik, A., Chauhan, A., Mittal, D. and Gupta, S., 2012. COCOMO estimates using neural networks. International Journal of Intelligent Systems and Applications, 4(9), pp.22-28.

[6] Singh, B.K., Tiwari, S., Mishra, K.K. and Punhani, A., 2021. Extended COCOMO: robust and interpretable neuro-fuzzy modelling. International Journal of Computational Vision and Robotics, 11(1), pp.41-65.

[7] Coelho, E. and Basu, A., 2012. Effort estimation in agile software development using story points. International Journal of Applied Information Systems (IJAIS), 3(7).

[8] Bedi, R.P.S. and Singh, A., 2017. Software Cost Estimation using Fuzzy Logic. Indian Journal of Science and Technology, 10, p.3.

[9] Singh, B.K. and Misra, A.K., 2012. Software effort estimation by genetic algorithm tuned parameters of modified constructive cost model for nasa software projects. International Journal of Computer Applications, 59(9).

[10] Nassif, A.B., Azzeh, M., Capretz, L.F. and Ho, D., 2016. Neural network models for software development effort estimation: a comparative study. Neural Computing and Applications, 27(8), pp.2369-2381.

[11] Tayyab M.R., Usman M., Ahmad W. (2018) A Machine Learning Based Model for Software Cost Estimation. In: Bi Y., Kapoor S., Bhatia R. (eds) Proceedings of SAI Intelligent Systems Conference (IntelliSys) 2016. IntelliSys 2016. Lecture Notes in Networks and Systems, vol 16. Springer, Cham.

[12] Sakhrawi, Z., Sellami, A. & Bouassida, N. Software enhancement effort estimation using correlation-based feature selection and stacking ensemble method.

[13] Kumawat P., Sharma N. (2019) Design and Development of Cost Measurement Mechanism for Re-Engineering Project Using Function Point Analysis. In: Kamal R., Henshaw M., Nair P. (eds) International Conference on Advanced Computing Networking and Informatics. Advances in Intelligent Systems and Computing, vol 870. Springer, Singapore.

[14] J. A. Khan, S. U. R. Khan, T. A. Khan and I. U. R. Khan, "An Amplified COCOMO-II Based Cost Estimation Model in Global Software Development Context," in IEEE Access, vol. 9, pp. 88602-88620, 2021.

[15] P. Keil, D. J. Paulish, and R. S. Sangwan, "Cost estimation for global software development," in Proc. Int. Workshop Econ. Driven Softw. Eng. Res. (EDSER), 2006, pp. 7–10.

[16] Menzies T, Brady A, Keung J, Hihn J, Williams S, El-Rawas O, Green P, Boehm B. Learning project management decisions: a case study with case-based reasoning versus data farming. IEEE Transactions on Software Engineering. 2013 Sep 16;39(12):1698-713.

[17] D. Nandal and O. P. Sangwan, "Software cost estimation by optimizing COCOMO model using hybrid BATGSA algorithm," Int. J. Intell. Eng. Syst., vol. 11, no. 4, pp. 250–263, 2018.

[18] A. B. Nassif, M. Azzeh, A. Idri, and A. Abran, "Software development effort estimation using regression fuzzy models," Comput. Intell. Neurosci., vol. 2019, pp. 1–17, Feb. 2019.

[19] Zaidi SA, Katiyar V, Abbas SQ (2017) Development of a framework for software cost estimation: design phase. Int J Tech Res Appl 5(2):68–72.

[20] Reena, Bhatia PK (2017) Application of genetic algorithm in software engineering: a review. Int Refereed J Eng Sci 6(2):63–69.

[21] V. Venkataiah, R. Mohanty, M. Nagaratna, Prediction of software cost estimation using spiking neural networks, in: Smart Intell. Comput. Appl. Smart Innov. Syst. Technol., Springer, Singapore, 2019, pp. 101–112, http: //dx.doi.org/10.1007/978-981-13-1927-3_11.

[22] V. Venkataiah, R. Mohanty, M. Nagaratna, Prediction of software cost estimation using spiking neural networks, Smart Innov. Syst. Technol. 105 (2019) 101–112, http://dx.doi.org/10.1007/978-981-13-1927-3_11.

[23] S. Kumari, S. Pushkar, Cuckoo search based hybrid models for improving the accuracy of software effort estimation, Microsyst. Technol. 24 (2018) 4767–4774, http://dx.doi.org/10.1007/s00542-018-3871-9.

[24] M. Pandey, R. Litoriya, P. Pandey, Validation of existing software effort estimation techniques in context with mobile software applications, Wirel. Pers. Commun. 110 (2020) 1659–1677, http://dx.doi.org/10.1007/s11277-019-06805-0.

[25] S. Goyal, P.K. Bhatia, Feature selection technique for effective software effort estimation using multi-layer perceptrons, Lect. Notes Electr. Eng. 605 (2020) 183–194, http://dx.doi.org/10.1007/978-3-030-30577-2_15.

[26] A.J. Singh, M. Kumar, Comparative analysis on prediction of software effort estimation using machine learning techniques, SSRN Electron. J. (2020) 1–6, http://dx.doi.org/10.2139/ssrn.3565822.

[27] M. Qin, L. Shen, D. Zhang, L. Zhao, Deep learning model for function point based software cost estimation -an industry case study, in: Proc. - 2019 Int. Conf. Intell. Comput. Autom. Syst. ICICAS 2019, 2019, pp. 768–772, http://dx.doi.org/10.1109/ICICAS48597.2019.00165.

[28] V. Resmi, S. Vijayalakshmi, Kernel fuzzy clustering with output layer self-connection recurrent neural networks for software cost estimation, J. Circuits, Syst. Comput. 29 (2019) 1–17, http://dx.doi.org/10.1142/S0218126620500917.

[29] M. Choetkiertikul, H.K. Dam, T. Tran, T. Pham, A. Ghose, T. Menzies, A deep learning model for estimating story points, IEEE Transactions on Software Engineering, 45 (2019), 637–656, http://dx.doi.org/10.1109/TSE.2018.2792473.

[30] Dragicevic, S., Celar, S., & Turic, M. (2017). Bayesian network model for task effort estimation in agile software development. Journal of Systems and Software, 127, 109- 119. DOI: 10.1016/j.jss.2017.01.027.

[31] http://promise.site.uottawa.ca/SERepository/datasets/cocomonasa_v1.arff

[32] Stanley, K.O., Miikkulainen, R., 2002a. Evolving neural networks through augmenting topologies. Evolutionary Computation 10 (2), 99–127.

[33] X Chhabra, S., Singh, H. Optimizing design parameters of fuzzy model based COCOMO using genetic algorithms. Int. j. inf. tecnol. 12, 1259–1269 (2020). https://doi.org/10.1007/s41870-019-00325-7.

[34] A. A. Fadhil, R. G. H. Alsarraj and A. M. Altaie, "Software Cost Estimation Based on Dolphin Algorithm," in IEEE Access, vol. 8, pp. 75279-75287, 2020, doi: 10.1109/ACCESS.2020.2988867.

Received: June 10, 2021. Revised: July 29, 2021.

INASS

International Journal of
Intelligent Engineering & Systems

http://www.inass.org/

Ant Colony Optimization Based Modified AODV for Secure Routing in Mobile Ad Hoc Networks

Mallikarjuna Anantapur[1]* **Venkanagouda Chanabasavanagouda Patil[1]**

[1]*Department of Electronics & Communication Engineering, Ballari Institute of Technology & Management, India*
* Corresponding author's Email: mallikarjunaa@bitm.edu.in

Abstract: Mobile Ad hoc Network (MANET) is an infrastructure-less wireless network that is characterized by multi-hop communication, dynamic network topology, open medium, and so on. MANET is generally vulnerable to security threats because of its decentralized control architecture. Therefore, the malicious attack is required to be avoided in the routing path for improving the network efficiency. In this paper, the Ant Colony Optimization (ACO) based Modified Ad-hoc On-Demand Distance Vector (MAODV) is proposed to obtain secure data transmission over the MANET. The ACO considers the four fitness functions such as trust, residual energy, distance, and node degree to detect an optimal path under the constraints of blackhole attacks. The main objective of the MAODV-ACO method is to improve the Packet Delivery Ratio (PDR) while minimizing the delay. The performance of the MAODV-ACO method is analyzed in terms of PDR, throughput, average End to End Delay (EED) and overhead. This proposed MAODV-ACO method is compared with Context-Aware Routing Protocol (CARP) and, Ad-hoc On-Demand Distance Vector (AODV) using Bayesian Approach and Dempster Shafer Theory (BA-DST) to evaluate the network performances. The PDR of the MAODV-ACO method is 99.66 % for 100 nodes, which is high when compared to the CARP and AODV-BA-DST.

Keywords: Blackhole attack, Mobile ad hoc network, Modified ad-hoc on-demand distance vector routing protocol, Trust, Packet delivery ratio.

1. Introduction

MANET is a set of self-organized wireless mobile nodes that can interact with each other without using fixed network infrastructure or centralized administration. Subsequently, the mobile nodes in the MANET communicate with each other over a wireless channel [1, 2]. The nodes of the MANET are used to accomplish both the hosts and routers for transmitting the data packets to the desired destination using the routing protocol [3, 4]. Moreover, the nodes in the MANET have three modes of operation which are transmission, calculation and sensing operation [5]. The node communication is restricted in the network based on the transmitter range. If two nodes are present within the transmission range, then the nodes can interact with each other. However, an intermediate node should be used, when the distance between a pair of nodes is too long in the network. This is obtained in two different ways such as single-hop and multi-hop routing methods [6]. Since, an important feature of the MANET are ease of organization, inexpensive, flexibility and multi-hop communication [7]. The aforementioned features make the MANET more applicable to real-time applications like battlefield communications, disaster management, environmental monitoring, and combat operations [8, 9].

Since the routing in the MANET is complex and difficult due to the frequent changes in the network topology and its higher unpredictable nature [10]. The nodes in the MANET are vulnerable to security threats because of the open structure and the restricted energy of the nodes. Some nodes are uncooperative or act maliciously which affects the efficiency, fairness, and reliability of the MANET [11, 12]. Therefore, the trust-based approaches are developed to collect the trust factors which evaluate

the target node using the trust model. Since the trust factor is information that defines the activities of the mobile nodes [13]. The trust established in the ad hoc networks is required to detect and avoid malicious nodes during the routing process [14]. The validation of trustworthiness is essential to assure resource sharing among only the trustworthy nodes. However, the trust level among the nodes is decreased, when there is an absence of the location which is updated in the ad-hoc on-demand vector protocol [15].

The major contributions of this research paper are given as follows:

- An AODV routing protocol is modified using the pheromone value of ACO which obtain to secure the data transmission from a source node to the destination node.
- The pheromone value of ACO is calculated using four different fitness values trust, residual energy, distance and node degree. Here, the trust value is computed based on the data forwarding among two nodes which used to detect the black hole attacks.
- Therefore, the black hole attacks present in the MANET are avoided using the trust value which assists to avoid the packet drop during the communication.

The overall organization of the paper is given as follows: Section 2 represents the literature survey about the trust-based routing algorithms developed for the MANET. A detailed explanation of the proposed MAODV-ACO method is described in Section 3. Section 4 presents the results and discussion of the MAODV-ACO method. Finally, the conclusion is made in Section 5.

2. Literature survey

Tripathy [16] presented the CARP that dynamically configures the routing operations according to the network. Here, the routing protocol was configured based on the following parameters such as the contextual features, behavioural dynamics and varying requirements. This adaptive routing protocol used control messages similar to the AODV protocol. Additionally, the recommendations from the adjacent nodes and behavioural inquiry of the nodes were used to design the trust model. Therefore, the developed context-aware routing was used to select the node with energy, trust and mobility. The calculation of the node was affected because of the recent activities of a node.

Pathan [17] developed the Trust-based Secure QoS Routing Scheme (TSQRS) that integrates the QoS trust and social trust. This TSQRS method was generated an appropriate path by selecting the node using the residual energy, channel quality and link quality. Moreover, the trust of adjacent nodes was used to identify and avoid intrusions during the communication. Next, the TSQRS method was used to minimize the route failure that increased the performances of the entire system. However, the path failure was occurred in the network due to the increment in breakage in links.

Xu [18] presented a Trust-based Probabilistic Broadcast scheme (TPB) to secure the data transmission. The previous communication among the nodes was used to compute the trust value of the nodes. Here, the rebroadcast order of the routing packets was computed using the rebroadcast delay based on the trust level. Next, the untrusted nodes were avoided in the route discovery using the probability of rebroadcast. This TPB method was used to minimize the amount of unwanted rebroadcasting packets. However, the TPB only considered the trust value of the nodes during the data transmission.

Vatambeti [19] developed the Grey Wolf Trust Accumulation (GWTA) approach to obtain trustful data transmission. The trust accumulation approach was accomplished in the grey wolf optimization to improve the identification and prevention approaches. This GWTA was used the monitoring node to observe the activities of the nodes. Moreover, the performance of the GWTA was affected due to the increment in the number of nodes.

Sarbhukan and Ragha [20] presented the BA and DST to calculate the trust value of the nodes. Here, the AODV routing protocol was used to transmit the data packets from the source to a destination node. The nodes with less trust value were avoided in the data transmission. Hence, the security of the MANET was increased using the unified trust management approach with the AODV protocol. But, this developed AODV protocol was considered the only trust during the communication which affected the MANET performances.

3. MAODV-ACO method

In this MAODV-ACO method, a MAODV routing protocol using ACO is used to avoid the blackhole attacks a secure data transmission over the MANET. The fitness function of the ACO considers four different fitness values like trust, residual energy, distance and node degree. Specifically, the trust value of nodes is considered in the ACO's fitness function helps to avoid the blackhole attacks while generating the path using the MAODV

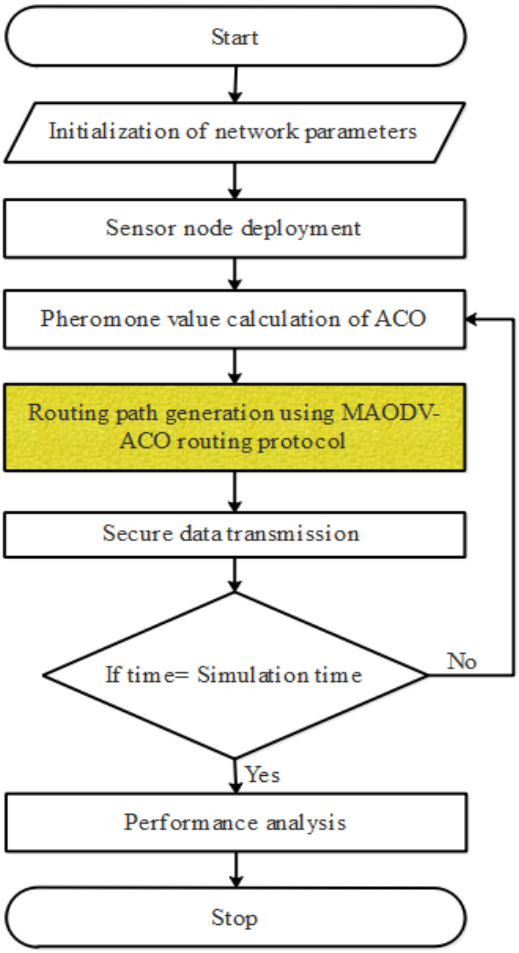

Figure. 1 Flowchart of the proposed method

protocol. However, the conventional AODV deliberates all the nodes in the MANET as cooperative which leads to susceptibility by the attacks. Therefore, the modified AODV routing protocol using ACO assists to avoid blackhole attacks which improves data transmission. The flowchart of the proposed method is shown in Fig. 1.

3.1 Calculation of pheromone value for ACO

In this proposed method, the conventional AODV routing protocol is combined with the ACO algorithm to avoid malicious attacks during data transmission. Here, the security is obtained by considering the trust values of the nodes in the fitness function of the ACO. Moreover, the fitness values of the ACO consider three more fitness values along with the trust such as residual energy, distance, and node degree which helps to improve the data transmission.

Generally, ACO is a metaheuristic algorithm that is inspired by the searching behavior of ants. In real life, the ants search together for identifying the route to the food source. The ants in the real-life emit the pheromone through the path, so that other ant discovers the trail in the same direction. Therefore, it has a better possibility for following the trail. Subsequently, the ants go in the same path and also emit some pheromone over the same path. Accordingly, the pheromone level of the path is exponentially increased as well as more ants probably use the same path for the searching process. Therefore, the ants follow the path which has the higher pheromone level. The same principle is combined in the AODV routing protocol to improve the searching process under blackhole attacks.

In the routing path identification, an adjacent node is not always considered desirable in the next-hop selection for the source node. Because the adjacent node may be an attacker node that drops the packet over the network. Hence, this scheme uses the pheromone value to select the next-hop and this pheromone value is expressed in Eq. (1).

$$PV = Trs + RE + D + ND \tag{1}$$

Where PV represents the pheromone value; Trs represents the trust value of the nodes; RE

represents the residual energy; D indicates the distance among the nodes and ND defines the node degree for the respective node.

3.1.1. Trust

Trust is considered an important objective in the MAODV-ACO method to improve security against blackhole attacks. The mobile nodes in the network establish communication based on mutual trust which is accomplished in a certain time interval. The trust value obtained from the direct communications is used as an important fitness value. Here, the trust between the nodes i and j is computed based on the forwarding ratio that is the ratio between the number of transmitted packets to the collected packets. The calculation of trust based on the forwarding ratio is expressed in Eq. (2).

$$Trs_{i,j}(t) = \frac{P_{i,j}^{T}(t)}{P_{i,j}^{C}(t)} \tag{2}$$

Where t defines the time; $P_{i,j}^{T}$ and $P_{i,j}^{C}$ represents the amount of transmitted and received packets between the nodes. The trust consideration in the ACO helps to avoid the blackhole attacks while generating the path.

3.1.2. Residual energy

The remaining energy in the node is defined as the residual energy which is used to perform different tasks like sensing, computation and communication. Therefore, the node with higher residual energy is preferred in routing path generation and Eq. (3) expresses the residual energy of the node.

$$RE = \frac{1}{E_i} \tag{3}$$

where, the residual energy of the i^{th} node is represented as E_i.

3.1.3. Distance

It defines the Euclidean distance between one node to another node. For an effective transmission, the routing path with a lesser distance to the DN is essential to minimize the energy consumption. The calculation distance between the node i and j is expressed in Eq. (4).

$$D = \sqrt{\left(x_i - x_j\right)^2 - \left(y_i - y_j\right)^2} \tag{4}$$

Where, x_i & y_i, and x_j & y_j are the coordinates of the node i and j.

3.1.4. Node degree

Node degree is defined as the number of nodes that are connected to the respective transmitter node in the network. In this MAODV-ACO, the node with a lesser amount of node degree is considered while generating the routing path.

3.2 Modified AODV routing using ACO

The calculated pheromone value from the ACO is integrated with the AODV routing to achieve a secure and reliable data transmission over the network. Generally, the conventional AODV is a reactive routing protocol that has two different phases as route discovery and route maintenance. There are four different types of control messages are used by this MAODV routing using ACO algorithm like Route Request (RREQ), Route Reply (RREP), Route Error (RERR), and hello (HELLO). The aforementioned control messages are used to discover the routing paths. Here, the pheromone value of the ACO is combined with the control messages of RREQ and RREP to avoid malicious attacks during the communication. This helps to minimize the packet drop in the network while minimizing the overhead of the MANET. The process of routing identification is accomplished, only when the source is required to forward the data packets to the destination node (DN).

3.1.5. Route identification process

The process of route identification of MAODV routing has three main steps.

Step 1: Initially, the source node (SN) broadcasts the RREQ messages to the adjacent nodes in the network. In this MAODV, the format of the RREQ message is changed by adding one more field namely the pheromone value. The modified RREQ message format and RREQ message distribution are shown in the following Fig. 2 and 3 respectively.

Here, the SN broadcasts the RREQ by fixing the pheromone value as 0. Each intermediate node adds the pheromone value with the previous node's pheromone value while propagating the RREQ messages in the network. Therefore, the pheromone value of the RREQ message defines the connectivity level, when it reaches the destination.

Step 2: The reverse route is generated with the SN, when an intermediate sensor doesn't have any route to the DN. After updating the collected RREQ

Src_address	Src_sequenceno	Request_id	Dest_address	Dest_sequenceno	Hop_Count	Pheromone level (PV)

Figure. 2 Modified RREQ format

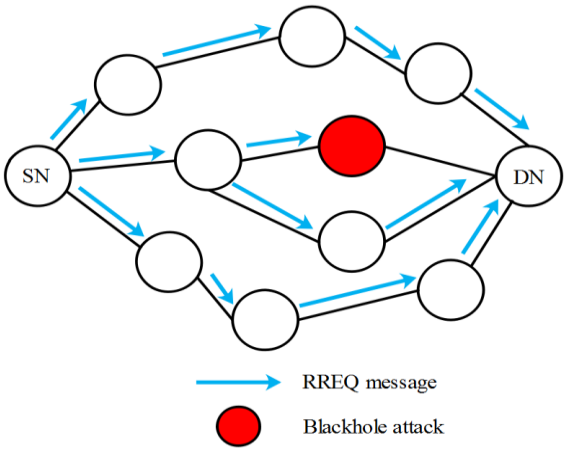

Figure. 3 RREQ message transmission of MAODV-ACO

message, the RREQ message is again broadcasted to the adjacent nodes in the network. A similar process is repeated until the RREQ message is received by the DN.

The pheromone value of the RREP message is updated in DN with the maximum pheromone value from the multiple RREQ messages. Subsequently, the path which has a higher pheromone value sends the RREP message. The RREP message is unicasted to the SN through the reverse routing when the DN receives the RREQ message. The RREP format is modified by adding one more extra field namely pheromone value as shown in Fig. 4. Next, the RREP transmission over the reverse route is illustrated in Fig. 5.

Step 3: In this step, the SN selects the routing path which has a higher pheromone value. Then the SN starts to forward the packets to the desired DN.

3.1.6. Route maintenance

The MAODV-ACO frequently transmits the HELLO messages to maintain the routes. If the HELLO message is not received from an adjacent node, then the MAODV-ACO considers that the respective link is broken during the communication.

Source_address	Destination_address	Destination_sequenceno	Lifetime	HopCount	Pheromone level (PV)

Figure. 4 Modified RREP format

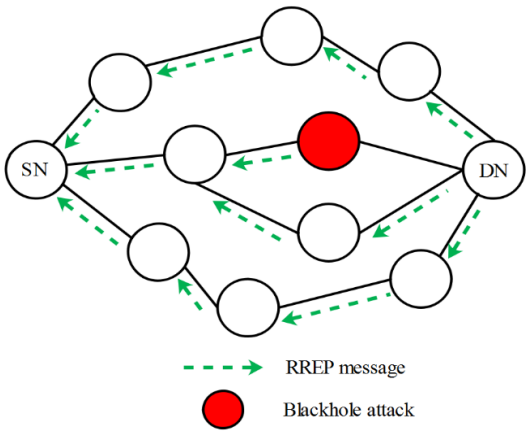

Figure. 5 RREP message transmission of MAODV-ACO

The secure data transmission over the MANET is obtained by considering the trust value of the nodes in the MAODV-ACO. An average EED is minimized by identifying the shortest path using the ACO. Moreover, the node failure is avoided in the MAODV-ACO by considering the residual energy during the routing path generation.

4. Results and discussion

The performance analysis of the proposed MAODV-ACO method is shown in this section.

Here, the NS-2 simulator with a version of 2.34 is used in the Ubuntu 16.04 OS platform to evaluate the performances of the MAODV-ACO method. Secure communication over the MANET is achieved using the ACO-based MAODV routing for data transmission. The simulation is carried out over the area of $300 \times 300\ m^2$ with the IEEE 802.11 MAC. Subsequently, the mobile nodes are varied as 80, 90 and 100 for demonstration purposes. The specifications used in the MAODV-ACO method are given in Table 1.

Table 1. Specification parameters

Parameter	Value
Area	$300 \times 300\ m^2$
Number of nodes	80, 90 & 100
Routing protocol	MAODV-ACO
Initial energy	2J
MAC protocol	IEEE 802.11
Packet size	512 Bytes
Traffic type	CBR/ UDP
Antenna model	Omnidirectional
Propagation model	Two ray ground
Network interface type	Phy/WirelessPhy
Attack	Blackhole attack
Simulation time	300s

4.1 Performance analysis

The performance of the MAODV-ACO method is analyzed as PDR, throughput, average end-to-end delay and overhead. Here, the MAODV-ACO method is compared with the CARP [16] and AODV-BA-DST [20] to justify the efficiency of the MAODV-ACO method. The performance analysis is described as follows:

4.1.1. Packet delivery ratio

PDR is defined as the ratio between the amount of received packets to the amount of generated packets which is expressed in Eq. (5).

$$PDR = \frac{\sum_0^n Packets\ received}{\sum_0^n Packets\ sent} \times 100\ \% \qquad (5)$$

Where, n defines the node count.

Fig. 6 and Table 2 show the PDR comparison for the MAODV-ACO method with the CARP [16] and AODV-BA-DST [20]. From Fig. 6 and Table 2, it is concluded that the PDR of the MAODV-ACO method is better than the CARP [16] and AODV-BA-DST [20]. For example, the MAODV-ACO is 99.48 % for 80 nodes which is high when compared to the CARP [16] and AODV-BA-DST [20]. The MAODV-ACO method achieves higher PDR to avoid link failure and blackhole attacks during the communication.

Table 2. Performance analysis of PDR

Number of nodes	CARP [16]	AODV-BA-DST [20]	MAODV-ACO
80	96 %	95 %	99.4877 %
90	97.5 %	88 %	99.8711 %
100	97 %	90 %	99.6644 %

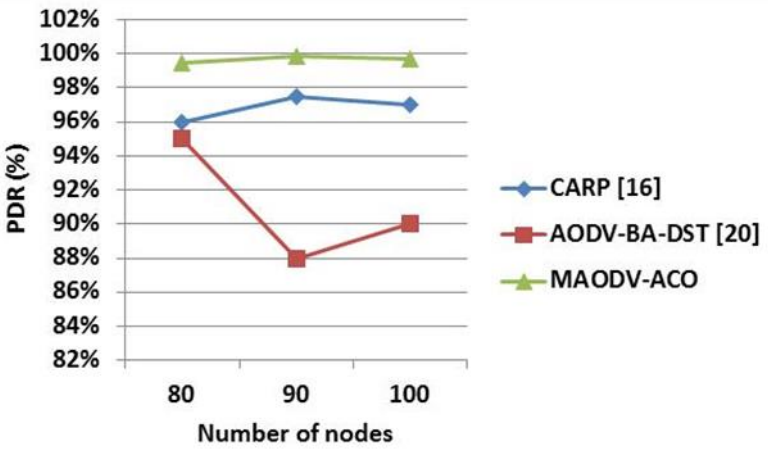

Figure. 6 Comparison of PDR

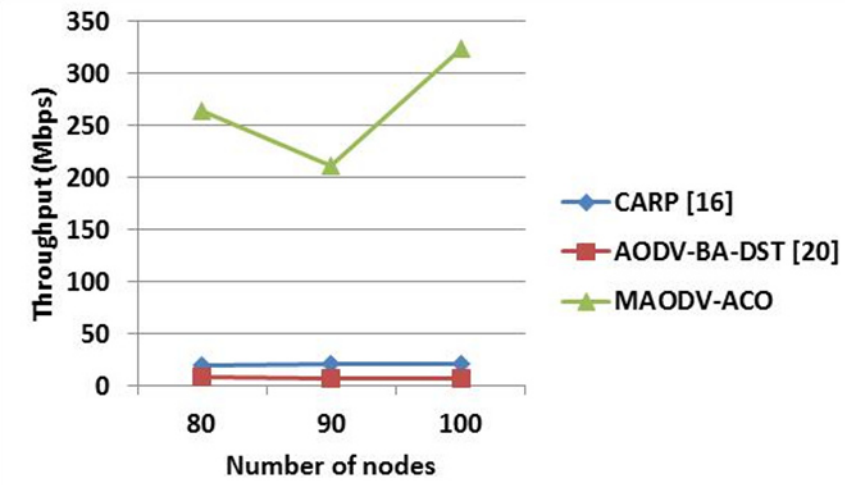

Figure. 7 Comparison of throughput

4.1.2. Throughput

The success rate of data transmission over the communication channel is defined as throughput which is analyzed in bits per second (bps). Moreover, the throughput is considered an important parameter to analyze the MAODV-ACO's efficiency. Eq. (6) expresses the throughput.

$$Throughput = \frac{\sum_0^n Packet\ received\ (n) \times Packetsize}{1000} \quad (6)$$

The throughput comparison among the CARP [16], AODV-BA-DST [20] and MAODV-ACO is presented in Table 3 and Fig. 7. From the analysis, it is concluded that the throughput of the MAODV-ACO is higher than the CARP [16] and AODV-BA-DST [20]. The throughput of the MAODV-ACO is increased based on the following reasons such as optimal node selection using the ACO's fitness function and 2) blackhole attack mitigation using the trust value of the nodes.

Table 3. Performance analysis of throughput

Number of nodes	CARP [16]	AODV-BA-DST [20]	MAODV-ACO
80	20.2 Mbps	8.23 Mbps	264.485 Mbps
90	20.9 Mbps	7.59 Mbps	211.098 Mbps
100	20.7 Mbps	6.83 Mbps	323.592 Mbps

4.1.3. Average end to end delay

Average EED is an average time required for the successful transmission of data packets from the source to the destination and this average EED is expressed in Eq. (7).

$$Average\ EED = \frac{1}{n}\left(\sum_0^n Packet\ received\ time\ (n) - Packet\ sent\ time\ (n)\right) \quad (7)$$

An average EED comparison among the CARP [16], AODV-BA-DST [20] and MAODV-ACO is presented in Table 4 and Fig. 8. From the analysis, it is concluded that the average EED of the MAODV-

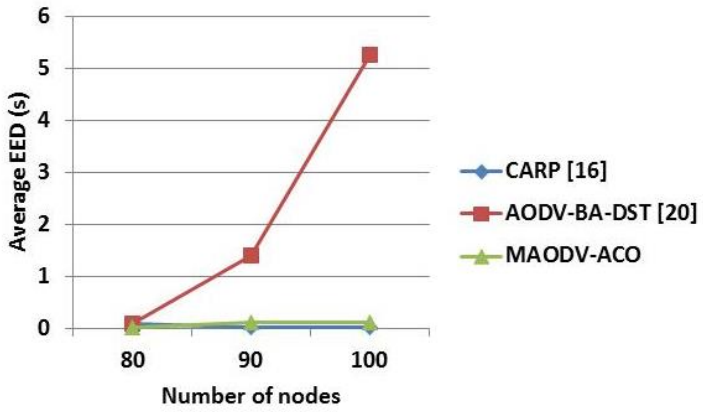

Figure. 8 Comparison of average EED

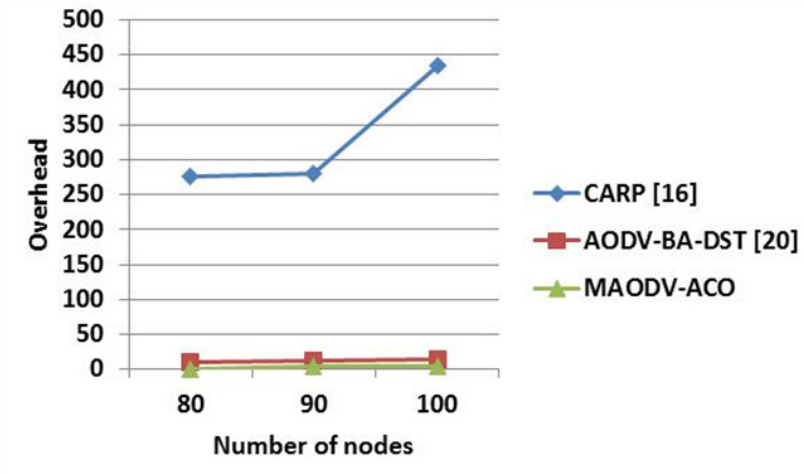

Figure. 9 Comparison of overhead

Table 4. Performance analysis of average EED

Number of nodes	CARP [16]	AODV-BA-DST [20]	MAODV-ACO
80	0.09 s	0.1 s	0.0321 s
90	0.02 s	1.4 s	0.1269 s
100	0.02 s	5.26 s	0.1180 s

ACO is improved than the CARP [16] and AODV-BA-DST [20].

The delay of the MAODV-ACO for 80 nodes is 0.0321 which is less than the CARP [16] and AODV-BA-DST [20]. However, the AODV-BA-DST [20] causes higher delay, because it doesn't consider the distance while generating the routing path.

4.1.4. Overhead

Overhead is the ratio among the amount of generated control packets to the amount of packets received by the destination.

Fig. 9 and Table 5 show the overhead comparison of the MAODV-ACO method with the CARP [16] and AODV-BA-DST [20]. Fig. 9 and Table 5, shows that the overhead of the MAODV-ACO method is less than the CARP [16] and AODV-BA-DST [20]. For example, the AODV-BA-DST [20] causes higher overhead because it transmits a high amount of control messages while generating the routing path. But, the MAODV-ACO method doesn't transmit more control packets due to the pheromone level considered in the fitness function.

Table 5. Performance analysis of overhead

Number of nodes	CARP [16]	AODV-BA-DST [20]	MAODV-ACO
80	275	10.8	0.424305
90	280	12.6	4.49677
100	435	13.8	4.93855

The data delivery of the MAODV-ACO method is improved based on the optimal node identification during the routing path generation and mitigation of blackhole nodes by using the trust values of the nodes. For example, the PDR of the MAODV-ACO method is 99.66 % for 100 nodes, which is high when compared to the CARP [16] and AODV-BA-DST [20]. Next, the MAODV-ACO method identifies the routing path with less transmission distance which results in lesser delay. Moreover, less overhead is achieved by the MAODV-ACO method, because of the pheromone level considered in the ACO algorithm. Therefore, the MAODV-ACO method provides better PDR while minimizing the overhead of the network.

5. Conclusion

In this paper, a MAODV-ACO routing protocol is utilized to mitigate the blackhole attacks to achieve a secure data transmission in the MANET. The pheromone value of the ACO is identified using four fitness values such as trust, residual energy, distance, and node degree. Here, the trust value computed from the data forwarding ratio is used to minimize the packet loss by mitigating the blackhole attack. Therefore, the selection of data forwarding nodes using MAODV-ACO helps to improve the PDR of the network. Moreover, the control packets transmitted for route establishment are minimized by avoiding link failure and blackhole attacks. Accordingly, the overhead of the MAODV-ACO is minimized as well as delay is minimized by identifying the shortest path in the MANET. The MAODV-ACO outperforms well when compared to the CARP and AODV-BA-DST. The PDR of the MAODV-ACO method is 99.66 % for 100 nodes, which is high when compared to the CARP and AODV-BA-DST. In future, the performance of the

MANET can be improved by using a novel optimization algorithm.

Conflicts of Interest

The authors declare no conflict of interest.

Author Contributions

The paper conceptualization, methodology, software, validation, formal analysis, investigation, resources, data curation, writing—original draft preparation, writing—review and editing, visualization, have been done by 1st author. The supervision and project administration, have been done by 2nd author.

References

[1] L. G. Delgado, E. P. Segarra, A. M. Mezher, and J. Forné, "A novel dynamic reputation-based source routing protocol for mobile ad hoc networks", *EURASIP Journal on Wireless Communications and Networking*, Vol. 2019, No. 1, pp. 1-16.

[2] M. M. Mukhedkar and U. Kolekar, "E-TDGO: An encrypted trust-based dolphin glowworm optimization for secure routing in mobile ad hoc network", *International Journal of Communication Systems*, Vol. 33, No. 7, pp. e4252, 2020.

[3] M. E. Semary and H. Diab, "BP-AODV: Blackhole protected AODV routing protocol for MANETs based on chaotic map", *IEEE Access*, Vol. 7, pp. 95197-95211, 2019.

[4] U. Venkanna, J. K. Agarwal, and R. L. Velusamy, "A cooperative routing for MANET based on distributed trust and energy management", *Wireless Personal Communications*, Vol. 81, No. 3, pp. 961-979, 2015.

[5] R. T. Merlin and R. Ravi, "Novel trust based energy aware routing mechanism for mitigation of black hole attacks in MANET", *Wireless Personal Communications*, Vol. 104, No. 4, pp. 1599-1636, 2019.

[6] M. Malathi and S. Jayashri, "Modified Bi-directional Routing with Best Afford Path (MBRBAP) for Routing Optimization in MANET", *Wireless Personal Communications*, Vol. 90, No. 2, pp. 861-873, 2019.

[7] S. Gurung and S. Chauhan, "A dynamic threshold based algorithm for improving security and performance of AODV under black-hole attack in MANET", *Wireless Networks*, Vol. 25, No. 4, pp. 1685-1695, 2019.

[8] M. Sirajuddin, C. Rupa, C. Iwendi, and C. Biamba, "TBSMR: A Trust-Based Secure Multipath Routing Protocol for Enhancing the QoS of the Mobile Ad Hoc Network", *Security and Communication Networks*, 2021.

[9] R. J. Cai, X. J. Li, and P. H. J. Chong, "An evolutionary self-cooperative trust scheme against routing disruptions in MANETs", *IEEE Transactions on Mobile Computing*, Vol. 18, No. 1, pp. 42-55, 2018.

[10] V. Keerthika and N. Malarvizhi, "Mitigate black hole attack using hybrid bee optimized weighted trust with 2-opt AODV in MANET", *Wireless Personal Communications*, Vol. 106, No. 2, pp. 621-632, 2018.

[11] M. N. Ahmed, A. H. Abdullah, H. Chizari, and O. Kaiwartya, "F3TM: Flooding Factor based Trust Management Framework for secure data transmission in MANETs", *Journal of King Saud University-Computer and Information Sciences*, Vol. 29, No. 3, pp. 269-280, 2017.

[12] K. R. Abirami, and M. G. Sumithra, "Preventing the impact of selfish behavior under MANET using Neighbor Credit Value based AODV routing algorithm", *Sādhanā*, Vol. 43, No. 4, pp. 1-7, 2018.

[13] S. Tan, X. Li, and Q. Dong, "Trust based routing mechanism for securing OSLR-based MANET", *Ad Hoc Networks*, Vol. 30, pp. 84-98, 2015.

[14] R. Menaka, V. Ranganathan, and B. Sowmya, "Improving performance through reputation based routing protocol for manet", *Wireless Personal Communications*, Vol. 94, No. 4, pp. 2275-2290, 2017.

[15] G. Dhananjayan and J. Subbiah, "T2AR: trust-aware ad-hoc routing protocol for MANET", *Springer Plus*, Vol. 5, No. 1, pp. 1-16, 2016.

[16] B. K. Tripathy, S. K. Jena, P. Bera, and S. Das, "An Adaptive Secure and Efficient Routing Protocol for Mobile Ad Hoc Networks", *Wireless Personal Communications*, Vol. 114, pp. 1339-1370, 2020.

[17] M. S. Pathan, N. Zhu, J. He, Z. A. Zardari, M. Q. Memon, and M. I. Hussain, "An efficient trust-based scheme for secure and quality of service routing in MANETs", *Future Internet*, Vol. 10, No. 2, p. 16, 2018.

[18] H. Xu, H. Si, H. Zhang, L. Zhang, Y. Leng, J. Wang, and D. Li, "Trust-based probabilistic broadcast scheme for mobile ad hoc networks", *IEEE Access*, Vol. 8, pp. 21380-21392, 2020.

[19] R. Vatambeti, "A Novel Wolf Based Trust Accumulation Approach for Preventing the Malicious Activities in Mobile Ad Hoc

Network", *Wireless Personal Communications*, Vol. 113, No. 4, pp. 2141-2166, 2020.

[20] V. V. Sarbhukan and L. Ragha, "Establishing secure routing path using trust to enhance security in MANET", *Wireless Personal Communications*, Vol. 110, No. 1, pp. 245-255, 2019.

BioNanoScience (2022) 12:439–450
https://doi.org/10.1007/s12668-022-00951-9

Design and Analysis of a Biosensor for the Detection of Estrogen Hormonal Levels

Javalkar Vinay Kumar[1,2] · N. Shylashree[1] · Spoorthi G. Gojanur[1] · G. Vishnu Teja Raju[1] · Vinay Varma Bhupathiraju[1] · Manjunatha Channegowda[3]

Accepted: 8 February 2022 / Published online: 16 February 2022

Abstract
Estrogenic levels in the human body have received considerable attention from the bio-medical sector due to their relevance in the early detection of cardiovascular risk in humans. In recent years, biosensors for detecting estrogenic levels have made commendable progress. This report focuses on designing an estrogenic biosensor with the adsorption mechanism and interaction, followed by its mathematical modelling and corresponding simulation results. Further, this report elaborates a comparative study of the various materials that could be used for the design regarding their efficiency, selectivity, and precision. This work concludes with the discussion and projections for the future development of biosensors for monitoring estrogen levels, and their fabrication.

Keywords Estrogen · Estradiol · Horseradish peroxide · Biosensor · COMSOL

1 Introduction

The ever-evolving technology manifests its growth in almost every walk of life, thus promoting inter-disciplinary research activities. The growing need for interdisciplinary research is fuelled by innovations made at the intersection of vastly different academic and research domains. Innovative hormonal detection methods are garnering attention from academia among the several other technological advancements being proposed in the healthcare sector. Hormonal values in the body have several health implications, thus aiding in diagnosis, treatment, and the prevention of various health adversities. Therefore, the conjunction of a biological phenomenon, chemical interactions, and electronic sensitivity for the development of biomedical devices does not take one by surprise. Further advances in this domain will improve the healthcare system, thus enabling them to diagnose diseases early on and treat them better.

One such hormone in the human body is estrogen. Apart from its primary role in the female reproductive system, this hormone plays an important factor in cardiovascular diseases in post-menopausal women. Thus, aberrant deviations from typical hormonal values strongly indicate a health anomaly in the human body. Therefore, there is a need for research into framing viable and reliable methods of Estrogen detection. Having said so, to keep financial and economic constraints in check, numerical modelling of designed sensors is essential for the eventual development and fabrication of the biosensor.

A study was conducted on 2834 middle-aged women, where they were monitored and followed up for 12 years. Their estrogen hormone levels were monitored and measured periodically and studied. The pattern in the study of Zhao, Di et al., led the author to conclude that post-menopausal women with a higher estradiol ratio (a component of

✉ N. Shylashree
shylashreen@rvce.edu.in

✉ Manjunatha Channegowda
manjunathac@rvce.edu.in; manju.chem20@gmail.com

Javalkar Vinay Kumar
javalkarvinay4u@gmail.com; vinaykumar@bitm.edu.in

[1] Department of Electronics and Communication Engineering, RV College of Engineering, Bengaluru-560059, Affiliated to VTU, Belagavi, Karnataka, India

[2] Department of Electronics and Communication Engineering, Ballari Institute of Technology and Management, Ballari-583101, Affiliated to VTU, Belagavi, Karnataka, India

[3] Department of Chemistry, RV College of Engineering, Bengaluru-560059, Affiliated to VTU, Belagavi, Karnataka, India

the estrogen hormone) were at a higher risk for heart-related diseases [1]. A similar study on lab rats was done by Todd Tolbert et al.; further, the study results established a strong connection between menopause and an increased risk of cardiovascular disease in women [2]. Hence, suggesting that estrogen levels were directly related to coronary blood flow and heart performance. A review report by S. P. Mohanty et al. is focusing on the modern biosensor developments for detecting estrogen introduced biosensors based on molecule, biosensors based on cell, and biosensors based on model organism and proposed the inclusion of nanomaterials for consideration [3].

A detailed discussion about the essential elements was elaborated by Wei Xia et al., which also included high-level overviews of different types of biosensors and their working principles, constructions, advantages, and applications of many [4]. Byung Kun Kim et al. in their paper suggested that the binding of 17-β estradiol (E2) to the estrogen receptor (ER), on the surface of the electrodes in the biosensor, increases the electron-transfer resistance and that usage of the gold electrode maximizes the association of E2 and ER [5]. An efficient electrochemical sensing mechanism for detecting E2 was evaluated by Farman et al., which included a system based on a modified platinum electrode of conductive polymer and horseradish peroxidase [6]. This detection approach is based on the idea that E2 and pyrocatechol (H2Q) are co-substrates for the horseradish peroxidase enzyme, which is immobilized on an electrode surface covered with an electro-conducting polymer called poly (4,7-bis(5-(3,4-ethylene dioxythiophene)thiophene-2-yl) benzothiadiazole. This method has also proved successful in detecting hormones in the presence of potential intervention chemicals such as ascorbic acid, estriol, estrone, uric acid, and cholesterol.

Similarly, Xin Lu et al. in their paper reported that the development of a nanostructure electrochemical biosensor based on ER linking to detect and monitor estrogenic compounds without the need for radio- or enzyme-labelled chemicals [7]. The biosensor was made again by immobilizing ER in a facilitated bi-lipid layer membrane (BLM) designed with gold nanoparticles (AuNP), and the characteristics of the modified electrodes were determined using cyclic voltammetry and electrochemical impedance spectroscopy (EIS).

Singh AC et al. in their paper have addressed the need to produce instruments capable of detecting analytes at levels as low as few pg mL^{-1} [8]. Zinc oxide nanorods (ZnONR) is an integrated, label-free, ultrasensitive biosensor with femtomolar sensitivity to the endocrine disruptor E2. ZnONR was formed on a silver electrode surface resulting in ZnONR.

Multi-walled CNT and AuNP are several nanocomposites synthesized and coated to screen printed working electrode (SPWE) for the immobilization of E2 in the analysis referred to the paper of Wang Y et al. [9]. Experimental findings showed that the immunoassay could perceive E2 as low as 10 pg mL^{-1} with a solid linear range. The electrochemical nanobiosensor analysis to analyze phenol in the presence of horseradish peroxidase enzyme was explored by Amir Kaffash et al.; further, the related interactive properties of horseradish peroxidase (hrp) were also explored [10]. The technique in this paper examined how the horseradish peroxidase enzyme specifically oxidizes phenol to o-quinone, which can be electrochemically reduced, producing a current output dependent on the phenol concentration. This model was simulated on the COMSOL Multiphysics tool.

The structure of the biosensor model in the paper of Parthasarathy P et al., consisting of an array of micro-pillars coated by TiO_2 and uricase enzyme to detect bio-molecules, is designed with modifiable parameters to analyze the influence of design on the accuracy of detection [11]. A review article by H. Sharma et al. [12], focuses on biosensors that can result in a much shorter time with selectivity and sensitivity comparable to the conventional methods [13]. It addresses the need to reduce the development time and costs of any sensor design. The design process is identifying an analyte and numerical method to study the electrochemical or optical functionality and then modelling a biosensor mathematically with different computational approaches.

D.R Thevenot et al. in their work proposed that the electrochemical biosensor is a contained integrated sensor and it can provide specific or semi-quantitative information using the biological recognition element, also called a bio-receptor [14]. This communicates with the electrochemical transducers. The uric acid biosensor developed by P. Panchatcharam et al., for arthritis using the uricase enzyme coated on TiO_2-CeO_2 nanocomposite, is based on the R-diffusions with irreversible catalytic reaction [15]. The experimental finding shows that the maximum change in response is due to the difference in the membrane thickness.

2 Design of Estrogen Biosensor

There are numerous mechanisms that can be implemented in a biosensor as discussed previously. However, keeping in mind the objective of the study, an in vitro biosensor with an enzymatic surface reaction mechanism was chosen.

Figure 1 depicts the working of an enzyme. When an enzyme reacts with a substrate, it forms a complex molecule that, under the right conditions, transforms into the desired product molecule, releasing the enzyme at the end. Enzymes are highly specific in their activity. The terms enzyme and receptor are used interchangeably.

As described in Fig. 2, the analyte, i.e., estrogen, reacts with the bio-element and a product is obtained, which is transduced into a signal, whereas if another hormone is

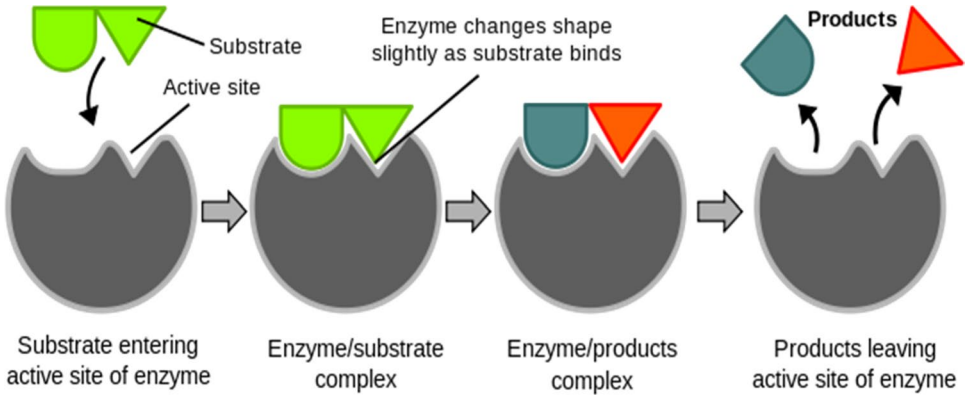

Fig. 1 Working principle of an enzyme

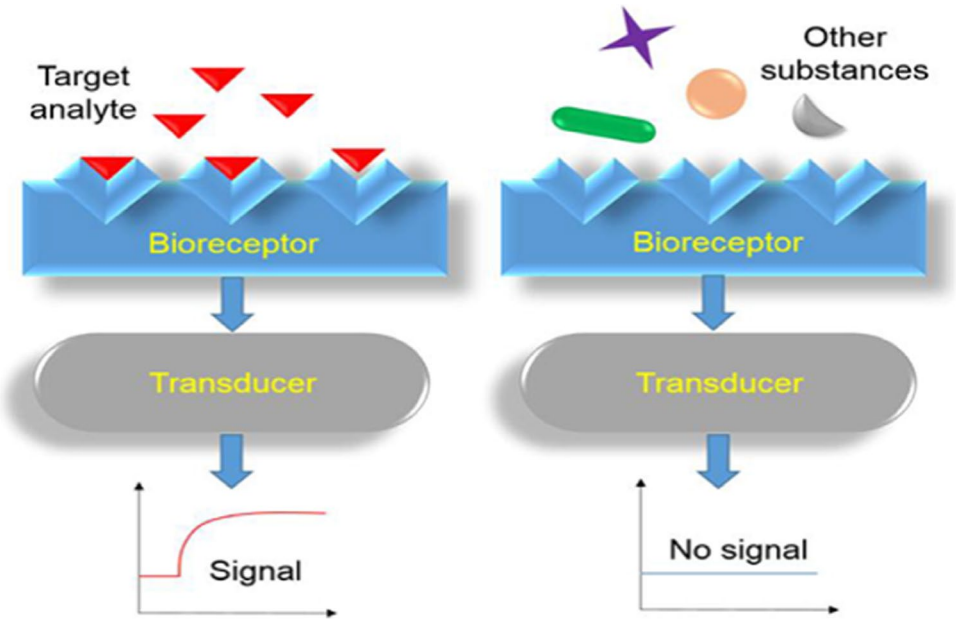

Fig. 2 Mechanism of enzymatic reaction

subjected to the bio-element, which does not react, and hence, no signal is produced. Estrone (E1), estradiol (E2), estriol (E3), and estetrol (E4) are the four most common estrogenic hormones, according to a thorough literature review. In reproductive years, E2 is the most prevalent estrogen, in both absolute serum levels and activity.

According to a study conducted on a group of 2834 post-menopausal middle-aged women over a period of 12 years, it was found that post-menopausal women are more likely to be prone to heart-related diseases such as coronary heart disease and cardiovascular disease. A total of 10% of the women in the study developed heart-related conditions. The estrogen hormone concentrations in these women were comparatively lower than those who did not develop any heart-related diseases.

The study concluded that the concentration of E2 was directly related to the development of heart-related diseases. The higher the estrogen levels, the better the heart performance. After a detailed literature survey of Spychalska et al., the horseradish peroxidase was the best choice for the receptor enzyme due to its high specificity to E2 and availability at economically nominal rates [16]. As shown in Fig. 3, many surface substrates can be used to coat the receptor.

Among the various substrates, the platinum (Pt), zinc oxide nanorods (ZnONR), and carbon nanotubes (CNT) were chosen to simulate because of the following features:

- Platinum is biocompatible, conductive, denser substance, ductile, resistance to corrosion, radiopaque, high melting point, catalytic nature, etc. [17].
- Zno provides large surface area, efficient enzyme immobilization, better stability, fabrication is simple, for long time monitoring, etc..[18]

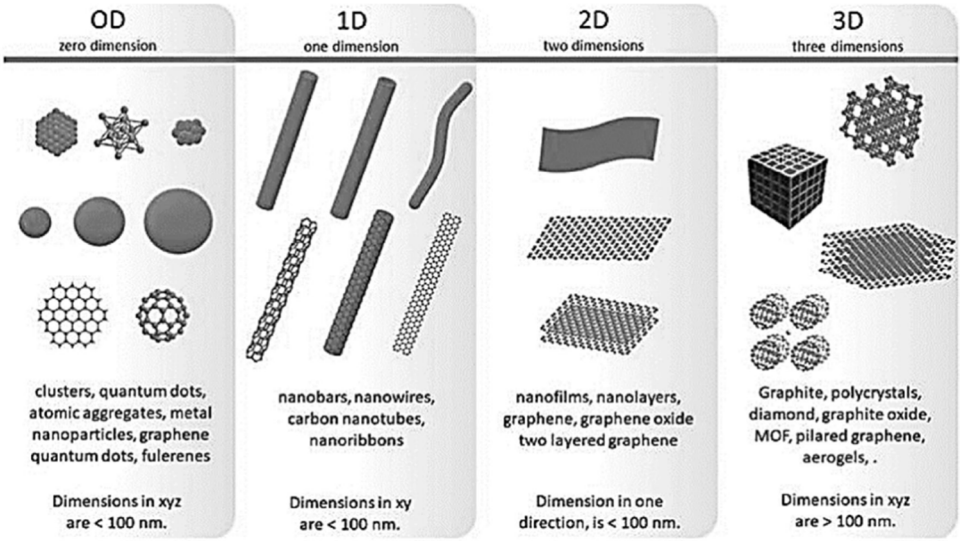

Fig. 3 Nanostructure material classifications

- Carbon nanotubes are 100 times stronger than steel, possess higher electrical conductivity, average diameter of 1.2–1.4 nm, light weight, etc. [19].

Based on above features, the substrates that were chosen to simulate are platinum, zinc oxide nanorods (ZnONR), and carbon nanotubes (CNT). This project aims to compare the performance of the above-stated surface substrates coated with the receptor (E2) in terms of adsorption and determine which surface substrate is most suited [20].

3 Role of COMSOL Multiphysics

COMSOL Multiphysics is a computer-aided, finite element analysis-based engineering platform with various analysis and solution functions. It is equipped with a wide range of applications covering almost physics. With several computing features, it can solve complex science and large-scale engineering problems. It eliminates the trivial and drab programming of finite elements. The ability to solve mixed Multiphysics phenomena simultaneously is one of the critical benefits of COMSOL Multiphysics.

The design flow of COMSOL Multiphysics is shown in Fig. 4.

Initially, the model environment is set up following the requirements solicited by design. These include the definitions of global parameters and functions.

Following the first step, the geometry is designed to support the requirements as much as possible and is optimized to the greatest extent both in design and simulation. Succeeding the geometrical structure, the material to be analyzed is defined. It can be either predefined or custom. Following the definition of the material, it is assigned to the geometrical domains on which its' analysis is to be performed. Subsequently, the physics to either aid or conduct the study on the design model is added. The required constraints are defined, keeping the boundary conditions and design specifications in mind. Following the definitions of physics, a mesh is created. It can be either predefined or custom based on the requirement.

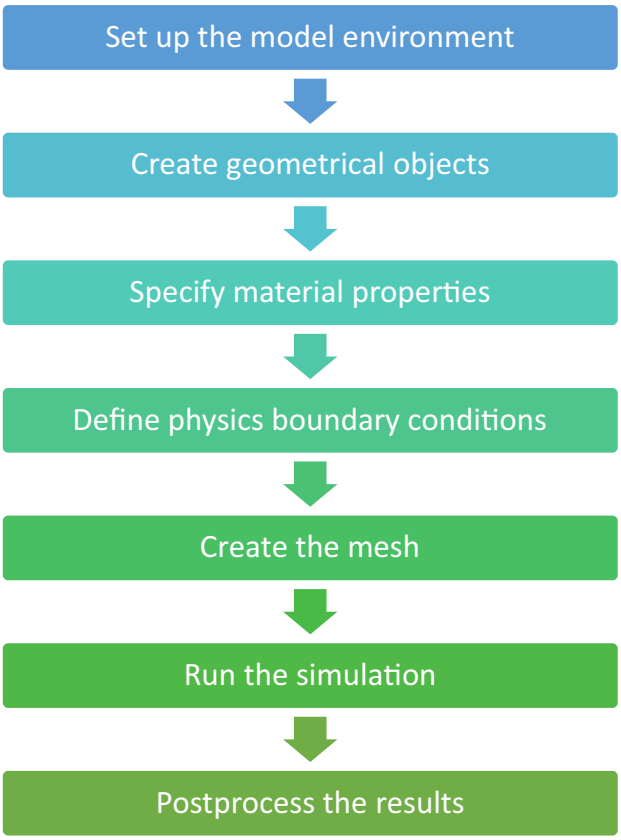

Fig. 4 Design flow of COMSOL

The type of simulation, i.e., the study, is chosen based on the need for appropriate settings for each study defined. Once computed, the results can be plotted using various kinds of plots like 3D plots, 2D plots, and regular graphical plots for numerical analysis.

The three stages of COMSOL Multiphysics are pre-processing, solution, and post-process. Pre-processing constitutes creating a finite element model and configuring the environment parameters. Mesh division and solving equations are included in the solution section. Visualization and interpretation of outcomes apply to post-processing.

Internally, COMSOL Multiphysics compiles a partial differential equation (PDE) set representing the whole model. COMSOL Multiphysics adapts the finite element approach to solve partial differential equation (PDE). The software uses several numerical solvers to perform finite element analysis with flexible meshing with feedback and error management.

4 Reagents, Materials, and Methods

4.1 Reagents

It can be observed that the compound horseradish peroxidase is the majorly used for detecting phenolic substances, especially estradiol (E2), due to its low cost and excellent specificity high reactivity [21].

4.2 Choice of Surface Substrate Material

Various surfaces offer a variety of reaction rates based on factors such as surface area [22]. This article compares the surface reaction rate between different surface substrates such as platinum, zinc oxide nanorods (ZnONR), and carbon nanotubes (CNT) simulated on COMSOL.

4.3 Reactions

A surface reaction mechanism is used where the adsorption and desorption of the analyte molecules (A_m) from the surface sites (S_s) on the substrate

$$A_m + S_s \overset{k_{ad}k_{des}}{\leftrightarrow} S_s \quad (1)$$

It is possible to convert the adsorbed analyte into a quenched state that does not add to the sensor signal.

$$A_m + S_s \overset{k_1k_2}{\leftrightarrow} Q_sS_s \quad (2)$$

The rate of adsorption is

$$r_{ads} = k_{ads}c_{Am}$$

where c_{Am} is the concentration of the A_m stream.

In the concentration of surface adsorbed species $c_{Am\ Ss}$, the rate of desorption is linear

$$r_{des} = k_{des}c_{Am}s_s$$

Analyte Stream Mass Transport:

Equations in the interface of the transport of diluted species describe the transport of the species A_m in the analyte stream:

$$\frac{dc_{Am}}{dt} + \Delta(-D_{am}.\Delta c_{Am}) + u.\Delta c_{Am} = 0$$

D_{Am} denotes the diffusion coefficient, c_{Am} denotes the species concentration, and u is the velocity vector (m/s).

Parameters that define the working of the biosensor are illustrated in Table 1. These parameters are given as input to the model developed on COMSOL to perform analyses.

The forward rate constant is the constant that describes the forward response rate, i.e., the rate of conversion from reactants to products [23]. The backward rate constant is the constant that characterizes the rate of reverse or backward reaction, i.e., the rate of conversion from product to reactants. Adsorption rate constant is the constant which describes the rate of adsorption onto the surface. The

Table 1 Description of various parameters

Parameter	Description
k_ads	Adsorption constant
k_des	Desorption constant
kf	Forward rate constant
kr	Reverse rate constant

Table 2 Parameters for horseradish peroxidase–coated platinum

Parameter	Value
k_ads	0.01 m/s
k_des	0.5 mol/(m^2 s)
kf	2×10^{-7} mol/(m^2 s)
kr	4×10^{-8} mol/(m^2 s)

Table 3 Parameters for ZnONR-coated horseradish peroxidase

Parameter	Value
k_ads	0.021 m/s
k_des	0.38 mol/(m^2 s)
kf	2.7×10^{-7} mol/(m^{2}s)
kr	3.6×10^{-8} mol/(m^2 s)

Table 4 Parameters for CNT-coated horseradish peroxidase

Parameter	Value
k_ads	0.041 m/s
k_des	0.44 mol/(m^2s)
kf	3.2×10^{-7} mol/(m^2s)
kr	4.1×10^{-8} mol/(m^2s)

Table 5 Physical properties of blood [25–27]

Properties	Value
Dynamic viscosity	0.00035 Pa · s
Density	1050 kg/m^3
Coefficient of thermal expansion	0.0003 1/K
Bulk viscosity	0.0004 Pa · s
Electrical conductivity	100 µS/m
Heat capacity(at constant pressure)	3617 J/ (kg · K)
Thermal conductivity	0.5 W/ (m · K)
Speed of sound	1570 m/s

desorption rate constant is the constant which describes the rate of desorption from the surface [24].

A comparative study is performed on three surface substrates: platinum,, and CNTs coated with horseradish peroxidase. The input values are taken as described in Tables 2, 3, and 4. The parametric values given as input to the designed model are mathematically approximated.

Table 2 depicts the values assigned to the parameters which describe a platinum surface.

Table 3 depicts the values assigned to the parameters which describe a ZnONR surface.

Table 4 depicts the values assigned to the parameters which describe a CNT surface.

Table 5 depicts blood's physical properties, which are utilised as flow modelling inputs.

A Gaussian function is implemented to model the flow of E2 into the designed biosensor model as shown in Fig. 5.

4.4 Geometry

The choice of an in-vitro biosensor resulted in geometry design, as shown in Fig. 6. A set of concave pillars are enclosed within a rectangular box of dimensions $10\times6\times1$ mm. Concave pillars are used as reacting surfaces to provide maximum surface area and excellent reaction rates [28, 29].

However, since the geometry is symmetrical, it can be divided and simulated for one part after defining the planes of symmetry (as highlighted in blue in Fig. 7). The simulation results for the whole model can be obtained owing to the flexibility of the COMSOL tool. This reduces computational time and reduces the memory requirement.

Mesh nodes allow the geometry to be divided into small units of simple shapes, referred to as mesh elements. Mesh is a division of continuous geometric space into discrete geometric cells [30].

The mesh should be fine in areas requiring high accuracy. Mesh is used in physical simulations like finite element analysis, computational fluid dynamics, and rendering on a computer screen [31].

In Fig. 8, it can be observed that the reacting pillars possess very fine mesh elements as the computation there has to be accurate, and the walls of the rectangular box possess relatively more significant mesh elements as it does not require high accuracy [32].

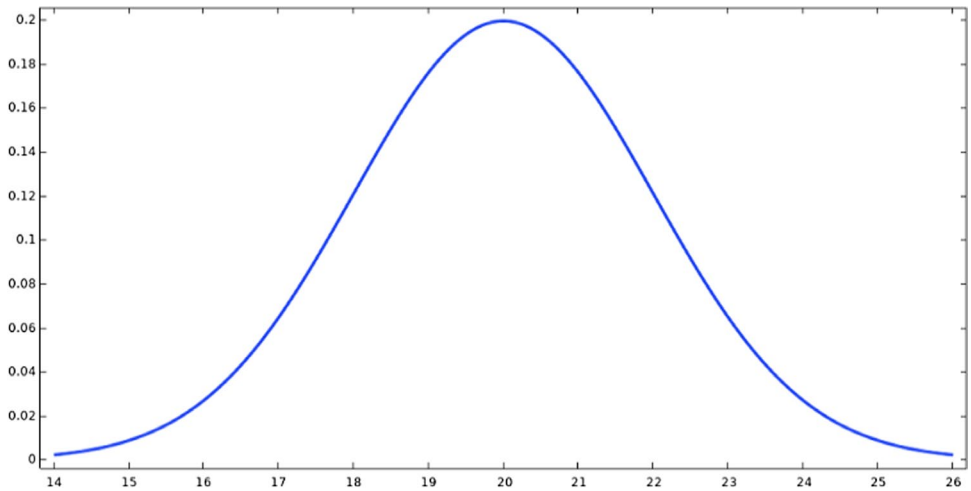

Fig. 5 Gaussian pulse function

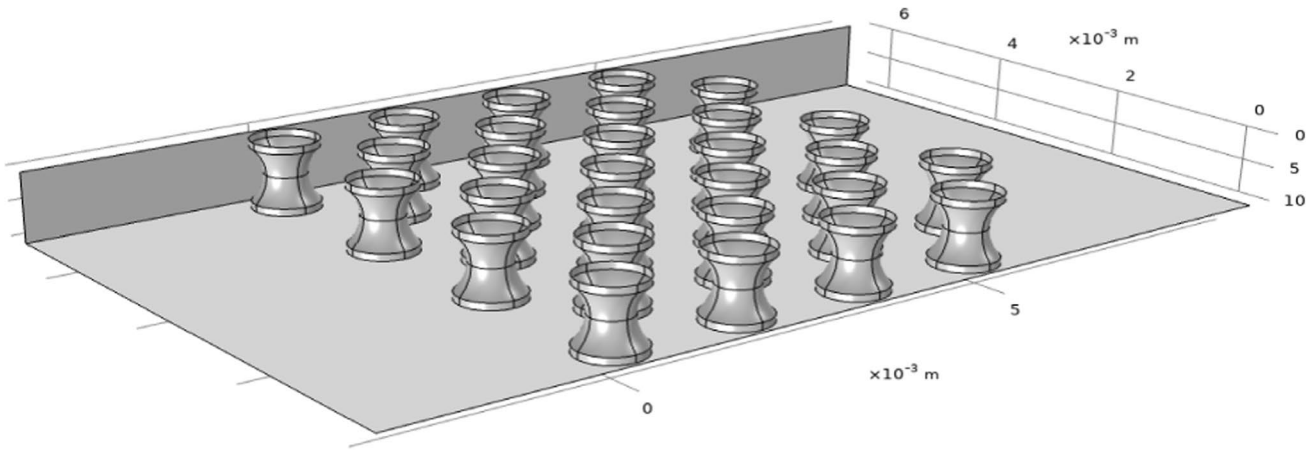

Fig. 6 Geometry of the biosensor model

Fig. 7 Computational geometry

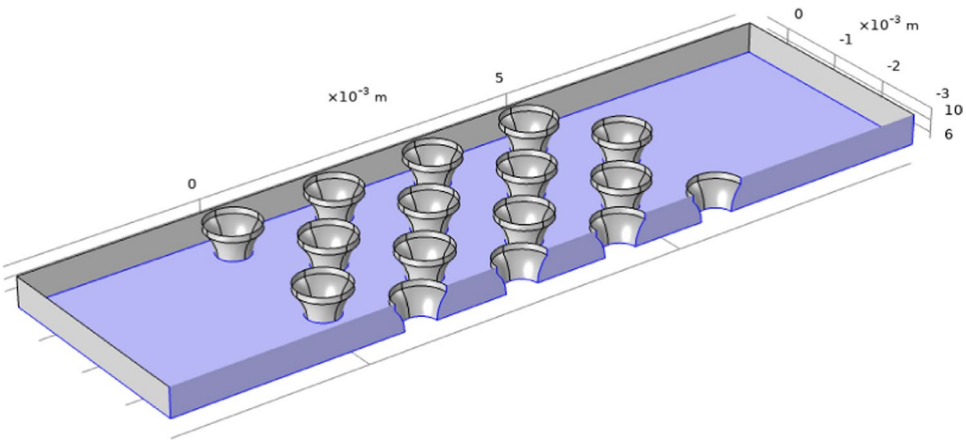

Fig. 8 Mesh model for mathematical simulations

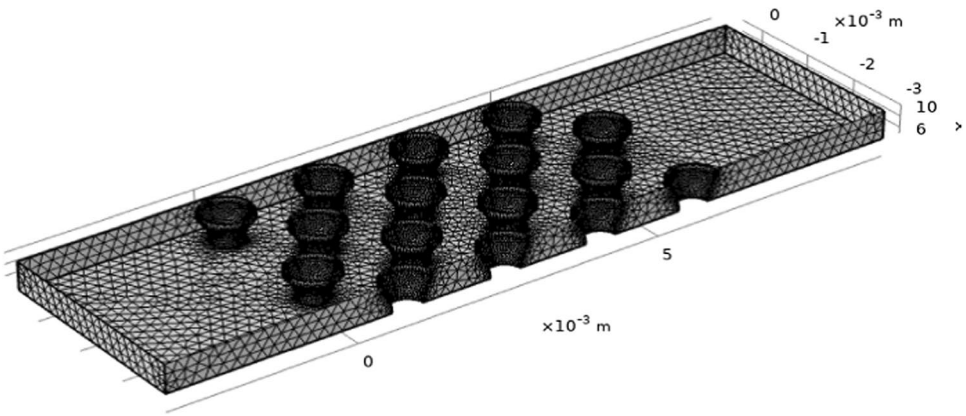

5 Results

5.1 Velocity Plot

It is the 3D plot of a 2D slice of fluid velocity. As per Fig. 9, the colour legend indicates the velocity amplitude of input liquid, i.e., estradiol (E2). It can be observed that the fluid velocity is maximum around the concave pillars and minimum at the walls of the rectangular enclosure.

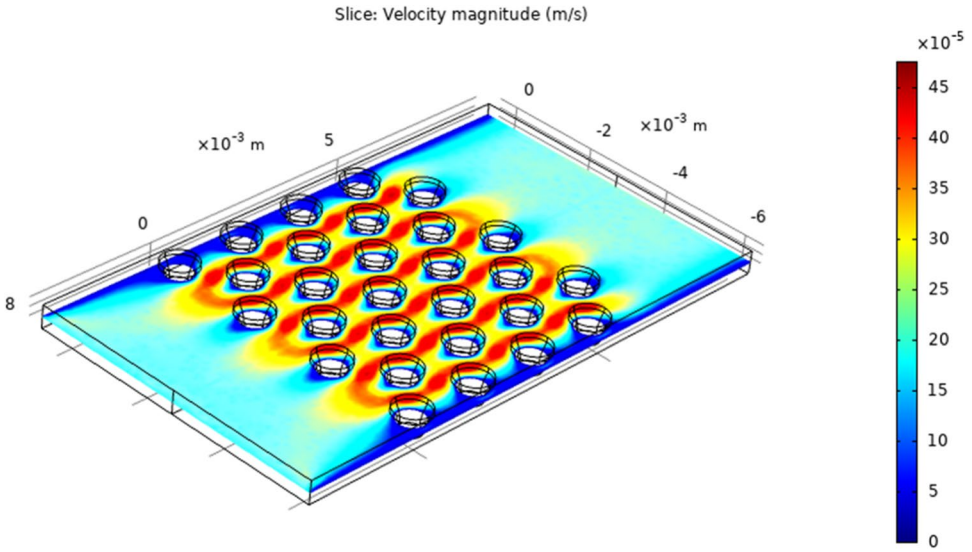

Fig. 9 Velocity magnitude representation of a input liquid, i.e., estradiol (E2)

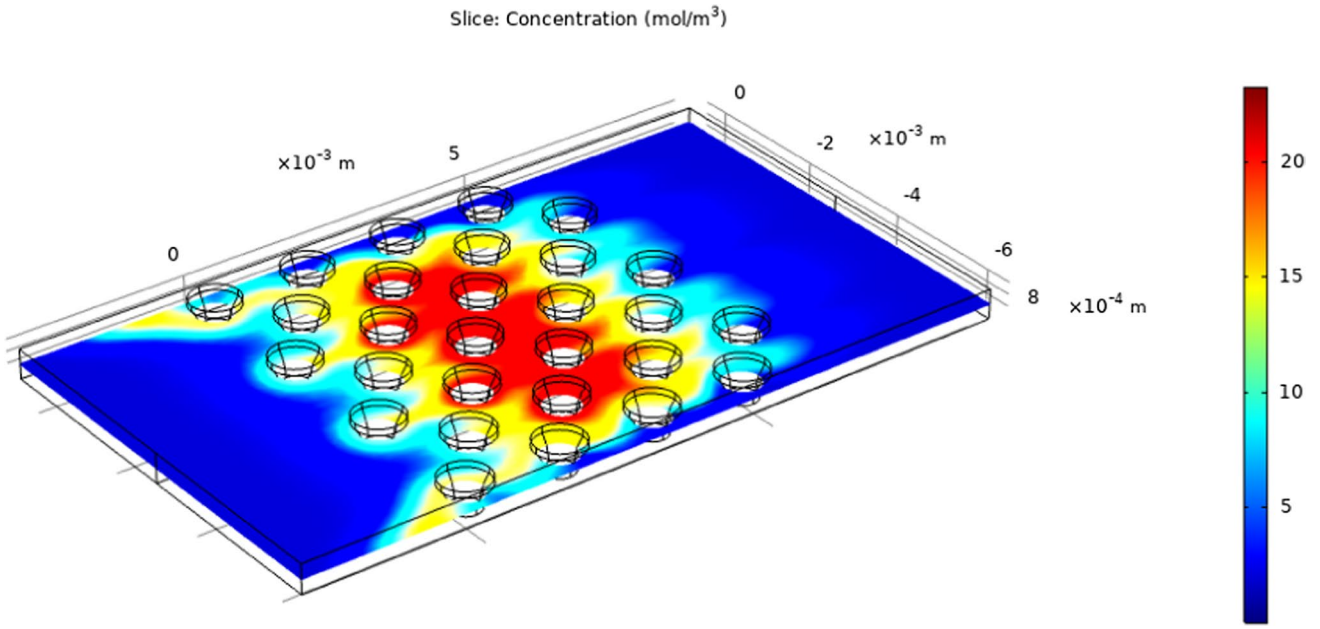

Fig. 10 Concentration flow plot of estradiol at a timestamp of 45 s

5.2 Concentration Plot

It describes the 3D plot of a 2D slice of concentration of the input liquid analyte, estradiol (E2). Figure 10 depicts the plot of E2 at a timestamp of 45 s. It can be noticed from Fig. 6 that the central region is red and is surrounded by a gradient of colours ranging from yellow to shades of blue.

When compared to the colour legend, it can be observed that only a fraction of the input consists of high concentration E2 (in red), and the other gradient colours indicate the lesser amount of E2 concentration.

The reason for that is using a Gaussian pulse input that has a peak at a particular window of time and is diminished elsewhere.

5.3 Adsorption Fraction Plot

It is a 2D plot of a fraction of sites adsorbed on the reacting surface vs time. The higher the fraction of adsorption, the better the surface substrate. It can be observed in Fig. 8 that the central region is highly concentrated at the time stamp of 45 s. On comparing Figs. 10 and 11, it can be observed that they correspond.

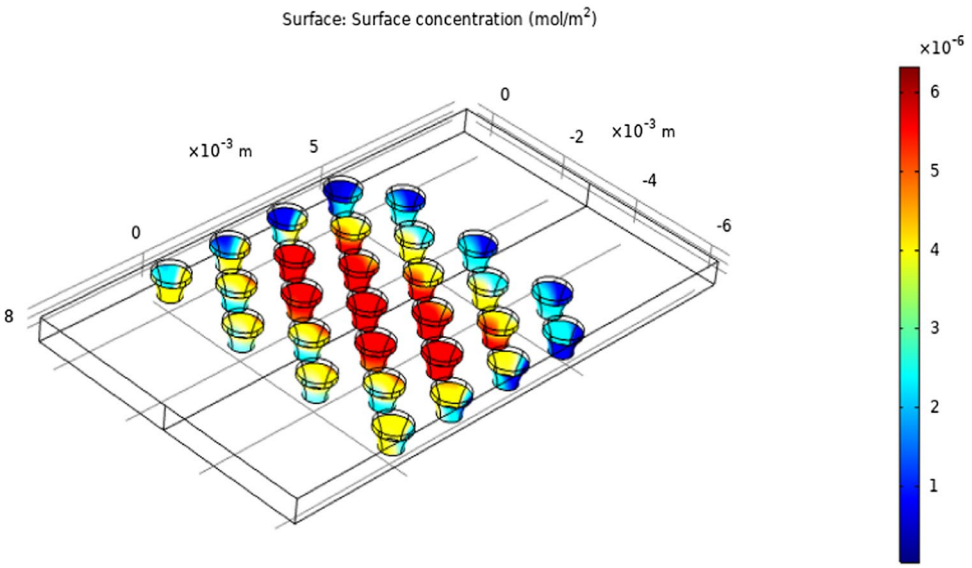

Fig. 11 Surface adsorption plot of input liquid analyte

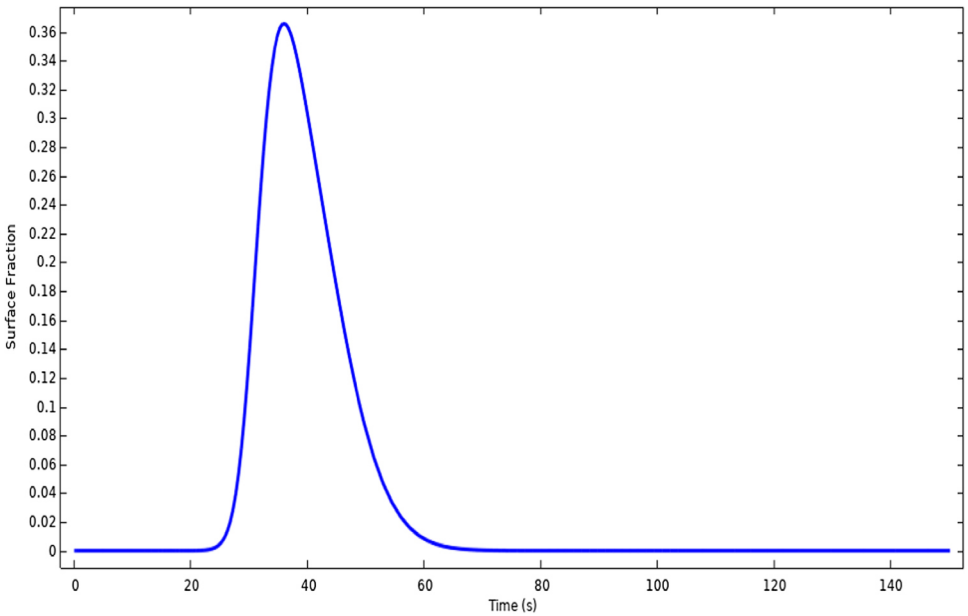

Fig. 12 Surface adsorption plot of biosensor using platinum surface substrate

A 2D plot of the fraction of sites adsorbed on the horseradish peroxidise–coated platinum surface substrate vs time is depicted in Fig. 12. This plot is for the centre pillar of first row whose surface adsorption fraction peaks at the 38th second. This substrate provides a surface adsorption of 37%.

A 2D plot of the fraction of sites adsorbed on the horseradish peroxidise–coated ZnONR surface substrate vs time is shown in Fig. 13.

This plot is for the centre pillar of first row whose surface adsorption fraction peaks at the 38th second. This substrate provides a surface adsorption of 59%.

A 2D plot of the fraction of sites adsorbed on the horseradish peroxidise–coated CNT surface substrate vs time is shown in Fig. 14. This plot is for the centre pillar of first row whose surface adsorption fraction peaks at the 38th second. This substrate provides a surface adsorption of 70%.

5.4 Comparison Between the Surface Substrates

The analyses and simulations performed for all surface substrates and the results are shown in Table 6. The results are analysed in terms of surface adsorption ratio.

From Table 2, it can be observed that CNT surface substrate gives the highest adsorption ratio of 70%, followed by ZnONR surface substrate gives an adsorption ratio of

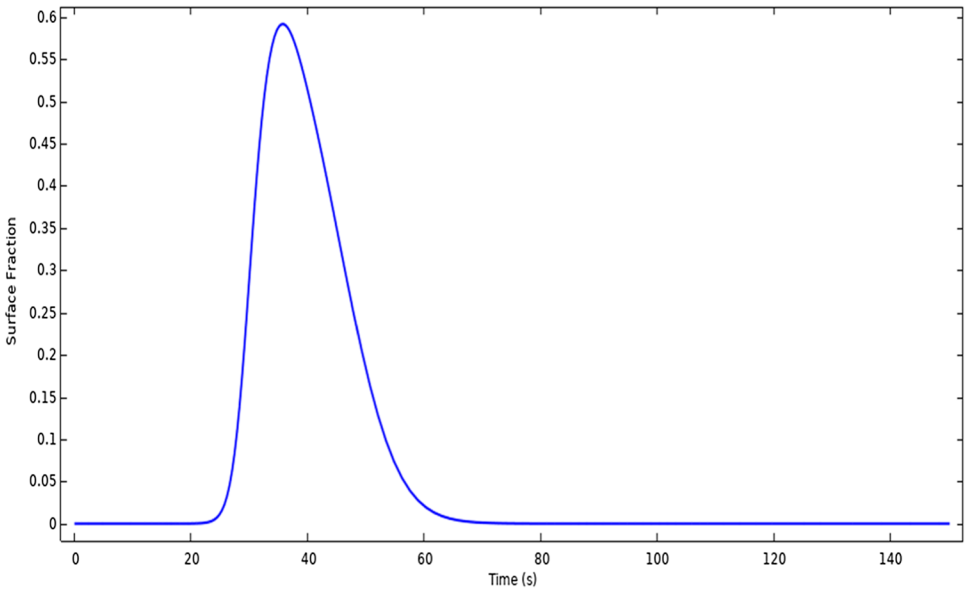

Fig. 13 Surface adsorption plot of biosensor using ZnONR surface substrate

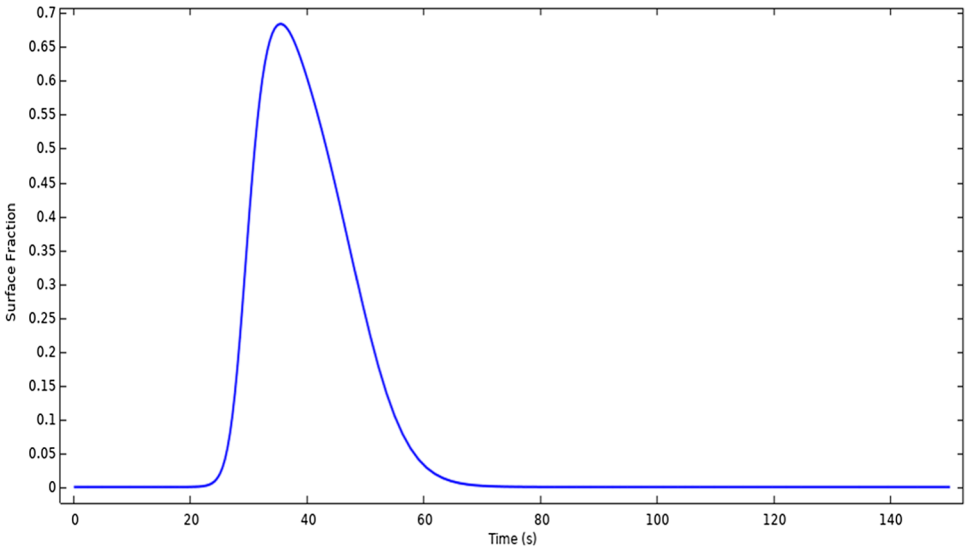

Fig. 14 Surface adsorption plot of biosensor using CNT surface substrate

Table 6 Comparison between substrates in terms of surface adsorption ratio

Substrate	Adsorption ratio
Platinum	37%
Zinc oxide nanorod (ZnONR)	59%
Carbon nanotube (CNT)	70%

59% and the platinum surface substrate which gives the least adsorption ratio of 37%.

6 Conclusions

The primary objective was to estimate the estrogen levels in the blood sample, successfully met. Secondary goals, including conducting a comparative study with different surface substrate materials and optimizing the model for better specificity and reliability, have also been completed with conclusive results. The biosensor design and model were carried out through the COMSOL Multiphysics simulator using the finite element analysis solver software package. For susceptibility and concentration measurement, the estrogen biosensor is modelled and successfully studied in blood samples. At the end of this article, it can be established that the carbon nanotubes are the

most suitable material for the surface substrate with surface adsorption of 70%, followed by zinc oxide nanorod surface substrate providing with adsorption of 59% and the platinum surface substrate which delivers the least adsorption of 37%. The results show excellent sensitivity, a wide range, and a reasonable detection limit. Moreover, literature reviews with these materials have shown satisfactory results. The optimized design, and more carefully calibrated parameters, has demonstrated improved efficiency and thus can be considered a plausible biosensor for applications in clinical diagnosis, pharmaceutical analysis, and the field of bio-electrochemistry.

Declarations

Conflict of Interest The authors declare no competing interests.

Research Involving Humans and Animals Statement Not applicable

Informed Consent Not applicable

Funding Statement Not applicable

References

1. Zhao, Di., et al. (2018). Endogenous sex hormones and incident cardiovascular disease in post-menopausal women. *Journal of the American College of Cardiology, 71*(22), 2555–2566. https://doi.org/10.1016/j.jacc.2018.01.083
2. Tolbert, T., & Oparil, S. (2001). Cardiovascular effects of estrogen. *American Journal of Hypertension, 14*(S3), 186S-193S. https://doi.org/10.1016/S0895-7061(01)02087-8
3. Mohanty, S. P., & Kougianos, E. (2006). Biosensors: A tutorial review. *IEEE Potentials, 25*(2), 35–40. https://doi.org/10.1109/MP.2006.1649009
4. Xia, W., Li, Y., Wan, Y., Chen, T., Wei, J., Lin, Y., Xu, S. (2010). Electrochemical biosensor for estrogenic substance using lipid bilayers modified by Au nanoparticles. *Biosensors and Bioelectronics*, 25(10), 2253–2258, ISSN 0956–5663. https://doi.org/10.1016/j.bios.2010.03.004
5. Kim, B. K., Li, J., Im, J-E., Ahn, K-S., Park, TS., Cho, SI., Kim, Y-R., Lee, W-Y. (2012). Impedometric estrogen biosensor based on estrogen receptor alpha-immobilized gold electrode. *Journal of Electroanalytical Chemistry*, 671, 106–111 ISSN 1572–6657,. https://doi.org/10.1016/j.jelechem.2012.02.022
6. Farman, H. H., Gustafsson, K. L., Henning, P., Grahnemo, L., Lionikaite, V., Movérare-Skrtic, S., Wu, J., Ryberg, H., Koskela, A., Tuukkanen, J., et al. (2018). Membrane estrogen receptor α is essential for estrogen signaling in the male skeleton. *Journal of Endocrinology, 239*, 303–312. https://doi.org/10.1530/JOE-18-0406
7. Lu, X., Sun, J., Sun, X. (2020). Recent advances in biosensors for the detection of estrogens in the environment and food, TrAC Trends in Analytical Chemistry, 127, 115882,ISSN 0165–9936, https://doi.org/10.1016/j.trac.2020.115882M
8. Singh, A. C., Asif, M. H., Bacher, G., Danielsson, B., Willander, M., & Bhand, S. (2019). Nano-immunosensor based on ZnO NanoRods for ultrasensitive detection of 17β-Estradiol. *Biosensors & Bioelectronics, 1*(126), 15–22. https://doi.org/10.1016/j.bios.2018.10.004.M
9. Wang, Y., Luo, J., Liu, J., et al. (2018). Electrochemical integrated paper-based immunosensor modified with multi-walled carbon nanotubes nanocomposites for point-of-care testing of 17β-estradiol. *Biosensors & Bioelectronics, 107*, 47–53. https://doi.org/10.1016/j.bios.2018.02.012
10. Kaffash, A., Rostami, K., Zare, H. R. (2019). Modeling of an electrochemical nano biosensor in COMSOL Multiphysics to determine phenol in the presence of horseradish peroxidase enzyme. *Enzyme and Microbial Technology*, 121, 23–28, ISSN 0141–0229, https://doi.org/10.1016/j.enzmictec.2018.11.001
11. Parthasarathy, P., Vivekanandan, S. (2020). Modelling and identification of suitable matrix for uric acid biosensor using COMSOL Multiphysics. *International Journal of Scientific & Technology Research*, 9(04), ISSN 2277–8616–3598
12. Sharma, H. and Mutharasan, R. (2013). Review of biosensors for foodborne pathogens andtoxins. *Sensors and Actuators B: Chemical*, 183, 535–549, ISSN:09254005. https://doi.org/10.1016/j.snb.2013.03.137
13. Wang, Q. (2011). Mathematical Methods for Biosensor Models. In *Doctoral Thesis*. Technological University Dublin. https://doi.org/10.21427/D7BS3C
14. Thevenot, D. R., Tóth, K., Durst, R. A. and Wilson, G. S. (1999). Electrochemical biosen-sors: Recommended definitions and classification. *Pure and Applied Chemistry*, 71(12), 2333–2348. https://doi.org/10.1351/pac199971122333 [Online].
15. Parthasarathy, P., & Vivekanandan, S. (2018). Investigation on uric acid biosensor model for enzyme layer thickness for the application of arthritis disease diagnosis. *Health Information Science and Systems, 6,* 5. https://doi.org/10.1007/s13755-018-0043-3.
16. Spychalska, K., Zając, D., & Cabaj, J. (2020). Electrochemical biosensor for detection of 17β-estradiol using semi-conducting polymer and horseradish peroxidase. *RSC Advances, 10*, 9079–9087. https://doi.org/10.1039/C9RA09902F
17. Stanca, S. E., Hänschke, F., Ihring, A., et al. (2017). Chemical and electrochemical synthesis of platinum black. *Science and Reports, 7*, 1074. https://doi.org/10.1038/s41598-017-01040-8
18. Napi, M. L. M., Sultan, S. M., Ismail, R., How, K. W., & Ahmad, M. K. (2019). Electrochemical-based biosensors on different zinc oxide nanostructures: A review. *Materials, 12*, 2985. https://doi.org/10.3390/ma12182985
19. Eatemadi, Ali, et al. (2014). Carbon nanotubes: Properties, synthesis, purification, and medical applications. *Nanoscale Research Letters, 9*(1), 393. https://doi.org/10.1186/1556-276X-9-393
20. Riggs, L., & Hartmann, L. (2003). Selective estrogen-receptor modulators: Mechanisms of action and application to clinical practice. *New England Journal of Medicine, 348*, 618–629. https://doi.org/10.1056/NEJMra022219
21. Valéra, M. C., Fontaine, C., Dupuis, M., Noirrit-Esclassan, E., Vinel, A., Guillaume, M., Gourdy, P., Lenfant, F., & Arnal, J. F. (2018). Towards optimization of estrogen receptor modulation in medicine. *Pharmacology & Therapeutics, 189*, 123–129. https://doi.org/10.1016/j.pharmthera.2018.05.002
22. Cooke, P. S., Nanjappa, M. K., Ko, C., Prins, G. S., & Hess, R. A. (2017). Estrogens in male physiology. *Physiological Reviews, 97*, 995–1043. https://doi.org/10.1152/physrev.00018.2016
23. Bouillon, R., Bex, M., Vanderschueren, D., & Boonen, S. (2004). Estrogens are essential for male pubertal periosteal bone expansion. *Journal of Clinical Endocrinology and Metabolism, 89*, 6025–6029. https://doi.org/10.1210/jc.2004-0602
24. Oldknow, K. J., Macrae, V. E., & Farquharson, C. (2015). Endocrine role of bone: Recent and emerging perspectives beyond osteocalcin. *Journal of Endocrinology, 225*, R1–R19. https://doi.org/10.1530/joe-14-0584
25. Baer, G., Small, W., Wilson, T., Benett, W., Matthews, D., Hartman, J., & Maitland, D. (2007). Fabrication and in vitro deployment of a laser-activated shape memory polymer vascular stent. *Biomedical engineering online., 6*, 43. https://doi.org/10.1186/1475-925X-6-43
26. Peng, T., O'Neill, D. P., & Payne, S. J. (2011). Mathematical study of the effects of different intrahepatic cooling on thermal ablation

zones. *Annual International Conference of the IEEE Engineering in Medicine and Biology Society, 2011*, 6866–6869. https://doi.org/10.1109/IEMBS.2011.6091693
27. Aaslid, R. (2006). Cerebral autoregulation and vasomotor reactivity. *Frontiers of neurology and neuroscience., 21*, 216–228. https://doi.org/10.1159/000092434
28. Alford, A. I., Kozloff, K. M., & Hankenson, K. D. (2015). Extracellular matrix networks in bone remodeling. *International Journal of Biochemistry & Cell Biology, 65*, 20–31. https://doi.org/10.1016/j.biocel.2015.05.008
29. Feng, X., & Teitelbaum, S. L. (2013). Osteoclasts: New insights. *Bone Res., 1*, 11–26. https://doi.org/10.4248/br201301003
30. Ono, T., & Nakashima, T. (2018). Recent advances in osteoclast biology. *Histochemistry and Cell Biology, 149*, 325–341. https://doi.org/10.1007/s00418-018-1636-2
31. Komori, T. (2019). Regulation of proliferation, differentiation and functions of osteoblasts by Runx2. *International Journal of Molecular Sciences, 20*, 1694. https://doi.org/10.3390/ijms20071694
32. Florencio-Silva, R., Sasso, G. R. D. S., Sasso-Cerri, E., Simões, M. J., & Cerri, P. S. (2015). Biology of bone tissue: Structure, function, and factors that influence bone cells. *BioMed Research International, 2015*, 421746. https://doi.org/10.1155/2015/421746

Journal of Robotics and Control (JRC)
Volume 2, Issue 5, September 2021
ISSN: 2715-5072 DOI: 10.18196/jrc.25113

Effective Human Activity Recognition Approach using Machine Learning

Abdul Lateef Haroon P. S.[1], Premachand D. R.[2]
[1, 2]Associate Professor's Department of ECE, BITM, Ballari, Karnataka, India.
Email: [1] abdulbitm@gmail.com, [2] premchandbitm@gmail.com

***Abstract*— The growing development in the sensory implementation has facilitated that the human activity can be used either as a tool for remote control of the device or as a tool for sophisticated human behaviour analysis. With the aid of the skeleton of the human action input image, the proposed system implements a basic but novel process that can only recognize the significant joints. A template for an activity recognition system is provided in which the reliability of the process of recognition and system quality is preserved with a good balance. The research presents a condensed method of extraction of features from spatial and temporal features of event feeds that are further subject to the mechanism of machine learning to improve the performance of recognition. The criticalness of the proposed study is reflected in the outcomes, which when trained using KNN, show higher accuracy performance. The proposed system demonstrated 10-15% of memory usage over 532 MB of digitized real-time event information with 0.5341 seconds of processing time consumption. Therefore on a practical basis, the supportability of the proposed system is higher. The outcomes are the same for both real-time object flexibility captures and static frames as well.**

***Keywords*— KNN, Human Activity Recognition, SVM, RHA.**

I. INTRODUCTION

An RHA aims to recognize, analyze, and predict human activity like moving, walking, standing, sleeping, etc [1]. The RHA uses RGB data to extract the skeletal joints, depth maps and identify human activity [2]. The applications of the RHA have widespread in many areas, such as in video surveillance, human-computer interaction, military applications, etc [3]. The RHA can be performed at different abstraction levels where the actions can be of motion, gesture or any activity. The motion is an activity of a single person that contains different gestures with temporal ordering while the gesture is the elementary movement of a human body [4]-[6].

The activities in general term include multiple numbers of operations (actions or motion) performed by various persons (example: Playing cricket, football, working on different computers by users). The RHA can be performed by using wearable sensors and external devices [7]-[11]. The conventional approaches of the RHA systems are fixed with the predefined point of interest; hence, the activities are dependent on the user interaction of sensors. The common example of the external sensor devices is Intelligent-Homes. These sensors are meant to recognize complex activities such as washing, eating, etc [12]-[15].

This extracted information is purely dependent on the sensor attached to objects or human and interaction among those. But the installing and managing cost of these sensor devices is quite high. To tackle these challenges, various researches have implemented wearable sensor devices for RHA [13]. In this paper wearable sensors, the human activity attributes (GPS and accelerometers), environmental attributes (humidity and temperature sensors), etc are used. This information helps to provide better recognition of human activity [15]-[19].

The past research studies over RHA has focused on the learning as well as recognition of human activities by using traditional cameras captured video sequences. These video sequences can be encoded with the high texture color information, and it helps in image processing. One of the most widespread challenges for the researchers is that taking pictures three-D motion from common cameras. As human things to do are carried out in 3D space, getting access to 3-D records plays a major function in the activity consciousness process. However, the Depth-Map approach is one of the high-quality techniques utilizing for a profitable human endeavour consciousness system compared with usual approaches, a depth-map strategy proven few benefits in the context of activity consciousness process.

II. CONCEPT OF RHA SYSTEM

A. General RHA System

The sensor(s) play an important role in the detection of human activity in traditional RHA [20]–[23]. Figure 1 demonstrates the cycle of recognition of human activity when a movement of the body is received as input. The sensor(s) collect the information obtained from the movement of the human body, and the recognition engine analyses the data and decides the activity type[24]–[29].

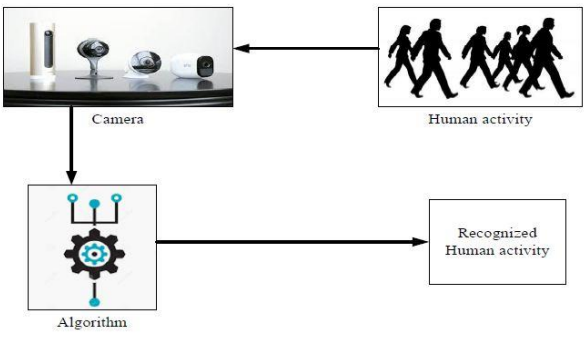

Fig. 1. General Structure of RHA system

To recognize human activities, a depth sensor is used in RHA systems. The depth sensor, in a nutshell, projects infrared beams into the scene and detects them using its

infrared detector to determine and measure the depth or distance of each beam from the sensor.

Affective approaches reflect human exercises as per an individual's affective state and passionate communications. Behavioural methods are designed to recognize behavioural attributes, multimodal non-verbal signs for example, motions, outward appearances, and hear-able signs. The phrases "event" and "actions" are typically used in the literature interchangeably. Such words were distinguished in this survey as the sense that the word "event" is used to describe a series of acts that suit specific body movements. On the other hand, the word "actions" is used to describe the activities and events associated with a single person's movements, emotional words, facial expressions, and auditory signs.

III. METHODS

The fundamental methodology used for RHA is to obtain the characteristics from the motion aspect of video or image sequences to facilitate the prediction of one or more specific actions. Nonetheless, one of the larger sets of dependencies associated with human activity identification is the method of extraction of features. Additional capabilities will always improve the recognition of the system's accuracy. Such a mechanism for capturing a higher number of features, however, will require two potential problems, e.g., i) requiring a large amount of processing time and ii) involving additional resources. Both of these two points are harmful to the computational performance of the system. While good progress has been made in research-based techniques related to human activity recognition, it is widely ignored to decide to pick effective features using a cost-effective computational model. Therefore, a system needs to evolve to ensure better quality in recognizing the set of features from the given data. The major research issues are as follows:

- The prior studies do not illustrate the computational difficulties involved with the collection of many features from a given human action data.
- The possibility of minimizing the computational effort of the extraction of features using joint attributes in the skeleton system has attracted less attention among research communities.
- There is currently a very small number of literatures dedicated to the exploration of an effective number of joints responsible for human activity recognition.
- Optimizing the use of depth maps has less research, and more research is aimed at applying machine learning to provide greater accuracy.

The framework takes an input of image sequences with defined standard human actions with the help of analytical research methodology. This process is followed by extracting the depth map from the data set input image, which is resumed to extract the predicted segments on three separate x-y-z axis planes. An algorithm is built that uses different types of identity-based attributes to test all the joints of the depth object skeleton. This method ultimately results in an appropriate number of joints responsible for the actual detection of the successful capture of the mechanism of awareness of human activity. The major contribution of the proposed model is that it delivers faster joint processing regardless of any selection of movement patterns and does not offer any form of dependency on the computation of an unnecessary number of joints to recognize effective human action.

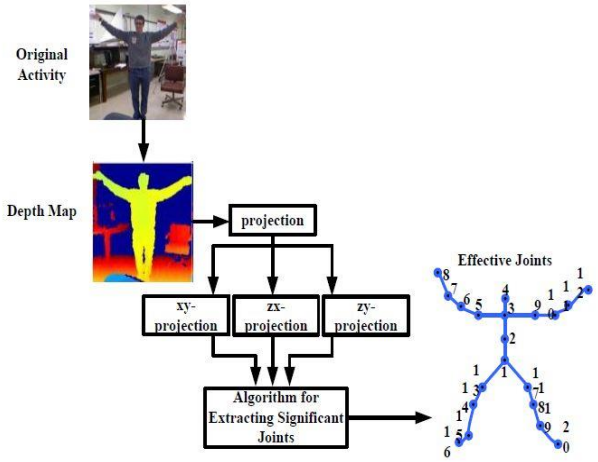

Fig. 2. Proposed Framework

IV. SYSTEM DESIGN

Depth cameras have received significant consideration from researchers in the vision and robotics community because of the financially cost-effective "Kinect." The camera depth has two main advantages. Firstly, to recover postures and recognize the activity, the depth sensor provides information about the 3D image structure. Secondly, the depth sensor can sense in darkness. These benefits are used from a depth map in interesting research points such as human skeleton detection. The skeletons measured from maps of depth are accurate and bring benefits to various applications, including recognition of actions and gestures. Depth map RHA can also be described as a sequence of object representation, extraction of features, and identification of these activities in its simplest form.

The proposed RHA takes advantage of the 3-D skeleton information provided from the 2.0 SDK Kinect. The Kinect 2.0 sensor has a high depth-fidelity that enables it to more clearly observe the tiny objects, resulting in highly accurate 3-D object building. The device can control each person's number of people and 20 skeletal joints. Figure.4.3 shows the skeletal 3-D view joints monitored by the 2.0 sensor Kinect. Many implementations move include the proposed RHA. The first step is to record and track the entire event process using a kinect2.0 sensor through the video sequence. Because activity is the cyclic locomotion, it detects the entire cycle of activity that provides consistent extraction of features. Figure 3 represents the practical implementation process of proposed RHA.

Relative joint angle (RJA) characteristics of various joints are measured over the entire operation period during this process. The major advantage of using RJA is that the process allows invariants to be scaled-up and perceived. Hence, motion recognition is not restricted by the constant distance from the Kinect or single person moving from the Kinect camera to the specific direction. To assess the relevance of the particular activity related RJA function, the device undergoes statistical analysis, which calculates the relative

joint pair angles based on activity movement. Here, systems find only the most relative joint angles based on RJA measurement and obtain the characteristics of operation. Once the feature extraction has been completed, the system continues to the classification process (i.e., FITCECOS), which is SVM's "Match multiclass classification models." The proposed RHA considers the collection of most appropriate RJA sequences from both training and testing data samples as parameters and assesses the non-similarity characteristics between them. The major advantage of the proposed RHA is that, due to object walking speed, it can validate the variable size RJA sequences initiated in different videos of the same person (5 data samples were considered in this). Finally, by evaluating skeletal joints, the system recognizes the individual.

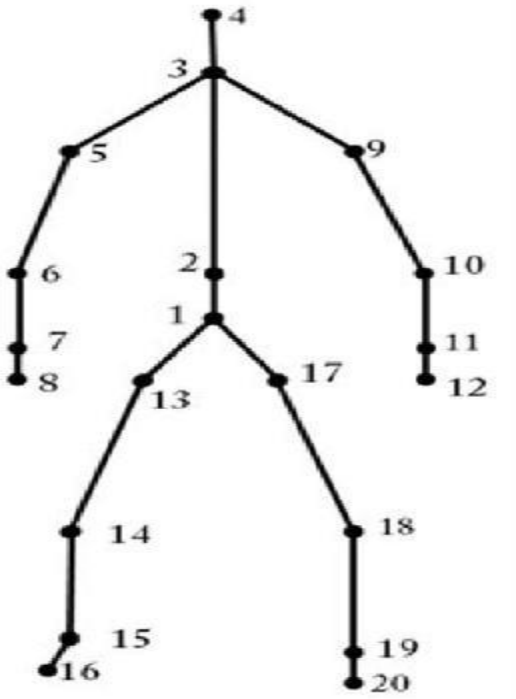

1 Hip center	11 Wrist right
2 Spine	12 Hand right
3 Shoulder center	13 Hip left
4 Head	14 Knee left
5 Shoulder left	15 Ankle left
6 Elbow left	16 Foot left
7 Wrist left	17 Hip right
8 Hand left	18 Knee right
9 Shoulder right	19 Ankle right
10 Elbow right	20 Foot right

Fig. 3. Skeletal joints tracked by Kinect sensor

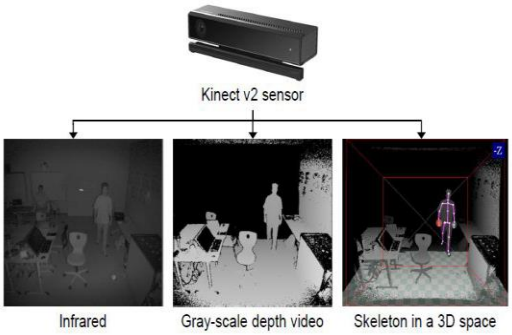

Fig. 4. Proposed model obtains various skeletal data streams

V. RESULTS

The proposed system is applied over various different video sequences samples to perform recognition of variable human activity. In this section sample video sequence is considered to assess the performance and efficiency of the proposed system. The programming is carried out for all human actions including high arm wave, sidekick, hammer, etc. The results of these actions are shown below. The depth silhouettes of the various activity offer the activity's shape details. The human activity of waving high arm is identified in the following Figure 5 in terms of depth silhouettes, and significant joints are tracked or marked. The joints are represented by a number (1, 2, 3, 20). Similarly, the joints in the 3D plane are given for xy, yz, and zx projections

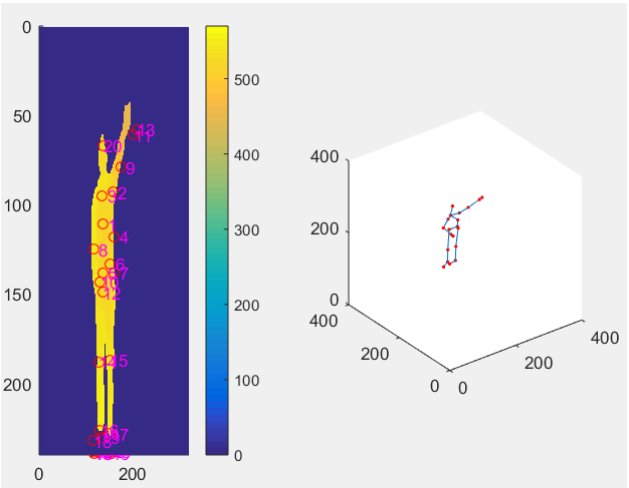

Fig. 5. Depth and Projection analysis of the high arm wave activity

The displacement analysis of the high arm wave activity against different frame is given in Figure 6. The standard deviation of the high arm wave is represented in Figure 7 where the higher deviation of the displacement is found about 10.

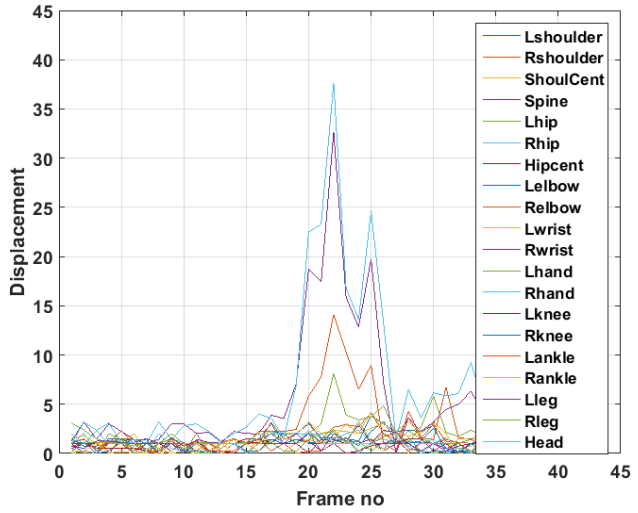

Fig. 6. Displacement at different frame numbers of high arm wave activity.

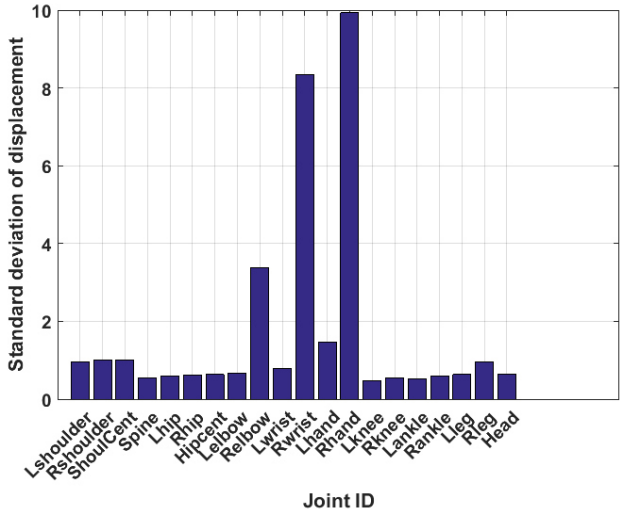

Fig. 7. Standard deviation of displacement at high arm wave activity

VI. CONCLUSION

The combined features of geometry and visual attributes may provide a synchronized platform to provide technology for the human to machine interaction (HMI). The active involvement of the human developed initially many HMI based application into the system, but in the future, much future vision of the smart, intelligent and ubiquitous applications requires the certain context of the humans such as their critical activities as an input. The process of finding a fast, accurate feature set of coordinates is a very challenging task for the accuracy of recognition of the activities. The Recognition of Human Activity (RHA) is an open research issue as there exists an evolving process in both imaging techniques and camera technology. The problem of RHA is portrayed as a "Three-level categorization problem," namely 1) Action primitives, 2) Actions/activities and 3) Interactions. The research study involves the understanding of the various approaches of image representation and classifications for vision-based activity recognition or human behaviour.

REFERENCES

[1] N. Käse, M. Babaee and G. Rigoll, "Multi-view human activity recognition using motion frequency," *2017 IEEE International Conference on Image Processing (ICIP)*, Beijing, 2017, pp. 3963-3967.

[2] D. Tao, L. Jin, Y. Yuan and Y. Xue, "Ensemble Manifold Rank Preserving for Acceleration- Based Human Activity Recognition," in *IEEE Transactions on Neural Networks and Learning Systems*, vol. 27, no. 6, pp. 1392-1404, June 2016.

[3] H. Zhang and L. E. Parker, "CoDe4D: Color-Depth Local Spatio-Temporal Features for Human Activity Recognition From RGB-D Videos," in *IEEE Transactions on Circuits and Systems for Video Technology*, vol. 26, no. 3, pp. 541-555, March 2016.

[4] W. Lu, F. Fan, J. Chu, P. Jing and S. Yuting, "Wearable Computing for the Internet of Things: A Discriminant Approach for Human Activity Recognition," in *IEEE Internet of Things Journal*, vol. 6, no. 2, pp. 2749-2759, April 2019.

[5] J. Qi, Z. Wang, X. Lin and C. Li, "Learning Complex Spatio-Temporal Configurations of Body Joints for Online Activity Recognition," in *IEEE Transactions on Human-Machine Systems*, vol. 48, no. 6, pp. 637-647, Dec. 2018.

[6] Abdul Lateef Haroon P.S., U.Eranna, "Insights of Research-based approaches in Human Activity Recognition" Communications on Applied Electronics (CAE), Volume 7- No.16, May- 2018

[7] Abdul Lateef Haroon P.S., U.Eranna, "An Efficient Activity Detection System based on Skeletal Joints Identification" International Journal of Electrical and Computer Engineering (IJECE), Vol.8, No.6, December-2018, pp. 4995~5003.

[8] Abdul Lateef Haroon P.S., U.Eranna, "A Simplified Machine Learning Approach for Recognizing Human Activity" International Journal of Electrical and Computer Engineering (IJECE), Vol.9, No.5, October-2019, pp. 3465~3473.

[9] Abdul Lateef Haroon P.S., U.Eranna, "Modelling Approach to select Potential Joints for Enhanced Action Identification of Human" 3rd IEEE International Conference on Electrical, Electronics, Communication, Computer Technologies and Optimization Techniques (ICEECCOT-2018), 2018.

[10] Abdul Lateef Haroon P.S., U.Eranna, "Human Activity Identification using Novel Feature Extraction and Ensemble-based learning for Accuracy" Artificial Intelligence Methods in Intelligent Algorithms, Proceedings of 8th Computer Science On-line Conference, Vol.2, 2019.

[11] Y. Guo *et al*., "Tensor Manifold Discriminant Projections for Acceleration-Based Human Activity Recognition," in *IEEE Transactions on Multimedia*, vol. 18, no. 10, pp. 1977-1987, Oct. 2016.

[12] L. Peng, L. Chen, X. Wu, H. Guo and G. Chen, "Hierarchical Complex Activity Representation and Recognition Using Topic Model and Classifier Level Fusion," in *IEEE Transactions on Biomedical Engineering*, vol. 64, no. 6, pp. 1369-1379, June 2017.

[13] J. Cheng, H. Liu, F. Wang, H. Li and C. Zhu, "Silhouette Analysis for Human Action Recognition Based on Supervised Temporal t-SNE and Incremental Learning," in *IEEE Transactions on Image Processing*, vol. 24, no. 10, pp. 3203-3217, Oct. 2015.

[14] X. Chang, W. Zheng and J. Zhang, "Learning Person–Person Interaction in Collective Activity Recognition," in *IEEE Transactions on Image Processing*, vol. 24, no. 6, pp. 1905-1918, June 2015.

[15] M. Ehatisham-Ul-Haq *et al*., "Robust Human Activity Recognition Using Multimodal Feature-Level Fusion," in *IEEE Access*, vol. 7, pp. 60736-60751, 2019.

[16] R. Xi *et al*., "Deep Dilation on Multimodality Time Series for Human Activity Recognition," in *IEEE Access*, vol. 6, pp. 53381-53396, 2018.

[17] Z. Yang, O. I. Raymond, C. Zhang, Y. Wan and J. Long, "DFTerNet: Towards 2-bit Dynamic Fusion Networks for Accurate Human Activity Recognition," in *IEEE Access*, vol. 6, pp. 56750- 56764, 2018.

[18] H. Zou, Y. Zhou, R. Arghandeh and C. J. Spanos, "Multiple Kernel Semi-Representation Learning With Its Application to Device-Free Human Activity Recognition," in *IEEE Internet of Things Journal*, vol. 6, no. 5, pp. 7670-7680, Oct.

[19] N. Alshurafa *et al*., "Designing a Robust Activity Recognition Framework for Health and Exergaming Using Wearable Sensors," in the *IEEE Journal of Biomedical and Health Informatics*, vol. 18, no. 5, pp. 1636-1646, Sept. 2014.

[20] G. Azkune and A. Almeida, "A Scalable Hybrid Activity Recognition Approach for Intelligent Environments," IEEE Access, vol. 6, pp. 41745–41759, 2018.

[21] C. Wang, Y. Xu, H. Liang, W. Huang, and L. Zhang, "WOODY: A Post-Process Method for Smartphone-Based Activity Recognition," IEEE Access, vol. 6, pp. 49611–49625, 2018.
[22] R. Xi et al., "Deep Dilation on Multimodality Time Series for Human Activity Recognition," IEEE Access, vol. 6, pp. 53381–53396, 2018.
[23] H. Wang, Y. Xue, X. Zhen, and X. Tu, "Domain Specific Learning for Sentiment Classification and Activity Recognition," IEEE Access, vol. 6, pp. 53611–53619, 2018.
[24] A. Yousefzadeh, G. Orchard, T. Serrano-Gotarredona, and B. Linares-Barranco, "Active Perception With Dynamic Vision Sensors. Minimum Saccades With Optimum Recognition," IEEE Trans. Biomed. Circuits Syst., vol. 12, no. 4, pp. 927–939, Aug. 2018.
[25] Y. Hsu, S. Yang, H. Chang, and H. Lai, "Human Daily and Sport Activity Recognition Using a Wearable Inertial Sensor Network," IEEE Access, vol. 6, pp. 31715–31728, 2018.
[26] L. Cai, X. Liu, H. Ding, and F. Chen, "Human Action Recognition Using Improved Sparse Gaussian Process Latent Variable Model and Hidden Conditional Random Filed," IEEE Access, vol. 6, pp. 20047–20057, 2018.
[27] W. Li, B. Tan, and R. Piechocki, "Passive Radar for Opportunistic Monitoring in E-Health Applications," IEEE J. Transl. Eng. Heal. Med., vol. 6, no. December 2017, pp. 1–10, 2018.
[28] Z. Yang, O. I. Raymond, C. Zhang, Y. Wan, and J. Long, "DFTerNet: Towards 2-bit Dynamic Fusion Networks for Accurate Human Activity Recognition," IEEE Access, vol. 6, pp. 56750–56764, 2018.
[29] S. Savvaki, G. Tsagkatakis, A. Panousopoulou, and P. Tsakalides, "Matrix and Tensor Completion on a Human Activity Recognition Framework," IEEE J. Biomed. Heal. Informatics, vol. 21, no. 6, pp. 1554–1561, 2017.

Experimental Modeling of the Residual Energy of a Rechargeable Battery-Powered Node in Wireless Networks

Naseeruddin and Venkanagouda Patil
Department of Electronics and Communication Engineering, Ballari Institute of Technology and Management Visvesvaraya Technological University, India

Abstract: *This paper proposes an effective method for experimental modeling of the remaining energy in terms of State Of the Charge (SOC) of a battery-powered node in a wireless network. The SOC of a battery is used to accurately determine the remaining energy of the battery. For experimentation, three practical applications (i.e., loads) were allowed to run on the Ni-MH rechargeable battery. The real-time variations in the battery terminal voltage are captured using IC INA219 fuel gauge and an empirical equation is derived from this captured data for each application. These empirical equations are used on a node as a programmable model to experimentally verify the SOC of the application discharge curves. The developed model randomly runs the application for a random duration of time and then computes the SOC of the node. The effectiveness of the randomness in the developed model has been analyzed and found to be practically worth. The proposed work can be scaled up to any number of nodes in a wireless network. This work can benefit the researchers and the academicians working in the area of wireless networks.*

Keywords: *Node modelling, state of the charge, fuel gauge, wireless mobile networks, discharge-curves.*

Received December 14, 2019; accepted October 25, 2020
https://doi.org/10.34028/iajit/18/5/6

1. Introduction

Effective utilization of the available battery charge or energy remains a major concern and a challenging task in the battery-powered nodes of a wireless network. This concern aggravates when more and more functionalities are added to the node. The researchers are making efforts to address this issue through their studies involving different battery chemistries under various environments. One such area of study involves the nodes of the Wireless Mobile Network (WMN) powered by batteries. The WMN is an infrastructure-less and highly dynamic network. The nodes of a WMN are typically battery-powered. The energy of the battery in each node becomes very important for improving the lifetime of the overall network. The nodes of a WMN are energy-constrained, and efforts are needed to optimize the consumption of the available battery energy. The residual energy or remaining energy of the battery is a function of the parameters such as State of the Charge (SOC), Depth Of Discharge (DOD), open circuit voltage and temperature.

The SOC is a battery metric that defines the remaining charge of the battery, which can be estimated by applying mathematical models [5]. The energy of a node not only depends on the radio transmission hardware but also on the processes and applications that run on it. Barboni and Valle [1] have experimentally found that processing and sensor data sampling are mainly responsible for the depletion of the battery rather than the radio transceiver. The work presented in this paper proposes an empirical modeling approach towards estimating the SOC of Nickel-Metal Hydride (Ni-MH) rechargeable battery chemistry. The authors of the proposed work claim that the applications running on the node are the significant factor in the determination of the lifetime of the WMN. It is further asserted that the above opinion is justified and validated through the implementation of a cost-effective experimental test-bed.

Remainder of this paper is structured as follows. The section 2 discusses related work primarily focusing on characterization of a rechargeable battery and modeling of SOC in WMN. The construction detail of the experimental setup is discussed in section 3. Section 4 discusses the application of the empirical model on a node and analyses the effectiveness of the application's randomness. Finally, the conclusion and future work of the presented work is given in section 5.

2. Related Work

This section discusses the related work. The work presented in this paper requires interdisciplinary research approach; hence for convenience the discussion is categorized in the following subsections.

2.1. Rechargeable Battery Modeling

The concept of battery modeling is very important in the estimation of the remaining lifetime of a portable device or a node in the WMN. A battery in this article refers to the rechargeable battery chemistry. The primary battery models can be classified as the data model, first principle model, surrogate first principle model, and hybrid model. In this paper, the proposed method considers and applies the empirical model. The empirical model belongs to the data modelling technique, in which battery characterization is done using equations that are derived based on the data [19].

2.2. Characterization of Rechargeable Battery-An SOC Perspective

The behaviour of the battery based on the time-dependent currents and behaviour of the rechargeable metal hydride chemistry can be easily predicted [17] under a constant current ripple. The experiment in [17] ascertains the requirement of a controller to mitigate the current pulse effect on the SOC if the battery is subjected to the pulsed current. An analytical model is proposed in [15] considers the temperature and the effect of the cycle of aging for predicting the remaining charge in the Li-ion battery. The model presented in [15] is validated using simulation results. The accuracy in predicting the charge of the remaining battery can be improved by measuring both current and voltage of a battery. There are significant benefits of applying a voltage and current integration method at higher SOC as described in [Work Book on Challenges and Solutions in Battery Fuel Gauging, Texas Instruments Incorporated, 2004] for estimating remaining charge of a battery. Nowadays combined voltage and current-based fuel gauge ICs are available that can improve SOC characterization of a rechargeable battery [20].

An improved Gaussian Process Regression (GPR) model is proposed in [13] for estimating the state of the health of the Li-ion battery. The data of the improved GPR model is compared with the sets of the Li-ion battery data from Aeronautics and Space Administration (NASA) to prove its accuracy. A method to implement a battery model for SOC indication system is described in [12] and the novel method adopted has shown improvement in the accuracy of the SOC indication for Li-ion battery chemistry. The parameters related to the battery such as Electro-Motive Force (EMF) and over-potential can also be measured and are used for modelling the SOC. These parameters are fed to a SOC algorithm to predict the remaining run-time of the portable applications. This paper proposes to use the fuel gauge IC to estimate the remaining charge in terms of SOC for the Ni-MH rechargeable battery.

2.3. Battery Modeling in WMN

It is learned from the related literature that the work in the direction of SOC modeling has progressed to a considerable extent but the application of the same in the modeling of the node in WMN is limited. An experimental analysis in [11] describes the battery discharge characteristics in Wireless Sensor Networks (WSN) and its related non-trivial implications in selecting the power control strategies. An analytical and experimental node energy model is presented in [18] for WSN. A detailed process for predicting the battery's state of health in wireless sensor applications is presented in [5]. The process has been validated experimentally by connecting the rechargeable battery to Telsob motes [8]. Snajder *et al*. [16] have constructed a measurement based wireless node model for data-intensive communication. The energy consumption in ZigBee motes and application of the Wi-Fi units for the transmission of a high-resolution image was analyzed with varied data rates. A mechanism is proposed in [3] to reduce the consumption of the average energy based on the application of the load balancing in the wireless network. A different strategy is used in [21] by exploiting the sleep period to increase the capacity of the battery. The simulation results of the proposed Battery Recovery Effect aware Connected Dominating Set (BRE-CDS) algorithm shows improvement in the network lifetime. An experimental validation of the analytical battery model called as Kinetic Battery Model (KiBaM) for WSN is presented in [14]. Based on the correctness of the model parameters, the KiBaM can be used to estimate the battery lifetime within the WSN context. A detailed comparative analysis of three Adhoc NETwork (MANET) routing protocols i.e., Ad Hoc On-Demand Distance Vector (AODV), Dynamic Source Routing (DSR), and Dynamic MANET On-demand Protocol (DYMO) under residual life estimator battery model is presented [4]. The work primarily focused on simulation studies using QualNet 5.0 considering the DURACELL-AA battery. Two models to evaluate the remaining lifetime of a battery are proposed in [7]. The first one is an analytical model which can be used with a network simulator and the second an empirical one to be used for the real test-bed. A set of experiments based on Advanced Configuration and Power Interface Basic Input-Output System (ACPI BIOS) measurements to evaluate energy consumption in IEEE 802.11 wireless network interface (a model of ad-hoc mobile terminals) is described. A routing method based on the prediction of node residual energy and minimum hop count is proposed [2]. Considering the example of AODV routing protocol, the simulation results have clearly shown significant improvement in terms of number of dead nodes, energy-efficiency, Packet Drop Rate (PDR) and normalized control overhead.

In summary, analytical or empirical battery models are widely used for modeling the energy source of a node. But, the energy consumption of the node depends on varying needs such as transmitting/receiving power, the number of applications running, sleep/wakeup power. The related work lacks in considering these varying needs in modeling the energy source. The proposed work is an effort to model the energy source of the node considering varying needs such as applications running on a WMN node.

2.4. Important Terms Related To Rechargeable Batteries

There are various metrics related to the characterization of battery performance. Important or most widely used metrics are good enough to characterize a battery. Hence, only the required metrics are defined below:

- A rechargeable battery consists of more than one cell arranged in a particular way to obtain the required current and voltage.
- Ampere-hour: Ampere-hour is the amount of current a battery can deliver for an hour before the voltage reaches the end of its life point.
- C Rate: The rate, at which a battery discharges relative to its maximum capacity, is defined as C rate. For example, 1C means discharging the entire battery in an hour.
- State of the Charge (SOC): is defined as the percentage of the present battery capacity to the maximum capacity.
- Depth of Discharge (DOD): is defined as the discharge expressed as a percentage of maximum capacity.
- Terminal voltage: is defined as the voltage across the battery terminals with load and the open circuit voltage is defined as the voltage across battery terminals without the load.

3. The Experimental Model

This section discusses experimental modeling of a rechargeable battery-powered node. The battery chemistry under consideration is Ni-MH and rated 3.6V, 600m AH. This model is generic and can be customized as per the requirements involving different battery chemistries and applications. The methodology adopted is known as fuel gauge method of measuring the SOC of a battery. All the experiments were carried out at room temperature. The specifications of the experiments are tabulated in Table 1. In terms of SOC, three applications are selected for practical modelling based on the node energy consumption. The applications are the combination of Direct Current (DC) motors and a 100K Ohm (1/2Watt) resistor. It is preferable to choose the applications that are easy to replicate owing to the fact that they are less time consuming and whose experimental model can be developed within a short period of time. The next part of this section describes a simplified methodology to construct an experimental model for a wireless node.

Table 1. Notations and meaning.

Battery Chemistry /Application	Voltage Rating(V)	Current Rating (mAH)	Remarks
Ni-MH	3.6	600	Variations are observed in the multi-meter measurements.
Application-1 (DC Motor)	3.2	60	Inductive load.
Application-2 (2 DC Motors)	3.2	60	Inductive load.
Application-3 (2 DC motor ,100K ohm)	3.2	60+100KOhm	Inductive+Resistive load.

3.1. SOC Modeling of Ni-MH Rechargeable Battery

Figure 1 shows a simplified view of the block diagram for SOC modeling having only one application. The fuel gauge-INA 219 (from Texas Instruments) sensor is used as the key element in determining the instantaneous voltage and current drawn by the load (or application). The microcontroller reads voltage and current from the INA 219 sensor. With a view to developing an empirical model, the application is run till the battery drains to a minimum value or until the application stops. The INA 219 can also read shunt, bus, and load voltages. These parameters are acquired for further analysis and modeling. Because of a particular load, the SOC can be determined by capturing variations in the terminal voltage or instantaneous voltage and the current drawn or any of these combinations.

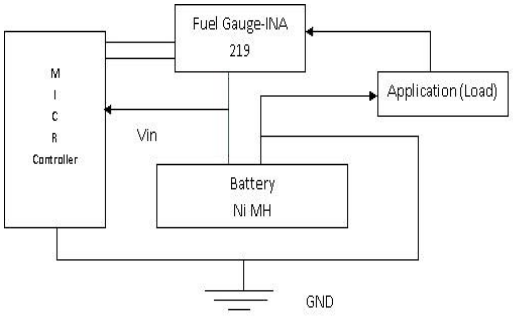

Figure 1. Block diagram of SOC modeling of a node having one application.

The work presented in this paper captures variations in the terminal voltage to determine the SOC of the battery with different applications (i.e., loads).

Figure 2 shows an integrated view of the model for determining the SOC of a battery having three different applications. Referring to Figures 1 and 2, *Vin* is the terminal voltage of the battery that is read directly by the microcontroller with respect to the ground.

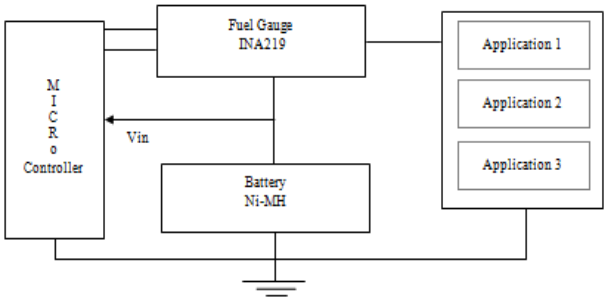

Figure 2. Block diagram of SOC modeling of a node having three applications.

For SOC modeling, it is assumed that at any given instant of time only one application is allowed to run for the duration as decided by the node (Microcontroller).

The duration of operation for each application or load depends on the type of load. The load may be resistive, inductive or capacitive as indicated in Table 1. The responses or load discharging curves are obtained from the acquired readings and are as shown in Figures 3 and 4.

3.2. SOC Empirical Modeling

The regression fitted responses for variations in the battery terminal voltage for application 1 (refer Table1) are shown in Figure 3. The response (discharging curve) in the blue colour is from the acquired data as per the block diagram of Figure 1. The response shown in the red colour is regression fitted response with an initial battery voltage of 4.22V. Even though the battery under consideration is rated 3.6 V, after every charge-discharge cycle it is found that the battery terminal voltage remained around 3.9V and sometimes above 3.9V.

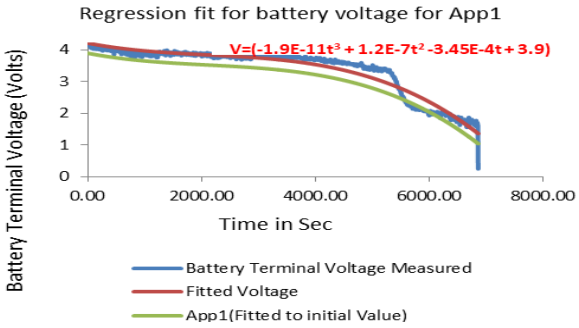

Figure 3. Regression fit response for application-1.

The battery initial readings always varied after each recharge-discharge cycle and, hence a method is devised for modeling the initial value of each application. After acquiring data for three applications under consideration, it was finally decided to fit the readings to a new initial value of 3.9V. The response shown in the green color is fit for application-1 with an initial value of 3.9V.

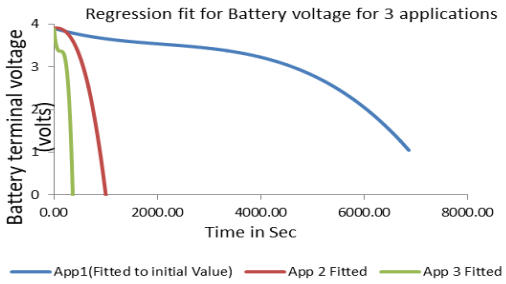

Figure 4. Regression fit responses for three applications with an initial value of 3.9V.

Figure 4 shows the regression responses for three applications with an initial value of 3.9V. From these responses, it is apparent that application 3 consumes the highest battery charge and application 1 consumes the least battery charge. This is in certain agreement with the values of Table 1.

A set of empirical equations is derived from the obtained responses. The battery terminal voltages are fitted as a function of time. The Equations (1), (2), and (3) are used to characterize the rechargeable Ni-MH battery behaviour with respect to the application.

$$V1 = (-1.9*10\text{-}11 * t3) + (1.20*10\text{-}7 * t2)- (3.45*10\text{-}4 * t)+3.9 \quad (1)$$

$$V2 = (-1.55*10\text{-}11 * t3) - (8.5*10\text{-}8 * t2)+ (0.00005 * t)+3.9 \quad (2)$$

$$V3 = (-1.99*10\text{-}9 * t3) + (3.87*10\text{-}8 * t2)- (0.0025 * t)+3.9 \quad (3)$$

Table 2 gives the initial and final voltage readings across the battery terminals without load (i.e., measured when the application stops). Sparse variations are observed in the measured final values of the battery terminal voltage. In this work, these values imply that the battery has reached the end point of its rated capacity or the application has stopped. The variations observed are obvious due to the battery performance that depends on many factors including temperature.

Table 2. Battery terminal voltage without load.

Battery Chemistry (Ni-MH)	Multi-meter Reading	
Load/Application	*Initial*	*Final*
Application-1 (DC Motor)	3.83	3.33
Application-2 (2 DC Motors)	3.87	3.30
Application-3 (2 DC motor ,100K ohm)	3.92	3.33

4. Application of the Empirical Model

This section discusses the application of the empirical equations in modeling a WMN node. The said equations are used to model the SOC of a node. The practical applicability of this approach is also briefly described at the end of this section.

4.1. The SOC Programmable Model

As the empirical equations depend on time, a programmable model (i.e., algorithm) is developed to determine the SOC at any instant of time with the random application running on a node. The programmable model should select an application randomly and run for a random duration. The

randomness in the selection of the running time and the application give realistic modelling of the battery-powered nodes.

Figure 5 gives the average (of five trials) response for battery terminal voltage variations as a function of time. The response is shown for a random runtime duration ranging from 30 to 60 seconds. From the response, it is observed that battery behaviour is not constant except at the beginning. The response in the middle shows a gradual drop and at the end, the response is abrupt. This approach is more realistic and it gives a better strategy in evaluating the performance for WMN nodes.

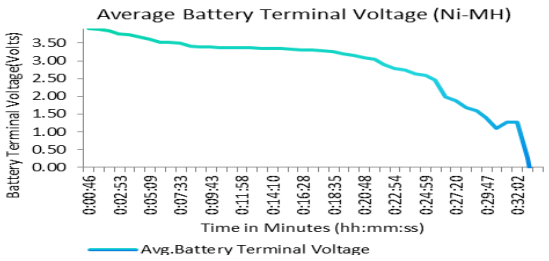

Figure 5. Average battery terminal voltage as a function of time (Ni-MH).

4.2. Analysis of Randomness of The SOC Programmable Model

The randomness factor involved is a very important metric in assessing the developed SOC model. It is necessary in the selection of the application and the duration to run on a node for the real world implementation.

It is evident from Figure 6 and Table 2 that application-3 has consumed the largest portion of the total charge. The analysis also shows that the maximum difference of the runtime duration considering all applications is approximately 2 minutes only. This is a very small difference indicating that randomness in the developed programmable model is very effective. If the effect of randomness is analyzed on the duration of the runtime of the applications, it is noticeable that the duration of the average random application remains the same for the three applications in the experiment (refer to Table 3).

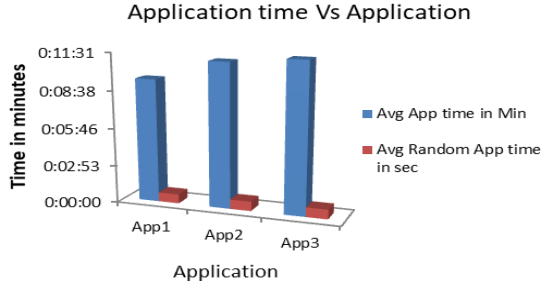

Figure 6. Application Time verses applications and average random time.

The randomness in selecting the application also shows that applications-2 and 3 ran for 15 times each and application-1 ran for 13 times. Thus randomness in selecting an application by the programmable model proves the effectiveness of the proposed methodology.

Table 3. Average application runtime analysis.

Parameter	Application 1	Application 2	Application 3
Average Application time in *min*	9.30	11.03	11.28
Average Random Application time in *Sec*	43	44	44
Average number of time the application runs	13	15	15

4.3. Examples of Applicability of the Proposed Empirical Model

The proposed empirical model considering the Ni-MH battery is experimented with practically by constructing a four-node test-bed. The SOC-based residual energy empirical model is used in [9, 10]. These papers show the elegant use of the proposed empirical approach for both Wireless Sensor Networks (WSN) and wireless Mobile Ad-hoc NETworks (MANETs). Further, this empirical model of the Ni-MH battery can be added to the NS3/NS2 tool and other simulators. Improvements in the performance evaluation of the MANET protocol can be made with this addition. Also, the concept of heterogeneity in energy in the WMN can be applied if other rechargeable battery empirical models such as mentioned in [6] are developed and incorporated in the simulators.

5. Conclusions and Future Work

A method for experimental modeling of the energy of a wireless node is proposed and implemented to determine the state of the charge of Ni-MH battery based on the application (i.e., load) discharge curves. It is evident that Ni-MH rechargeable battery behaviour is acceptable until a sudden drop starts to affect the performance of the battery. The randomness analysis corroborates the practical viability of the proposed model as shown in [9, 10]. The developed empirical model can be used to estimate the remaining energy or time of a battery based on the terminal voltage. This work can be extended to the Wireless MANETs, WSN and any kind of wireless network having any number of nodes and evaluate the performance. Further characterization of these models is determined by the nature (rechargeable or non-rechargeable) of the battery used. However, the selection of the type of battery depends on the deployment scenario of a WMN.

The presented SOC model can be used to construct an experimental wireless network test-bed involving a number of nodes. In future, the developed empirical model will be used to model nodes of a wireless network and also it is intended to derive similar empirical models for different rechargeable battery

chemistries. The temperature factor is significant for accurate estimation of the SOC in a battery. Hence, in future, the effect of temperature on the proposed model will be incorporated to improve the effectiveness of the proposed model.

References

[1] Barboni L. and Valle M., "Experimental Analysis of Wireless Sensor Nodes Current Consumption," *in Proceedings of 2nd International Conference on Sensor Technologies and Applications*, Cap Esterel, pp. 401-406, 2008.

[2] Er-Rouidi M., Moudni H., Faouzi H., Mouncif H., and Merbouha A., "Enhancing Energy Efficiency of Reactive Routing Protocol in Mobile Ad-Hoc Network with Prediction on Energy Consumption," *The International Arab Journal of Information Technology*, vol. 14, no. 4A, pp. 632-638, 2017.

[3] Wen Y., Liena T., and Lin F., "Application Association and Load Balancing to Enhance Energy Efficiency In Heterogeneous Wireless Networks," *Computer and Electrical Engineering*, vol. 68, pp. 348-365, 2018.

[4] Kandari S. and Pandey M., "Impact of Residual Life Estimator Battery Model on QoS Issues in MANET," *Wireless Personal Communications*, vol. 86, pp. 601-614, 2016.

[5] Lajara R., Perez-Solano J., and Pelegrı-Sebasti J., "Predicting the Batteries State of Health in Wireless Sensor Networks Applications," *IEEE Transactions on Industrial Electronics*, vol. 65, no. 11, pp. 8936-8945, 2018.

[6] Liang Y., Zhao C., Yuan H., Chen Y., Huang W., Yu D., Liu Y., Titirici M., Chueh Y., Yu H., and Zhang Q., "A Review of Rechargeable Batteries for Portable Electronic Devices," *InfoMat*, vol. 1, no. 1, pp. 1-27, 2019.

[7] Lochin E., Fladenmuller A., Moulin J., and Fdida S., "Energy Consumption Models for Ad-Hoc Mobile Terminals," *in Proceedings of Med-Hoc Net 2003*, Mahdia, pp. 8, 2003.

[8] Moteiv orporation. Datasheet tmote sky (2006). Availableonline: http://www.eecs.harvard.edu/~konrad/projects/shimmer/references/tmot, Last Visited, 2019.

[9] Naseeruddin. and Patil V., "Application-Prioritized Hierarchical Routing Protocol for Wireless Sensor Networks," *International Journal of Engineering and Advanced Technology*, vol. 8, no. 5, pp. 753-763, 2019.

[10] Naseeruddin. and Patil V., "Application-Energy Prioritized Routing Algorithm for Wireless MANETs and its Experimental Evaluation," *International Journal of Engineering and Advanced Technology*, vol. 8, no. 5, pp. 664-670, 2019.

[11] Park C., Lahiri K., and Raghunathan A., "Battery Discharge Characteristics of Wireless Sensor Nodes: an Experimental Analysis," *in Proceedings of 2nd Annual IEEE Communications Society Conference on Sensor and Ad Hoc Communications and Networks*, Santa Clara, pp. 430-440, 2005.

[12] Pop V., Bergveld H., Op-het-Veld B., Regtien P., Danilov D., and Notten P., "Modeling Battery Behavior for Accurate State of Charge Indication," *Journal of Electrochemical Society*, vol. 153, no. 11, pp. A2013-A2022, 2006.

[13] Richardson R., Osborne M., and Howvey D., "Gaussian Process Regression for Forecasting Battery State of Health," *Journal of Power Sources*, vol. 357, pp. 209-219, 2017.

[14] Rodrigues L., Montez C., Vasques F., and Portugal P., "Experimental Validation of A Battery Model for Low-Power Nodes in Wireless Sensor Networks," *in Proceedings of IEEE World Conference on Factory Communication Systems*, Aveiro, pp. 1-4, 2016.

[15] Rong P. and Pedram M., "An Analytical Model for Predicting the Remaining Battery Capacity of Lithium-Ion Batteries," *IEEE Transactions on VLSI Systems*, vol. 14 , no. 5, pp. 441-451, 2006.

[16] Snajder B., Jelicic V., Kalafatic Z., and Bilas V., "Wireless Sensor Node Modelling for Energy Efficiency Analysis in Data-Intensive Periodic Monitoring," *Ad hoc Networks*, vol. 49, pp. 29-41, 2016.

[17] Sritharan T., Yan D., Dawson F., and Lian K., "Characterizing Battery Behavior for Time-Dependent Currents," *IEEE Transactions on Industrial Applications*, vol. 50, no. 6, pp. 4090-4097, 2014.

[18] Stamatescu G., Chitu C., Vasile C., Stamatescu I., Popescu D., and Sgˆarciu V., "Analytical and Experimental Sensor Node Energy Modeling in Ambient Monitoring," *in Proceedings of 9th Conference on Industrial Electronics and Applications*, Hangzhou, pp. 1615-1620, 2014.

[19] Suresh R., Tanneru H., and Rengaswamy R., "Modeling of Rechargeable Batteries," *Journal of Current Opinion in Chemical Engineering*, vol. 13, pp. 63-74, 2016.

[20] Yang D., Zhang X., Pan R., Wang Y., and Chen Z., "A Novel Gaussian Process Regression Model for State-Of-Health Estimation of Lithium-Ion Battery Using Charging Curve," *Journal of Power Sources*, vol. 384, pp. 387-395, 2018.

[21] Zhang C., Wan S., Yao Z., Zhang B., and Li C., "A Distributed Battery Recovery Aware Topology Control Algorithm for Wireless Sensor Networks," *Wireless Communications and*

Mobile Computing, vol. 16, no. 17, pp. 2895-2906, 2016.

Naseeruddin is a member of Institution of Engineers (IE) India, received his PhD in Faculty of Electrical Engineering Sciences from Visvesvaraya Technological University, Karnataka. Currently he is working as an associate professor in the Department of Electronics and Communication Engineering, Ballari Institute of Technology and Management, Ballari, India. He has more than 12 years of teaching and research experience. His fields of interests include: wireless mobile adhoc networks, antenna design, robotics, wireless communication, machine learning in wireless networks, embedded systems and VLSI low power design.

Venkanagouda Patil PhD, is working as Professor in the Department of Electronics and Communication Engineering, Ballari Institute of Technology and Management, Ballari, India. He has more than 27 years of teaching experience in the field of engineering and technology. His research areas include: wireless mobile adhoc networks and wireless sensor networks. At present he is guiding eight research scholars toward PhD under Visvesvaraya Technological University, India.

International Journal of e-Collaboration
Volume 18 • Issue 1

Human Activity Recognition Using Significant Skeletal Joints

Abdul Lateef Haroon P. S., Ballari Institute of Technology and Management, India
Rashmi P., Sri Siddhartha Academy of Higher Education, India
Supriya M. C., Sri Siddhartha Institute of Technology, Sri Siddhartha Academy of Higher Education, Tumkur, India

ABSTRACT

The growing development in sensory implementation has facilitated human activity and can be used either as a tool for remote control of the device or as a tool for sophisticated human behaviour analysis. The prime contribution of the proposed system is to harness the potential of the learning approach in order to carry out computational efficiency towards the activity recognition process. A template for an activity recognition system is also provided in which the reliability of the process of recognition and system quality is preserved with a good balance. The research presents a condensed method of extraction of features from spatial and temporal features of event feeds that are further subject to the mechanism of machine learning to enhance the recognition accuracy. The importance of the proposed study is reflected in the results, which, when trained using KNN, show higher accuracy performance. The proposed system demonstrated 10-15% of memory usage over 532 MB of digitized real-time event information with 0.5341 seconds of processing time consumption.

KEYWORDS

K-Nearest Algorithm of the Neighbor (KNN), Recognition of Human Activity (RHA), Support Vector Machine (SVM)

INTRODUCTION

An RHA aims to recognize, analyze and predict human activity like moving, walking, standing, sleeping, etc. The RHA uses RGB data to extract the skeletal joints, depth maps and identify human activity. The applications of the RHA have been widespread in many areas, such as in video surveillance, human-computer interaction, military applications, etc. (Tao et al., 2016). The RHA can be performed at different abstraction levels where the actions can be of motion, gesture or any activity. The motion is an activity of a single person that contains different gestures with temporal ordering while the gesture is the elementary movement of a human body. The activities in general terms include multiple numbers of operations (actions or motion) performed by various persons (example: Playing cricket, football, working on different computers by users). The RHA research area

DOI: 10.4018/IJeC.304377

has witnessed various methods or techniques, but they lag with some challenging issues in adapting the approaches in real-time applications (Lu et al., 2019).

The RHA can be performed by using wearable sensors and external devices. The conventional approaches of the RHA systems are fixed with the predefined point of interest; hence, the activities are dependent on the user interaction of sensors. The common example of the external sensor devices is Intelligent-Homes. These sensors are meant to recognize complex activities such as washing, eating, etc (Chen et al., 2019). This extracted information is purely dependent on the sensor attached to objects or humans and interaction among those. But the installing and managing cost of these sensor devices is quite high. To tackle these challenges, various researchers have implemented wearable sensor devices for RHA. In this work wearable sensors, the human activity attributes (GPS and accelerometers), environmental attributes (humidity and temperature), etc. are used. This information helps to provide better recognition of human activity.

REVIEW OF LITERATURE

The existing approaches based on conventional Local Spatio-Temporal (LST) are suffered from various challenges like dynamic background and illumination. To enhance this problem, the work of Zhang and Parker (2016), provides a multi-dimensional colour-depth LST feature-based feature detector technique to represent various features such as shape, pose variation, texture with local maxima as a region of interest. The authors have also used a support vector machine (SVM) with feature representation to build an effective action detection system. The study uses different standard datasets to demonstrate the effectiveness of the presented technique.

The work of Lu et al. (2019), presented a time-frequency distribution-based approach for detecting human daily activities where S-transform is used for feature extraction in a supervised learning approach and adopted for learning features from the raw feature subspace. The authors have compared their study with different datasets and provided a better performance result. The study of Qi et al. (2018), introduced an automatic joint configuration learning technique based on dictionary learning and sparse representation for Spatio-temporal recognition of a human body. The presented technique is to collect the information of Spatio-temporal geometric configuration of each joint of the body, collect information from handcraft features design, this technique replaces the conventional bag. The experimental result tested on three existing public human activity recognition and provides better performance. In the indoor environment, the work of recognition and the analysis of human activity is carried out by Wang et al. (2019). The authors have presented a flexible fibre-optic sensor-based pressure sensing system, a binary sensing scheme is applied in this system to describe the workload of data and also the design of bipedal movement-based space encoding technique to collect and capture the human geometric information. This technique is tested in some indoor environments like offices and in which observed and captured with the movement of the walk, work, rest, and talk of a human body. The experimental outcomes demonstrate that the individual accuracy of the recognition of this technique is higher than 90% and the perception rate is 80%. The study of Vishwakarma et al. (2017), have presented a combined framework for RHA through the analysis of spatial distribution of gradients (SDGs) on average energy silhouette images (AESIs). The experimental result illustrates that the presented framework is tested on three different datasets like Weizmann, KTH, Ballet, and provide better result. An intensive learning model based on a combined approach of establishment neural network (ENN) and recurrent neural networks (RNN) is presented by the work of Xu et al. (2019). In this waveform, data from the sensor is used as input values, and multiple kernel-oriented convolution layers obtain multi-dimensional features. The experimental validation of this study is done on a widely used public HAR dataset. The outcome suggests that the presented approach shows consistently better performance than the conventional one. A careful study of existing systems reveals that most existing systems take a summary of the input image directly from the data set and then place the processed image in their corresponding algorithms. It has also been observed that many

Collaborative Project Management: Challenges and Opportunities for Distributed and Outsourced Projects

Jerry Fjermestad and Nicholas C. Romano Jr. (2006). *International Journal of e-Collaboration (pp. 1-7).*

International Journal of Cast Metals Research

ISSN: (Print) (Online) Journal homepage: https://www.tandfonline.com/loi/ycmr20

Synthesis of Fe_3O_4–aluminium matrix composites: mechanical and corrosion characteristics

Shivaramakrishna A, Yadavalli Basavaraj & Raghavendra Subramanya

To cite this article: Shivaramakrishna A, Yadavalli Basavaraj & Raghavendra Subramanya (2022): Synthesis of Fe_3O_4–aluminium matrix composites: mechanical and corrosion characteristics, International Journal of Cast Metals Research, DOI: 10.1080/13640461.2022.2078551

To link to this article: https://doi.org/10.1080/13640461.2022.2078551

Published online: 26 May 2022.

INTERNATIONAL JOURNAL OF CAST METALS RESEARCH
https://doi.org/10.1080/13640461.2022.2078551

Taylor & Francis
Taylor & Francis Group

RESEARCH ARTICLE

Synthesis of Fe_3O_4–aluminium matrix composites: mechanical and corrosion characteristics

Shivaramakrishna A[a], Yadavalli Basavaraj[a] and Raghavendra Subramanya[b]

[a]Department of Mechanical Engineering, Ballari Institute of Technology and Management, Ballari, India; [b]Department of Mechanical Engineering, Sai Vidya Institute of Technology, Bangalore, India

ABSTRACT

The aim of this study is to investigate at the mechanical characteristics of Fe_3O_4 particle reinforced with 7075 aluminium alloy composite. The composites of different weight percentage 2%, 4%, 6%, and 8% of Fe_3O_4 reinforcement were prepared using stir casting technique. Prepared composite samples were examined for mechanical properties like tensile percentage elongation and hardness test along with scanning electron microscopy. Additionally, corrosion was also conducted on the prepared samples. The results of mechanical properties reveal that improvement in hardness and tensile strength and corrosion resistance values with different weight percentage combinations. When compared to the original Al7075 alloy, the Ultimate Tensile Strength is highest at a value of 64.563% for 8% Fe_3O_4 reinforcement, and variation in Ultimate Tensile Strength is highest at a value of 21.865% for an increase in reinforcement percentage from 4% to 6% weight, according to the experimental studies. .

ARTICLE HISTORY
Received 14 July 2021
Accepted 12 May 2022

KEYWORDS
Hardness; corrosion; aluminium; iron oxide; composites

1. Introduction

There is now a lot of interest in particle-reinforced metal-matrix composites, particularly those based on existing aluminium alloys. This is due to the fact that the addition of ceramic particles to aluminium alloys can increase mechanical and tribological characteristics [1]. Current technology advancement in aerospace, automotive, marine, construction and ease industries has made the demand for materials having high strength-to-weight ratio, good corrosion resistance and good thermal conductivity to be on the increase [2]. In the literature [3,4] studies reveal that the increase in reinforcement particles in matrix-metal results in the increase of mechanical properties like hardness, tensile strength, impact strength, etc. Al-Fe alloys are attractive for applications at temperatures beyond those normally associated with conventional Al alloys because of the stability of Fe in Al. In addition, alloying Al with Fe increases its high-temperature strength due to the dispersion of second-phase particles [5]. Compared to solid-phase processing, the liquid-phase processing methods are attractive as they are economical and also capable to produce large structural components with complex geometry. However, a major challenge in the liquid-phase processing is to achieve uniform distribution of reinforcement and to obtain strong interfacial bonding between the reinforcement and the matrix [6]. The development of $Al_{13}Fe_4$ composite provides higher hardness and improved tensile strength with much loss of ductility as compared to base alloy. Both composite and base alloy exhibit ductile mode of facture [7].

Due to its low cost and greater free energy thermite reaction with aluminium, magnetite (Fe_3O_4) is also good filler. This reaction can increase the wettability of magnetite and aluminium matrix while also providing more energy for the operation. It is also a highly regarded filler material due to its outstanding magnetic characteristics.

Additionally, corrosion behaviour is an important factor to consider when using composites as structural materials. Reinforcing particles may interact with the matrix chemically, mechanically, or electrochemically, speeding up corrosion.

Furthermore, galvanic interactions between the matrix and reinforcement might accelerate corrosion. Several corrosion experiments of Al matrix composites were carried out in order to determine their corrosion susceptibility in NaCl. Different research studies have revealed that increasing the SiC volume and optimising the quantity of SiC improved the AMC's corrosion resistance [8–10].

The presence of reinforcements sometimes restricts the continuity of the aluminium alloy and the surface oxide coating primarily to the formation of galvanic couples at the boundary/interface between the aluminium substrate and the reinforcing material precipitates. This increases the number of potential places for electrochemical process [11].

CONTACT Raghavendra Subramanya rvs.sdly@gmail.com Department of Mechanical Engineering, Sai Vidya Institute of Technology, Bangalore, Karnataka, India

Corrosion in metal matrix composites is also affected by ambient conditions and manufacturing procedures, which modify the microstructure. The processing techniques and composite composition influence void size, dislocation density, and active-phase precipitation in aluminium matrices owing to reinforcement/matrix interactions that produce new intermetallic phases [12].

The number of researches on Al-based matrix composites reported in the literature has been based on the 2XXX and 6XXX series. The Al-Mg-Si alloys of the 6XXX family are commonly employed as medium strength structural alloys because of their superior weldability, corrosion resistance, and resistance to stress corrosion cracking [13]. However, little is known about the usage of Al 7XXX alloy as a metal matrix.

The objectives of this paper are to develop an aluminium metal matrix composite with varying weight percentages of Fe_3O_4 as reinforcement in order to determine the best quantity of Fe_3O_4 to add to this metal matrix composite. The composite's microstructure (using Scanning Electron Microscope), hardness, tensile, and corrosion characteristics along with the open-circuit potential were also evaluated. This is significant mentioning that the findings of this study will support in the development of a Metal Matrix composite by finding the best quantity of Fe_3O_4 filler that may be used in a variety of applications. The importance of this research attributed to the fact that aluminium (Al7075 series), iron oxide alloys have crystalline structure phases, the most important of which are alumina and iron, as well as the presence of a fine cellular structure and corrosion resistance. As a result, this type of aluminium iron oxide alloy can be used in the aerospace, aeronautics, and automobile industries.

Table 1. Chemical compositions of Al-7075.

Siz	Mnz	Zn	Cuz	Ti	Mg	Cr	Alz
0.4	0.3	6.1	2	0.2	2.9	0.28	88

2. Materials and methods

The aluminium 7075 alloy used as the matrix-metal in the experiment for the fabrication of composite that has been reinforced with a different weight percentage of Fe_3O_4 (2%,4%,6% and 8% wt). The pure aluminium 7075 procured from, Perfect metal works, Bangalore, India. The chemical composition of aluminium is shown in Table 1. Fe3O4 (magnetite ore particles 300Mesh size were selected from Bellary Iron ore Region, Karnataka, India.

The stir casting process is used to create the composition. Figure 1 illustrates the stir casting system, which includes a furnace, reinforcement feeding, and mechanical stirrer. This stirrer is coupled to a variable speed motor, and its rotation speed is controlled by a regulator attached to the motor. The processing of the composite is carried out at a temperature of 700°C with a string speed of 300 rpm. The reinforced (Fe_3O_4) particle was heated in the muffle furnace before being added at a consistent rate to the molten aluminium alloy, which was thoroughly agitated for a constant amount of time. Then it is poured into the split die which is preheated. Then the molten metal was allowed to solidify. The steps are repeated for various compositions by keeping speed and time constant for stirring.

The hardness testing of the Al-7075 reinforced with $Fe_3O_4$is conducted as per IS 1500 part1, Brinell's hardness values were determined for different Fe_3O_4 weight % reinforced with Al-7075 Aluminium composites. The tests were carried out using a 5 mm diameter indenter and a 250 kg (2452.5 N) indent force.

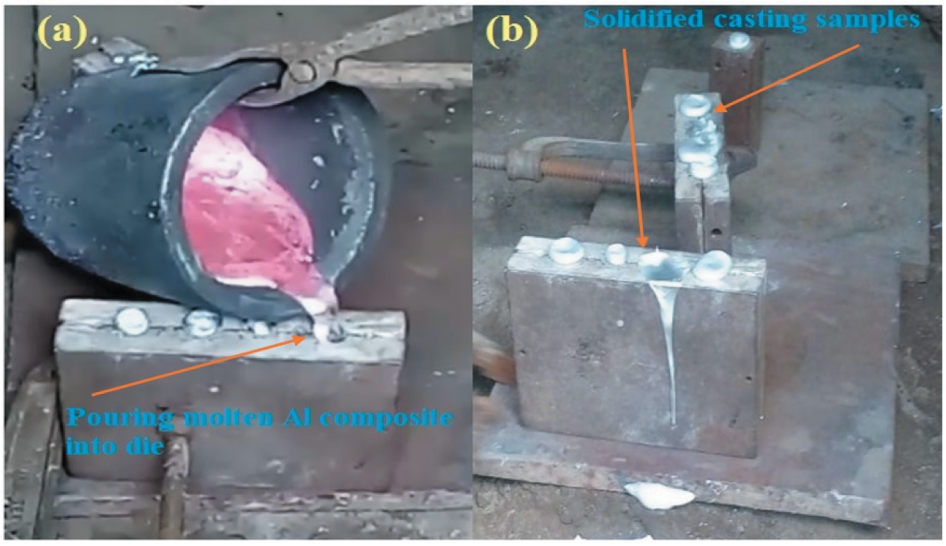

Figure 1. a) pouring of the Al7075/Fe_3O_4 composite into Dies, b) solidified composite samples.

Tensile tests were carried out on tensile sample composites in accordance with the ASTM B557 standard. The tensile test specimens were machined in a round form with a diameter of 9 mm and a gauge length of 36 mm. Tensile test were carried out on KIC-2-1000c machine, and at a test speed of 1 mm/min.

The surface of the composite specimen was observed in scanning electron microscopy (make TESCAN VEGA3) to study the surface morphology. The specific compositions of the alloys were analysed by spark emission spectrometer [Model: Polyspek- JNR, Optic Spectrometer system]

2.1 Corrosion test

A synthetic saltwater solution produced in accordance with ASTM D-1141 was utilised as the test electrolyte. A three-electrode electrochemical cell was employed, with a saturated calomel electrode (SCE) as the reference electrode and a sintered graphite rod as the auxiliary electrode (AE). At air pressure and room temperature, all electrochemical analysis was carried. Open-circuit potential corrosion test was performed in aerated solution of 3.5% sodium chloride solution at 30°C ± 0.5°C . Surface working electrodes To expose a top surface, Al7075-Fe3O4 alloy samples were created. The Autolab PGSTAT 30 potentiostat system, which was coupled to a microprocessor, was used to detect corrosion potentials (Ecor).

3. Results and discussion

3.1 Energy dispersion X-ray spectroscopy

EDX (energy dispersion X-ray spectroscopy) is a technique for determining the element type in samples. Iron ore was brought in from the Ballari Karnataka, India. The particle size of the ore in its natural form ranges from 0.1 to 100 µm.

The reactive oxides (iron ore) that have been poured are expected to react with the liquid metal and produce a variety of reaction products. The nature of the reinforcing phase has an effect on composites' strength. As a result, X-Ray diffraction investigations have been analysed to recognise the particle formed by the chemical process.

EDS image of the Al7075-2%, 4%, 6%, and 8% weight of Fe_3O_4 composite is shown in Figure 2(a-d), respectively, and it confirms the presence of Fe content in the Al7075 alloy.

Other atomic percentages such as Mg, Cu, Si, Zn, and O were found in the spectra, in addition to the aluminium atomic percentage as the major share. Fe atomic reinforced Al-7075Alloy with 8% wt, 6% wt, 4% wt, and 2% weight Fe_3O_4. The Fe element atomic percentages in Fe_3O_4 reinforced Al-7075Alloy were 0.79, 0.46, 0.88, and 0.62%, respectively, in 8% wt, 6% wt, 4% wt and 2% wt Fe_3O_4 reinforced Al-7075 Composite.

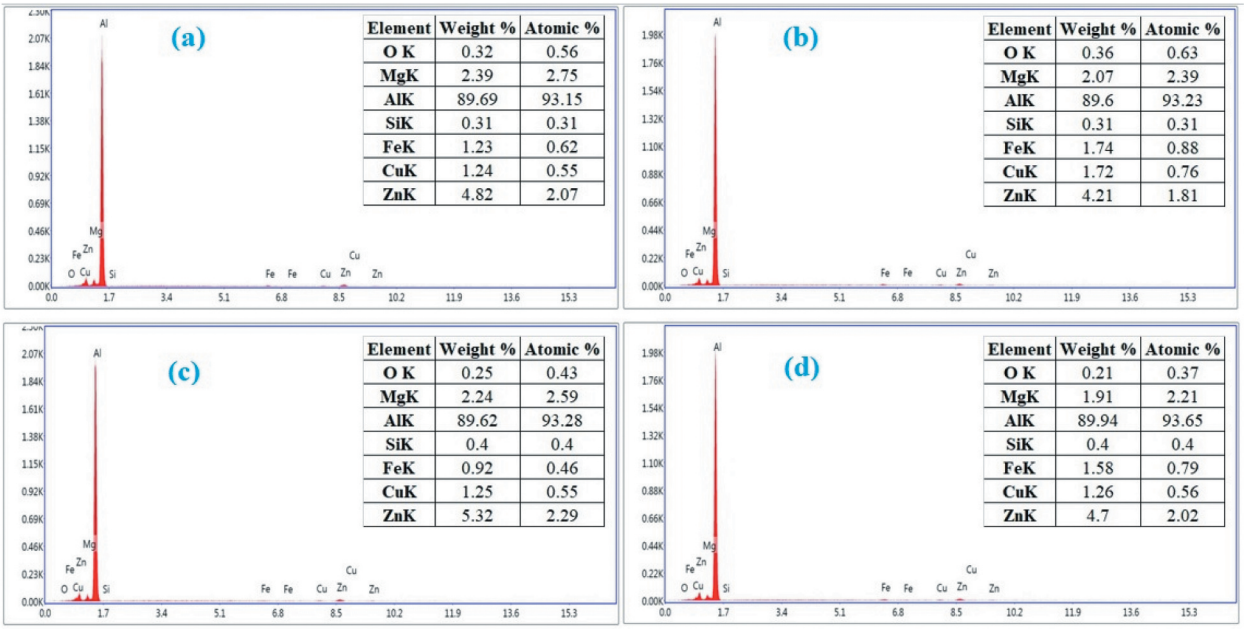

Figure 2. EDS spectrum of composite composition a) Al7075/2 wt% Fe_3O_4, b) Al7075/4 wt% Fe_3O_4, c) Al7075/6 wt% Fe_3O_4, d) Al7075/8 wt%.

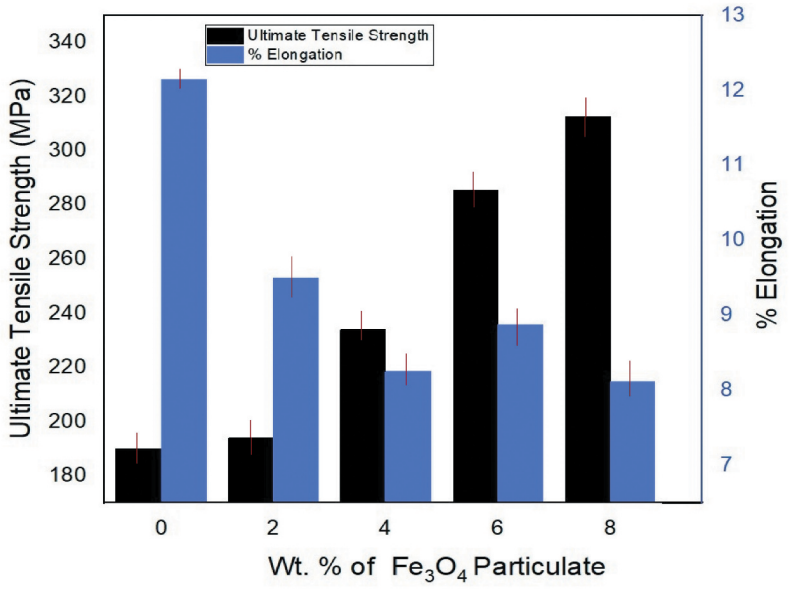

Figure 3. Graphical representation of ultimate tensile strength and percentage elongation of Al7075/Fe_3O_4 composites.

3.2 Ultimate tensile strength

The Ultimate Tensile strength of the Al7075/Fe3O4 composite with different reinforcement percentages was measured using a universal testing machine and the results were recorded. The Ultimate Tensile strength shows the final point of fracture in a ductile material and the Ultimate Tensile strength of the Al7075/Fe_3O_4 composites was compared against that of pure aluminium alloy Al7075 and the results are graphically represented in Figure 3. The Ultimate Tensile strength of the composite is directly proportional to the percentage of reinforcement in the aluminium alloy. The Figure 3 also shows that the sudden increase in Ultimate Tensile Strength is highest for 6% weight reinforcement of Fe_3O_4 as compared to other weight percentage reinforcement of Fe_3O_4.

3.3 Brinell hardness test

The Brinell's hardness value was obtained for the Aluminium composite Al7075/Fe_3O_4 at different reinforcement percentages. The test was conducted using an indenter of 5 mm diameter and an indent load of 250 kg or 2452.5 N. The test was performed multiple times and the average of the obtained values was used as the final result. The graphical representation of these values is shown in Figure 4. The values show that there is an increasing trend in the hardness of the composite as the percentage of reinforcement increases with a slightly higher increase seen at 8% Fe_3O_4 reinforcement.

From the investigation it is observed that increasingly change in weight percentage reinforcement of Fe_3O_4 in Al7075 alloy, hardness of the

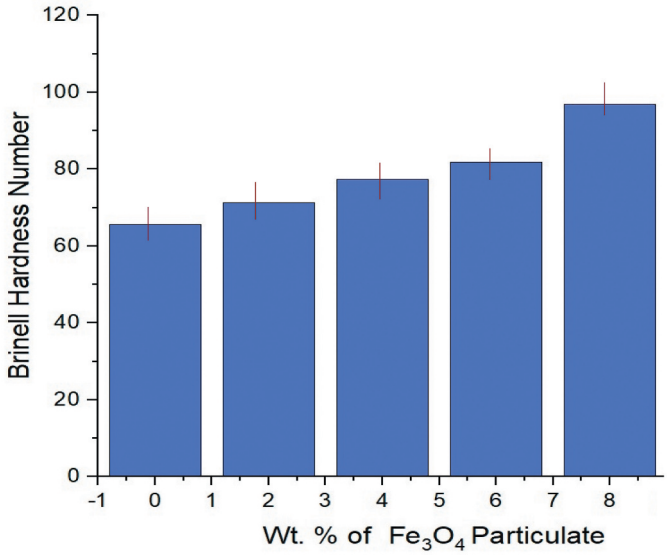

Figure 4. Graphical representation of BHN of Al7075/Fe_3O_4 composites.

Al7075/Fe_3O_4 composite increases subsequently. The hardness value is observed to be highest at a value of 47.5346% for 8% Fe_3O_4 reinforcement after compared with original Al7075 alloy and the least value of 8.569% for 2% Fe_3O_4 reinforcement when compared with the original Al7075 alloy. Although when compared to the differences of weight percentages of 2%, 4%, 6% and 8% of Fe_3O_4 weight reinforcement, the experimental result reveals that at 8% weight reinforcement shows the highest increase in the hardness value, which indicates that 8% weight reinforcement has the highest impact on the hardness of the Al7075/Fe_3O_4 composites. The lowest variation is seen at 6% reinforcement, which indicates that this value has the lowest impact on the hardness of the Al7075/Fe_3O_4 composite.

3.4 SEM analysis

The microstructure of the composite of 2%, 4%, 6% and 8% weight of reinforcement Fe_3O_4 in Al7075 alloy reveals that the distribution of Fe_3O_4 particles is uniformly distributed in the Al7075 alloy matrix Figure 5. Also, $Fe_3O_4$are well-bounded with Al7075 alloy and clustering of Fe_3O_4particles was not seen in the composite.

3.5 Effectiveness of corrosion protection

The potentiodynamic polarisation methodology was used to examine the samples' corrosion and passivation kinetics. The Al-2%Fe_3O_4, Al-4%Fe_3O_4, Al-6%Fe_3O_4, and Al-8%Fe_3O_4 specimens were subjected to an artificial saltwater media in this experiment. Table 2 presents the results of corrosion current density (Icorr), corrosion potential (Ecorr), and corrosion rate.

Ecorr denotes the substrate's inclination to erode, whereas Icorr reflects the effectiveness of corrosion prevention. The Ecorr values for all of the examined samples lie within the range of 654 to 715 mV, as shown in Table 2. The Icorr value of Al 15 Fe_3O_4 is 6.157 10–4 A; however, raising the wt percent Fe_3O_4 improves the value of corrosion resistance. Furthermore, the findings from Polarisation curves Figure 6 demonstrated that Fe_3O_4 reinforced composites had a stronger corrosion resistance than aluminium matrix composites. It's worth noting that the pitting corrosion found in aluminium base metal was not caused by Fe_3O_4 particles.

Many factors influence the corrosion resistance of an aluminium matrix composite, including the manufacturing method, matrix properties, reinforcing quantity, and environmental factors [14]. Mosaad Mohamad Sadawy studied the corrosion behaviour of Al_2O_3 on Steel materials, Fe3O4 reinforced composites have greater corrosion

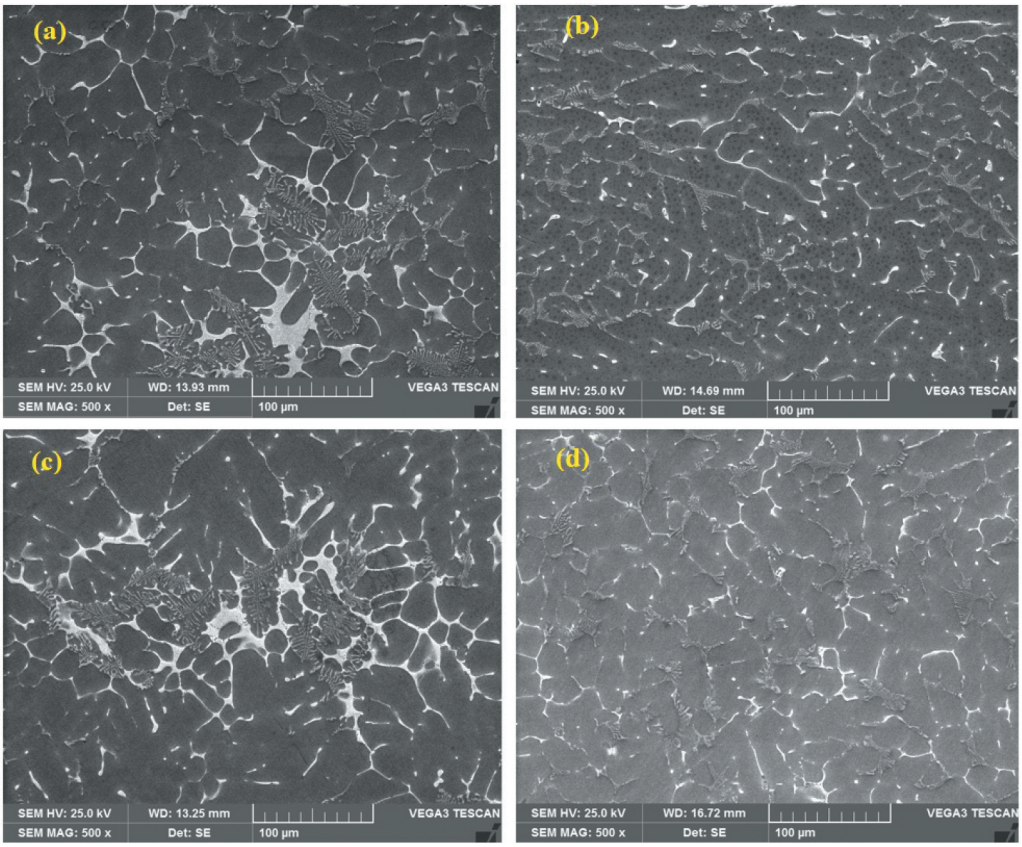

Figure 5. SEM micrograph of a) Al7075/2 wt% Fe_3O_4, b) Al7075/4 wt% Fe_3O_4, c) Al7075/6 wt% Fe_3O_4, d) Al7075/6 wt% Fe_3O_4 composite.

Table 2. Data on corrosion current density (Icorr), corrosion potential (Ecorr), polarisation resistance (Rp), corrosion rate, and corrosion protection effectiveness (P.E.).

Parameter	Al-0% Fe_3O_4	Al-2% Fe_3O_4	Al-4% Fe_3O_4	Al-6% Fe_3O_4	Al-8% Fe_3O_4
Ecorr/mV	−702.421	−715.584	−654.146	−691.258	−674.365
Icorr/A	$6.061x10^{-4}$	$6.157x10^{-4}$	$7.342x10^{-5}$	$5.597x10^{-5}$	$1.514x10^{-6}$
Log(| <I>/A |)					
Weight of sample (gm)	2.24	2.20	2.78	2.50	2.89
Corrosion rate mm/year	$8.1x10^{-4}$	$8.4x10^{-4}$	$0.87x10^{-4}$	$0.8x10^{-4}$	$0.6x10^{-4}$

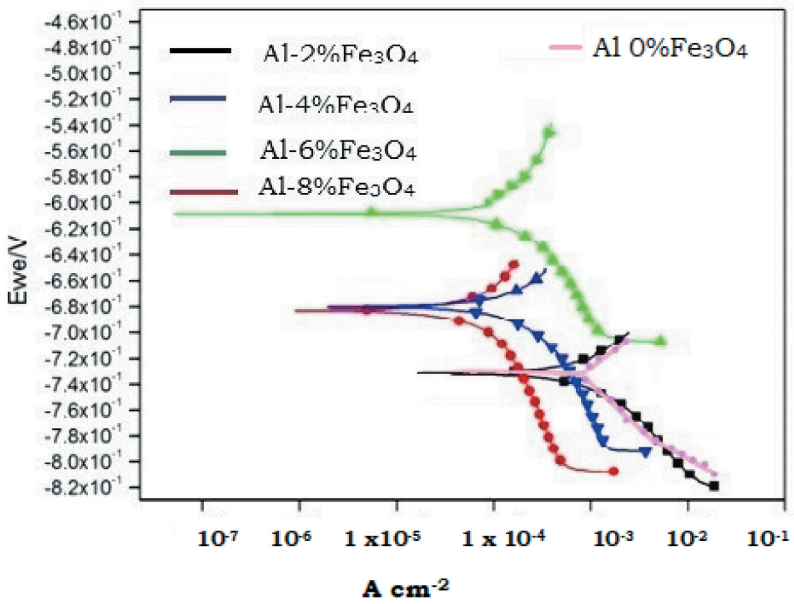

Figure 6. Polarisation curves of a) Al7075/0 wt% Fe_3O_4 b) Al7075/2 wt% Fe_3O_4, c) Al7075/4 wt% Fe_3O_4, d) Al7075/6 wt% Fe_3O_4, e) Al7075/8 wt% composite samples.

resistance than the aluminium matrix, according to the findings. There was no evidence of pitting corrosion in aluminium base metal when Fe_3O_4 particles were present. This could be due to the presence of Al_3Fe intermetallic phases, which act as cathodes in the metal matrix and improve pitting corrosion resistance [15].

The contact between the matrix and the reinforcement is the weakest component of composites. As a result, the strength or weakness of the interfacial connection is critical in the corrosion process. Al7075/8% weight composite samples showed better corrosion resistance among all.

3.6 Open-circuit potential

The corrosion resistance of the composites is slightly greater than that of the matrix, as seen in the graphs. The similar pattern can be seen in open circuit potential experiments, where the potential created for MMCs and matrix decreases with exposure time and eventually becomes constant after 489 seconds as shown in Figure 7, Open-circuit potential curve during immersion in 3.5% sodium chloride solution at 30°C. When compared to matrix, the potentials encountered by MMCs are lower. The tests will result in the formation of a black coating on the sample. A probable passivation of the matrix alloy is indicated by the characteristic of steadily reducing corrosion rate.

The black film is made up of an aluminium hydroxide compound is formed over the sample after corrosion test, according to Castle et al. [16]. Further corrosion in acidic environments is prevented by this layer. The creation of pits and fractures on the surface is primarily responsible for the corrosion rate of the composites and the matrix alloy in this circumstance. The severity of the base alloy utilised causes surface cracking. Potentiostat test results in various sodium chloride concentrations are illustrated in Figure, during the acidic medium, Fe_3O_4 reinforcement particles operate as an insulator and stay inert.

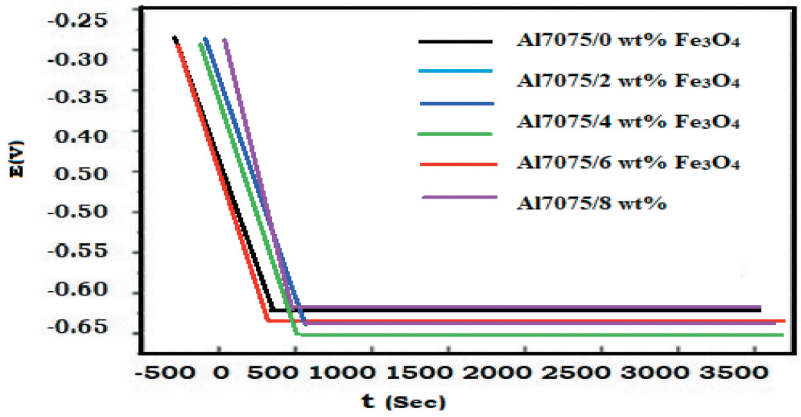

Figure 7. Open-circuit potential of Al7075-Fe_3O_4 alloy with 0,2,4,6 and 8%wt Fe_3O_4, during immersion in 3.5% sodium chloride solution at 30°C.

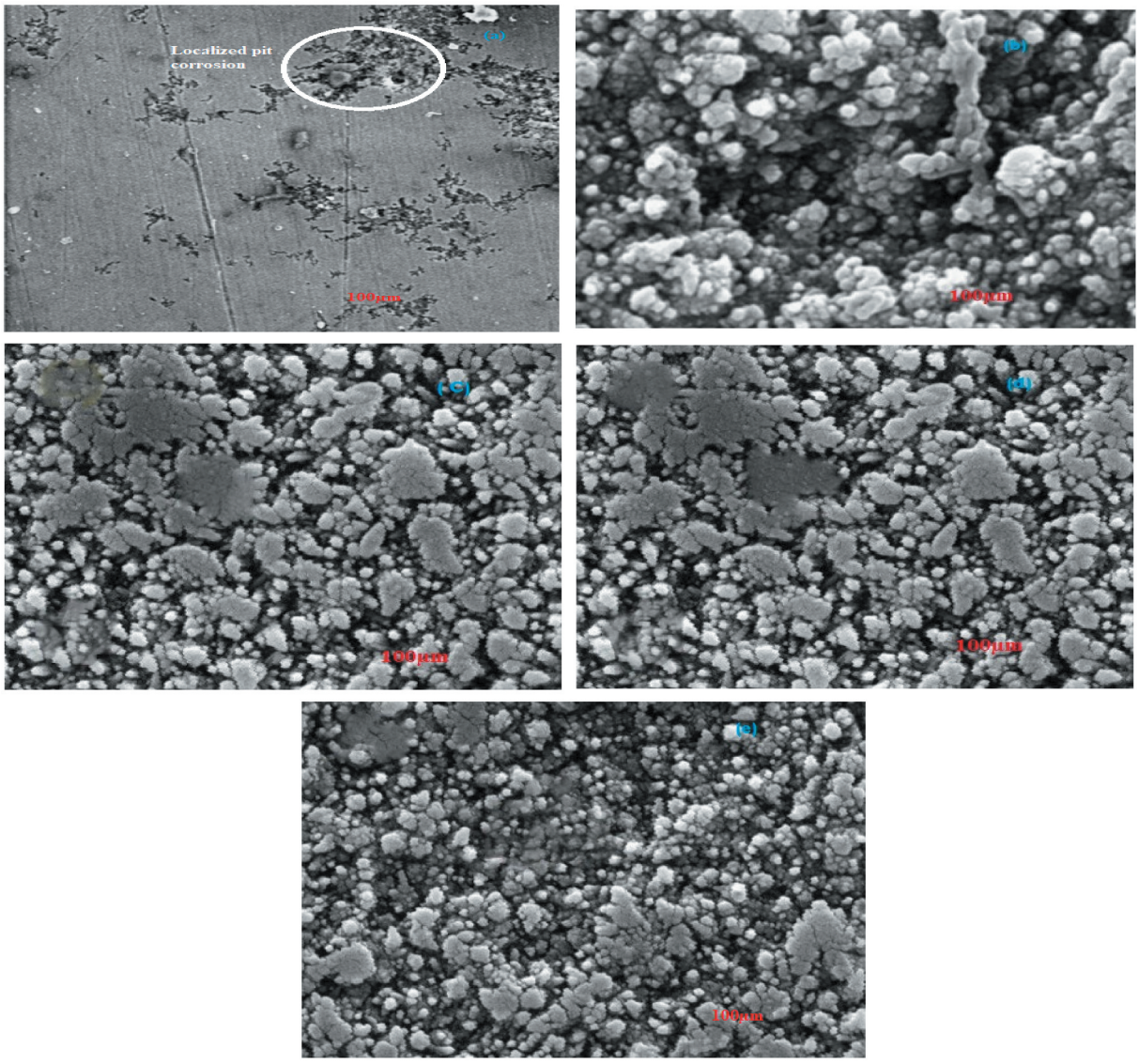

Figure 8. Corrosion morphology of a) Al7075/0 wt% Fe_3O_4 b) Al7075/2 wt% Fe_3O_4, c) Al7075/4 wt% Fe_3O_4, d) Al7075/6 wt% Fe_3O_4, e) Al7075/8 wt% composite samples.

The iron oxide reinforcement particles serve as an insulator and stay inert in the acidic liquid during the test, as can be shown. When a result, as the iron concentration in MMCs increases, the corrosion rate lowers, potentially reducing the area of alloy exposure as the reinforcement increases. In corrosion tests, the MMCs were exposed to less harsh chloride conditions, resulting in less pitting and corrosion than the matrix alloy.

3.7 Corrosion morphology study

In a 3.5% sodium chloride solution at 30°C, corrosion morphology of Al 7075 cast and composite specimens is shown in Figure 8.

Pit-type corrosion is present in all composite specimens, and white debris may be seen on the specimen's surface. Additional corrosion products are deposited while the specimen is submerged in a solution for a longer period of time, causing more fractures and flakes to develop on the surface. The 2, 4,6, and 8% Fe3O4 reinforced specimens show greater corrosion product (figure 8(b-e)), which might be related to discontinuities that appear more on the surface than other samples.Similar trend was also observed in the study of Sambathkumar et al. [17], Al 7075 metal matrix composites provided lower corrosion rate than the base matrix in 3.5% NaCl solution. Increasing the volume percentage of red mud reduces the corrosion rate of the composites, Due to the tendency of iron oxide reinforced Al 7075 alloy to fill holes, cracks, and discontinuities, corrosion products are less similar to pure Al 7075 (figure 8(a)). The development of pits and cracks on the surfaces of composites diminishes as the reinforcing content in the composite increases, indicating that corrosion is being reduced.

4. Conclusion

In the present study, Al7075 composite reinforced with uniformly distributed Fe_3O_4particulates have been prepared successfully using the stir casting method. Al7075 MMC reinforced with $Fe_3O_4$of weight 2%, 4%, 6%, and 8% were added. Based on the studies of the Al7075/Fe_3O_4 composite the following conclusions were drawn. The results are arrived at with an average of three values, for the Ultimate tensile strength, percentage of elongation, and hardness studies.

(1) Al7075 reinforced with weight 2%, 4%, 6% and 8% Fe_3O_4 Metal Matrix composites prepared using stir-casting method with fairly uniform distribution of particulates in the matrix were successfully produced.
(2) The addition of Fe_3O_4 Particulates to the Al7075 matrix has resulted in enhanced mechanical properties when related to the Al matrix alone. The Ultimate Tensile Strength is seen to be highest at a value of 21.865% for an increase in reinforcement percentage from 4% to 6% wt. The decrease in Percentage Elongation is seen to be highest at a value of 27.985% for an increase in reinforcement percentage from 0% to 2% and the increase in percentage elongation is seen at a value of 7.057% being for an increase in reinforcement percentage from 4% to 6% weight. The percentage change in the hardness value is seen to be highest at a value of 47.54% for the 8% weight Fe_3O_4 reinforcement.
(3) From the SEM images, it can be observed that the distribution of reinforcement is fairly uniform.
(4) The Fe_3O_4 reacts with the melt in a significant way, resulting in finer particles of complicated oxides. The oxide particles and unreacted iron ore particles yield considerable increase in the composite's tensile strength and hardness.
(5) Strengthening of composites is due to particle reinforcement, dispersion strengthening and solid solution strengthening.
(6) The addition of Fe_3O_4 particles to the aluminium matrix significantly increased corrosion resistance.
(7) From a 3.5% NaCl solution, Al 7075 metal matrix composites had a lower corrosion rate than the base matrix. The corrosion rate of composites is reduced by increasing the volume percentage of iron oxide.

Acknowledgements

The authors wish to appreciate Visvesvaraya Technological University, Belagavi, Ballari Institute of Technology and Management, Ballari and Sai Vidya institute of Technology, Bangalore for their support.

Disclosure statement

No potential conflict of interest was reported by the author(s).

Funding

The authors have no funding to report.

ORCID

Raghavendra Subramanya http://orcid.org/0000-0003-4276-9638

References

[1] Arun KS, Panneerselvam T, Raghuraman S. Study on mechanical properties of aluminium based metal matrix composites by hybrid reinforcement. Appl Mech Mater. 2015;813–814:116–120.

[2] Oluropo Adeosun S, Ajibola Ayoola W, Bodude M, et al. Strength and hardness of directionally-rolled AA1230 aluminum alloy. J Emerg Trends Eng Appl Sci. 2011;2 (3):440–444.

[3] Kumar A, Lal S, Kumar S. Fabrication and characterization of A359/Al2O3 metal matrix composite using electromagnetic stir casting method. J Mater Res Technol. 2013;2(3):250–254.

[4] Fono-Tamo RS, Tien-Chien J. Effect of reinforcememt particles preheating on mechanical and microstructural properties of AMC. Acta Metall Slovaca. 2018;24 (4):337–346.

[5] Fathy A, El-Kady O, Mohammed MMM. Effect of iron addition on microstructure, mechanical and magnetic properties of Al-matrix composite produced by powder metallurgy route. Trans Nonferrous Met Soc China English Ed. 2015;25(1):46–53.

[6] Hashim J, Looney L, Hashmi MSJ. Particle distribution in cast metal matrix composites - Part II. J Mater Process Technol. 2002;123(2):258–263.

[7] Pradhan SK, Chatterjee S, Mallick AB, et al. A simple stir casting technique for the preparation of in situ Fe-aluminides reinforced Al-matrix composites. Perspect Sci. 2016;8:529–532.

[8] Ferreira L, Bayraktar E, Robert M. Magnetic and electrical properties of aluminium matrix composite reinforced with magnetic nano iron oxide (Fe3O4). Adv Mater Process Technol. 2016;2:165–173.

[9] Roseline S, Paramasivam V. Corrosion behaviour of heat treated aluminium metal matrix composites reinforced with fused zirconia alumina 40. J Alloys Compd. 2019;799:205–215.

[10] Boutouta A, Yacine Debili M. Microstructural and thermal characteristics of the sintered Al-Fe2O3 composites. Eng Rev. 2020;40(1):32–38.

[11] Irfan A, Zhang Q, Xiang M. Corrosion inhibition of SiCp/5A06 aluminum metal matrix composite by cerium conversion treatment. Chin J Aeronaut. 2009;22(6):670–676.

[12] Gopinath K, Balasubramaniam R, Murthy VSR. Corrosion behavior of cast Al-Al2O3 particulate composites. J Mater Sci Lett. 2001;20(9):793–794.

[13] Christy T, Murugan N, Kumar S. A comparative study on the microstructures and mechanical properties of Al 6061 Alloy and the MMC Al 6061/TiB_2/12_p. J Miner Mater Charact Eng. 2010;9(1):57–65.

[14] Eftekhari M, Movahedi M, Kokabi AH. Microstructure, strength, and wear behavior relationship in Al-Fe3O4 nanocomposite produced by multi-pass friction stir processing. J Materi Eng and Perform. 2017;26 (7):3516–3530.

[15] Sadawy MM. Effect of Al2O3 additives on the corrosion and electrochemical behavior of steel embedded in ordinary Portland cement concrete. Am J Mater Res. 2014;4:53–58.

[16] Castle JE, Sun L, Yan H. The use of scanning Auger microscopy to locate cathodic centres in SiCp/6061 Al MMC and to determine the current density at which they operate. Corros Sci. 1994;36(6):1093–1110.

[17] Sambathkumar M, Sasikumar KS, Gukendran R, et al. Investigation of mechanical and corrosion properties of Al 7075/Redmud metal matrix composite. Rev Metal. 2021;57(1):e185.

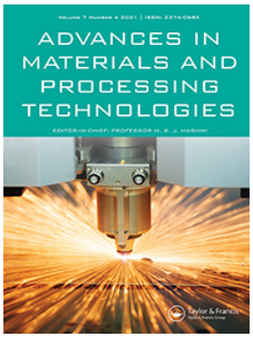

Taylor & Francis
Taylor & Francis Group

Advances in Materials and Processing Technologies

ISSN: (Print) (Online) Journal homepage: https://www.tandfonline.com/loi/tmpt20

Tensile hardness and wear properties of iron oxide (Fe_3O_4) reinforced aluminium 7075 metal matrix composites

Shivaramakrishna a, Raghavendra Subramanya & Yadavalli Basavaraj

To cite this article: Shivaramakrishna a, Raghavendra Subramanya & Yadavalli Basavaraj (2022): Tensile hardness and wear properties of iron oxide (Fe_3O_4) reinforced aluminium 7075 metal matrix composites, Advances in Materials and Processing Technologies, DOI: 10.1080/2374068X.2022.2079227

To link to this article: https://doi.org/10.1080/2374068X.2022.2079227

ADVANCES IN MATERIALS AND PROCESSING TECHNOLOGIES
https://doi.org/10.1080/2374068X.2022.2079227

Taylor & Francis
Taylor & Francis Group

Tensile hardness and wear properties of iron oxide (Fe_3O_4) reinforced aluminium 7075 metal matrix composites

Shivaramakrishna a[a], Raghavendra Subramanya[b] and Yadavalli Basavaraj[a]

[a]Department of Mechanical Engineering, Ballari Institute of Technology and Management, Ballari, India;
[b]Department of Mechanical Engineering, Sai Vidya Institute of Technology, Bangalore, India

ABSTRACT

The Al-7075 aluminium alloy has been proposed for widespread use in automotive applications. This material has been researched in composite structures with various reinforcements in order to improve its usage. In this study, Fe_3O_4 (magnetite) is reinforced in an Al-7075 matrix to create a metal matrix composite by a stir casting process. Aside from the Neat Matrix samples, five samples were produced by adding Fe_3O_4 to Al 7075 matrix in various weight proportions such as 2, 4, 6, 8, and 10. The mechanical properties of the fabricated composite specimens were determined by different tests, including hardness, tensile, compression, and wear strength. The results were compared to a standard matrix alloy. In addition, SEM with EDAX studies was performed to examine the dispersion of the reinforced particles in the chosen matrix alloy. The homogeneous distribution of Fe_3O_4 particles in composites was observed to be intragranular in origin. Furthermore, Fe_3O_4 particles were found to be well attached to the matrix alloy, with a clean interface. The composite's hardness and tensile strength along with wear resistance were also found to increase as the Fe_3O_4 concentration increased.

ARTICLE HISTORY
Accepted 13 May 2022

KEYWORDS
Stir casting; hardness; aluminium; wear; metal matrix composites

1. Introduction

Aluminium is very attractive due to its low density, high thermal conductivity, and environmental resistance; however, it has a high thermal expansion coefficient and low mechanical strength.

Al-7075 has quite a broad range of uses, therefore it requires further reinforcing. The aluminium alloy is utilised as a matrix material and is reinforced with single and multiple reinforcement particles such as SiC, Al_2O_3, Gr, TiO_2, B_4C, fly ash, and other materials to create composites with better strength than the basic alloy material.

The potential of MMCs to significantly alter characteristics (thermal expansion, density), mechanical properties (tensile and compressive behaviour), tribological properties, and other qualities by changing constituent or filler material phase has recently attracted researchers' attention [1].

CONTACT Raghavendra Subramanya rvs.sdly@gmail.com Department of Mechanical Engineering, Sai Vidya Institute of Technology, Bangalore, Karnataka, India

In terms of the combination of profile attributes, no monolithic material has yet to equal Al MMCs. Al MMCs have emerged and developed as a preferred material for structural and thermal systems and mild steel bearing applications, as well as components such as cylinder liners, brake drums, cylinder blocks, crankshafts, disc brakes, and other applications [2]. The versatility of casting to manufacture those complex shapes with precise dimensions at a high production rate and low cost is the reason for its widespread appeal [3].

These areas of application indicate that a large number of components for which Al MMCs are designed are subject to significant wear rates. To deepen our understanding of how these composites behave in service, it is important to look at their wear characteristics. It has been revealed that the wear properties of materials are determined in a complicated manner by a range of material and operating factors [4].

Because of their weak wear resistance and low hardness value, aluminium alloys must increase their wear resistance in high-performance tribological applications. Materials will wear out quickly in some environments. To overcome this difficulty, particle reinforcement may be utilised; these reinforcements, such as silicon carbide, are known for their high specific strength, which leads to the development of metal matrix composites to meet the requirement for wear and corrosion-resistant material [5].

There is also a desire for materials that are very wear-resistant. From an economic standpoint, research in this field is critical since cost is directly involved. Silicon carbide particles offer excellent mechanical characteristics, a low coefficient of thermal expansion, and a low market price [6].

Due to its low cost and increased free energy thermite reaction with aluminium, magnetite is also a good filler. This reaction can increase the wettability of magnetite and aluminium matrix while also providing more energy for the operation. It is also a highly regarded filler material due to its great magnetic characteristics.

Because of their remarkable stiffness-to-weight and strength-to-weight ratios, reinforced (Fe_3O_4-iron oxide) aluminium matrix composites are increasing enormously in structural applications. The thermal conductivity and wear resistance of these materials are generally good for aviation applications. Bayraktar and Katundi developed an Al-based metal matrix composite reinforced with nano-Fe_30_4 magnetic particles. Wear resistance exhibits moderate behaviour, even if its tribological features demonstrate its suitability for many applications. It is discovered that interfacial shear stress may be the primary cause of matrix and reinforced filler interface damage [7].

Many articles on this material have been published in the literature; essentially, a detailed investigation of the strain hardening behaviour of Al-Fe powder metallurgical composites was conducted, and a novel constitutive relationship for the strain hardening behaviour of Al-Fe powder composites was proposed [8,9].

Fly ash and cast iron powder up to 6% may be effectively added to Al 7075 through the stir casting process to generate a hybrid composite, according to the findings. The hardness and tensile strength of cast iron powder rose as the concentration of the powder increased. As the concentration of cast iron powder in the aluminium matrix increased, the wear and frictional force reduced. Impact strength varies very slightly as the weight percentage of Grey Cast Iron increases [10].

Friction stir technique was used to successfully produce surface composite layers on an A 1050-H24 aluminium plate using distributed iron and magnetite particles. Fe and Fe3O4 powders have been put into a groove with a width of 3 mm and a depth of 1.5 mm, cut on an aluminium plate and covered with a 2-mm-thick aluminium sheet. As a result of the triple FSP passes, it was reported that the Fe particles were uniformly dispersed across the nugget zone at a rotating speed of 1000 rpm. There were just a few interfacial reactions between the Fe particles and the aluminium matrix [11].

Micro-arc oxidation was used to improve the wear resistance of a 304 stainless steel reinforced AA7075 aluminium matrix bimetal composite. At the 304 SS/AA7075 interface, a constant interfacial reaction layer consisting of -Fe4Al13 and -Fe2Al5 phases was formed. These phases increased the wear resistance of bimetal composites by significantly lowering adhesive wear [12-14].

The influence of iron oxide (Fe_2O_3) and graphite (Gr) reinforcement on the mechanical behaviour of the AA7075-Fe_2O_3-Gr Hybrid composite was examined in this study. Stir casting was used to make five hybrid composites of AA7075 reinforced with Fe2O3 and Gr particles. The amount of Fe_2O_3 was kept constant (5 wt%), however the percentage of Gr was changed from 0 to 8% by weight. With an increase in Gr particles up to 4 wt%, the composites' micro hardness and compressive strength showed an increasing trend [12].

Fabrication techniques for various MMCs are determined by factors such as matrix type and composition, wettability and uniform distribution of reinforcing particles in the base matrix, and manufacturing cost. The matrix material is heated above its liquefaction temperature in liquid-state manufacturing, and the reinforcement is added to the molten matrix, which in aluminium-based composites is aluminium and its alloys. Stir casting, squeeze casting, reactive in situ method and spray co deposition have all been thoroughly addressed under this heading.

Stir casting is a composite material production technology in which reinforcing components are combined with an aluminium matrix using a stirrer that can be manually or mechanically operated. Interfacial processes between metallic particles and molten aluminium are inevitable, and the composite contains a considerable proportion of intermetallic. Also, due to density variations and the formation of porosity, certain agglomerates may form, reducing the material property of the composite [15–21].

Shiva Kumar et al. examined the damping capability of an iron oxide reinforced aluminium matrix composite. Using the stir casting procedure, the composites were made with 2%, 4%, and 6% iron oxide by weight, with different particle sizes of 40 m and 500 nm in equal quantities. The 500 nm size with 4 wt% iron oxide demonstrated increased dynamic characteristics, according to the data. Iron oxides coupled with aluminium matrix have been discovered to provide novel replacements for conventional low damping materials [21].

In other investigations, wear properties and dielectric spectroscopy are investigated. The result shows that the addition of filler elements to the aluminium matrix increased both dielectric and wear resistance [22]. Adding micro particles to a composite alters its properties, according to prior studies. The composite reinforcements have significantly greater wear resistance and strength than aluminium. Reinforcement weight %, chemical interaction with matrix, reinforcement particle size, and production technique are all factors that influence the composite's properties [23,24].

The objective of this paper is to make aluminium matrix composites with various weight percentages of Fe3O4 particles as reinforcement in order to determine the optimal quantity of Fe3O4 in this composite. The composite's microstructure, hardness, tribological, and tensile characteristics were also evaluated. It is important to note that the information obtained from the study will contribute in the development of a new hybrid composite in terms of determining the optimal quantity of particle fillers that can be used in a variety of applications.

2. Materials and method

The pure aluminium 7075 procured from Perfect Metal Works, Bangalore, India. Fe_3O_4 (300 mesh size) particles are supplied from Gogia Chemicals, Hospet, Karnataka, India.

The chemical composition of alloy is shown in Table 1.

The hardness testing of the Al-7075 reinforced with Fe_3O_4 is conducted as per IS 1500 part 1, and Brinell's hardness values were determined for different Fe3O4 wt% reinforced with Al-7075 aluminium composites. The tests were carried out using a 5-mm-diameter indenter and a 250 kg (2452.5 N) indent force.

Tensile tests were carried out on tensile sample composites in accordance with the ASTM B557 standard. The tensile test specimens were machined in a round form with a diameter of 9 mm and a gauge length of 36 mm. Tensile test was carried out on KIC-2-1000c machine and at a test speed of 1 mm/min

Dry sliding wear test was conducted as per ASTM-G99-95 standard on 10 mm diameter × 40 mm length specimens against a rotating EN32 steel disc having hardness 65Rc. Pin-on-Disc wear test machine (Make: Ducom Instruments Pvt. Ltd., Model: TR20LE) was used to carry out tests.

The surface of the composite specimen was observed by scanning electron microscopy (make TESCAN VEGA3) to study the surface morphology. The specific composition of the alloys was analysed by spark emission spectrometer [Model: Polyspek-JNR, Optic Spectrometer system].The surface morphology of worn surface were peformed using a JEOL 6480 LV scanning electron microscope (SEM).

Stir casting is a liquid state process of fabricating composite materials in which a dispersed phase (ceramic particles, short fibres) is mechanically mixed with a molten matrix metal. After that, the liquid composite material is cast using traditional casting techniques (shown in Figure 1). First, aluminium was melted in a muffle furnace heated by resistance and then cast in a clay graphite crucible. While stirring at 600 rpm, the preheated Fe_3O_4 (300 mesh size, density 5.25 g/cm^3) particles were added to the liquid melt aluminium (density 2.720 g/cm^3). Before pouring the liquid Al7075-Fe_3O_4, the mould is preheated. The melt temperature was increased to 750°C for this, and the gas was removed using hexachloro ethane tablets. The aluminium Fe_3O_4 (2%, 4%, 6%, 8%

Table 1. Chemical compositions of Al-7075.

Siz	Mnz	Zn	Cuz	Ti	Mg	Cr	Alz
0.4	0.3	6.1	2	0.2	2.9	0.28	88

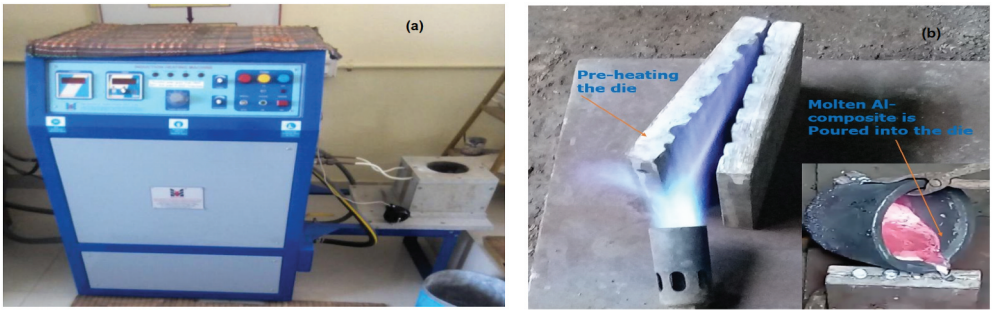

Figure 1. Image of (a) induction furnace and (b) preheating of die and pouring of molten Al Fe_3O_4.

and 10%) composites were then produced using the stir casting method. From rule of mixture, it is found that density of 2%, 4%, 6%, 8% and 10% reinforced Fe_3O_4 composites were 2.75, 2.77, 2.80, 2.83 and 2.86 g/cm^3, respectively.

3. Result and discussion

Figure 2 illustrates the powder morphology and X-ray diffraction peaks of as-received pure Al 7075 graphite powder particles. The Al 7075 powder particles are spherical, with a few irregularly shaped particles.

The X-ray diffraction patterns of the starting powders (Al 7075, respectively) are depicted in Figure. As shown in Figure, all of the primary peaks of Al 7075 belonged to Al with an FCC crystal structure, with detected peaks including (111), (200), (220) and (311) at diffraction angles (2θ) = 38, 45, 65 and 78, respectively.

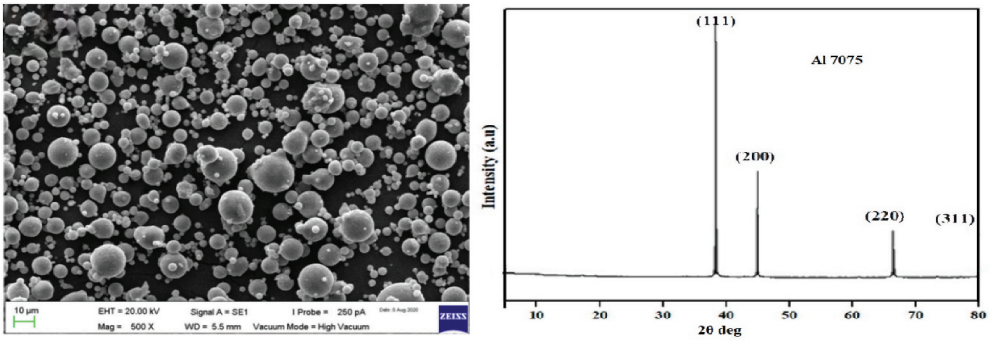

Figure 2. SEM image and XRD patterns of Al 7075 alloy.

3.1. Brinell's hardness test

The test was iterated, with the mean value of the obtained results considered as the final values. Table 2 shows the results of the Brinell's hardness test for alloy Al-7075 without reinforcement and the wt percentage variation of different reinforcements such as Fe_3O_4 in Al-7075 alloy MMCs.

Table 2. Hardness measurement.

Sample no.	Sample name	Brinell hardness number
1	Al-7075	65.7
2	Al-7075 + 2% Fe_3O_4	71.33
3	Al-7075 + 4% Fe_3O_4	77.3
4	Al-7075 + 6% Fe_3O_4	81.87
5	Al-7075 + 8% Fe_3O_4	96.93
6	Al-7075 + 10% Fe_3O_4	107.4

Table 3. Wear rate results of Al7075/Fe_3O_4 composites (2 m/s sliding speed, sliding distance 1500 m, load 30 N and speed 382 rpm).

Sl. no	Fe_3O_4 reinforcement % in Al7075	Wt. loss (g)	Specific wear rate (m^3/N-m)
1	0%	0.0114	1.01E-14
2	2%	0.0143	1.14E-14
3	4%	0.0137	1.09E-14
4	6%	0.0125	9.82E-15
5	8%	0.011	8.60E-15
6	10%	0.0103	7.99E-15

The hardness of Al-7075 alloy and Al-based MMCs reinforced with varying wt% Fe_3O_4 is shown in Table 2. When compared to the original Al-7075 alloy, the change in hardness in percentage is high for the Fe_3O_4 reinforcement of 10% weight and lowest for the Fe_3O_4 reinforcement of 2% weight, with a value of 38.846% for the Fe_3O_4 reinforcement of 10% weight.

It is due to the fact that red mud has a higher hardness than Al-7075 alloy. The composite's hardness is determined by the hardness of the reinforcing particles and the matrix. Since the coefficient of thermal expansion of ceramic particles is lower than that of Al alloy, during the solidification process, an extensive number of dislocations are developed at the particle–matrix interface; this improves the matrix hardness even further.

The more the particle-matrix interface, more the dislocations hardens the material. Contact there is the more dislocations harden the material. When compared to bigger particle reinforced composites with the same volume of Al reinforcement, smaller ceramic particle reinforced composites have more particle–matrix interactions. Even as a result, as the particle size decreases and the volume fraction grows, the composite hardness rises.

3.2. Tensile test

Three tests were done, with the best results being averaged. For Al-7075 alloy, Al-7075-2%, 4%, 6%, 8% and 10%wt, various tensile characteristics and % elongation were investigated.

The yield strength of the Al-7075/Fe_3O_4 composite with various reinforcing percentages was tested and recorded using universal testing equipment. The yield strength of the Al-7075/ Fe_3O_4 composites was compared to the yield strength of pure aluminium alloy, and the findings are graphically shown in Figure 3.

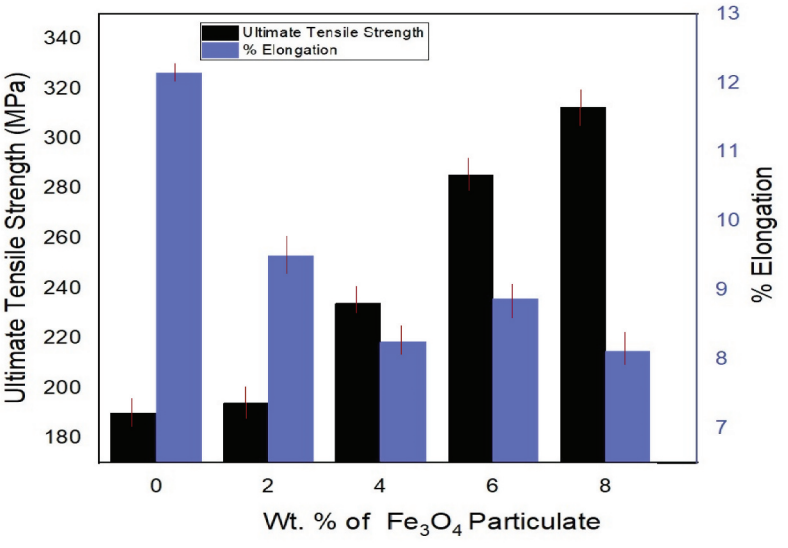

Figure 3. Ultimate tensile strength and yield strength of Al Fe_20_3.

As the percentage of reinforcement in the aluminium alloy rises, the composite's yield strength increases.

The percentage change in the yield strength of the composite when compared to the original aluminium alloy is seen to be highest at a percentage of 144.609% for 10% Fe_3O_4 reinforcement and the lowest is seen at a percentage of 36.240% for 2% Fe_3O_4 reinforcement. The change in yield strength is seen to be highest at a value of 40.744% for an increase in reinforcement percentage from 2% to 4% and the lowest at a value of 6.381% being for an increase in reinforcement percentage from 4% to 6%.

The Ultimate Tensile strength of the composite is directly proportional to the percentage of reinforcement in the aluminium alloy. The percentage change in the Ultimate Tensile Strength of the composite when compared to the original aluminium alloy is seen to be highest at a percentage of 73.737% for 10% Fe_3O_4 reinforcement and the lowest is seen at a percentage of 2.102% for 2% Fe_3O_4 reinforcement. The change in Ultimate Tensile Strength is seen to be the highest at a value of 21.865% for an increase in reinforcement percentage from 4% to 6% and the lowest at a value of 2.102% being for an increase in reinforcement percentage from 0% to 2%.

However, the tensile strength of the friction stir-treated aluminium composite alloy with Fe_3O_4 reinforcement was significantly improved. Despite the presence of Fe particles, stirring causes mechanical rupture of intrinsic grain boundaries, resulting in the development of high angle grain boundaries. The free movement of grain will be restricted by these high-angle grain boundaries. These high-angle grain boundaries prevent dislocations from moving freely, increasing the strength and hardness of surface composites.

Higher elastic modulus, macroscopic yield, and tensile strength were reported with increasing reinforcement volume percentage, however reduced ductility was detected. As the volume fraction increases, more loads are transmitted to the reinforcement,

resulting in a higher ultimate tensile strength. The work hardening rate increases as the volume percentage of reinforcement increases (while the matrix volume decreases) [25].

Individually greater hardness of Fe particles and the Orowan process could cause an increase in hardness. This process describes how dislocations interact with non-shearable Fe particles. It was observed that the addition of iron oxide reinforced particles, which act as a barrier to dislocations, enhanced the tensile strength and hardness. Dislocations make paths and reroute the particles which act as barriers to the movement of dislocations. This increases the composite layer's strength and hardness on the surface.

3.3. Micro structural observation of different Al-7075/Fe_3O_4 composite specimens

EDX spectra and SEM images of all prepared samples are shown in Figure 4(a-j). The atomic percentages of the elements within the samples were calculated by the spectrometer software.

Apart from aluminium atomic percentage as a major share, additional atomic percentages of elements such as Mg, Cu, Si, Zn and O were detected in the spectra. .In 10% wt, 8% wt, 6% wt, 4% wt and 2% wt Fe_3O_4 reinforced Al-7075Alloy, the Fe element atomic percentages were 1.37%, 0.79%, 0.46%, 0.88% and 0.62%, respectively.

The decrease in wear rate with distance is due to surface cover and clogging, as well as mechanical hardening caused by longer distances associated with high normal load and sliding speed. Wear is greatly reduced when iron ore content is included (results shown in Table 3). This is supported by the amount of wear seen in aluminium 7075 and composites containing 2%, 4%, 6%, 8% and 10% Fe_3O_4. Because of the presence of hard iron particles, the total bulk hardness will rise.

Sahin [26] used pin-on-disc tests and Al2O3 and SiC emery paper as counterparts with different particle sizes to investigate the wear behaviour of SiC particles reinforcing aluminium composites, finding that composites have higher wear resistance than the matrix when the normal load, particle size of the emery paper, or test distance increase. This study also revealed a similar trend in wear resistance.

Miyajima et al. [27] investigated the wear behaviour of composites composed of aluminium alloys and reinforced with various types of alumina and silicon carbide (particles, fibres, and whiskers). It was reported that the geometry of the reinforcement and the volume introduced to the matrix had a significant impact on the wear behaviour of composites.

They also revealed the optimal quantity of reinforcements for whiskers, fibres and particles, 22, 10, and 2 vol.%, respectively, despite the fact that in the case of particles, there was a modest drop in wear rate between 2 and 10 vol.% of reinforcement. Investigators reached the conclusion that particle reinforcements perform better than fibres and whiskers.

A similar trend is observed in the current study, and wear rate reduced with reinforcement content in the matrix.

The type, nature, shape, and size of reinforcements are significant elements in the wear performance of Al MMCs, accordingly they must be specifically selected. According to a study on the wear behaviour of Al2 composites [28] the Iron oxide

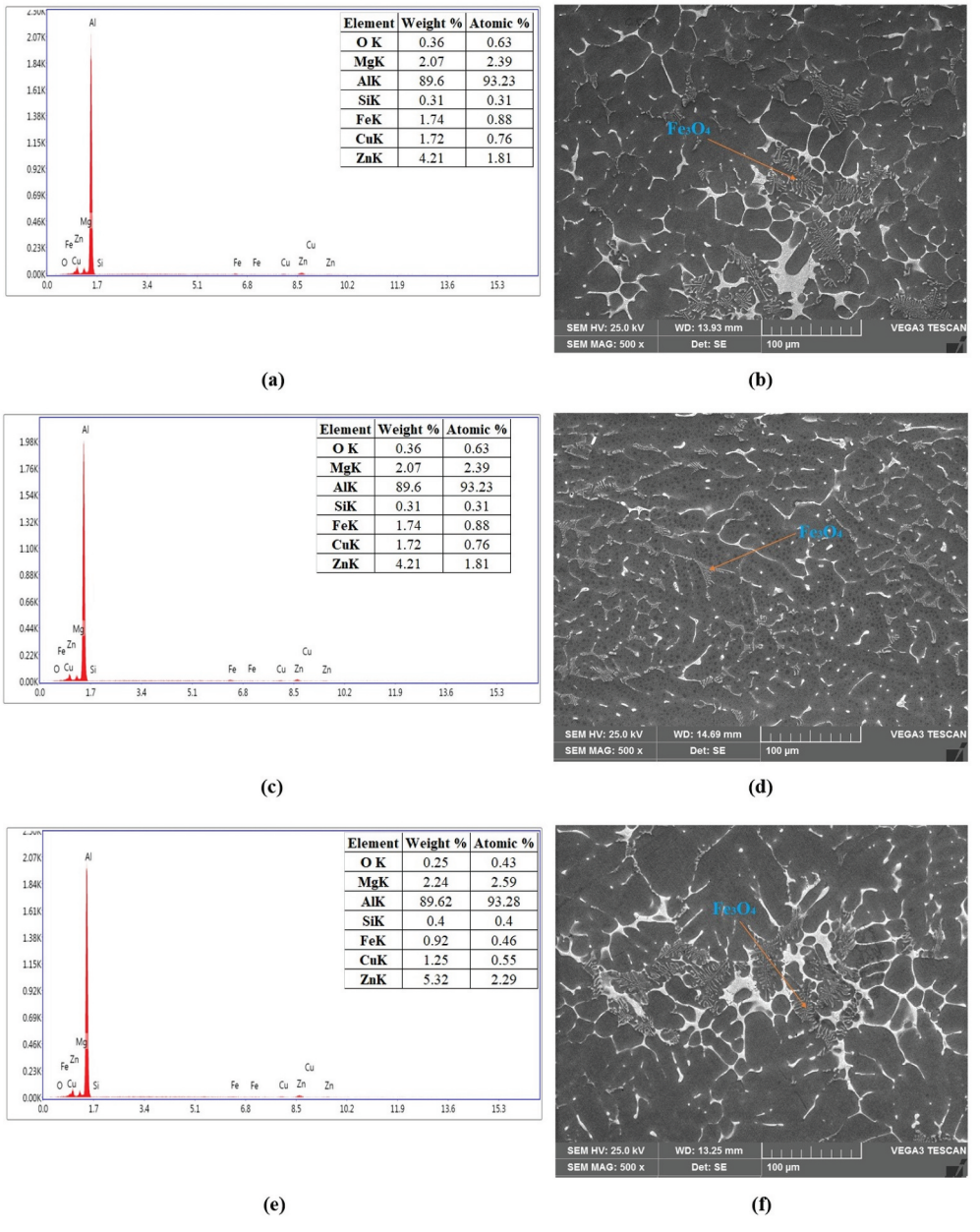

Figure 4. EDS spectra and SEM image of composite sample with (a,b) Al-7075-2% wt Fe_3O_4, (c,d) Al-7075-4%wt Fe_3O_4, (e,f) Al-7075-6%wt Fe_3O_4, (g,h) Al-7075-8%wt $Fe3O_4$ and (i,j) Al-7075-10%wt Fe_3O_4.

reinforced aluminium matrix composite exhibited superior wear resistance, most likely owing to the action of the iron particle reinforcements that were present. The particles presented significant resistance to the abrasive micro-cutting of the composite, resulting in a reduction in the rate at which material was pulled from the composite surface.

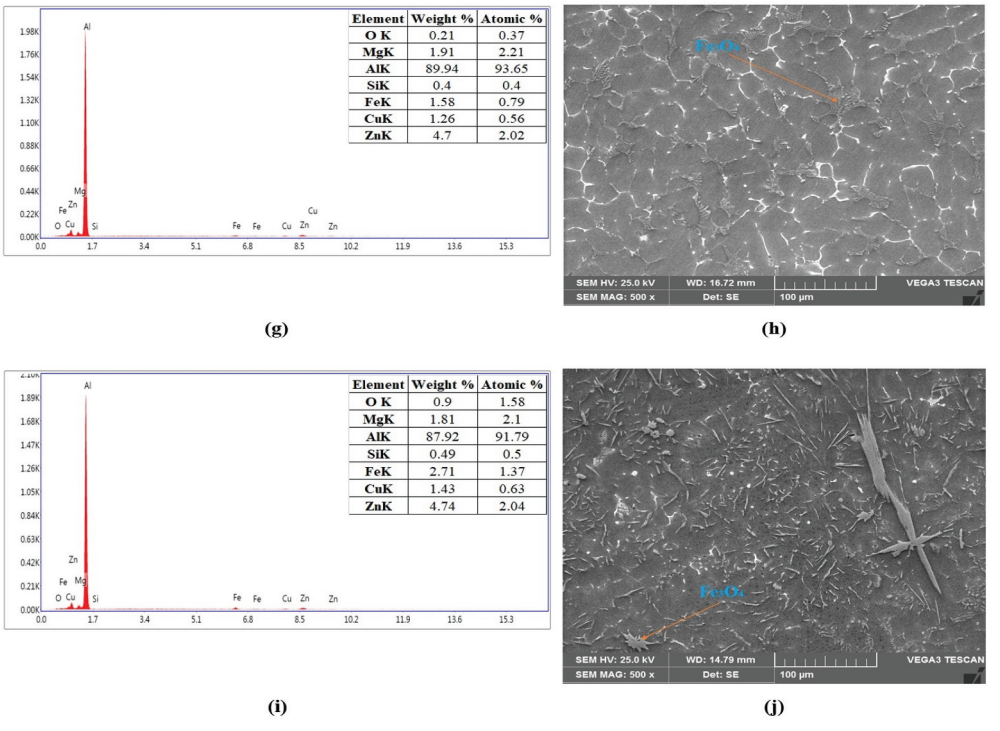

Figure 4. (Continued).

It is evident from the SEM image shown in Figure 4(a-f), in the early stages of wear, that the reinforced particles serve as load bearing components as well as resistors of plastic deformation and matrix material adherence. The worn particles get displaced from their matrix locations and mixed with the wear debris as the wear regime progresses.

The wear debris from the surface, which contains matrix material, worn particles, and iron, is forced into the craters created by particle dislodging and acts as load bearing elements.

3.4. Scanning electron microscopy

Tensile fractured surfaces are subjected to a fractography study using scanning electron microscope. Figure 5 shows the formation of spherical dimples and ridges along the cutting surface causes a ductile fracture in pure Al7075 alloy. The failure mechanism is shown to be ductile with the existence of ridges and voids owing to elastic deformation along the surface after the addition of 2 wt% iron oxide to the matrix. An increase in the amount of reinforcement reduces the presence of dimples and voids, resulting in less elastic deformation. The particle protrusion shown here might be owing to the interfacial toughening process. The figure represents the production of micro cracks as the proportion of iron oxide increases (8 wt%). This increase in Fe particles has resulted in particle

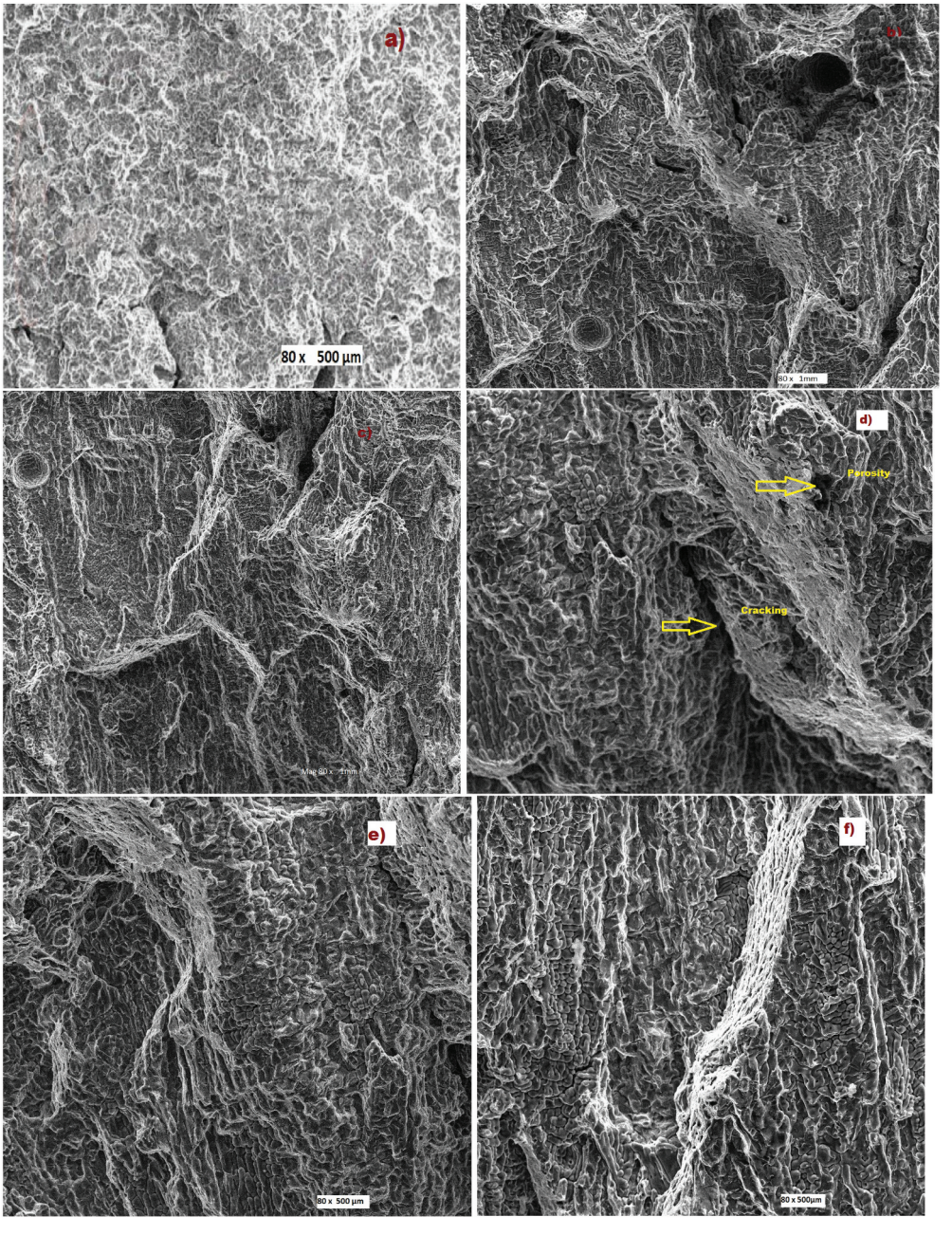

Figure 5. SEM micrographs of tensile fractured surface of the aluminium 7075-Fe_3o_4 composite sample with: (a)Al-7075, (b) Al-7075-2% Fe_3O_4, (c) Al-7075-4% Fe_3O_4, (d) Al-7075-6%Fe_3O_4, (e) Al-7075-8%Fe_3O_4 and (f) Al-7075-10%Fe_3O_4.

de-bonding at the contact. Further addition of Fe particles to 10% wt indicated crack development and particle breakage over the surface, indicating a brittle mechanism of failure.

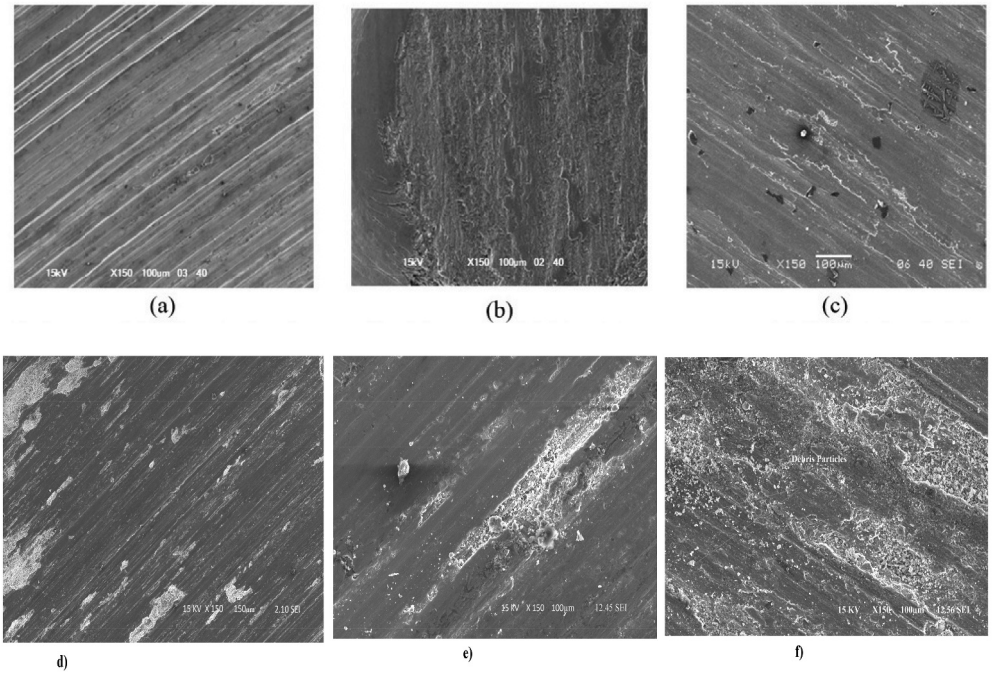

Figure 6. SEM micrographs of worn surface of the aluminium 7075-Fe_3O_4 composite sample with (a) Al-7075, (b) Al-7075-2% Fe_3O_4, (c) Al-7075-4% Fe_3O_4, (d) Al-7075-6%Fe_3O_4, (e) Al-7075-8%$Fe3O_4$, and (f) Al-7075-10%Fe_3O_4.

Under optical and scanning electron microscopy, the worn surfaces of Al-7075 with Fe_3O_4 composites reveal (shown in Figure 6) that at lower loads, the worn surface has less ploughing and cutting, as presented in the figure. However, fragmented particles are commonly found on the worn surface under elevated loads and sliding velocities.

The analysis of wear tracks at various applied loads and sliding velocities reveals fragmented Fe oxide particles on wear tracks, deep grooves, and surface delamination. The wear rate was shown to decrease steadily as the composite hardness increased.

The results clearly show that force builds up on the sliding surface and subsurface level, causing plastic deformation and the creation and propagation of microcracks, which eventually leads to wear failure and material loss at the interface.

The type, nature, shape, and size of reinforcements are significant elements in the wear performance of Al MMCs, accordingly they must be specifically selected. According to a study on the wear behaviour of Al2 composites [28] the Iron oxide reinforced aluminium matrix composite exhibited superior wear resistance, most likely owing to the action of the iron particle reinforcements that were present. The particles presented significant resistance to the abrasive's micro cutting of the composite, resulting in a reduction in the rate at which material was pulled from the composite surface. Changes in friction coefficient values can be linked to changes in wear morphology and oxidation extent. These findings are consistent with those of Kim et al. [29]. In fact,

they demonstrated the role of oxygen in the evolution of wear morphology. Furthermore, Yerokhin et al. [30] attribute this discovery to the transition from the wear mechanism of the steel/aluminium couple (ductile) to that of an oxide film (brittle) formed by oxidation, which reduces the friction coefficient.

Wear debris is produced by the material during wear testing attributable to sliding action. If the stress created in the material during sliding motion exceeds the fracture stress of the particles, the load-bearing capacity of the material is affected. The pin surface is subjected to significant plastic stresses due to the aluminium matrix's direct contact with the counter face. Cracks occur as a result of this. Debris formation is further enabled by delamination of the wear surfaces.

4. Conclusion

The following conclusions may be drawn from this work

1. By using the stir casting process, Fe_3O_4 up to 10% by weight may be effectively added to aluminium to form composites that can be die cast.

2. The interaction between the Fe_3O_4 and the aluminium is significant, resulting in finer particles of various oxides.

3. The Fe_3O_4 particle reinforced aluminium matrix composites improved the tensile strength and hardness of the composite.

4. Increased reinforcing has the effect of increasing wear resistance and decreasing coefficient of friction in metal matrix composites.

5. The metal matrix composites have a higher wear resistance due to their greater load bearing capacity, which results in a significant increase in the composite's strength and hardness.

Acknowledgments

The authors wish to appreciate Visvesvaraya Technological University, Belagavi, Ballari Institute of Technology and Management, Ballari and Sai Vidya institute of Technology for their support.

Disclosure statement

No potential conflict of interest was reported by the author(s).

Funding

The authors have no funding to report.

ORCID

Raghavendra Subramanya http://orcid.org/0000-0003-4276-9638

References

[1] Smith WF, Hashemi J. Materials science and engineering. New Delhi Press: Tata Mc Graw Hill Education Private Limited; 2008.

[2] Dayanand S, Satish Babu B, Auradi V. Experimental investigations on microstructural and dry sliding wear behavior of Al-AlB2 metal matrix composites. Mater Today Proc. 2018;5 (10, Part 3):22536–22542.

[3] Sijo MT, Jayadevan KR. Analysis of stir cast aluminium silicon carbide metal matrix composite: a comprehensive review. Procedia Technol. 2016;24:379–385.

[4] Gargatte S, Upadhye R, Dandagi V, et al. Preparation & characterization of Al-5083 alloy composites. J Miner Mater Charact Eng. 2013;1(1):8–14.

[5] Fenghong C, Chang C, Zhenyu W, et al. Effects of silicon carbide and tungsten carbide in aluminium metal matrix composites. Silicon. 2019;11(6):2625–2632].

[6] B.zhang J, Yang S, Chen Z, et al. Graphene encapsulated SiC nanoparticles as tribology-favoured nanofillers in aluminium composite. Compos B Eng. 2019;162:445–453].

[7] Bayraktar E, Katundi D. Development of a new aluminium matrix composite reinforced with iron oxide (Fe3O4. J Achieve Mater Manuf Eng. 2010;38(1):7–14.

[8] Zićbowicz B, Szewieczek D, Dobrzaěski LA. New possibilities of application of composite materials with soft magnetic properties. J Achieve Mater Manuf Eng. 2007;20:207–210.

[9] Sarraf M, Dabbagh A, Abdul Razak B, et al. Noor Hayaty Abu Kasim, Hadijah Abdullah, Nazatul Liana Sukiman, highly-ordered TiO_2 nanotubes decorated with Ag_2O nanoparticles for improved bio functionality of Ti6Al4V. Surf Coat Technol. 2018;349:1008–1017.

[10] Jamaluddin H, Achuta Kini U, Sharma SS. Mechanical characterisation of stir cast aluminium 7075 matrix reinforced with grey cast iron & fly ash " International Journal of Mechanical and Production Engineering (IJMPE).2016;4(6):127–132.

[11] Mahmoud ERI, Tash MM. Characterization of aluminum-based-surface matrix composites with iron and iron oxide fabricated by friction stir processing. Materials. 2016;9(7):505.

[12] Ridvan G, Yurekturk Y, Tekoglu E, et al. Improving wear resistance of 304 stainless steel reinforced AA7075 aluminum matrix composite by micro-arc oxidation. Surf Coat Technol. 2019;368:15–24.

[13] S.M. Sivagami, M. Meignanamoorthy, T. Raja Vijay, K. Punitharani, M. Ravichandran. Effect of iron oxide and graphite reinforcement on mechanical properties of AA7075 hybrid composite. Materials Today: Proceedings. 2020;10.1016/j.matpr.2020.10.863

[14] Gopalakrishnan S, Murugan N. Production and wear characterisation of AA 6061 matrix titanium carbide particulate reinforced composite by enhanced stir casting method. Compos Part B Eng. 2012;43(2):302–308.

[15] Singla M, Dwivedi DD, Singh L, et al. Development of aluminium based silicon carbide particulate metal matrix composite. J Miner Mater Charact Eng. 2009;8(6):455–467.

[16] Taherzadeh Mousavian R, Azari Khosroshahi R, Yazdani S, et al. Fabrication of aluminum matrix composites reinforced with nano to micrometer-sized SiC particles. Mater Des. 2016;89:58–70.

[17] Ezatpour HR, Torabi-Parizi M, Sajjadi SA. Microstructure and mechanical properties of extruded Al/Al2O3 composites fabricated by stir-casting process. Trans Nonferrous Met Soc China. 2013;23(5):1262–1268.

[18] Shorowordi KM, Laoui T, Haseeb ASMA, et al. Microstructure and interface characteristics of B4C, SiC and Al2O3 reinforced Al matrix composites: a comparative study. J Mater Process Technol. 2003;142(3):738–743.

[19] Baradeswaran A, Elaya Perumal A. Influence of B4C on the tribological and mechanical properties of Al 7075-B4C composites. Compos Part B Eng. 2013;54(1):146–152.

[20] Moses JJ, Dinaharan I, Sekhar SJ. Prediction of influence of process parameters on tensile strength of AA6061/TiC aluminum matrix composites produced using stir casting. Trans Nonferrous Met Soc China. 2016;26(6):1498–1511.

[21] Shivakumar SP, Sharan AS, Sadashivappa K. Experimental investigations on vibration properties of aluminium matrix composites reinforced with iron oxide particles. Appl Mech Mater. 2019;895:122–126.
[22] Idusuyi N, Olayinka JI. Dry sliding wear characteristics of aluminium metal matrix composites: a brief overview. J Mater Res Technol. 2019;8(3):3338–3346.
[23] Towhidul Islam Nayim SM, Zahid Hasan M, Prakash Seth P, et al. Effect of CNT and TiC hybrid reinforcement on the micro-mechano-tribo behaviour of aluminium matrix composites. Mater Today Proc. 21(3):1421–1424 2214-7853 doi:10.1016/j.matpr.2019.08.203 2020 .
[24] Sudhakar I, Madhu V, Madhusudhan Reddy G, et al. Enhancement of wear and ballistic resistance of armour grade AA7075 aluminium alloy using friction stir processing. Defence Technol. 2015;11(1):10–17.
[25] Chawla N, Shen Y-L. Mechanical behavior of particle reinforced metal matrix composites. Adv Eng Mater. 2001;3(6):357–370.
[26] Sahin Y. Wear behaviour of aluminium alloy and its composites reinforced by SiC particles using statistical analysis. Mater Des. 2003;24(2):95–103.
[27] Miyajima T, Iwai Y. Effects of reinforcements on sliding wear behavior of aluminum matrix composites. Wear. 2003;255(1–6):606–616.
[28] Ravindranath VM, Shankar GSS, Basavarajappa S, et al. Dry sliding wear behavior of hybrid aluminum metal matrix composite reinforced with boron carbide and graphite particles. Mater Today Proc. 2017;4(10):11163–11167.
[29] Kim H-J, Emge A, Karthikeyan S, et al. Effects of tribooxidation on sliding behavior of aluminum. Wear. 2005;259(1–6):501–505.
[30] Yerokhin AL, Nie X, Leyland A, et al. Plasma electrolysis for surface engineering. Surf Coat Technol. 1999;122(2–3):73–93.

“Rolling regression technique and cross-sectional regression: A tool to analyze Capital Asset Pricing Model”

AUTHORS	Soumya Shetty Janet Jyothi Dsouza Iqbal Thonse Hawaldar

ARTICLE INFO	Soumya Shetty, Janet Jyothi Dsouza and Iqbal Thonse Hawaldar (2021). Rolling regression technique and cross-sectional regression: A tool to analyze Capital Asset Pricing Model. *Investment Management and Financial Innovations*, *18*(4), 241-251. doi:10.21511/imfi.18(4).2021.21
DOI	http://dx.doi.org/10.21511/imfi.18(4).2021.21
RELEASED ON	Thursday, 25 November 2021
RECEIVED ON	Wednesday, 01 September 2021
ACCEPTED ON	Thursday, 18 November 2021
LICENSE	This work is licensed under a Creative Commons Attribution 4.0 International License
JOURNAL	"Investment Management and Financial Innovations"
ISSN PRINT	1810-4967
ISSN ONLINE	1812-9358
PUBLISHER	LLC “Consulting Publishing Company “Business Perspectives”
FOUNDER	LLC “Consulting Publishing Company “Business Perspectives”

NUMBER OF REFERENCES	NUMBER OF FIGURES	NUMBER OF TABLES
50	1	5

BUSINESS PERSPECTIVES

LLC "CPC "Business Perspectives"
Hryhorii Skovoroda lane, 10,
Sumy, 40022, Ukraine

www.businessperspectives.org

Soumya Shetty (India), **Janet Jyothi Dsouza** (India), **Iqbal Thonse Hawaldar** (Bahrain)

ROLLING REGRESSION TECHNIQUE AND CROSS-SECTIONAL REGRESSION: A TOOL TO ANALYZE CAPITAL ASSET PRICING MODEL

Abstract

The Capital Asset Pricing Model (henceforth, CAPM) is considered an extensively used technique to approximate asset pricing in the field of finance. The CAPM holds the power to explicate stock movements by means of its sole factor that is beta co-efficient. This study focuses on the application of rolling regression and cross-sectional regression techniques on Indian BSE 30 stocks. The study examines the risk-return analysis by using this modern technique. The applicability of these techniques is being viewed in changing business environments. These techniques help to find the effect of selected variables on average stock returns. A rolling regression study rolls the data for changing the windows for every 3-month period for three years. The study modifies the model with and without intercept values. This has been applied to the monthly prices of 30 BSE stocks. The study period is from January 2009 to December 2018. The study revealed that beta is a good predictor for analyzing stock returns, but not the intercept values in the developed model. On the other hand, applying cross-section regression accepts the null hypothesis. α, β, $\beta 2 \neq 0$. Therefore, a researcher is faced with the task of finding limitations of each methodology and bringing the best output in the model.

Keywords investments, asset pricing, portfolio choice, rolling regression, finance

JEL Classification E22, G12, G11, C32, F65

Received on: 1st of September, 2021
Accepted on: 18th of November, 2021
Published on: 25th of November, 2021

Soumya Shetty, MBA, Research Scholar, Ballari Institute of Technology and Management, India.

Janet Jyothi Dsouza, Ph.D., Associate Professor, Finance Faculty, Ballari Institute of Technology and Management, India.

Iqbal Thonse Hawaldar, Ph.D., Professor, Department of Accounting and Finance, College of Business Administration, Kingdom University, Bahrain. (Corresponding author)

Conflict of interest statement:
Author(s) reported no conflict of interest

INTRODUCTION

CAPM plays an important role in the field of finance. This model has been more often used to know the cost of equity capital. The model strongly believes in a direct relationship between beta and stock return based on market returns (Kumar et al., 2018; Bolar et al., 2017). The theory states that beta is always proportional to gain an extra premium in a given market. CAPM has been around since 1964, and the person behind upholding the theory is William Sharpe. Gradually this theory has been developed by Lintner (1965) and Black et al. (1972). An extension of this model was made possible by a principle given by Markowitz (1952) in his modern portfolio theory. Later, the year criticism emerged in different backgrounds by researchers such as Banz (1981) who favored size effect on stock returns; the Fama-French three-factor model stated beta remained flat for the stock of higher returns (Fama & French, 1992), Arbitrage theory, Multi-factor model (Fama & French, 1996) and so on. Black (1993) raised an argument against Banz (1981) stating that the size effect was not able to agree with the viewpoints of the CAPM theory. Black (1993) found that the limitation of CAPM was wrongly misinterpreted. He found that data mining needs to be applied to prove the CAPM. Gradually, many more theories appeared with their strong viewpoints saying the beta alone cannot be the deciding factor for stock price movements, rather

there are many more factors that need to be considered. Most of previous works experimented on economically advanced countries (Iqbal et al., 2007; Kumar et al., 2020). Some theories like the three-factor model (Fama & French, 1993) considered value premium, size factors along with beta factors, multifactor model (Fama & French, 1996), new anomalies on CAPM (Fama & French, 2008). This study's purpose is to apply a rolling regression technique and cross-sectional regressions to check the soundness of the CAPM model in the framework of the Indian stock market for the present scenario. The study aims to analyze the risk-return analysis of the CAPM model for the study period 2009 to 2018. The study answers the question of does beta still hold the power to predict the variability of stock returns. The rolling regression application gives an understanding of mean-variance efficiency employing cross-sectional regression techniques. This technique considers two variables such as intercept and beta. By bringing modifications to these parameters, the effectiveness of the models has been examined. The reason for selecting CAPM is that it has not lost its power to explain stock returns, and this has been understood with the supportive statement of many researchers. This study examines CAPM from the latest period point of view in the changing business environment. It has been verified whether the market risk holds good for the present scenario. Nevertheless, from the previous study it is clear that rolling regression can produce most accurate results and a suitable technique to check this single factor model. With the sample size of 30 BSE SENSEX stocks and five portfolios, the study can provide appropriate conclusions to the issue concerned. If the results favor the beta power, one can definitely use it as one of the criteria to choose the security. Meanwhile, applying the present methodology interchangeably makes one prove the strength of the beta coefficient in predicting expected stock returns.

1. LITERATURE REVIEW

There have been many studies examining CAPM in Indian and international contexts. It has been observed that the scarce literature supported the relevance of CAPM in the markets, and some studies sharply criticized this theory. Iqbal (2011) reviewed 36 prominent research publications on the relevance of CAPM on the Indian and international stock market and concluded that there is no conclusive evidence to prove that CAPM is relevant to measuring risk and return. Iqbal (2015) empirically tested CAPM on Bahrain Bourse and concluded that the intercept test of the capital asset pricing model proves the theory, and the beta test goes against the standard theory. Hawaldar (2016) tested the cross-sectional variation in portfolio returns based on a sample of 30 companies listed on Bahrain Bourse and found that the results of the F-test indicate that the regression is not a good fit in the majority of the years of the study. Al-Afeef's (2017) study result proclaims that only 20% ability to make changes in stock returns is due to beta factors, and the remaining portions are because of other governing factors. Bajpai and Sharma (2015) show the support to CAPM in considering beta variables in the constrained model. The traditional model fails to fulfill the belief of CAPM theory. Hasan et al. (2011) reveal that intercept values and unique risks are not consistent as per the CAPM hypothesis, but the security market line (market risk) is in support of the CAPM. Choudhary and Choudhary (2010) disclose that beta has a linear relationship for its risk and return but not residual variance. Diwani and Asgharian (2010) uncover the intercept and slope coefficient are not in the line with significance. The residual variance also shows the non-linearity to stock returns but beta values are consistent with stock returns. Dhankar and Saini (2007) expose contradictory results as it brings consistency in the result of different sub-periods between different portfolio returns and systematic risk but not for the portfolios and price earning ratios. On the whole, this study can justify CAPM expectations. Gursoy and Rejepova (2007) show that the Mac Beth (1973) and Pettengill methodology results in different outcomes. The Pettengill methodology is consistent with the CAPM model, and the Macbeth methodology is not supportive of the CAPM model. Iqbal (2014) and Iqbal and Brooks (2007) conclude that the beta can explain changes in stock returns. Ansari (2000) has strongly upheld CAPM on the ground that parameter selection made by different authors is the reason for concluding the paper was unsupportive to the CAPM model. He found a deficiency in their asset pricing theories in terms of sample selection, methodology application, analysis mismatch, and

http://dx.doi.org/10.21511/imfi.18(4).2021.21

market proxy selection. He also found that the sample selection bias fails to understand human behavior and psychology. This study understood that the expected return for the stock is possible because of covariance between stocks and the market index. Andor et al. (1999) demonstrate partial consistent results related to the CAPM model. This is because beta does not show a higher percentage in explaining stock returns and r^2 is only to the extent of 15%-20%. Fletcher (1997) announces a significant risk-return relationship under conditional approaches but not in the case of unconditional approaches. The whole study emphasizes power of beta in stock returns. Isakov (1999) (the residual risk (unique risk)) shows the negative results on average returns of the stocks. The study concluded that beta maintained its power on return on portfolios. Black (1993) emphasized that rational investors consider systematic risk in their investment decisions to estimate positive stock returns. He focused on data mining issues of authors to disprove the CAPM theory. Lau (1974) claims that in the Japanese stock market, CAPM holds under the time series regression model, as well as the cross-sectional regression model. Black et al. (1972) justified a linear relationship between risk and return in sample data. The study also found the prominence of beta in deciding asset pricing. Jensen (1968), in the study of beta stability, found out that mutual fund stocks are more stable than stock returns. Lintner (1965) examined the correlation between diversification in investment with different parameters such as security prices, degree of risk, and stock gains. The study interprets that common stocks are risky investments, and there is an indirect relationship between risk and different considered parameters. Sharpe (1964) revealed that the activeness in the economic activity expected returns of efficient combinations shows perfect correlation in the results. Markowitz (1952) revealed that an investor's judgemental behavior, as well as rational thinking and action, reflects favorable results in stock returns and variance.

Zhou et al. (2018) found no significant relationship between risk and return in both test methodologies. Shaikh et al. (2017) proved that for the chosen sample, CAPM does not show any relevant results. Bhatnagar and Indies (2013), in justifying only the three-factor model of 2006, show superior and achievable results as compared to CAPM that fails to meet the linearity in the return and value premium relationship for the United Kingdom Stocks. Hanif and Bhatti (2010) used sample data of 360 stocks and found that only 28 observed results were consistent with CAPM principles, while the rest were not. Therefore, the study does not accept the CAPM model as the right model to predict the required rate of return. Olakojo and Ajide (2010) experimented with ARCH tests that do not show consistency with the CAPM theory. The study found that residual risk also does not show any linearity between risk and return for different stocks. Amihud et al. (1992) have proved that beta is a good predictor to estimate expected stock returns. Theriou et al. (2010) show that the conditional approach and unconditional approach will not result in a positive risk and return relationship. Fama and French (2006) concluded a positive relationship between beta and value premium for the 1926 to 1963 study period and not for the study period of 1963 to 2004. There is non-linearity between beta and stock returns for the study period 1926 to 2004. Bartholdy and Peare (2005) inform that the CAPM model and the Fama-French three-factor model are not good to use for the estimation of stock returns because CAPM finds only 3% variation in the return, whereas 5% in the case of the FF three-factor model. Fama and French (1996) examined anomalies in the CAPM. The study results support the theory of ICAPM and arbitrage pricing theories. Fama and French (1995) state that only the market index and size factor can predict stock returns positively but not market-to-book value. The market-to-book value shows negative results to stock returns. Berk (1995) theoretically justified that there is always an inverse relationship between the size and risk of any stock. This brings changes in average stock returns. Fama and French (1992) examined cross-sectional expected returns in considering three factors such as beta, size, and value premium. The study stated that beta remained flat for the stock of higher returns, and size and market-to-book ratios have direct relations to stock returns. Wong and Tan's (1991) study results are not consistent with the theory of CAPM. The study found negative and weak results for the CAPM by using variables like beta, beta square, unsystematic risk, total risks, and skewness. Fama and French (1993) in their study emphasize that five risk factors have a direct influence on the returns of stocks and bonds.

http://dx.doi.org/10.21511/imfi.18(4).2021.21

2. OBJECTIVES OF THE STUDY

This study aims to find the applicability of the CAPM for the present scenario for the study period 2009 to 2018, using two analytical tools such as rolling regression analysis and cross-sectional regression.

3. HYPOTHESES OF THE STUDY

H_{01}: *There is no relationship between risk and return of stocks under the rolling regression technique.*

$$H_{01} = \alpha \neq 0,$$

$$H_{01} = \beta \neq 0.$$

H_{02}: *There is no relationship between market risk and its variance to the average stock returns under cross section regression method.*

$$H_{02} = \beta \neq 0,$$

$$H_{02} = \beta^2 \neq 0.$$

4. DATA AND METHODOLOGY

4.1. Data

The data for the study is taken from the BSE website. The sample size is 30 BSE Sensex stocks. The BSE Sensex index is taken as a market benchmark to understand the relationship between risk and return. The risk-free rate of return is taken from the RBI bulletin. The study considered the implicit yield of 91-day treasury bills at the cut-off price. The study period commences from January 2009 to December 2018. This 10-year study considers monthly stock prices of each stock for the test period. The finding of beta is done using the first-stage regression.

To ensure the stability of stock prices, stock returns are determined using log-returns each month for ten years for all the stocks. This is as follows:

$$R_i = \ln \frac{P_t}{P_{t-1}}, \quad (1)$$

where R_i – the return of each stock, $\ln$ – log returns of the stocks, P_t – current month price of the stocks, and P_{t-1} – previous month price of the stocks.

4.2. Methodology

The capital asset pricing model is tested using two stages of regression. In the first stage regression, each stock returns R_i are regressed for market returns R_M. With this, α and β can arrive. The equation for the first stage regression is as follows:

$$R_{it} = \alpha_i + \beta_i R_{mt} + E_{it}, \quad (2)$$

where R_{it} – return of each stock for the time period, α_i – intercept value of the stock, β_i – slope coefficient excess of market risk premium, R_M – return of the market, and E_{it} – error term.

In the second stage, the regression market risk premium is calculated using the following equation:

$$\left[E\left(R_{it} - R_{ft}\right)\right] = \beta_{im}\left[E\left(R_{mt} - R_{ft}\right)\right]. \quad (3)$$

where R_{ft} – risk free rate of return, $\left[E\left(R_{it} - R_{ft}\right)\right]$ – expected average rate of return, $E\left(R_{mt}\right)$ – average expected market return, and β_{im} – market risk premium for each stock reach portfolios.

β_{im} – can be calculated with the slope function or by applying the following formula:

$$\beta_i = \frac{Cov\left(r_i \cdot r_m\right)}{\sigma^2\left(r_m\right)}. \quad (4)$$

The CAPM is tested using a rolling regression model. The rolling regression model gives an accurate picture of the validity of the CAPM model. To do this, data were divided into 29 sub-periods. Here three-year rolling regression was formed by moving windows every three months. This is done for the entire ten years of study periods. There are 29 sub-periods. The data are overlapping from current to previous sub-periods. Each sub-period includes 30 stocks for three years. The Capital Asset Pricing Model is applied to the portfolio. A total of 30 stocks are taken for the study, six portfolios can be formed. Each portfolio includes five stocks. This avoids the diversifiable risk factor. The portfolios are grouped based on the beta values of the stocks. A stock that has higher beta values is

http://dx.doi.org/10.21511/imfi.18(4).2021.21

categorized as the first portfolio against least portfolios that have smaller beta values.

The sample has been tested using a two-stage regression model. This is done by modifying the intercept values. In the first case of application of the cross-sectional regression model, intercept values are considered, and to find the significance of the CAPM, the intercept value has to be zero. In the second case of the application, the intercept values will not be considered. The soundness of CAPM is verified using the regression slope co-efficient (β), *F*-statistics, and explanation power of market index on stock returns (r^2). This helps to know whether the application of these two methods makes any significant difference in the results or not.

5. RESULTS AND DISCUSSION

To examine the relevance of the CAPM model, two-stage regressions were applied for each sub-period for each of the portfolios. In the first case, intercept values were considered. The results of each portfolio for different sub-periods are as follows.

5.1. Rolling regression results for different sub-periods with an intercept

$$\left[E\left(R_p - R_f\right)\right] = \alpha_p + \beta_p\left[E\left(R_m - R_f\right)\right]. \quad (5)$$

Table 1 presents the results of rolling regression when the regression model has an intercept. The intercept values of all the sub-periods stand the negative figure, which indicates that intercept values are significant, and this does not show any constant return. This is not aligning with the CAPM theory. To accept the CAPM model, the intercept value has to be zero, which has to be statistically insignificant. This shows the occurrence of the abnormal return due to some external unknown fac-

Table 1. The results of rolling regressions for different sub-periods in consideration of an intercept

No	Sub-period	Beta	*p*-values	intercept	*p*-values	Adj. r^2	*f* value	*p*-values	*t*-values
1	Jan 09 to Dec 11	1.081	0.001	–0.007	0.391	0.571	71.891	0.001	7.757
2	April 09 to March 12	1.103	0.001	–0.006	0.392	0.573	72.571	0.001	7.841
3	July 09 to June 12	1.045	0.000	–0.007	0.393	0.470	45.103	0.000	6.180
4	Oct 09 to Sep 12	1.021	0.002	–0.009	0.360	0.442	39.823	0.002	5.798
5	Jan 10 to Dec 12	1.042	0.002	–0.010	0.341	0.440	42.085	0.002	5.872
6	April 10 to March 13	1.071	0.002	–0.010	0.376	0.442	42.435	0.002	5.895
7	July 10 to June 13	1.085	0.002	–0.011	0.341	0.444	45.420	0.002	6.021
8	Oct 10 to Sep 13	1.158	0.002	–0.012	0.370	0.460	41.264	0.002	5.968
9	Jan 11 to Dec 13	1.170	0.000	–0.009	1.052	0.511	47.902	0.000	6.032
10	April 11 to March 14	1.207	0.002	–0.008	0.540	0.484	43.931	0.002	6.223
11	July 11 to June 14	1.240	0.001	–0.009	0.503	0.506	47.299	0.001	6.495
12	Oct 11 to Sep 14	1.231	0.001	–0.009	0.454	0.505	61.247	0.001	6.994
13	Jan 12 to Dec 14	1.293	0.002	–0.013	0.397	0.357	28.674	0.002	4.822
14	April 12 to March 15	1.328	0.001	–0.016	0.301	0.360	25.647	0.001	4.746
15	July 12 to June 15	1.390	0.001	–0.018	0.197	0.339	21.979	0.001	4.470
16	Oct 12 to Sep 15	1.358	0.001	–0.018	0.159	0.339	21.611	0.001	4.483
17	Jan 13 to Dec 15	1.346	0.001	–0.017	0.168	0.327	20.579	0.001	4.341
18	April 13 to March 16	1.307	0.000	–0.016	0.183	0.380	25.164	0.000	4.849
19	July 13 to June 16	1.302	0.000	–0.016	0.191	0.383	25.100	0.000	4.863
20	Oct 13 to Sep 16	1.317	0.000	–0.014	0.203	0.431	32.115	0.000	5.438
21	Jan 14 to Dec 16	1.289	0.000	–0.014	0.213	0.414	30.216	0.000	5.255
22	April 14 to March 17	1.283	0.000	–0.013	0.231	0.421	30.744	0.000	5.315
23	July 14 to June 17	1.229	0.001	–0.015	0.185	0.391	28.811	0.001	4.991
24	Oct 14 to sep 17	1.231	0.001	–0.014	0.256	0.399	27.156	0.001	5.034
25	Jan 15 to Dec 17	1.201	0.000	–0.012	0.250	0.442	31.322	0.000	5.469
26	April 15 to March 18	1.083	0.000	–0.010	0.253	0.449	35.044	0.000	5.662
27	July 15 to June 18	1.092	0.000	–0.011	0.184	0.435	31.904	0.000	5.448
28	Oct 15 to Sep 18	1.144	0.000	–0.012	0.155	0.458	35.261	0.000	5.724
29	Jan 16 to Dec 18	1.1153	0.0001	–0.0137	0.133	0.474	37.559	0.000	5.912

tors and this is not within the limit of the sample market index. But the market risk premium shows positive results. This shows the support for the CAPM model. The correlation between market returns and stock returns is quite strong in most of the sub-periods. The maximum $\left(r^2\right)$ (57.29%) arrives in the sub-period 2 (April 09 to March 12) and minimum $\left(r^2\right)$ (32.69%) is in the sub-period 17 (Jan 13 to Dec 15). The value of F-statistics shows significant results for all the sub-periods.

5.2. Rolling regression for different sub-periods without an intercept formula

$$\left[E\left(R_p - R_f\right)\right] = \beta_p\left[E\left(R_m - R_f\right)\right]. \quad (6)$$

Table 2 gives the result of rolling regression without an intercept. If we compare rolling regression with an intercept, this table shows the comparatively lesser performance, but this favors the CAPM model. The adjusted $\left(r^2\right)$ is satisfactory. The maximum $\left(r^2\right)$ (54.73%) is found in the sub-period 2 (April 09 to March 12) and the minimum $\left(r^2\right)$ (29.46 %) is in the sub-period 15 (July 12 to June 15). F-statistics shows the statistically significant result for all the sub-periods except for the sub-period 15 (July 12 to June 15). The market risk premiums show statistically insignificant results for all the sub-periods and are positive outcomes. The study found statistically insignificant differences in the expected returns. The risk component is proportional to stock returns, and risk is within the purview of the market risk coefficient. This study accepts the null hypothesis that beta is zero or there is a positive direct relationship between stock returns and the risk of individual stocks. This study accepts the theory of the CAPM model. The overall study with the techniques of rolling regression says that beta has a positive impact in both cases but not the intercept of the regression model.

Table 2. Rolling regression for different sub-periods without an intercept

No	Sub-periods	Market risk premium	*p*-values	Adj. r^2	*f*-values	*p*-values	*t*-values
1	Jan 09 to Dec 11	1.0683	0.0008	0.5462	72.13	0.0008	7.7610
2	April 09 to March 12	1.0915	0.0008	0.5473	72.74	0.0008	7.8202
3	July 09 to June 12	1.0456	0.0004	0.4494	44.88	0.0004	6.1669
4	Oct 09 to Sep 12	1.0303	0.0013	0.4266	40.28	0.0013	5.8394
5	Jan 10 to Dec 12	1.0538	0.0013	0.4254	42.80	0.0013	5.9237
6	April 10 to March 13	1.0871	0.0013	0.4295	43.69	0.0013	5.9856
7	July 10 to June 13	1.1014	0.0012	0.4311	46.65	0.0012	6.1017
8	Oct 10 to Sep 13	1.1942	0.0015	0.4563	43.81	0.0015	6.1699
9	Jan 11 to Dec.13	1.1908	0.0002	0.5010	50.10	0.0002	6.7086
10	April 11 to March 14	1.2184	0.0013	0.4697	44.96	0.0013	6.3006
11	July 11 to June 14	1.2357	0.0006	0.4840	47.26	0.0006	6.4860
12	Oct 11 to Sep 14	1.2039	0.0009	0.4797	60.60	0.0009	6.9393
13	Jan 12 to Dec 14	1.2234	0.0025	0.3252	25.56	0.0027	4.6863
14	April 12 to March 15	1.2624	0.0009	0.3207	22.22	0.0011	4.4629
15	July 12 to June 15	1.3105	0.0011	0.2946	18.87	0.0428	3.8007
16	Oct 12 to Sep 15	1.3277	0.0005	0.3041	19.45	0.0010	4.2480
17	Jan 13 to Dec 15	1.3291	0.0007	0.2982	19.04	0.0011	4.1939
18	April 13 to March 16	1.2911	0.0003	0.3508	23.92	0.0003	4.7240
19	July 13 to June 16	1.2788	0.0003	0.3493	23.49	0.0003	4.6981
20	Oct 13 to Sep 16	1.2863	0.0001	0.3944	30.30	0.0002	5.2544
21	Jan 14 to Dec 16	1.2872	0.0002	0.3879	29.55	0.0003	5.1816
22	April 14 to March 17	1.2670	0.0003	0.3903	29.63	0.0006	5.1970
23	July 14 to June 17	1.2338	0.0008	0.3668	26.58	0.0014	4.9205
24	Oct 14 to Sep 17	1.2432	0.0001	0.3709	26.22	0.0009	4.9363
25	Jan 15 to Dec 17	1.1978	0.0002	0.3607	29.88	0.0001	5.3272
26	April 15 to March 18	1.0898	0.0002	0.4198	33.99	0.0002	5.5577
27	July 15 to June 18	1.0816	0.0002	0.4035	30.59	0.0002	5.3206
28	Oct 15 to Sep 18	1.1143	0.0002	0.4169	32.28	0.0001	5.4713
29	Jan 16 to Dec 18	1.0853	0.0002	0.4262	33.69	0.0001	5.5856

http://dx.doi.org/10.21511/imfi.18(4).2021.21

6. CROSS-SECTIONAL REGRESSION

The cross-sectional regression is calculated using the following regression model: Equation (3) is applied to estimate the risk coefficient of various variables, which produces the risk-return relationship. To prove the CAPM theory β_i^2, the coefficient should not be different from zero. This gives the output of a positive relationship between risk and return. This has been discussed below:

$$\overline{Rl} = \alpha_0 + \alpha_1\beta_i + \alpha_2\beta_i^2 + \\ +\alpha_3 ur_i + \alpha_4 skw_i + U_i, \quad (7)$$

where $\overline{R}$ – average return of the whole sample, α_0 – the intercept value of the whole sample, β_i – beta coefficient obtained by regressing value of R_i with R_m, β_i^2 – the square of beta, ur_i – unsystematic risk= $\sigma_i^2 - \beta_i^2 \cdot \sigma_m^2$, skw_i – the average skewness of entire sample calculated through descriptive statistics, and U_i – the regression residuals.

The results of ordinary least square regression are arrived at after verifying the residual standard errors across its data sets. If there is not much variance in the standard error of various variables, the results give accurate answers, through this, the right conclusions can be drawn. To check this, two normally distributed diagnostic tests have been applied. These are the heteroscedasticity test and the Jarque-Bera normality test. The results showed that there is no heteroscedasticity in the data sets, and the results of the Jarque-Bera test show the residuals are normally distributed.

6.1. Heteroscedasticity tests

To ensure the accurate results of cross-sectional regression, different risk coefficients must be free from standard errors among the independent factors. To do this, two diagnostic tests have been applied such as heteroscedasticity tests and Jarque-Bera normality tests.

Hypothesis testing

Null hypothesis:There is no heteroscadesity.

Table 3. Heteroskedasticity tests using the Breush-Pagan-Godfrey method

Statistics	Coefficient	Probability	p-values
F-statistic	2.447407	Prob. *F*(4,25)	0.0726
Obs**R*-squared	8.441852	Prob. Chi-Square(4)	0.0767
Scaled explained SS	5.364881	Prob. Chi-Square(4)	0.2519

Table 3 shows the results of heteroscadasticity using the Breusch-Pagan-Godfrey method. The results show that at a 5% significance level, Chi-Square tests support the null hypothesis.

6.2. Jarque-Bera normality tests

Jarque-Bera tests were applied to check whether residual variances are normally distributed or not.

Hypothesis testing

Null hypothesis: Residuals are normally distributed.

Alternative hypothesis: Residuals are not normally distributed.

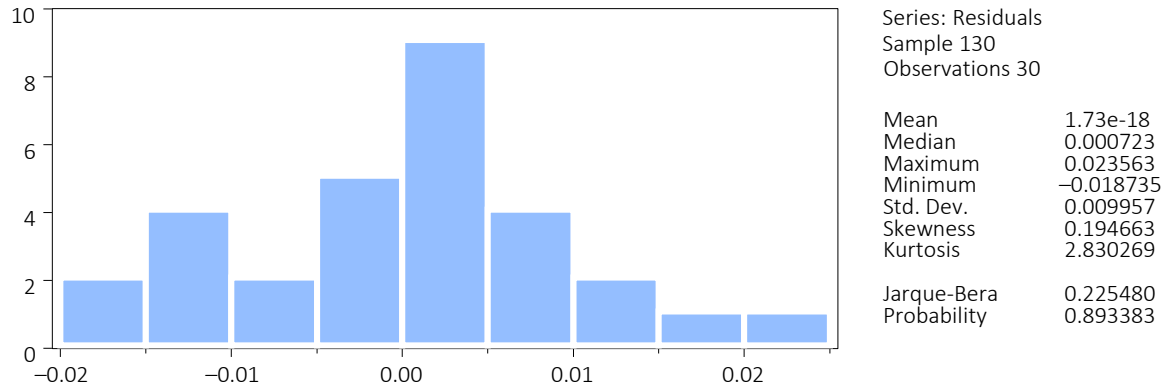

Figure 1. Jarque-Bera normality test

Table 4. Summary statistics of the first stage regression

Statistics	$\overline{R}$	$Avg\beta$	$Avg\beta^2$	$Avg\ ur$	$Avg\ skw$
Average values	0.006	1.12	1.50	0.017	–3.23
Standard deviation	0.01	0.48	1.21	0.01	3.30
Minimum	–0.01	0.31	0.09	0.00	–9.12
Max	0.03	2.22	4.96	0.05	1.17
Median	0.006	1.10	1.21	0.01	–2.99

Table 5. Results of OLS estimates

Statistics	α_0	β_i	β_i^2	ur_i	skw_i
Coefficients	–0.00	0.02	–0.01	0.33	0.00
T-stat	–0.32	1.21	–1.33	1.02	1.78
P-value	0.74	0.23	0.19	0.31	0.08
Ajda square	0.03				
F-value	1.28	0.30			

Figure 1 favors the null hypothesis stating residuals are normally distributed at a 5% significance level. This assures the authenticity of sample data for further research.

6.3. Results and analysis based on the cross-sectional regression method

The first stage regression model is applied to know the beta, alpha and other important variables of BSE 30 stocks. The average values of different variables and descriptive statistics of stocks are shown in Table 4.

Table 4, the first stage regression, gives satisfactory results as average return and beta values show the positivity. As skewness stands in the negative figure, which is –3.2342, this gives the implication that the data sets of average returns are asymmetric. It has been found that data are not normally distributed. The result reveals positive unsystematic risk.

6.4. OLS estimate results

Table 5 shows cross-sectional regression results. The different coefficients are considered to check the relationship between average return and risks. This includes beta, beta square, unsystematic risk and skewness. Thus, the CAPM theory analyzes if there is any positive impact on these different coefficients. But looking at the table, the results reveal that all coefficients are insignificant and do not favor the CAPM model. The adjusted square implies that all these coefficients are not impacted much by the average return of the stocks.

CONCLUSION

The empirical study of the risk-return relationship using cross-sectional regression by taking different risk ratios, as well as rolling regression techniques, shows contradictory results. Rolling regression supports the CAPM model taking into consideration beta factors but not intercept factors. The study shows significant results to intercept values, but beta coefficients support the CAPM theory under the rolling regression method. But in the case of the cross-sectional method, all the tested coefficients show negative values in order to justify the CAPM model. On the whole, this study concludes that under rolling regression techniques, the CAPM perform as expected, but not in the case of cross-sectional regression for the chosen test period. There is no doubt that the beta still holds its power to estimate stock prices. This study also assures that different methodologies can yield different results. This indicates that the choice of an appropriate methodology makes the study supportive or not. Thus, this gives the scope for the future researcher to test the most suitable methodology to conclude the validity of the CAPM.

http://dx.doi.org/10.21511/imfi.18(4).2021.21

AUTHOR CONTRIBUTIONS

Conceptualization: Soumya Shetty, Janet Jyothi Dsouza.
Data curation: Soumya Shetty.
Formal analysis: Soumya Shetty, Janet Jyothi Dsouza.
Funding acquisition: Iqbal Thonse Hawaldar.
Investigation: Janet Jyothi Dsouza.
Methodology: Janet Jyothi Dsouza.
Project administration: Iqbal Thonse Hawaldar.
Validation: Iqbal Thonse Hawaldar.
Writing – original draft: Soumya Shetty, Janet Jyothi Dsouza.
Writing – review & editing: Iqbal Thonse Hawaldar.

REFERENCES

1. Al-Afeef, M. A. M. (2017). Capital Asset Pricing Model, Theory and Practice: Evidence from USA (2009-2016). *International Journal of Business and Management, 12*(8), 182. https://doi.org/10.5539/ijbm.v12n8p182
2. Amihud, Y., Christensen, B. J., & Mendelson, H. (1992). Further Evidence on the Risk-Return Relationship. In *Research paper series*.
3. Andor, G., Ormos, M., & Szabó, B. (1999). Empirical tests of capital asset pricing model (CAPM) in the Hungarian capital market. *Periodica Polytechnica Social and Management Sciences, 7*(1), 47-64.
4. Ansari, V. A. (2000). Capital asset pricing model: Should we stop using it? *Vikalpa, 25*(1), 55-64. https://doi.org/10.1177/0256090920000114
5. Bajpai, S., & Sharma, A. K. (2015). An Empirical Testing of Capital Asset Pricing Model in India. *Procedia – Social and Behavioral Sciences, 189,* 259-265. https://doi.org/10.1016/j.sbspro.2015.03.221
6. Banz, R. W. (1981). The relationship between return and market value of common stocks. *Journal of Financial Economics, 9*(1), 3-18. https://doi.org/10.1016/0304-405X(81)90018-0
7. Bartholdy, J., & Peare, P. (2005). Estimation of expected return: CAPM vs . Fama and French. *International Review of Financial Analysis, 14,* 407-427. https://doi.org/10.1016/j.irfa.2004.10.009
8. Barua, S. K. (1981). The Short-Run Price Behaviour of Securities: Some Evidence on Efficiency of Indian Capital Market. *Vikalpa: The Journal for Decision Makers, 6*(2), 93-100. https://doi.org/10.1177/0256090919810204
9. Basu, S. (2013). Investment Performance of Common Stocks in Relation to Their Price-Earnings Ratios. *The Journal of Finance, 32*(3), 663-682. https://doi.org/10.2307/2326304
10. Berk, J. B. (1995). A Critique of Size-Related Anomolies. *The Review of Financial Studies, 8*(2), 275-286. https://doi.org/10.1093/rfs/8.2.275
11. Bhandari, L. C. (1988). Debt/Equity Ratio and Expected Common Stock Returns: Empirical Evidence. *The Journal of Finance, 43*(2), 507-528. https://doi.org/10.1111/j.1540-6261.1988.tb03952.x
12. Bhatnagar, C. S., & Indies, T. W. (2013). The capital asset pricing model versus the three-factor model: A United Kingdom Perspective. *International Journal of Business and Social Research, 2*(1), 51-65. https://doi.org/10.18533/ijbsr.v2i1.204
13. Black, F. (1993). Beta and Return. *The Journal of Portfolio Management, 20*(1), 8-18. https://doi.org/10.3905/jpm.1993.409462
14. Black, F., Jensen, M. C., & Scholes, M. (1972). The Capital Asset Pricing Model : Some Empirical Tests. *Studies in the Theory of Capital Markets,* 1-54. Retrieved from http://ssrn.com/abstract=908569
15. Choudhary, K., & Choudhary, S. (2010). Testing Capital Asset Pricing Model: Empirical Evidences from Indian Equity Market. *Eurasian Journal of Business and Economics, 3*(6), 127-138. Retrieved from https://www.ejbe.org/index.php/EJBE/article/view/44
16. Cohen, K. J., Hawawini, G. A., Maier, S. F., Schwartz, R. A., & Whitcomb, D. K. (1980). Implications of Microstructure Theory for Empirical Research on Stock Price Behavior. *The Journal of Finance, 35*(2), 249. https://doi.org/10.2307/2327381
17. Dhankar, R. S., & Saini, R. K. (2007). Portfolio Performance in Relation to Price Earning Ratio: A Test of Efficiency under different Economic Conditions. *Icfai Journal of Applied Finance, 13*(1), 223-232. https://doi.org/10.1007/978-81-322-3950-5_14
18. Diwani, M., & Asgharian, H. (2010). Testing the CAPM in the Indian A study that investigates the validity of the CAPM in Bombay Stock Exchange Sensex 30. *Exchange Organizational Behavior Teaching Journal.*
19. Fama, E. F., & French, K. R. (1992). The Cross-Section of Expected Stock Returns. *Source: The Journal*

of Finance, 47(2), 427-465. https://doi.org/10.2307/2329112

20. Fama, E. F., & French, K. R. (1995). Size and Book to Market Factors in Earnings and Returns. *The Journal of Finance, L*(1), 131-155. https://doi.org/10.1111/j.1540-6261.1995.tb05169.x
21. Fama, E. F., & French, K. R. (1996). Multifactor explanations of asset pricing anomalies. *Journal of Finance, 51*(1), 55-84. https://doi.org/10.1111/j.1540-6261.1996.tb05202.x
22. Fama, E. F., & French, K. R. (2006). The value premium and the CAPM. *Journal of Finance, 61*(5), 2163-2185. https://doi.org/10.1111/j.1540-6261.2006.01054.x
23. Fama, E. F., & French, K. R. (2008). Dissecting anomalies. *Journal of Finance, 63*(4), 1653-1678. https://doi.org/10.1111/j.1540-6261.2008.01371.x
24. Fama, E. F., & MacBeth, J. D. (1973). Risk, Return, and Equilibrium: Empirical Tests. *The Journal of Political Economy, 81*(3), 607-636.
25. Fama, E. F., & French, K. R. (1993). Common risk factors in the returns stocks and bonds. *Journal of Financial Economics, 33,* 3-56. https://doi.org/10.1016/0304-405X(93)90023-5
26. Fletcher, J. (1997). An examination of the cross-sectional relationship of beta and return: UK evidence. *Journal of Economics and Business, 49*(3), 211-221. https://doi.org/10.1016/s0148-6195(97)00006-4
27. Gursoy, C. T., & Rejepova, G. (2007). Test of Capital Asset Pricing Model in Turkey. *Dogus Universitesi Dergisi, 8*(1), 47-58. https://doi.org/10.31671/DOGUS.2019.241
28. Hanif, M., & Bhatti, U. (2010). Validity of Capital Assets Pricing Model: Evidence from KSE-Pakistan. *European Journal of Economics, Finance and Administrative Sciences*, (20). Retrieved from https://ssrn.com/abstract/=1544287
29. Hasan, M. Z., Kamil, A. A., Mustafa, A., & Baten, M. A. (2011). A Validity Test Of Capital Asset Pricing Model for Dhaka Stock Exchange. *Journal of Applied Sciences, 11*(20), 3490-3496. https://doi.org/10.3923/jas.2011.3490.3496
30. Hawaldar, I. T. (2016). The Cross-Sectional Variations in Portfolio Returns Evidence from Bahrain Bourse. *British Journal of Economics, Finance and Management Sciences, 12*(2), 1-11.
31. Iqbal, J., & Brooks, R. (2007). A Test of CAPM on the Karachi Stock Exchange. *International Journal of Business, 12*(4), 429-444. Retrieved from https://www.researchgate.net/publication/228267073
32. Iqbal, T. H. (2011). Relevance of Capital Asset Pricing Model – A Review. *Journal on Banking Financial Services and Insurance Research, 1*(2), 85-97.
33. Iqbal, T. H. (2014). Seasonal analysis of abnormal returns after quarterly earnings announcements. *International Journal of Accounting and Financial Reporting, 4*(2), 501-519.
34. Iqbal, T. H. (2015). Empirical Testing of Capital Asset Pricing Model on Bahrain Bourse. *Asian Journal of Finance & Accounting, 7*(2), 107-119. https://doi.org/10.5296/ajfa.v7i2.8356
35. Iqbal, T. H., Mallikarjunappa, T., & Nayak, P. (2007). Stock Price Adjustments to Quarterly Earnings Announcement: A Test of Semi-strong Form of Efficiency. *Gyan Management, 1*(2), 25-42.
36. Isakov, D. (1999). Is beta still alive? Conclusive evidence from the Swiss stock market. *The European Journal of Finance, 5*(3), 202-212. https://doi.org/10.1080/135184799337046
37. Jensen, M. C. (1968). The Performance of Mutual Funds in the Period 1945-1964. *The Journal of Finance, 23*(2), 389-416. https://doi.org/10.1111/j.1540-6261.1968.tb00815.x
38. Kumar, A., Soni, R., Hawaldar, I. T., Vyas, M., & Yadav, V. (2020). The Testing of Efficient Market Hypotheses: A Study of Indian Pharmaceutical Industry. *International Journal of Economics and Financial Issues, 10*(3), 208-216. https://doi.org/10.32479/ijefi.9764
39. Kumar, K. R. N., Hawaldar, I. T., & Mallikarjunappa, T. (2018). Windows of Opportunity and Seasoned Equity Offerings: An Empirical Study. *Cogent Economics & Finance, 6*(1), 1-18. https://doi.org/10.1080/23322039.2018.1528688
40. Lau, S. C., Quay, S. R., & Ramsey, C. M. (1974). The Tokyo Stock Exchange and the Capital Asset Pricing Model. *The Journal of Finance, 29*(2), 507. https://doi.org/10.2307/2978820
41. Lintner, J. (1965). The Valuation of Risk Assets and the Selection of Risky Investments in Stock Portfolios and Capital Budgets. *The Review of Economics and Statistics, 47*(1), 13. https://doi.org/10.2307/1924119
42. Markowitz, H. (1952). Portfolio Selection. *The Journal of Finance, 7*(1), 77-91. https://doi.org/10.1111/j.1540-6261.1952.tb01525.x
43. Olakojo, S. A., & Ajide, K. B. (2010). Testing the capital asset pricing model (CAPM): The case of the nigerian securities market. *International Business Management, 4*(4), 239-242. https://doi.org/10.3923/ibm.2010.239.242
44. Rahman, M., Baten, A., & Ashraf-Ul-Alam. (2006). An empirical testing of capital asset pricing model in Bangladesh. *Journal of Applied Sciences, 6*(3), 662-667. https://doi.org/10.3923/jas.2006.662.667
45. Sehgal, S., & Balakrishnan, A. (2013). Robustness of Fama-French Three-Factor Model: Further Evidence for Indian Stock Market. *Vision: The Journal of Business Perspective, 17*(2), 119-127. https://doi.org/10.1177/0972262912483526
46. Shaikh, S. A., Shaikh, R., & Shaique, M. (2017). Applicability of CAPM: An Evidence from Pakistan Stock Exchange. *Journal of Business Strategies, 11*(2), 21-34. Retrieved from http://www.greenwichjournals.com/index.php/businessstudies/article/view/374

http://dx.doi.org/10.21511/imfi.18(4).2021.21

47. Sharpe, W. F. (1964). Capital Asset Prices: a Theory of Market Equilibrium Under Conditions of Risk. *The Journal of Finance, 19*(3), 425-442. https://doi.org/10.1111/j.1540-6261.1964.tb02865.x

48. Sreenu, N. (2018). An Empirical Test of Capital Asset-pricing Model and Three-factor Model of Fama in Indian Stock Exchange. *Management and Labour Studies, 43*(4), 294-307. https://doi.org/10.1177/0258042x18797770

49. Theriou, N. G., Aggelidis, V. P., Maditinos, D. I., & Šević, Ž. (2010). Testing the relation between beta and returns in the Athens stock exchange. *Managerial Finance, 36*(12), 1043-1056. https://doi.org/10.1108/03074351011088441

50. Wong, K. A., & Tan, M. L. (1991). An assessment of risk and return in the Singapore stock market. *Applied Financial Economics, 1*(1), 11-20. https://doi.org/10.1080/758520133

Journal of Polymer Research (2021) 28:371
https://doi.org/10.1007/s10965-021-02734-4

ORIGINAL PAPER

Sodium metavanadate dispersed in Polyaniline composite matrix film for sensing application

T. Machappa[1] · S. Badrunnisa[2]

Received: 7 May 2021 / Accepted: 27 August 2021

Abstract

Composite of sodium metavanadate ($NaVO_3$) and polyaniline (PANI) was formed by in-situ chemical polymerization in one step. Characterization techniques such as X-Ray diffraction, Scanning electron micrograph, and Fourier transform infra-red spectra confirm mixed phase of formation $NaVO_3$inPANI emeraldine salt. Conductivity decreases with an increase in wt of $NaVO_3$in PANI, the conductivity increases with temperature is due to an increase in disorderliness, induction of conformational changes within the composite, and thermally activated exponential behavior. The composites have shown high sensitivity in the low humidity range with the decrease in electrical resistance when exposed to humidity in the range of 20 to 50% RH. The moisture absorption is due to capillary condensation within the composite, which decreases the conductivity of the matrix with humidity. The transfer of charges from sensing material to analyte gas (donor) by penetration with enlargement of the polymer composites decreases the conductivity with the concentration of LPG.

Keywords Polyaniline · Sodium MetaVenadate · Conductivity · Humidity · Liquefied petroleum gas

Introduction

For the past 31 years, ever since the discovery of conducting polymers by Alen MacDiarmid et.al, in 1980 has made significant attention for the researches due to their extensive variety of technical applications, such as electrical and electronic devices, rechargeable batteries, light-emitting devices, supercapacitors, humidity sensors and gas sensors [1–6]. Among the conducting polymers, polyaniline has the added advantage of its simple synthesis, doping, stability, and moderate conductivity has attracted much researches. In the past years, an extensive study on emerging cost-effective sensors for the monitoring toxic gases and humidity using inorganic semiconducting metal oxides such as tin oxide (SnO_2), zinc oxide (ZnO), titanium oxide (TiO_2), Zinc tungstate ($ZnWO_4$), cadmium oxide (CdO_2), Cerium oxide (CeO_2) [7–9].

An accidental leaks of domestic liquefied petroleum gas (LPG) causes combustion accidents and a toxic CO gas combines with hemoglobin quickly resulting in human death, also they are potentially hazardous, the consistent and sensitive gas sensing instruments to increase the safety at home and industry is required. Detection of toxic and hazardous gas was started from early stages, most of the previous research focused on a new type of sensing materials where lack sensitivity, selectivity, and stability. Researchers have made their attention towards the study of sensing signal of the sensor material, the reports show that it is possible to distinguish different gases by measuring the features of sensor response [10]. Butane (C_4H_{10}), Propane (C_3H_8), butylenes (C_4H_8), and propylene (C_3H_6) are the normal constituents of the LPG, also it contains other similar gases in trace quantities, these are not chemically pure hydrocarbons but butane and propane are marked as quality products commercially. Researchers explored butane and propane but minimum work has been carried out on the LPG sensors. The earlier reports reveal, currently available sensors have two disadvantages low sensitivity and operating temperature is high, one has to compromise with any one of them. The high sensitive sensor works at a high temperature which increases the

✉ T. Machappa
machappat@rediffmail.com

S. Badrunnisa
badrunnisa.s@gmail.com

[1] Department of Physics, Ballari Institute of Technology and Management, Ballari 583 104, Karnataka, India

[2] Krupanidhi Degree College, Bangalore 560 035, Karnataka, India

Published online: 09 September 2021

power consumption and on the other side, low-temperature sensors are not sensitive enough to detect LPG at trace level [11–13].

For the past two and half decades conducting polymer composites are used in batteries, electrochromic devices, biosensors, etc. The derivatives of polyaniline are found well in humidity sensors, chemically synthesized PANI is considered as p-type doping, according to buildup model an unbounded electron pair on the nitrogen atom forms protonated. The nano-crystalline composites including ceramics and ceramic/conducting polymer are highly encouraging materials, which may be used for humidity and gas sensing applications because they exhibit improved sensing performance. Large surface areas are necessary for sensing, which can be obtained by highly-dispersed oxide particles. Large surface regions can provide high reaction contact between gas sensing materials and test gases. The standard structure of a metal oxide gas sensor is to have a porous structure for the large surface areas of interaction. The porous structure can be assembled by many small grains with empty spaces with pores among them. It is also indicated that a small grain size is suitable to improve the sensitivity [14–17].

The current report aims to study the electrical and sensing property of PANI and PANI / $NaVO_3$ composites for room temperature low humidity and LPG sensing.

Experimental

Synthesis

Pure polyaniline

5 ml Aniline is added to 200 ml of hydrochloric acid (0.1 M) to form aniline hydrochloride. 14.6×10^{-3} kg ammonium persulfate [$(NH_4)_2S_2O_8$] is dissolved in 300 ml of hydrochloric acid (0.1 M) to form ammonium per-sulfate hydrochloride. The polymerization of aniline is done by adding ammonium per-sulfate hydrochloride solution dropwise to aniline hydrochloride solution, with nonstop stirring for 6–8 h in the freezing mixture at 0–5 °C. The dark greenish precipitate of pure PANI was vacuum filtered, cleaned with deionized water, and to achieve constant weight the precipitate is dried for 24 h in the oven and achieved the yield of 3.2 to 3.6×10^{-3} kg per preparation of pure PANI [18].

Polyaniline/sodium metavanadate composite

5 ml Aniline is added to 200 ml of hydrochloric acid (0.1 M) mixed to have aniline hydrochloride and finely crushed sodium metavanadate ($NaVO_3$) weight as0.1 (0.34×10^{-3} kg), this is against the average yield of PANI is mixed with aniline hydrochloride. The particle suspension is confirmed by vigorous stirring using a magnetic stirrer. Aniline was polymerized in presence of $NaVO_3$ particles by drop-wise addition of14.6×10^{-3} kg of ammonium persulfate [$(NH_4)_2S_2O_8$]dissolved in 300 ml of hydrochloric acid (0.1 M), with nonstop stirring for 6–8 h at 0–5 °C. The dark greenish precipitate of PANI/$NaVO_3$composite was vacuum filtered, cleaned with deionized water, and dried for 24 h in the oven. The above procedure repeated for 0.2 (0.68×10^{-3} kg),0.3 (1.02×10^{-3} kg),0.4(1.36×10^{-3} kg) and 0.5 (1.7×10^{-3} kg) weight$NaVO_3$, the composite powder is were stored in airtight container for further studies. [19].

Characterization

The composites were used for the X-Ray diffraction (X-RD) studies to confirm retention of crystallinity and presence of $NaVO_3$ in PANI matrix using an X-ray diffractometer (Phillips—PW3710) with the source of radiation Cu Kα. Fourier Transform Infra-Red (FTIR) spectra were recorded on a spectrophotometer (Perkin—Elmer 1600)in the medium of KBr for the confirmation of polymerization and composite formation along with pure PANI and $NaVO_3$, the frequency peaks thus recorded of all three samples used for further analysis. The images of Scanning Electron Micrographs (SEM) images of pure PANI and PANI/$NaVO_3$composite were taken on Environmental Scanning Electron Microscope (Phillips XL 30) to know the surface morphology of composite and distribution of $NaVO_3$ in pure PANI.

Electrical conductivity

For the measurement of conductivity, the composite is pressed to have 10 mm diameter and 2 mm thickness pellets, these pellets were obtained by being subjected to a pressure of 98 k Pausing Universal testing machine (UTM-40). These pellets are provided by silver electrodes on both sides of the pellet with silver paste for temperature-dependent conductivity studies. Pellet sample was placed in temperature-controlled oven connected with Keithley multimeter (Model USA-2100) to record planar resistance of the composites and temperature-dependent electrical conductivity is calculated.

Sensor studies

For sensor studies, PANI / $NaVO_3$ composite powder is sintered on an insulating substrate to form a film-like structure to expose the large surface area of the composite to test gas or humidity. Electrodes are provided at the two ends of a film with silver past for the measurement of planar resistance.

Humidity sensor studies

PANI / $NaVO_3$ composite film was placed in the closed self-designed humidity sensor chamber of glass and planar resistance was recorded by High accuracy multimeter (Dot-tech). The humidity sensing studies were carried out by reducing the humidity to 20% RH by placing calcium chloride in a closed glass chamber and then humidity was increased steadily bypassing controlled water vapors into the chamber up to 50% RH. The planar resistance of the sensing composite in the chamber was recorded versus humidity from 20 to 50% RH at room temperature [20].

Gas sensor studies

PANI / $NaVO_3$ composite film was placed in the closed self-designed gas sensor chamber of glass and connected to High accuracy multimeter (Dot-tech) to record planar resistance. The planar resistance of the composites was measured with reference environment air without test gas as initial resistance. Through the flow meter, the gas (LPG)was introduced into the sensor chamber with a rate of 25 ml/min by controlling the flow from the gas cylinder with a regulator. The planar resistance of PANI / $NaVO_3$ composite films in presence of test gas was measured every 20 s, such that 0.417 ml/sec gas flows into the chamber, slowly the gas concentration increases to 8.34 ml for every 20 s of the measurement. The change in resistance was calculated from the resistance of the composites with reference atmosphere air and the resistance of the composite in the presence of test gas (LPG) at regular intervals of time [21].

Results and discussions

X-Ray diffraction study (X-RD)

The X-RD diffraction pattern was recorded for all samples of PANI/$NaVO_3$ composites having the different weight of $NaVO_3$, however X-RD pattern of PANI/ $NaVO_3$ composite having 0.5 wt of $NaVO_3$ is selected for the analysis as the concentration of $NaVO_3$ is more in 0.5 wt, because of which the intensity peaks will be high. The amorphous nature with micro-crystallinity of polyaniline was in Fig. 1a observed with a broad peak centered around $2\theta \approx 27°$ is in consistence with earlier reported data, maximum intensity peak at 25.25^0.

The X-RD diffraction pattern of pure $NaVO_3$ reveals that, crystal structure as monoclinic (S.G: 12/a(15), PSC: mC20), having lattice parameters, a = 10.325 Å, b = 9.468 Å, c = 5.789 Å and $\beta = 104.22^0$. The prominent peaks $2\theta = 18.73^0$, 24.65^0, 32.08^0, 37.32^0, 41.41^0, 52.88^0, 63.27^0 and 68.11^0 are from crystal planes (020), (021),

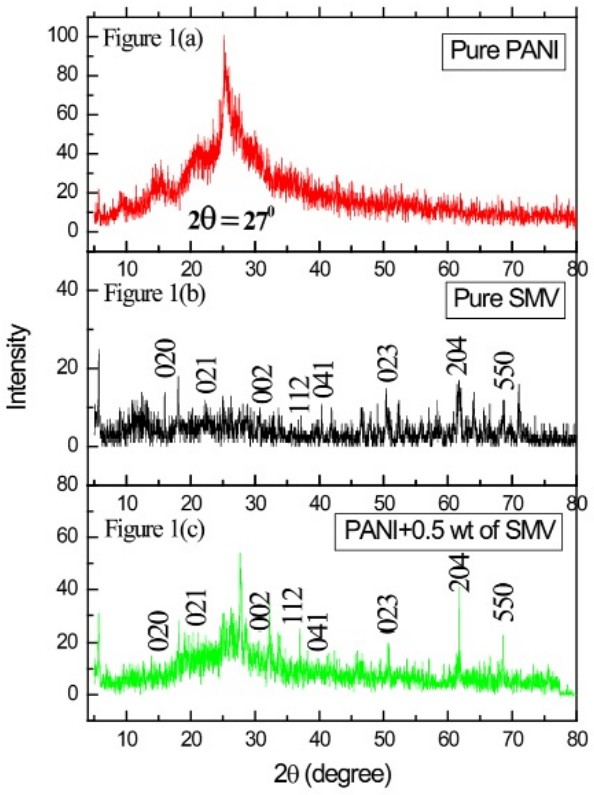

Fig. 1 **(a)** X-RD pattern of pure PANI, **(b)**X-RD pattern of pure $NaVO_3$, **(c)**X-RD pattern of PANI / $NaVO_3$ composite having 0.5 wt of $NaVO_3$ in PANI

(002), (112), (041), (023), (204) and (550) as shown in Fig. 1b.These peaks are confirmed from the reported standard data of JCPDS 70 – 1015 of $NaVO_3$, equally Fig. 1c shows the amorphous nature of PANI with the monoclinic peak of $NaVO_3$ indicating the crystalline nature of the composite. X-RD pattern showing the same peaks in all cases when compared with the composite and pure $NaVO_3$ reveals $NaVO_3$ particle presence. This indicates that $NaVO_3$ has maintained its structure during the polymerization reaction and confirmed the distribution of $NaVO_3$in PANI [22].

Fourier Transform Infrared Spectra (FTIR)

The significant peaks observed in the case of FTIR spectra pure PANI (Fig. 2a), confirms the polymerization of monomer aniline into polymer polyaniline by the occurrence of spectral intensity peaks at 3428×10^{-2} m^{-1} is due to N–H stretching, 1625×10^{-2} m^{-1} is due to Benzenoid—Ring stretching, 1563×10^{-2} m^{-1} is due to Quinoid—Ring stretching, 1485×10^{-2} m^{-1} is due to C—C stretching + C = N stretching, 1293×10^{-2} m^{-1} is due to CH bending + C—N stretching and 1239×10^{-2} $m^{-1}$is due to C—C stretching + C—N stretching from FTIR spectrum

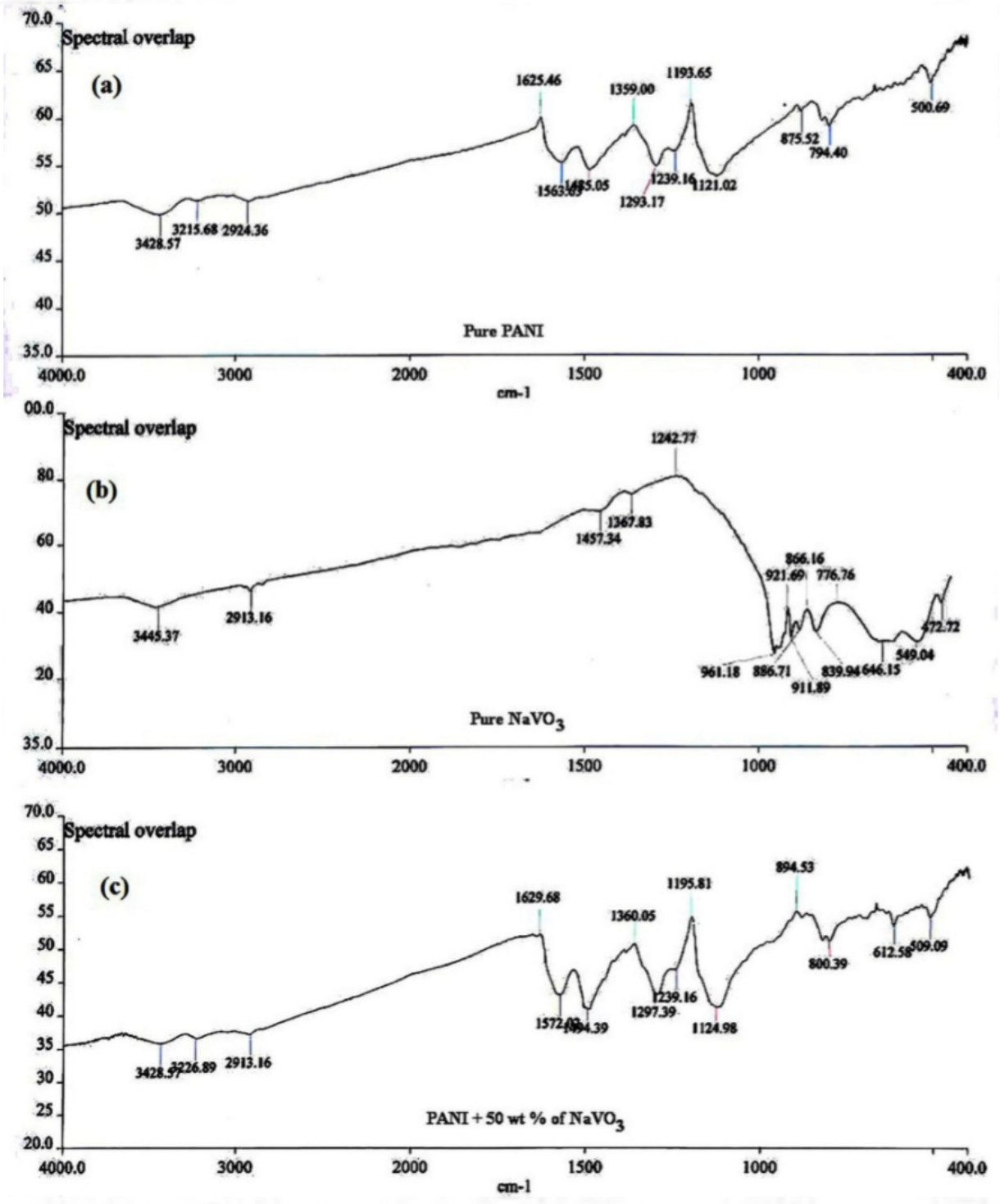

Fig. 2 (**a**) FTIR Spectra of pure PANI, (**b**) FTIR Spectra of pure $NaVO_3$, (**c**) FTIR Spectra of PANI / $NaVO_3$ composite

of pristine PANI. The important spectral peaks of FTIR Spectra of pure $NaVO_3$ (Fig. 2b) at 776 & 549×10^{-2} $m^{-1}$of pristine$NaVO_3$ are due to metal and oxygen bond stretching frequency. In FTIR Spectra of PANI/ $NaVO_3$composite (Fig. 2c), the prominent spectral peaks observed at similar stretching frequencies are found in pristine PANI and pure $NaVO_3$ spectra [23, 24]. The important intensity peaks observed in the case of pristine PANI, pristine $NaVO_3$, and PANI / $NaVO_3$ composites are listed in Table 1 below. The comparison of stretching frequencies shows that the PANI / $NaVO_3$composite stretching frequencies in the case of benzenoid—ring stretching and quinoid—ring stretching in the pristine PANI are more than those observed to the PANI / $NaVO_3$ composite, here these frequencies are moved little towards higher frequency side in the formation of composite, this confirms the week bond (Vander wall's) interaction between PANI Chain and $NaVO_3$. These results are consistent with earlier reported data in the literature [25].

Scanning Electron Microscopy (SEM)

The pure PANI image of SEM shown in Fig. 3a, clearly shows a smooth and homogeneous structure. The presence of micro-crystalline structure distributed throughout can be seen and the presence of micro-crystalline structures in PANI is confirmed from X-RD studies, a granulated morphology with micro-crystalline structures is consistent with other reports. The SEM image of PANI/$NaVO_3$ composite shown in Fig. 3c, possesses crystalline grains of $NaVO_3$ in PANI matrix, further Fig. 3b, d shows the high-resolution

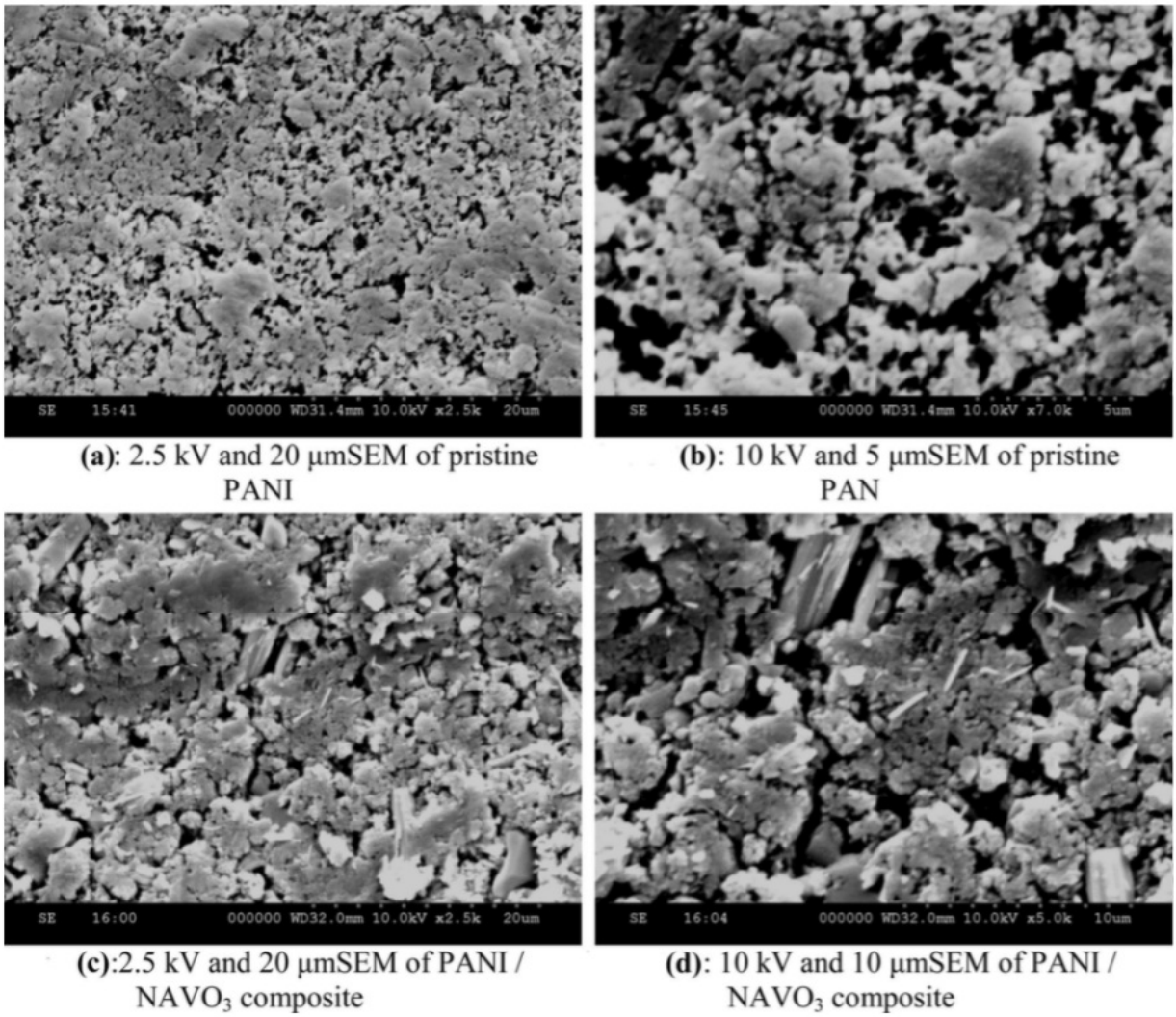

Fig. 3 (**a**) 2.5 kV and 20 µmSEM of pristine PANI, (**b**) 10 kV and 5 µmSEM of pristine PAN, (**c**) 2.5 kV and 20 µmSEM of PANI / $NAVO_3$ composite, (**d**) 10 kV and 10 µmSEM of PANI / $NAVO_3$ composite

studies at 10 kV and 5 µm and 10 kV and 10 µm respectively, these images of SEM shows that the porous structure with capillary pores connected. Such a pours composite is possible to enable the adsorption of the vapors due to its large surface area available for interaction inside the capillary pores. The uniform spreading of $NaVO_3$ micro-crystals in the PANI matrix was seen from SEM and also increase the poursivity of the composite [26].

Electrical conductivity

It is observed that the electrical conductivity increases as temperature increases in both PANI and PANI/$NaVO_3$ composites as shown in Fig. 4a, b, this suggests that electrical conductivity is thermally activated. The change in conductivity is very low up to 110 °C in both PANI and PANI/NaVO3 composites, but it increases exponentially with the temperature above 110 °C.In conducting polymers the variation in electrical conductivity was explained by the Variable Range Hopping (VRH) model of Mott. According to Mott VRH-model, in non-metallic disordered materials like polymer composites and ceramics, the electron motion is specified by the thermally helped hopping of charge between localized states for electrons traps, these electron traps are distributed randomly within the sample [27, 28]. The conductivity in non-metallic disordered materials is given by

$$\sigma(T) = exp\left[-\frac{T_0}{T^{\frac{1}{(\alpha-1)}}}\right]$$

$$where\ T_0 = \frac{\lambda\alpha^3}{\rho_0 k}$$

where: α—Coefficient of exponential decay of localized states, ρ_0-Density of states at Fermi level and λ -Dimensional constant. However, several simulations or models of conductivity predict that $\sigma \propto T^{-0.5}$.

In conducting polymers the increase in electrical conductivity depends on the conjugation length of the polymer chain, due to the phenomenon of the thermal curling effect, the conjugation length increase which leads to an increase in conductivity. On heating, the molecular arrangement makes the molecular conformation favorable for electron delocalization [29]. The conductivity of PANI / $NaVO_3$ composites is more than that of pure PANI, which may be attributed to the percolation of PANI in presence of dispersed $NaVO_3$ in the PANI matrix.

The variation of conductivity with wt of $NaVO_3$ in PANI is shown in Fig. (5), the conductivity decreases as the

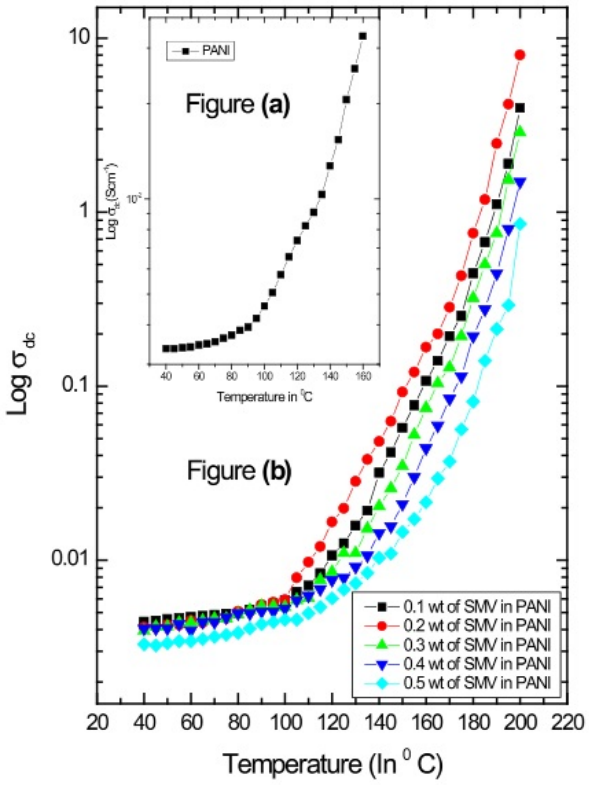

Fig. 4 **(a)** Variation of σ_{dc} verses temperature Pure PANI, **(b)** Variation of σ_{dc} verses temperature PANI / $NaVO_3$ composites

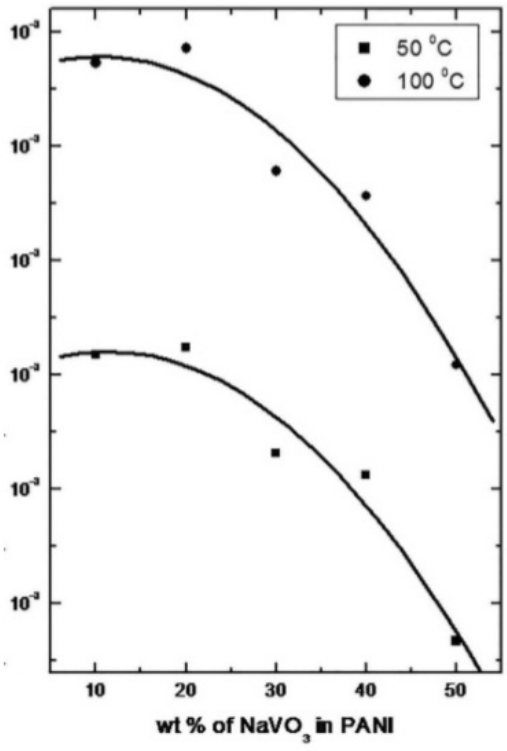

Fig. 5 Variation of σ_{dc} verses wt of $NaVO_3$ in PANI at two constant temperatures of 50 °C and 100 °C

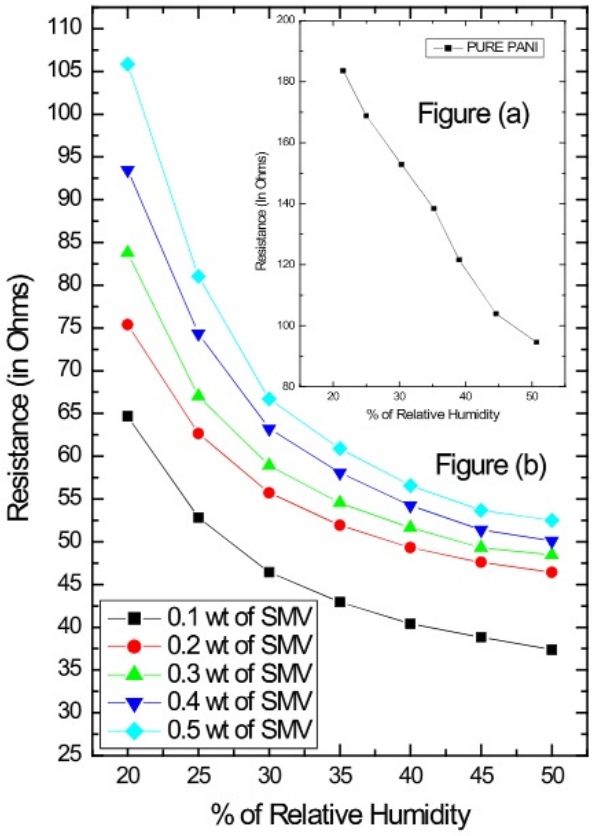

Fig. 6 **(a)** Variations of resistance as verses % RH of Pure PANI, **(b)** Variations of resistance versus % RH of PANI / $NaVO_3$ composites

concentration of $NaVO_3$ increases in PANI. The disorderliness of composite is seen from X-RD and SEM data of these composites, the disorderliness will increase as wt of $NaVO_3$ increases in PANI, this disorderliness leads to reduce conformational charges in PANI. The decrease in conformational charges will reduce the order and delocalization length of the polymer chain, which reduce the conductivity.

The increase in conductivity depends on the hopping of charge carriers between localized sites, the hopping of charge carriers depends on polymer chain length, if chain length is extended then the charge carriers will have sufficient energy to hopp hence conductivity increases, if the chain length reduces then charge carrier hopping is blocked then charge are unable to hopp between localized sites hence decrease in conductivity [30]. In our study, it is found that extended chain length is observed in 0.2 wt of $NaVO_3$ in PANI, for all other composites reduction in chain length is observed. Hence increase in conductivity for only 0.2 wt of $NaVO_3$ in PANI was observed. The electrical conductivity of PANI/$NaVO_3$ composites is higher than that of pristine PANI, this increase in conductivity is due to $NaVO_3$ molecules facilitate sufficient energy for hopping of charge carriers in the polymer chine.

Humidity sensing study

The decrease in resistance with an increase in humidity was observed in both PANI and PANI / $NaVO_3$ composites as shown in Fig. 6a, b. This may be attributed to $NaVO_3$ ion mobility attached to polymer chain and the mobility of ions depends on humidity, the mobility increases as humidity increases, hence resistance decreases. Conducting polymer is coil up into compact form in dry conditions (low humidity) and the compact coil will uncoil into a straight-chain in wet conditions (high humidity). In conducting polymers this geometry of straight-chain is favorable to enhance the mobility of ions or enhance the transfer of charge carriers across the polymer chain, this charge transfer of charges and mobility of ions will reduce resistance and increase conductivity [31]. On the other hand, the conductivity depends on the condensation of water molecules in capillary pours within the sensing material, this pours structure will also cause the change in conductivity.

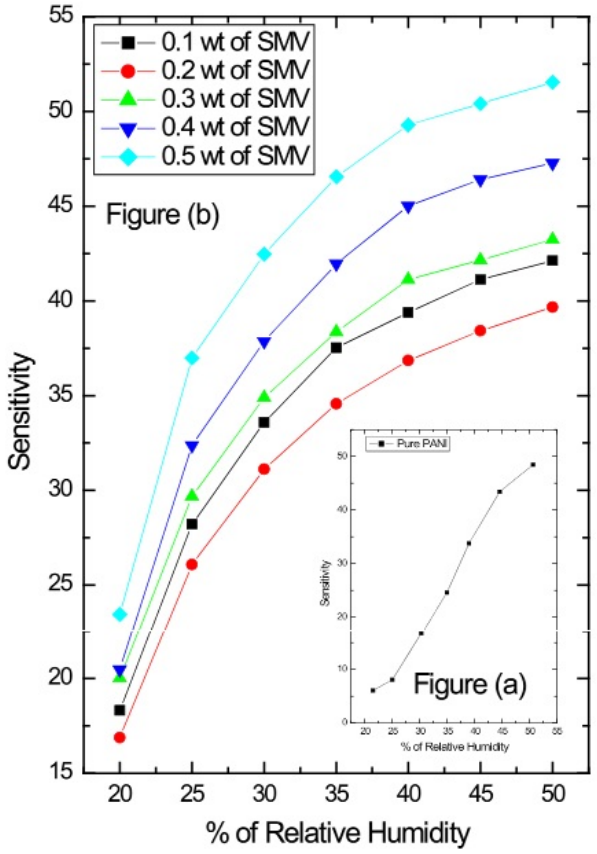

Fig. 7 **(a)** Sensitivityverses humidity of pristine PANI, **(b)** Sensitivityverses humidity of PANI / $NaVO_3$ of composites

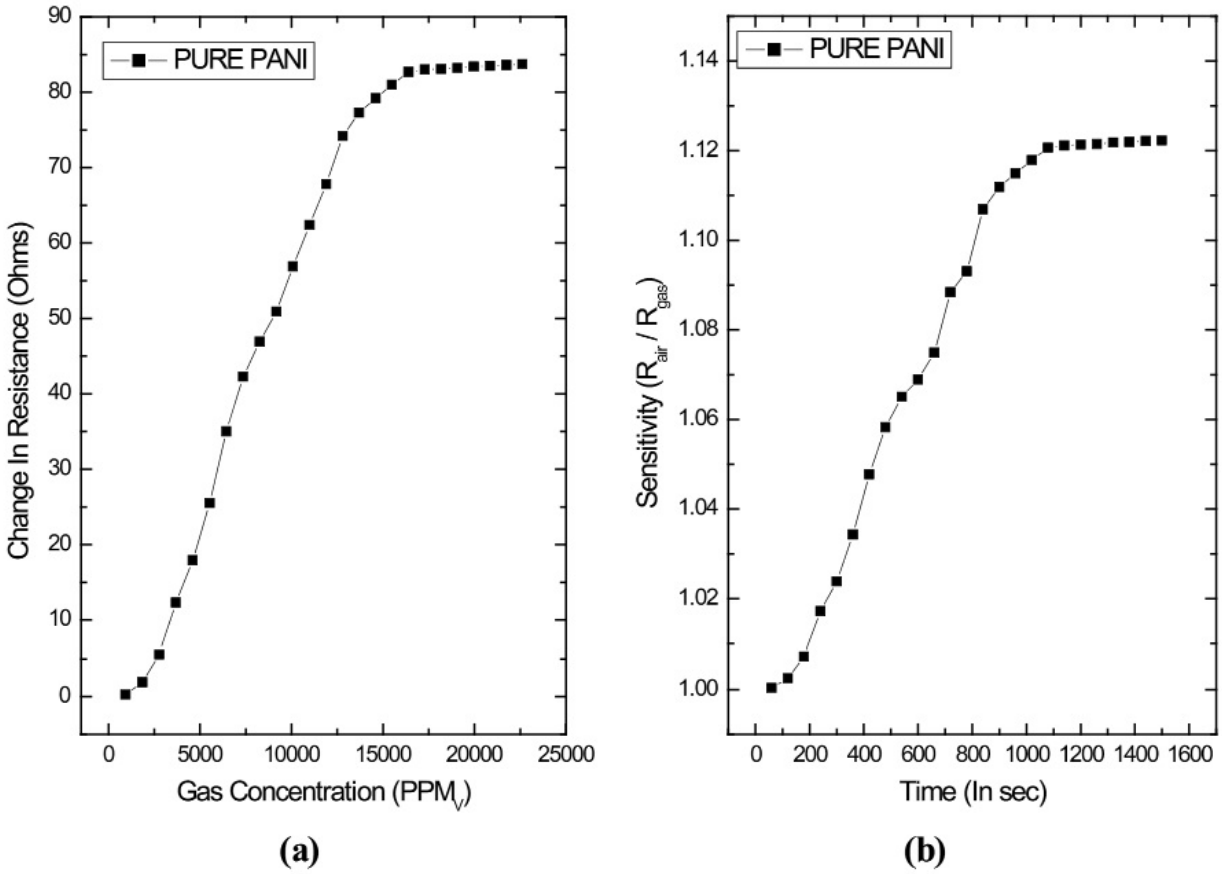

Fig. 8 (**a**) Change in resistance versus concentration of LPG of pure PANI, (**b**) Sensitivity versus expose time of pure PANI to LPG

Humidity sensor performance characteristics such as sensitivity, reproducibility, time response, etc., will depend on its microstructure. These characteristics are determined by the specific interaction surface area between analyte and sensing materials, but the specific area of interaction depends on its poursivity, as poursivity increases the specific area of interaction also increases. SEM microstructure revealed the presence of capillary pores in PANI / $NaVO_3$ composite, thus the specific area of interaction is the principle microstructure for low humidity conditions. Therefore a definite correlation is established between the number of water molecules taken by the capillary pores and the resistance of the sensing material [32].

The sensitivity (S) of the sensing material in the detection of humidity is given by

$$S_H = \left| \frac{Change\ in\ resistance}{Initial\ resistance} \right| \times 100$$

Change in resistance is $(RH_2 - RH_1)$, where RH_1 is the initial resistance of the sample and RH_2 is the resistance at the next level of humidity, the next level of humidity depends on the measurement of resistance versus relative humidity in the chamber. Figure 7 gives the variation of sensitivity with humidity and wt of $NaVO_3$ in PANI. In our study it is clear that sensitivity increases with an increase in humidity and follows an exponential growth, also the sensitivity increases as wt of $NaVO_3$ increases in PANI, it is a fund that at 40%RH the percentage of sensitivity is 36.85, 38.39, 41.12, 45.01 and 49.27 for 0.1, 0.2, 0.3, 0.4 and 0.5 wt of $NaVO_3$ in PANI respectively. The increase in sensitivity with an increase in wt of $NaVO_3$ is due to an increase in porsivity of the composite, hence a large surface area available for the interaction of water vapors with the composite to have a considerable change in resistance.

Gas sensing study

The change in resistance with the concentration of LPG in parts per million (PPM) at a constant volume of pure PANI is shown in Fig. 8a. The gas is made to flow at a constant rate of 25 ml/min into the sensing chamber. It is found that change in resistance increases with the concentration of gas. The change in resistance of pure PANI is due to absorption of the gas, this may be attributed

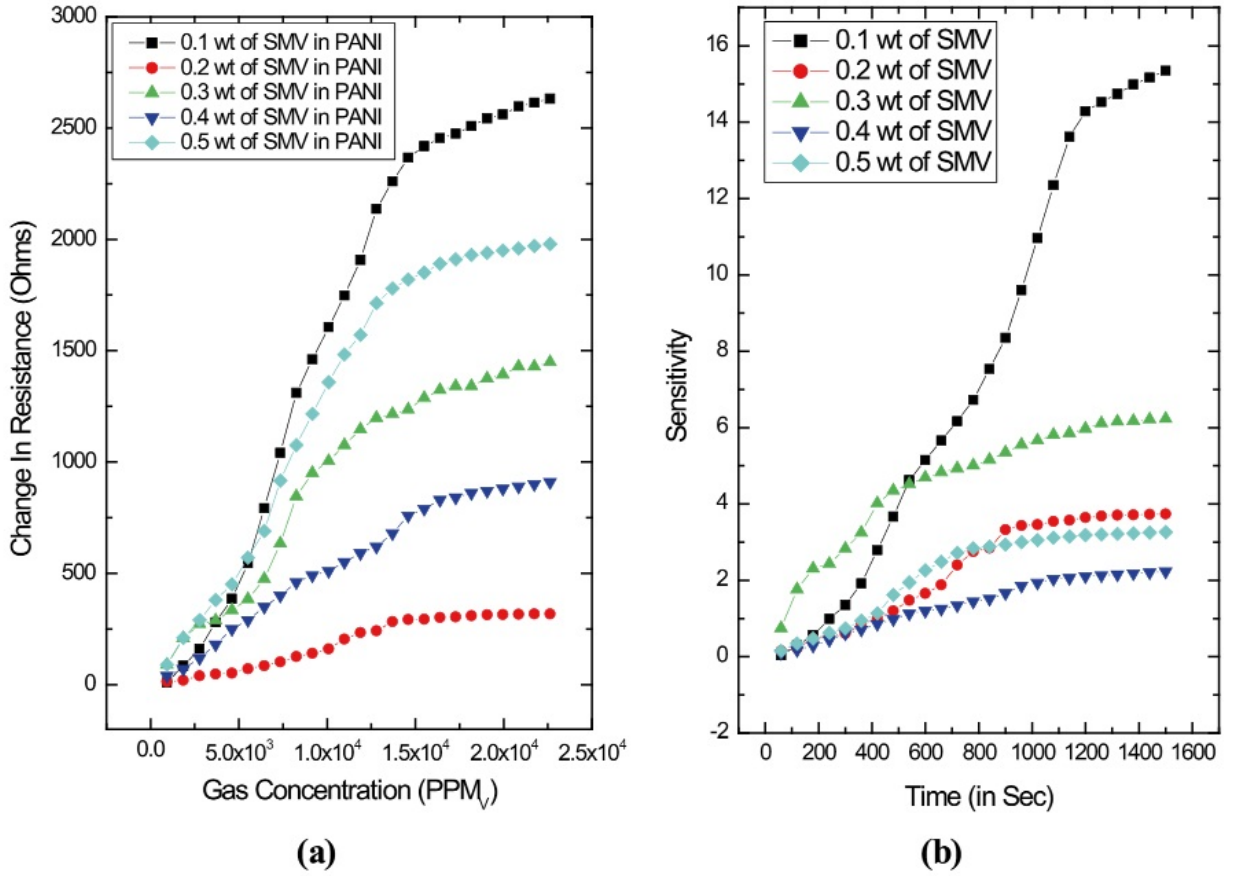

Fig. 9 (**a**) Change in resistance versus concentration of LPG of PANI / $NaVO_3$ composites (**b**) Sensitivity versus expose time of composite to LPG

as a two-stage process. Firstly swelling of polymer matrix due to penetration of gas and secondly diffusion of gas into the swelled material with an increased rate of flow. In this process, the transfer of charge carriers from sensing material to analyte gas molecules takes place, i.e. the charge exchange from sensing surface to test gas. The week

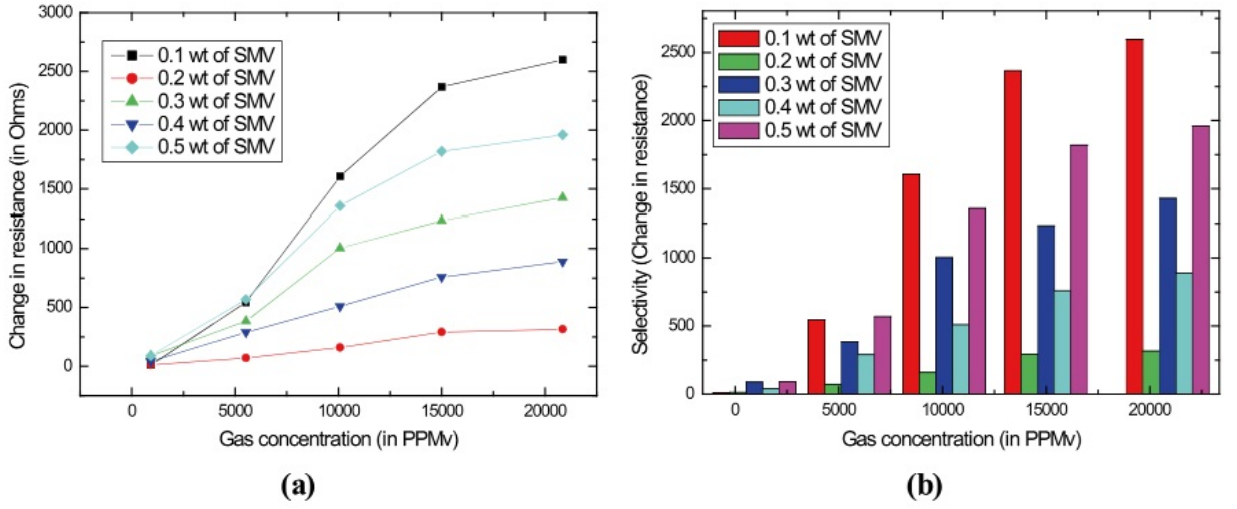

Fig. 10 (**a**) Change in resistance versus gas concentration (**b**) Selectivity from the change in resistance versus gas concentration

Table 1 Observed peaks of FTIR spectra with group assignments

Sample	Wave number ($\times 10^{-2}$ m^{-1})	Assignment
Pure PANI	3428	N–H stretching
	1625	Benzenoid—Ring stretching
	1563	Quinoid—Ring stretching
	1485	C—C stretching + C = N stretching
	1293	CH bending + C-N stretching
	1239	C—C stretching + C-N stretching
Pure $NaVO_3$	776, 549	Metal oxygen stretching
PANI / $NAaO_3$ composite	3428	N–H stretching
	1629	Benzenoid—Ring stretching
	1572	Quinoid—Ring stretching
	1494	C—C stretching + C = N stretching
	1297	CH bending + C-N stretching
	1239	C—C stretching + C-N stretching
	894	PANI – NAVO3
	800	Metal oxygen stretching
	612	Metal oxygen stretching

charge—transfer between the polymer matrix and test gas is responsible for the removal of charge, here the polymer matrix acts as donor, and test gas LPG act as an acceptor [33, 34]. The sensitivity of pure PANI is shown in Fig. 8b.

It is observed that the electrical resistance increases with the concentration of LPG for all five composites as in Fig. 9a. The variation of resistance of the composite depends on the type of doping material to PANI, dopants like metal oxides, bi-metal oxides, bio-materials, etc., The mechanism of gas sensing is explained in terms of variation in conductivity or variation in resistance of sensing materials, one is the absorption of atmospheric oxygen molecule on the sensing composite surface and other is the direct reaction with lattice / interstitial oxygen by test gas. The atmospheric oxygen absorbed on the composite surface will extract an electron from the sensing material and transfer it to the test gas and/or lattice / interstitial oxygen will interact to transfer the electron from sensing material to test gas, these are mostly accountable for the detection of test gases [35].

The sensing mechanism of swelling and surface charge transfer as explained earlier are responsible for the change in resistance within the sensing material. From Fig. 9a it is clear that change in resistance has started from 30 s and is very rapid at low concentrations and saturates after 15.5 min.

The response of a gas sensor is a function of the concentration of the gas, in our study we have recorded resistance of the composite versus change in the concentration of gas in a closed sensor chamber. If R_a is the initial resistance of the composite in the air (no test gas) and R_g is the resistance of the composite in presence of the test gas (LPG) atmosphere, then the sensitivity of the gas is defined as the response of the sensor in presence of the test gas (LPG) to reference atmosphere (air) and is given by.

$$S_g = \left[\frac{R_a}{R_g}\right]$$

Sensitivity is very high for 10 wt% of $NaVO_3$ in PANI among all the composites as shown in Fig. 9b, the gas is introduced into the chamber is at a study rate of 25 ml/min, the composite response starts by changing its resistance instantaneously after the introduction of gas, the sensitivity of sensing composite is due to the presence of the large number of pores which is revealed by SEM, hence 0.1 wt of $NaVO_3$ in PANI is highly sensitive to detect LPG. The.

It has been reported from our study, 0.1 wt of $NaVO_3$ in PANI has shown the highest change in resistance among all the composites in the presence of test gas LPG as in Fig. 10a. The change in resistance for 925 PPMV (low concentration) is 10 Ω, but for 22,624 PPMV (high concentration) is 3.21 kΩ, for 0.5 wt of $NaVO_3$the change in resistance for 925 PPMV (low concentration) is 90 Ω, but for 22,624 PPMV (high concentration) is 1.98 kΩ.the difference of change in resistance from low concentration of LPG to high concentration is 3.2 kΩ and 1.89 kΩ for 0.1 and 0.5 wt. Among all five composites, 0.1 and 0.5 wt of $NaVO_3$ in PANI have the highest sensitivity and selectivity with good response for LPG detection, Fig. 10b shows there is a large difference in resistance is sufficient to produce an electrical signal from the composite in presence of LPG with good resolution[36].

Table 2 The performance of the detection of LPG of present work compared with the previous reports

SN	Composite	wt%	Resistance at Gas Concentration		Resistance Range (in Ohm)	Ref
			952 (in PPMv)	22,624(in PPMv)		
01	PANI / $MgCrO_4$	40 wt%	14.3	102	87.7	[21]
02	PANI / $MgCrO_4$	50 wt%	9.8	94	84.2	[21]
03	PANI / $Sr_3(AsO_4)_2$	20 wt%	54	1544	1490	[35]
04	PANI / $Sr_3(AsO_4)_2$	30 wt%	16	1077	1061	[35]
05	PANI / $NaVO_3$	10 wt%	10	3210	3200	Present work
06	PANI / $NaVO_3$	50 wt%	90	1980	1890	Present work

The sensing mechanism is either oxidation or reduction; that is an electron transfer from sensing material to gas decreases the resistance or gas to sensing material increases the resistance, which depends on the surface area of interaction. As the surface area of interaction increases, the sensitivity also increases, this surface area of interaction depends on poursivity of the sensing material. In our study, we find that poursivity is more for 0.1 and 0.5 wt of $NaVO_3$ composites as reviled by SEM.

The performance of detection of LPG earlier reported composites are as shown in Table 2. We observe that the range of change in resistance in the present work is much more than the previous work, hence PANI / $NaVO_3$ composite is a competent material for LPG sensing.

Thus the PANI / $NaVO_3$ composites have high sensitivity towards the presence of LPG, hence it is found to be a promising composite for low humidity and LPG sensing material for the fabrication of sensor devices.

Conclusions

Polyaniline and PANI / $NaVO_3$composites are synthesized by in situ chemical polymerization method. The X-RD pattern confirms the monoclinic crystalline structure of $NaVO_3$ and it has reserved its crystalline structure after it is distributed in the PANI matrix during the formation of the composite.FTIR spectra confirm the polymerization of aniline and PANI /$NaVO_3$ composite, by showing metal–oxygen stretching frequency and moved towards higher frequency side, this is attributed to week Vanderwall bond interaction between $NaVO_3$ and polyaniline chain. SEM reveals that the distribution of crystalline grains of $NaVO_3$ in PANI matrix, further the porous structure with capillary pores connected. Thermally activated dc-conductivity was observed, wherein conductivity increases with temperature for all the composites. The decrease in the conductivity with an increase in $NaVO_3$ in the PANI matrix is attributed to the blocking of charge carriers hopp due to the reduced chain length polymer matrix. The decrease in the resistance with increasing humidity is due to the mobility of $NaVO_3$ due to the capillary condensation of water molecules within the sensing material. The increase in resistance, hence decrease in conductivity with the concentration of LPG is due to the week charge-transfer complex between the polymer matrix and test gas is responsible for charge removal, here the polymer matrix acts as a donor, and test gas LPG act as an acceptor. This sensors composite works at room temperature which is an added advantage over conventional ceramic sensors which work at elevated temperatures. The 0.1 and 0.5 wt of $NaVO_3$ in PANI has shown the highest sensitivity and selectivity for the detection of LPG at room temperature.

References

1. Mac Diarmid AG, Chiang JC, Richter AF, Epstein AJ (1987) Polyaniline: A new concept in conducting polymers. Synth Met 18(1–3):285–290
2. MacDiarmid AG, Yang LS, Huang WS, Humphrey BD (1987) Polyaniline: Electrochemistry and application to rechargeable batteries. Synth Met 18:393–398
3. Machappa T, Ambika Prasad MVN (2009) Low-frequency AC conduction in Polyaniline / Zinc tungstate (PANI/$ZnWO_4$) composite. Ferroelectrics 392:71–80
4. Majunatha S, Machappa T, ASunilkumar, Y TRavikiran, (2018) Tungsten disulfide: An efficient material in the enhancement of AC conductivity and dielectric properties of polyaniline. J Mater Sci Mater Electron 29:11581–11590
5. Sunilkumar A, Manjunatha S, Machappa T, Chethan B, Ravikiran YT (2019) A tungsten disulphide-Polypyrrol composite based – humidity sensor at room temperature. Bullion of Materials Science 42(271):1–5
6. Khened BS, Machappa T, Ambika Prasad MVN, MSasikala, (2012) Studies on DC conductivity and LPG sensing behavior of PANI/CeO_2 composite. Int J Sci Res 1(4):180–184
7. Patil RC, Patil SF, Mulla IS, Vijayamohanan K (2000) Effect of protonation media on chemically and electrochemically synthesized polyaniline. Polym Int 49:189–196
8. Cantalini C, MPelino, (1992) Microstructure and humidity-sensing characteristics of α-Fe_2O_3 ceramic humidity sensors. J Am Ceram Soc 75:546–551
9. Trivikrama Rao GS, Tarakarama Rao D (1999) Gas sensitivity of ZnO based thick film sensor to NH_3 at room temperature. Sens Actuators B 55:166–169
10. Nakata S, Takemur K, Neya K (2001) Non-linear dynamic responses of a semiconductor gas sensor: evaluation of kinetic parameters and competition effect on the sensor response. Sens Actuators B 76:436–441
11. Khened BS, Machappa T, Pradeep MVN, Ambika Prasad MVN, Sasikala M (2016) Studies on LPG Sensing Property of Polyaniline / $BaZrO_3$ Composites. Mater Today: Proc 3:369–375
12. Srivastava A, Rashmi KJ (2007) Study on ZnO – doped tin oxide thick film gas sensors. Mater Chem & Phys 105:385–390
13. Wagh MS, Jain GH, Patil DR, Patil DR (2007) Surface customization of SnO_2 thick film using RuO_2 as a surfactant for the LPG response. Sens Actuators B 122:357–364
14. Scrosati B (1993) Encyclopedia of polymer science and engineering London: Chapman and Hall, Chapter 7
15. Palmisano F, De Benedetto GE, Zambonin CG (1997) Lactate amperometric biosensor based on an electrosynthesizedbilayer film with covalently immobilized enzyme. Analyst 122:365–369
16. Bai H, Shi G (2007) Gas sensors based on conducting polymers. Sensors 7(3):267–307
17. Lee CY, Lee GB (2005) Humidity Sensors: A Review. Sens Lett 3(1–4):1–15
18. Majunatha S, Machappa T, Ravikiran YT, Chethan B, Sunilkumar A (2019) Polyaniline based stable humidity sensor operable at room temperature. Phys Rev B Condens Matter 561:170–178
19. Sasikala M, Anilkumar KR, Prasad MA (2009) Humidity sensing behavior of polyaniline/strontium arsenate composite. Sens Transducers 107(8):77–85
20. Machappa T, Anilkumar KR, Sasikala M, Prasad MA (2008) Design of sensor setup and study of humidity sensing behaviour of conducting polyaniline/ceramic composites. In2008 3rd International Conference on Sensing Technology Nov 30-Des 3, (Tainan, Taiwan) 284–288
21. Machappa T, Sasikala M, Prasad MA (2010) Design of Gas Sensor Setup and Study of Gas (LPG) Sensing Behavior of Conducting

Polyaniline/Magnesium Chromate ($MgCrO_4$). IEEE Sensors Journal 10(4):807–813
22. Manjunatha S, Sunilkumar A, Ravikiran YT, Machappa T (2019) Effect of holmium oxide on impedance and dielectric behavior of polyaniline - holmium oxide composite.Journal of material science. Materials Electronics 30:10332–10341
23. Koenig JL (1999) Spectroscopy of polymers. Amsterdam: Elsevier, 2nd ed
24. Pavia DL, Lampman GM, Kriz GS (2001) Introduction to spectroscopy. Fort Worth: Harcourt College Publishers, 3rd ed
25. Machappa T, M V NAmbika Prasad, (2009) AC Conductivity and Dielectric Behavior of Polyaniline / Sodium Metavenadate (PANI/NaVO3) Composites. Phys B 404(21):4168–4172
26. Manjunatha S, Ravikiran YT, Chethan B, Devendrappa H, Machappa T (2020)Alternating current response studies on polyaniline – neodymium oxide composite. AIP: Conference proceedings 2244:08009:1–4
27. Mott NF, Davis E (1979) Electronic process in non-crystalline materials. (ede) Clarendon press, Oxford
28. Salunkhe RR, Shinde VR, Lokhande CD (2008) Liquefied petroleum gas (LPG) sensing properties of nanocrystallineCdO thin films prepared by chemical route: Effect of molarities of precursor solution. Sensors and Actuators B 133:296–301
29. Kobayashi A, Ishikawa H, Amano K, Satoh M, Hasegawa E (1993) Electrical conductivity of annealed polyaniline. J Appl Phys 74(1):296–301
30. Olmedo L, Chanteloube I, AGermain, M Petit, E M Genies, (1989) Characterization of electrochemically prepared conductive polymers by in-situ conductivity measurements. Synth Met 28(1–2):165–170
31. Sunilkumar A, Manjunatha S, Chethan B, Ravikiran YT, Machappa T (2019) Polypyrrole–Tantalum disulfide composite: An efficient material for fabrication of room temperature operable humidity sensor. Sensors and Actuators A 298(111593):1–8
32. Machappa T, Prasad MA (2012) Humidity sensing behaviour of polyaniline/magnesium chromate (MgCrO 4) composite. Bull Mater Sci 35(1):75–81
33. Roy AS, Anilkumar KR, Sasikala M, Machappa T, Prasad MV (2011) Sensitivity enhancement for LPG detection by employing cadmium oxide doped in nanocrystalline polyaniline. Sens Lett 9:1–7
34. Hosseini SH, Abdi OS, Entezami AA (2005). Toxic gas and vapor detection by polyaniline gas sensors. Iran Polym J (English) 14(4(58)):333–344
35. Machappa T, Badrunnisa S (2020) Strontium arsenate doped conducting polyaniline matrix as gas sensor. InJournal of Physics: Conference Series 1706(012015):1–7
36. Roy AS, Machappa T, Prasad MA, Anilkumar KR (2011) Sensitivity and selectivity studies on polyaniline/molybdenum trioxide composites to liquid petroleum gas. Sens Transducers 125(2):220–228

Asian Journal of Chemistry; Vol. 33, No. 10 (2021), 2455-2464

ASIAN JOURNAL OF CHEMISTRY

https://doi.org/10.14233/ajchem.2021.23202

Synthesis, Spectroscopic Investigation and Catalytic Behaviour of Histidine Substituted Nickel(II) Phthalocyanine

K.R. VENUGOPALA REDDY[1,*], T.M. SHARANAKUMAR[1,2], MOUNESH[1], N.Y. PRAVEENKUMAR[1], SURESH[2] and N.H.M NANDINIBABY[3]

[1]Department of Studies and Research in Chemistry Vijayanagara Sri Krishnadevaraya University, Bellary-583105, India
[2]Department of Chemistry, Ballari Institute of Technology and Management, Jnana Gangotri Campus, Bellary-583104, India
[3]Department of Physics, Ballari Institute of Technology and Management, Jnana Gangotri Campus, Bellary-583104, India

*Corresponding author: E-mail: venurashmi30@gmail.com

Received: 9 March 2021; *Accepted*: 11 August 2021; *Published online*: 20 September 2021; AJC-20520

In this work, the oxidation behaviour of phenol and chlorophenol contaminants present in the water catalyzed by histidine substituted nickel(II) phthalocyanine (NiPc) is reported. This work comprises synthesis, characterization and study the catalytic behaviour of histidine substituted NiPc on the oxidation of phenol and their substrates like 2- and 4-chlorophenols with 4-aminoantipyrine utilizing molecular oxygen. The products from the oxidation can be analyzed by UV-Vis spectroscopy and the results confirmed the formation of superoxide anion radical were crucial for the formation of product and a feasible mechanism including a successive transfer of single electron from phenolic compounds to O_2 through the axis of histidine Ni(II)Pc was reported.

Keywords: Histidine, Nickel(II) phthalocyanine, 4-Aminoantipyrine, Phenol, Chlorophenol, 2,4-dichlorophenol, Catalytic oxidation.

INTRODUCTION

Chlorophenols, which are employed as intermediates in the synthesis of pesticides, herbicides, fungicides, paper industries and dyes are the one of the most abundant environmental contaminants [1-5]. Contamination with numerous phenol substrates is observed in drinking water and industrial wastewaters, and toxic compounds are found in the atmosphere [6,7]. Presently, several methods are used for the estimation and analysis of phenol pollutants in soil or water. An estimation method involves the oxidation of phenol substrate with 4-aminoantipyrine (4-AAP) to form a pink antipyrilquinoneimine dye. This catalytic oxidation reaction (COR) can be catalyzed through many catalysts [8-12]. The reactive ability and nature of catalysts directly influences its sensitivity and accuracy. With 4-aminoantipyrine, phenol substrates undergo oxidation through molecular oxygen [13]. Molecular oxygen is readily available, eco-friendly, presents outstanding oxidative behaviour and has led to green chemistry development [14]. 4-Aminoantipyrine is a metabolite of antipyrine, which serves as anti-inflammatory and antipyretic agents [15]. 4-Aminoantipyrine causes cations and anions to become detectable in the chemosensing method [16-18]. The products of 4-aminoantipyrine can be highly effectively used to estimate phenols, phenol substrates, glucose contents in phenols, uric acid and peroxidase in hydrogen peroxide [19].

The complexes of metal phthalocyanine (MPc) exhibit low environmental hazards, show an excellent catalytic activity, and present critical applications dye industries. MPcs have stable higher oxidation states and electro-active central metal ions; thus, they are important in chlorophenol COR. MPcs assist in numerous oxidation reactions, such as nitrile and nitrate oxidation [20], L-cysteine oxidation [21], molecular O_2 reduction [22], olefin oxygenation [23] and water electrolysis [24]. Few researchers [25,26] have reported catalyst applications to acquire a substitute for activators and found the means to conduct reactions at low temperatures with less reaction time.

In this study, the HisNiPc complex was synthesized through a reaction between histidine, tetracarboxylic acid and Ni(II) phthalocyanine (NiTcPc). The FTIR, UV-visible, elemental analysis results supported HisNiPc formation. The thermal stability of the complex was studied using thermogravimetric estimation and its molecular morphology was investigated through PXRD. The HisNiPc was used for the first time in the

catalytic oxidation reaction (COR) of phenol contaminant substrates and phenol in water. Phenolic compounds, including phenol, *p*-chlorophenol (*p*-CP), *o*-chlorophenol (*o*-CP) and 2,4-dichlorophenol (DCP), readily undergo oxidation by using dissolved oxygen in the presence of prepared catalyst, HisNiPc. Phenol substrates vigorously react with 4-aminoantipyrine to produce a pink dye. The catalytic oxidation reaction (COR) and their products were investigated through UV-visible spectroscopy. The results confirmed the chromogenic recognition of phenolic pollutants.

EXPERIMENTAL

All chemical compounds, solvents and reagents were of high grade and used without purification (Sigma-Aldrich, India). The reaction was performed under the nitrogen atmosphere. Some chemicals were prepared in oxygen-free distilled water. Nickel(II) phthalocyanine (NiTcPc) was synthesized by known procedure [27,28]. The FT-IR spectra have been recorded with a Perkin-Elmer 1600 FT-IR spectrophotometer using KBr pellets. Electronic spectra were recorded on a Perkin-Elmer Lambda 25 spectrophotometer in DMF. The XRD spectra was measured by Bruker D8 diffractometer Cu*K*α radiation source. Thermal stability of the synthesized HisNiPc was analyzed by thermogravimetric analysis method by way of STA-6000 system in the temperature range of 0 to 1000 ºC with the scan rate of 20 ºC min^{-1} under blow rate of 20 mL/min oxygen.

Synthesis of histidine substituted Ni(II)phthalocyanine (HisNiPc) complex: A mixture of histidine (0.05 mmol), tetracarboxylic-Ni(II)-phthalocyanine (NiTcPc) (0.003 M), K_2CO_3 (0.06 mM), DCC (10 mg) and DMF 30 mL in 250 mL and kept for stirring under nitrogen environment for 30 h at 28 ºC (**Scheme-I**). The green colour product was filtered, washed with warm water then rinsed with ethanol followed by distilled water. Finally, the HisNiPc precipitate was dried at 40 ºC for 1 h Yield: 70%. Anal. calcd. (found) % for $C_{60}H_{46}N_{20}O_{12}Ni$ (*m.w.*: 1295.82): C, 55.527 (55.501); H, 3.572 (3.551); N, 21.584 (21.576); O, 14.793 (14.773), Ni, 4.522 (4.506).

RESULTS AND DISCUSSION

FT-IR studies: The key IR bands of HisNiPc complex was observed at 1652-1621, 1560-1480, 1440-1410, 1325-1315, 1290-1245, 1231-1210, 1140-1120, 1110-1050, 935-930, 830-820, 780-740 and 710-670 cm^{-1}. While for NiTcPc complex, the key IR bands were observed at 3400-3200 (amide peak), 3000-2800 (C=N), 1652-1621 (C=C), 1560-1480 (-C=C-N=), 1325, 1315, 1299, 1245, 1230, 1210, 1137 (C-O), 1120, 1050, 930, 820, 740, 710 cm^{-1} (Fig. 1).

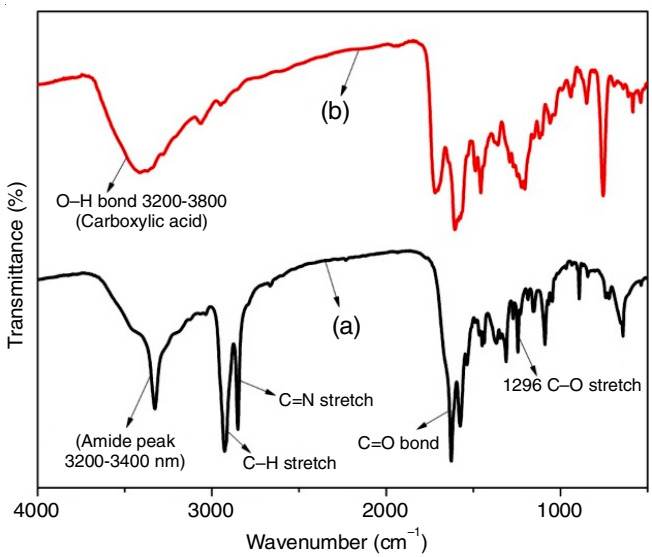

Fig. 1. FT-IR spectra (cm^{-1}) of (a) HisNiPc complex (b) NiTcPc complex

UV-Vis studies: The UV-Vis spectra of HisTcPc and NiTcPc in DMSO (Fig. 2), which is the characteristic absorptions range between 600-700 nm in the Q band region [29,30]. The Q band observed was ascribed to the π-π* transition from the HOMO to the LUMO of phthalocyanine (Pc) ring. The other bands (B) in the UV region at 290-390 nm were observed due to the transitions from the deeper π levels to the LUMO. The HisNiPc complex obtained in this study did not give

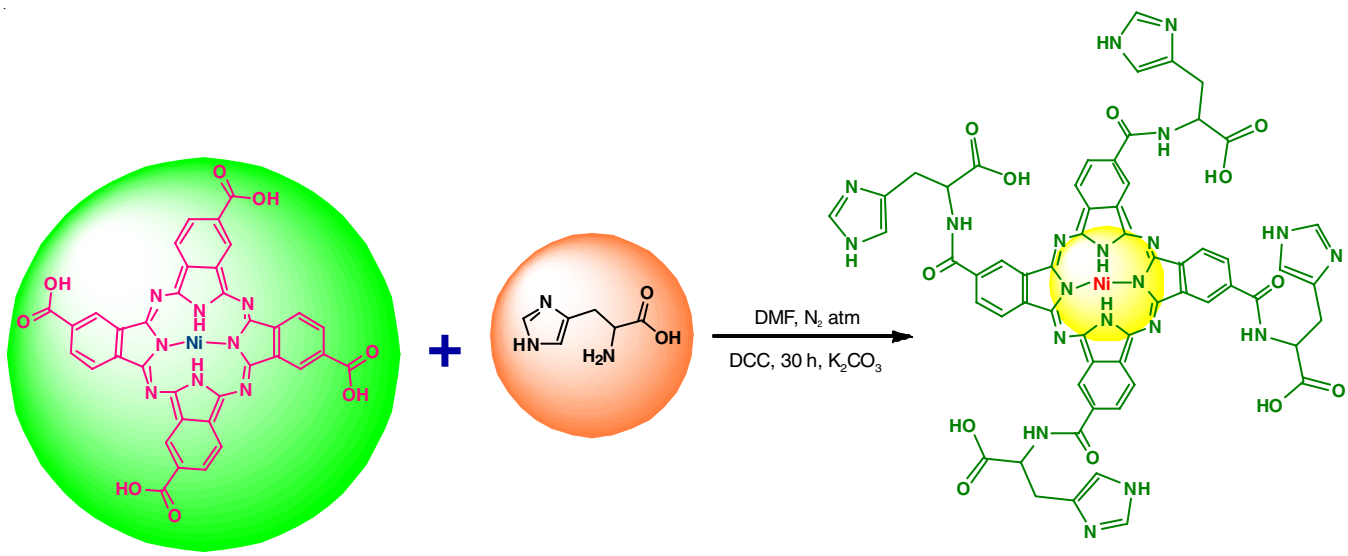

Scheme-I: The synthetic route for the preparation of HisNiP complex

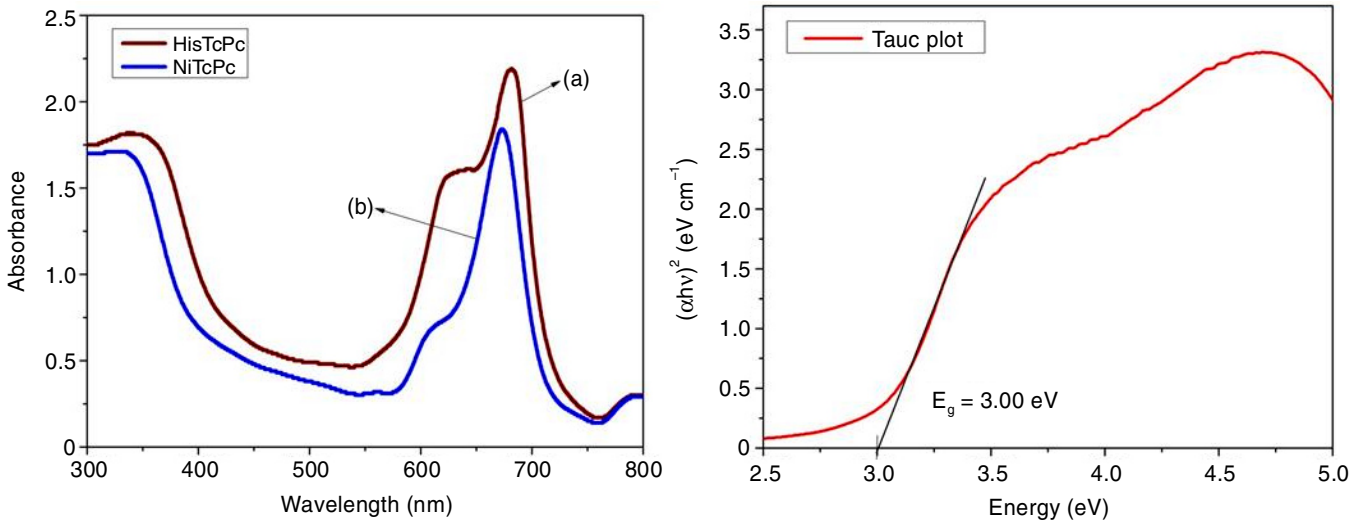

Fig. 2. UV-vis spectra of (a) HisNiPc complex (b) NiTcPc complex (S2) Tauc Plot of the HisNiPc complex

shoulder spectrum in DMSO while NiTcPc gave shoulder at 608 nm. The electronic spectrum showed monomeric behaviour evidenced by a single Q band, typical for metal bonded phthalocyanine complexes.The optical band gap was determined from the Tauc plot using eqn. 1:

$$\alpha h\nu = \alpha_0(h\nu - E_g)^n \quad (1)$$

Mass studies: The theoretical observation of mass spectra of HisNiPc complex was 1297.82 and the experimental mass of the HisNiPc exhibits molecular ion peak at 1295.82 (Fig. 3), which is in the agreement with the the proposed structure of the compound.

Thermal studies: Fig. 4 showed the thermal stability of HisNiPc complex. In the first step, the evaporation of water took place at 235.75 ºC; in the second step, HisNiPc undergoes the degradation and decomposition of the substituent with 29.6% of weight loss occured at 286.66 ºC and in the third step, the phthalocyanine ring decomposed with 7.45% of weight loss, finally, metal was converted into metal oxide 20.23% of weight loss at 580.60 ºC [31,32]. The experimental results showed that the HisNiPc complex exhibited good thermal stability at 235.75 ºC. It indicates that the melting point and stability of the HisNiPc complex was high ≥ 580.60 ºC. Therefore, the HisNiPc complex was suitable for an electrochemical and chemical reaction.

XRD studies: The powder XRD of HisNiPc complex was obtained by a Cu*K*α radiation source (λ = 1.540 Å) [31,33-36]. The diffraction pattern of HisNiPc complex shows the broad peaks with different diffused intensity, the intensity of peak increased by histidine group (Fig. 5). The less intensity and short peak observed at 2θ values of 100º, 150º, 160º, 170º, 190º, 200º, 300º and 450º. A highly long and sharp peak was observed at 2θ values of 50º, 60º, 120º, 130º and 180º indicates that HisNiPc was amorphous. The XRD analysis also shows the good microstrain and dislocation density of the HisNiPc complex.

Catalytic oxidation: The catalytic oxidation reactions (CORs) of substituted phenols with 4-aminoantipyrine (4-AAP) using HisNiPc as catalyst were carried out (**Schemes II and III**). In a 100 mL beaker, 30 mL demineralized water, 6 mL of 4-AAP (1.5×10^{-3} mol/L) and 6 mL of substituted phenol were thoroughly mixed followed by the addition of 0.01 mM of HisNiPc. The reaction mixture was ultrasonicated for 5 min with continous stirring at 30 ºC. The product was filtered and analyzed with a UV-visible spectrophotometer. The product was then washed with deionized water until pink colour disappeared and kept for drying in 30 ºC in an oven. The dry HisNiPc powder was washed finally with hot water and dried at 110 ºC.

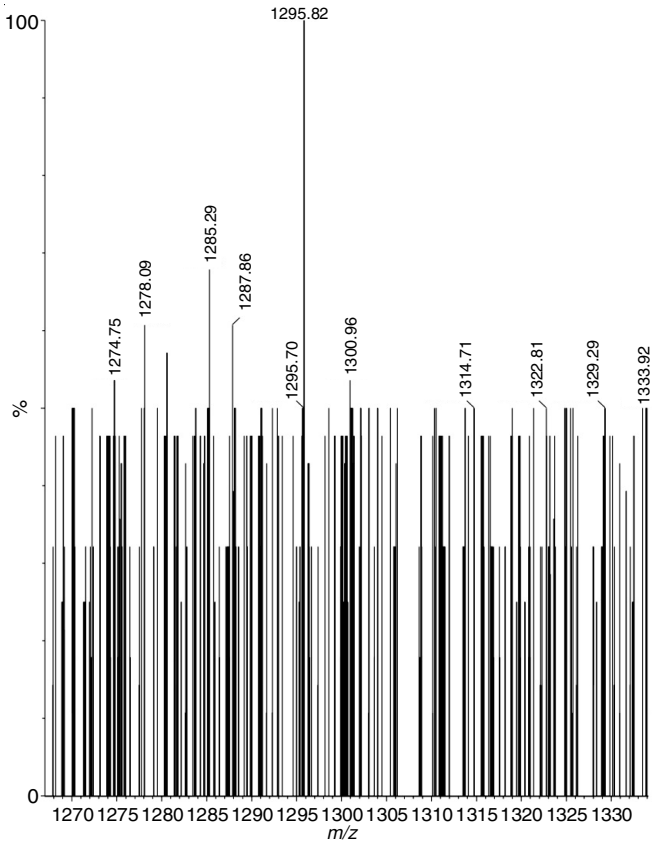

Fig. 3. Mass spectrum of HisNiPc complex

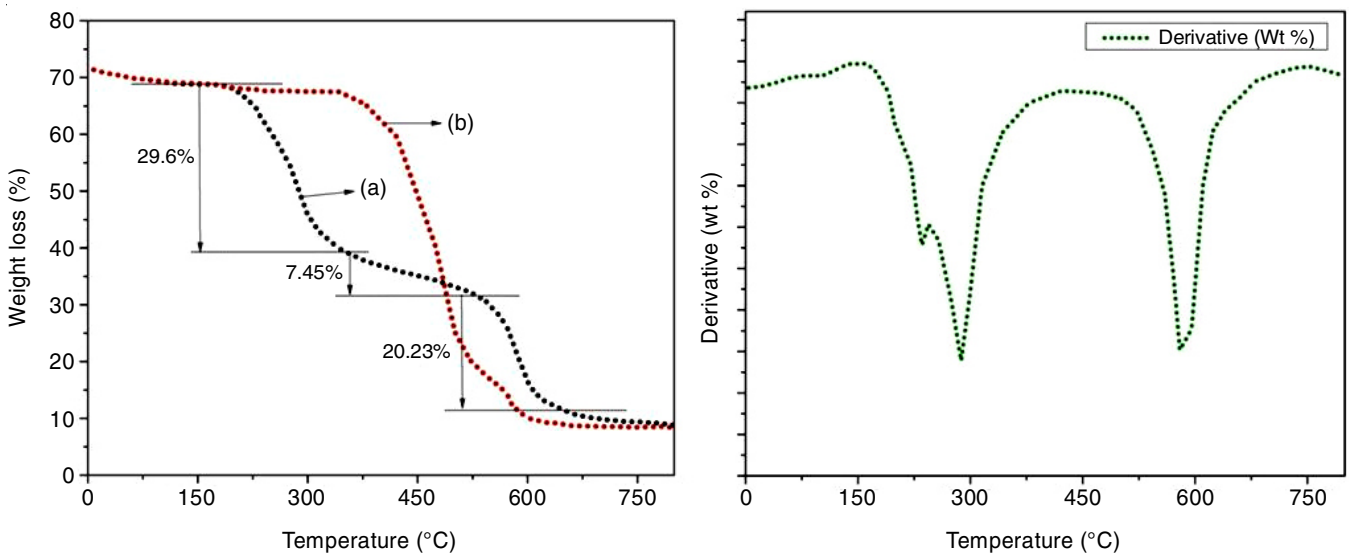

Fig. 4. Thermo gravimetric analysis of (a) HisNiPc complex (b) NiTcPc complex derivative (wt.%) of HisNiPc complex

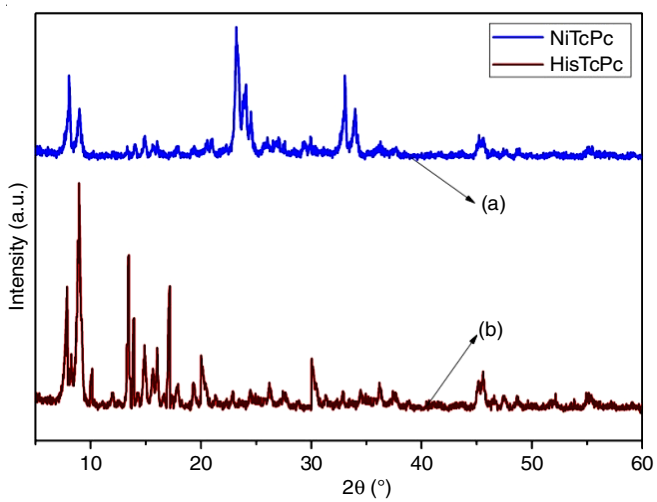

Fig. 5. XRD spectra of (a) NiTcPc (b) HisNiPc

Catalytic-oxidation of phenols and chloro phenols by UV-visible method: The UV-Vis chromogenic absorption spectra of *o*-CP, DCP, *p*-CP and phenol with 4-aminoantipyrine in the presence of HisNiPc as catalyst at regular intervals is shown in Fig. 6. The characteristics peaks corresponds to the formation of dye at 520 nm indicates that COR of phenols converted into chloro substituted anti-pyrilquinoneimine dye [37]. The intensity of dye can be observed more in the range of 500-530 nm or observed at low intense in the range of 210-350 nm within 120 min. After 120 min, no further change was observed in the absorption, thus considered as the endpoint of a reaction. The absorption intensity was observed at 520 nm, the catalytic reactivity trends for various phenol compounds were in the order of *o*-CP > DCP > phenol > *p*-CP.

Catalytic oxidation of phenol substrates by varying pH: The COR of phenols with 4-aminoantipyrine (4-AAP) was carried out with different pH conditions [38]. The pK_a value for the deprotonation of *o*-CP and DCP, the hydroxyl species is 8.49 and 7.86, respectively; therefore, phosphate buffer solution (PBS, pH 9 and 10) and acetic acid buffer solution (pH 4 and 5) as well as demineralized water was utilized to study the catalytic reaction by varying with pH.

Fig. 7 shows the dye formation process in *o*-CP, DCP, *p*-CP and phenol system at various pH. In *o*-CP system (Fig. 7a), the catalytic reaction was over after 2 h at pH-7.0 and 2.5 h at pH 4 and 5, while the reaction was continued after 4 h at pH 9 and 10. From these results, the COR of *o*-CP in demineralized water, more dye formed at pH 7 within 120 min. The formation of dye at pH 4 and 5 occured after 150 min, and at pH 9 and 10 occured at ≥ 240 min. The reactions of DCP at studied pH (Fig. 7b) was also similar to *o*-CP.

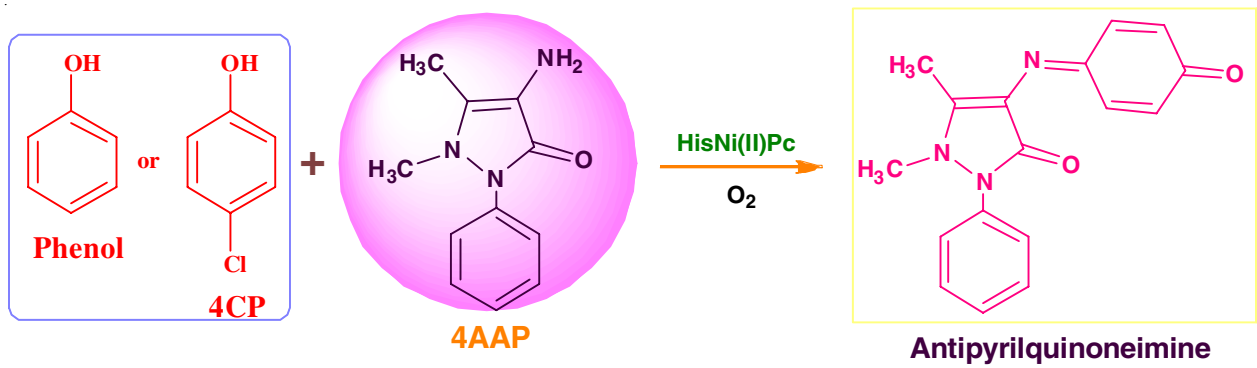

Scheme-II: Phenol and *p*-CP oxidized with 4-AAP in the existence of dioxygen and HisNiPc catalyst

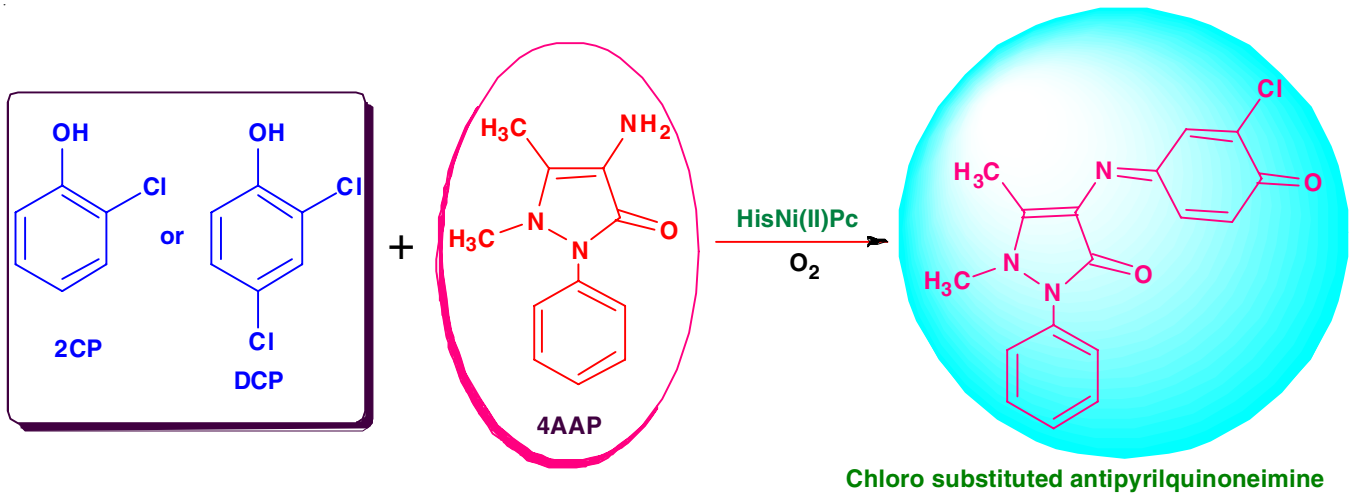

Scheme-III: Catalytic oxidation of *o*-CP and DCP with 4-aminoantipyrine in the existence of dioxygen and HisNiPc catalyst

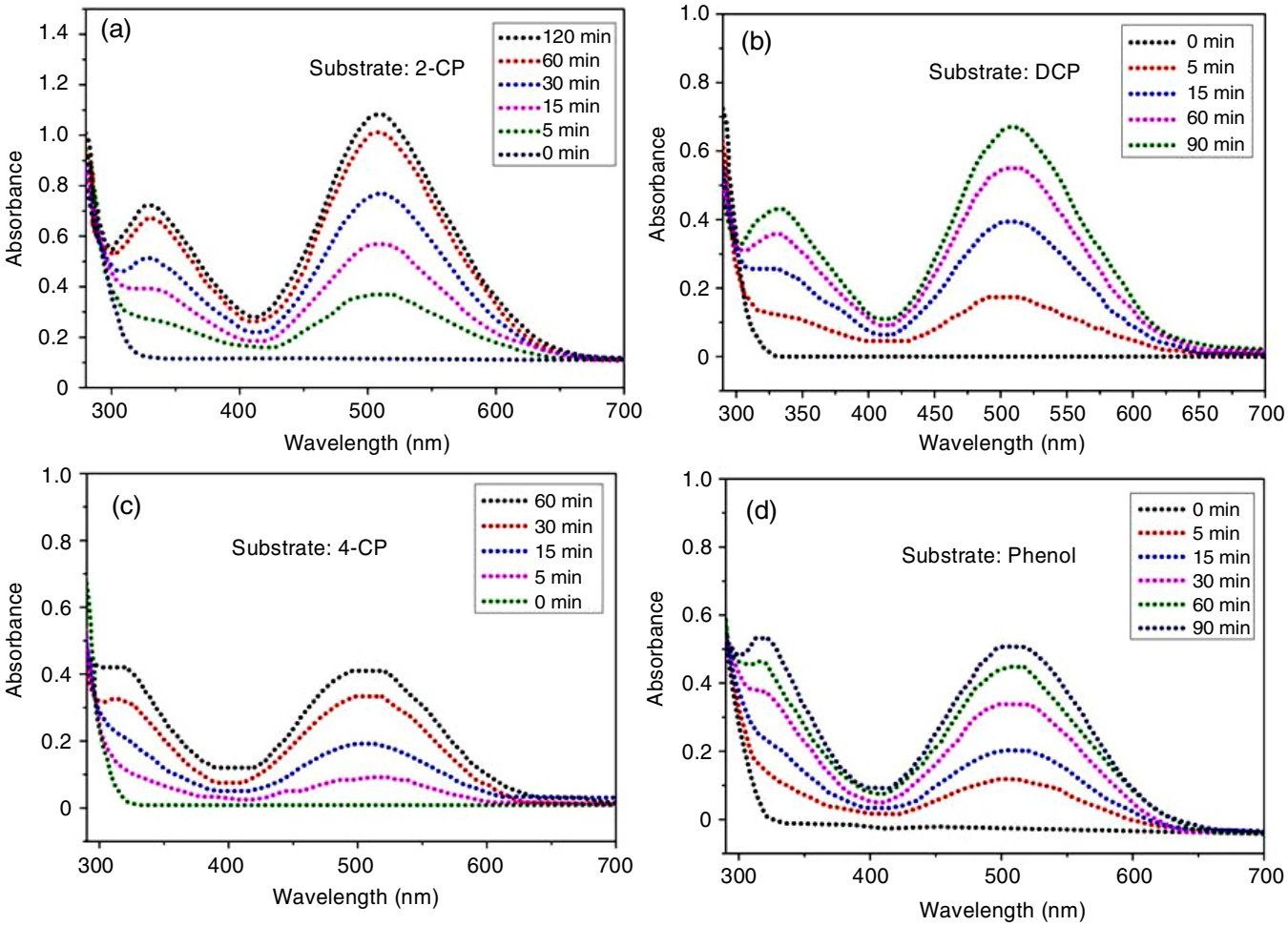

Fig. 6. Catalytic oxidation of phenol substrate with 4-aminoantipyrine in the existence of O_2 and HisNi(II)Pc catalyst (a) *o*-CP (b) DCP (c) *p*-CP and (d) phenol

In *p*-CP (Fig.7c), the reaction was over after 2.5 h at pH 7.0 and 3.0 h at pH 4 and 5, while the reaction proceeded after 5 h at pH 9 and 10. From these results, the COR of *p*-CP in demineralized water, maximum dye yield at pH 7.0 was occured at ≥ 150 min. The formation of dye at pH 4 and 5 occured after 180 min and at pH 9 and 10, the dye formed after 300 min. The reaction of phenol of studied pH was similar to *p*-CP but small variation was observed at pH 9 and 10, as shown in Fig. 7d.

Catalytic oxidation of phenol substrates by the catalytic quantity: The catalytic role is important in the formation of dye yield. The HisNiPc catalytic dosage of 10 mg, 15 mg, 20

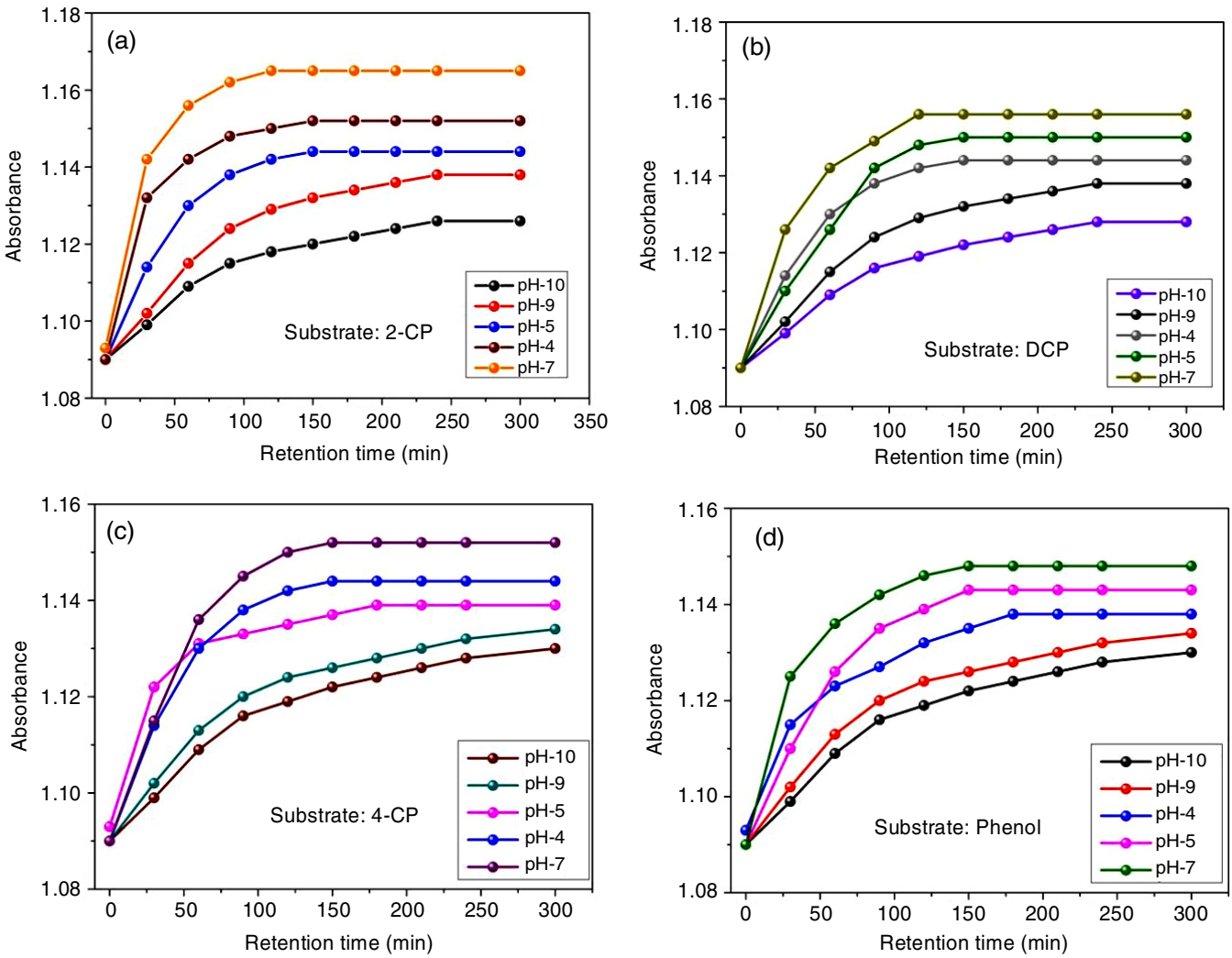

Fig. 7. Catalytic-oxidation of phenol substrate by UV-vis absorption method by variation of pH of (a) *o*-CP (b) DCP (c) *p*-CP and (d) phenol

mg, 25 mg and 30 mg was used for the catalytic oxidation of *o*-CP, DCP, *p*-CP and phenol. The maximum absorption was monitored within 300 min as shown in Fig. 8. The *o*-CP, DCP, *p*-CP and phenol results showed that 20 mg of HisNiPc catalyst contributed to the maximum formation of dye, since at this amount, the activation energy reduces more and the reactants easy to convert into the product. However, excess of catalyst 30 mg did not contributed the good catalytic efficiency because of the dye deposited on the catalytic site. Thus, 20 mg HisNiPc catalyst was optimized for the formation of dye in *o*-CP, DCP, *p*-CP and phenol after 180 min.

Catalytic oxidation of phenol substrates by varying temperature: The COR of phenol substrates was performed at various temperatures *viz*. 5, 25, 40 and 60 ºC, the maximum absorption was monitored within 300 min. The results revealed that at 40 ºC, the reaction rate was faster due to COR of phenols related to the fast concussion of the radical species, therefore more dye formation takes place as shown in Fig. 9. At 60 ºC, less dye formed due to the small effect of rate of reaction on COR and it involves the pseudo-first-order reaction [37] and according to the Arrhenius theory, the rate of side reactions depends upon the yield of the dye. At 15 ºC and 25 ºC, the rate of reaction was slow thus less yield formed at low temperature. The above data indicates that the temperature was also affected by the COR of phenols and chloro phenols reactions.

Catalytic oxidation under aerobic and anaerobic conditions: The catalytic oxidation reactions of *o*-CP, DCP, *p*-CP and phenol were carried out in presence of air and no other oxidant was used. The reaction was done in a neutral atmosphere by the continuous supply of N_2 gas in the reaction mixture. Under anaerobic conditions (Fig. 10a), the rate of dye formation was more forbidden compared to typical catalysis (Fig. 10d), which indicates that oxygen is essential for the oxidation of phenols. Usually, the electrons gained by oxygen molecule to become active oxygen radical ($O_2^{\bullet-}$ and OH^-) and thus facilitating the oxidation reaction (**Scheme-IV**) [39]. The $O_2^{\bullet-}$ is also an important for the chromogenic reaction and an $O_2^{\bullet-}$ mediator in the oxidation of phenol mechanism of HisNiPc catalysis was confirmed. Further, the typical catalysis could also proceed efficiently in absence of light (Fig. 10b), which gives the evidence that in the absence of sunlight and with the presence of catalyst *o*-CP, DCP, *p*-CP and phenol, the catalytic oxidation process proceeds. The overall reaction mechanism proceeds in three steps [40] (**Scheme-V**) *viz*. step-I: formation

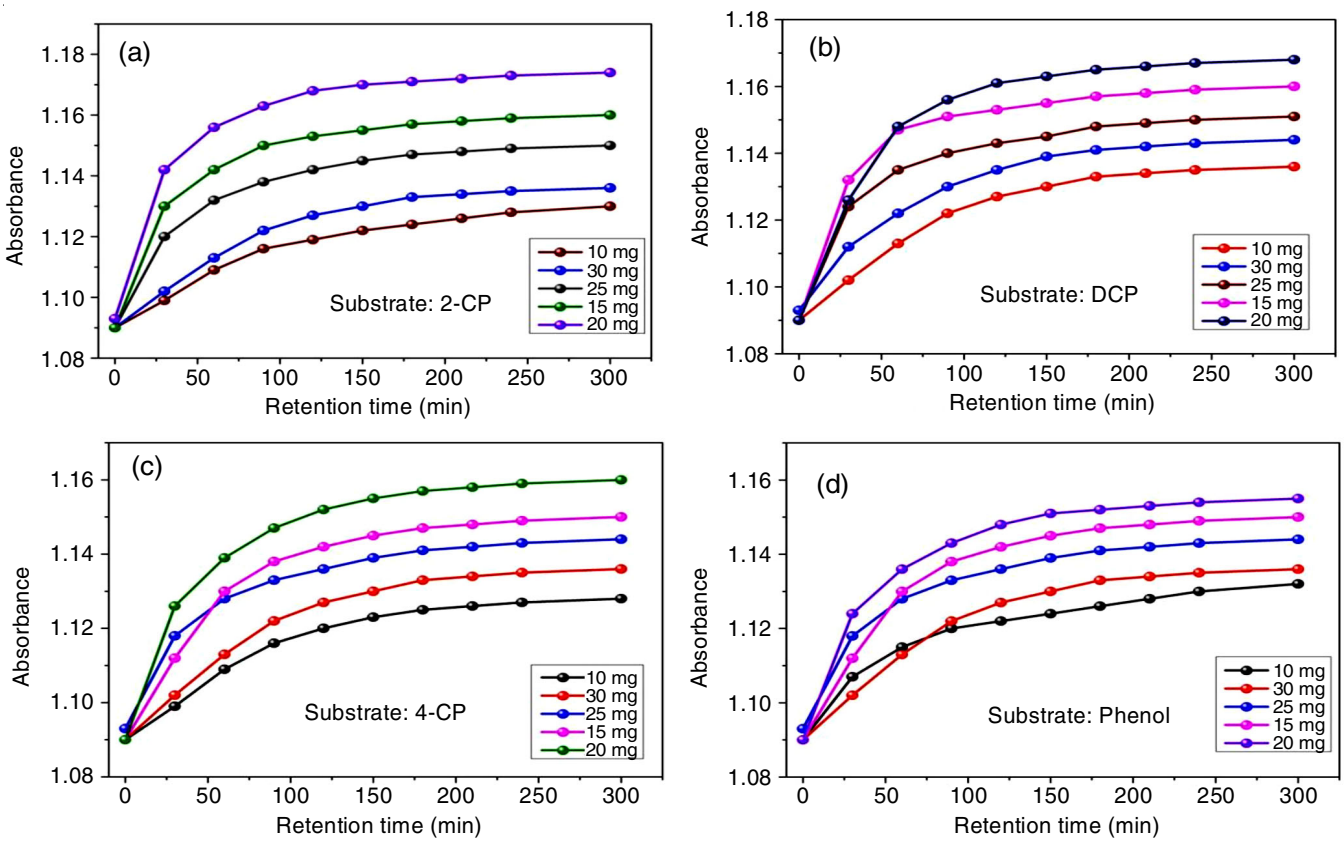

Fig. 8. Catalytic-oxidation of phenol substrate by UV-vis absorption method by variation of catalytic quantities of (a) *o*-CP (b) DCP (c) *p*-CP and (d) phenol

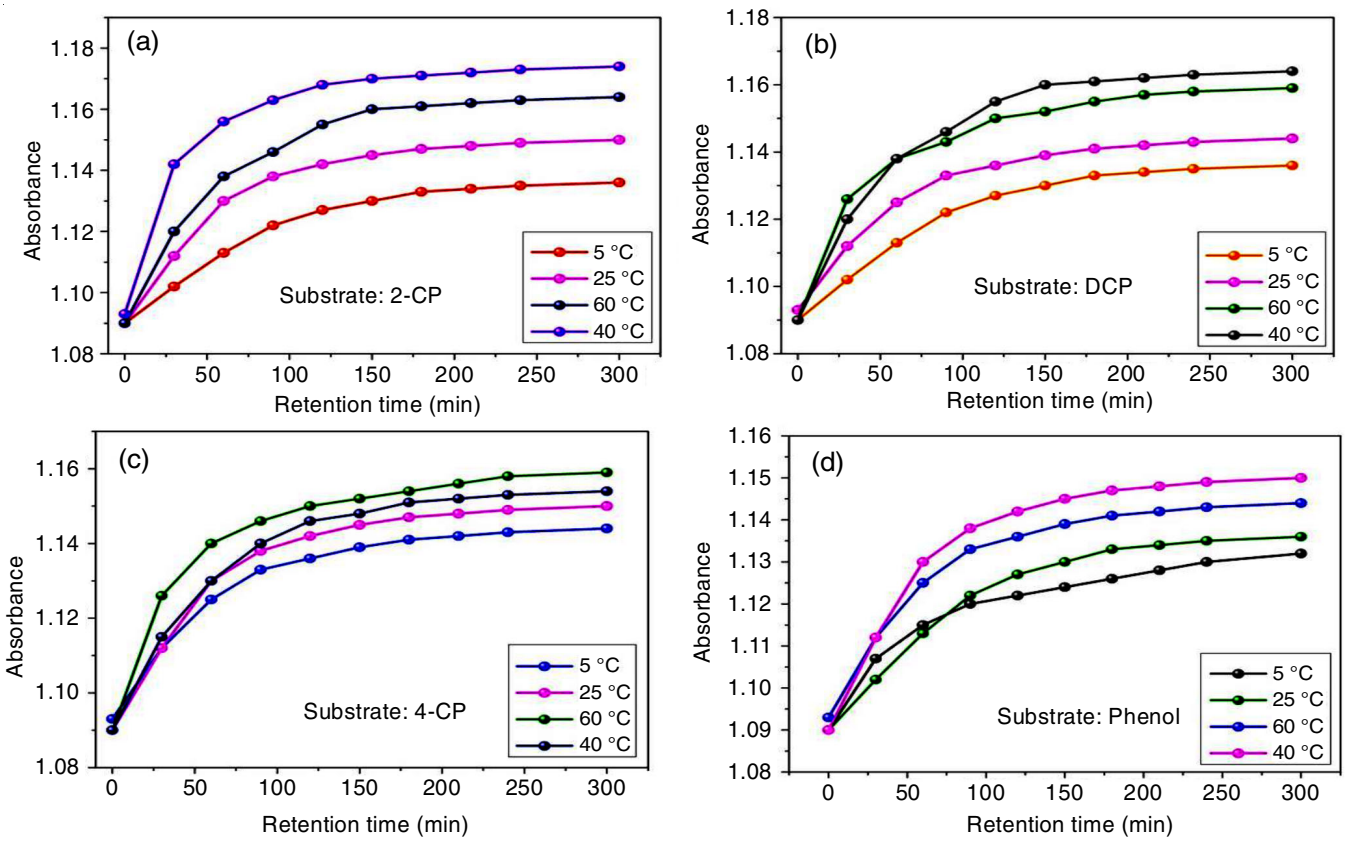

Fig. 9. Catalytic oxidation of phenol substrate by UV-vis absorption method by variation of temperature of (a) *o*-CP (b) DCP (c) *p*-CP and (d) phenol

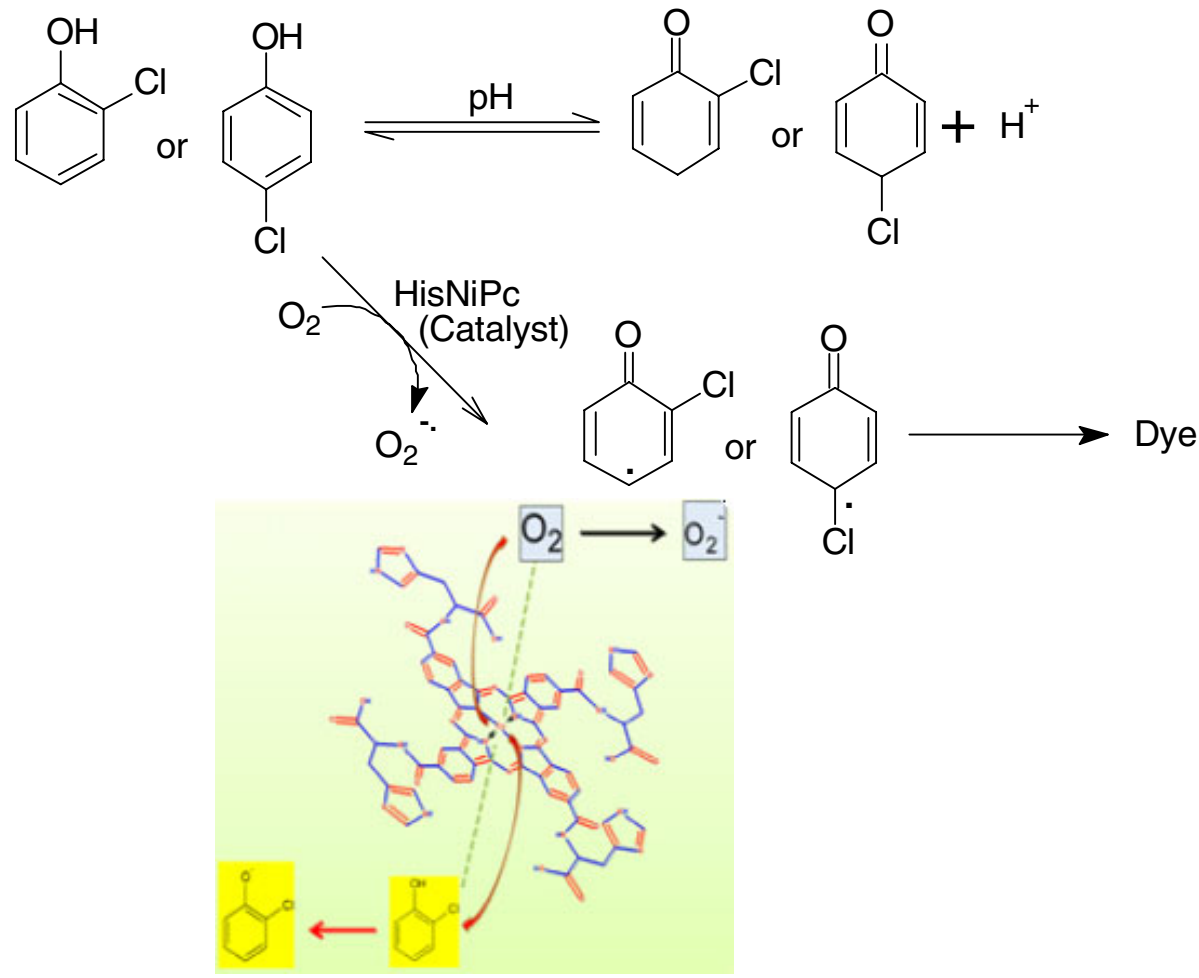

Scheme-IV: The effect of dissolved O_2 on the catalytic-oxidation of phenol substrate by UV-vis absorption method.

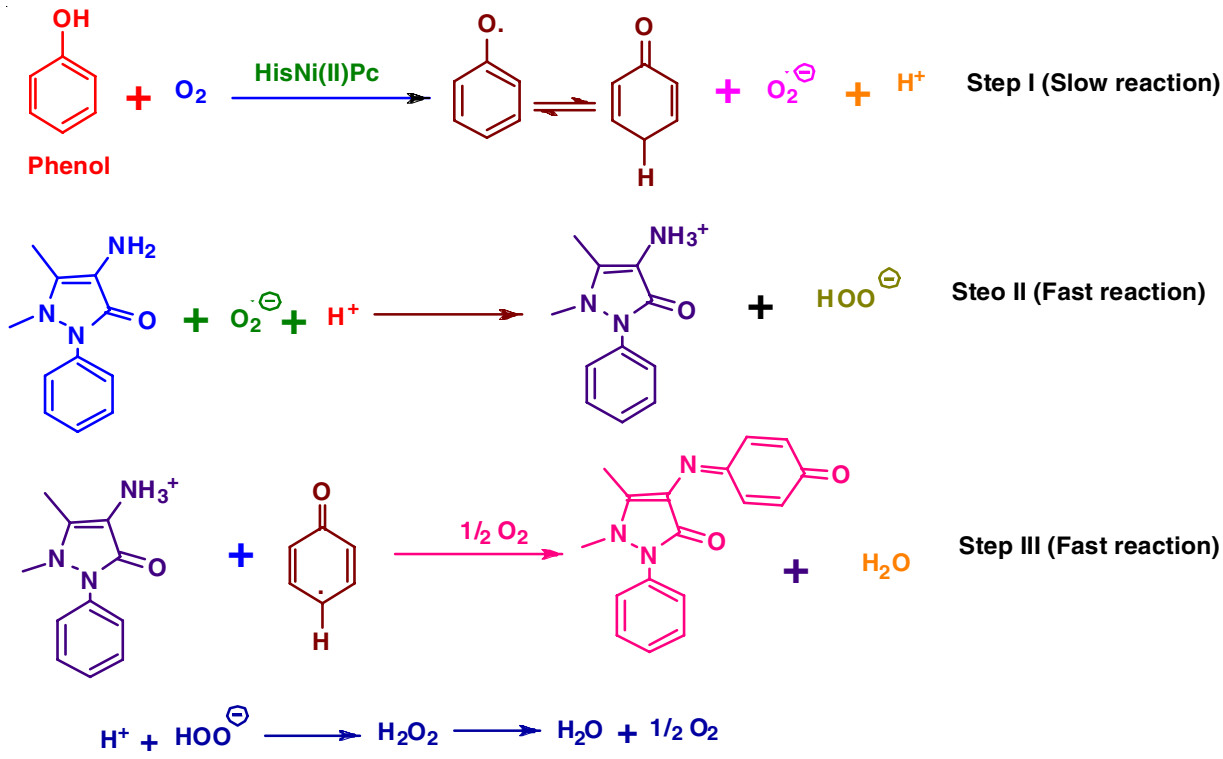

Scheme-V: The mechanism involved in the oxidation of phenol substrate (the same mechanism applicable for *o*-CP, *p*-CP and DCP)

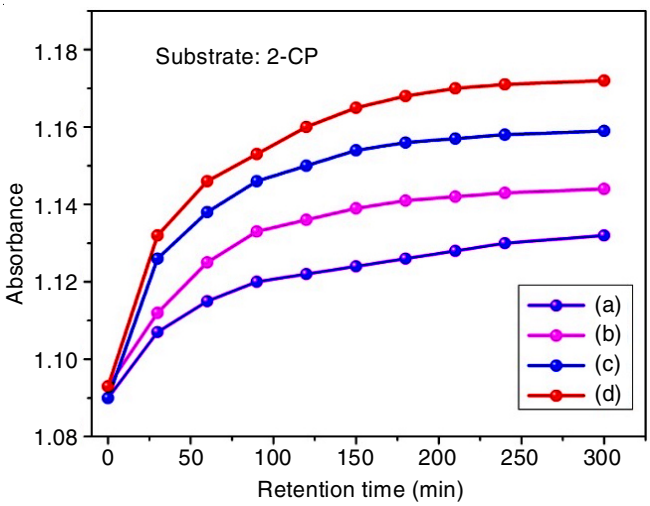

Fig. 10. Reaction curve in presence of (a) under N_2 environment with catalyst (b) dark condition with catalyst (c) sunlight (d) excess of oxygen

of *p*-quinoid radical by treating with phenol and oxygen; step-II: formation of antipyrine-NH_3^+; and step-III: formation of chloro substituted antipyrilquinoneimine dye.

Conclusion

A novel histidine substituted nickel(II) phthalocyanine (HisNiPc) complex was synthesized and chacterized by mass, FT-IR, UV-visible, elemental analysis, X-Ray diffraction and Thermogravimetric techniques. Furthemore, the catalytic oxidation behaviour of new complex against phenols and chloro phenols in water was also carried out reported. The results indicated that several phenolic compounds like *p*-chlorophenol (*p*-CP), *o*-chlorophenol (*o*-CP), 2,4-dichlorophenol (DCP) and phenol were easily oxidized in the presence of HisNiPc catalyst and rapidly reacts with 4-aminoantipyrine to produce pink dye. The formation of the pink dye involved the transfer of a single electron to dioxygen using the HisNiPc catalyst.

ACKNOWLEDGEMENTS

One of the authors (TMS) thanks Vijayanagara Sri Krishnadevaraya University and Ballari Institute of Technology and Management College, Ballari, India for extending their support to carry out this research work.

CONFLICT OF INTEREST

The authors declare that there is no conflict of interests regarding the publication of this article.

REFERENCES

1. M.Y. Ghaly, G. Härtel, R. Mayer and R. Haseneder, *Waste Manag.*, **21**, 41 (2001); https://doi.org/10.1016/S0956-053X(00)00070-2
2. C. Guillard, J. Disdier, C. Monnet, J. Dussaud, S. Malato, J. Blanco, M.I. Maldonado and J.M. Herrmann, *Appl. Catal. B*, **46**, 319 (2003); https://doi.org/10.1016/S0926-3373(03)00264-9
3. K. Abburi, *J. Hazard. Mater.*, **105**, 143 (2003); https://doi.org/10.1016/j.jhazmat.2003.08.004
4. X.M. Zhang and J. Wiegel, *Appl. Environ. Microbiol.*, **56**, 1119 (1990); https://doi.org/10.1128/AEM.56.4.1119-1127.1990
5. F.A. Banat, B. Al-Bashir, S. Al-Asheh and O. Hayajneh, *Environ. Pollut.*, **107**, 391 (2000); https://doi.org/10.1016/S0269-7491(99)00173-6
6. A. Sorokin, B. Meunier and J.-L. Seris, *Science*, **268**, 1163 (1995); https://doi.org/10.1126/science.268.5214.1163
7. B. Meunier and A. Sorokin, *Acc. Chem. Res.*, **30**, 470 (1997); https://doi.org/10.1021/ar960275c
8. J. Santhanalakshmi, J. Kasthuri and N. Rajendiran, *J. Mol. Catal. Chem.*, **265**, 283 (2007); https://doi.org/10.1016/j.molcata.2006.10.012
9. S. Sgalla, G. Fabrizi, S. Cacchi, A. Macone, A. Bonamore and A. Boffi, *J. Mol. Catal., B Enzym.*, **44**, 144 (2007); https://doi.org/10.1016/j.molcatb.2006.10.002
10. M. Mifune, T. Tai, A. Iwado, H. Akizawa, J. Oda, N. Motohashi and Y. Saito, *Talanta*, **54**, 319 (2001); https://doi.org/10.1016/S0039-9140(00)00655-X
11. B. Tang, G.Y. Zhang, Y. Liu and F. Han, *Anal. Chim. Acta*, **459**, 83 (2002); https://doi.org/10.1016/S0003-2670(02)00087-9
12. H. Biava and S. Signorella, *Polyhedron*, **29**, 1001 (2010); https://doi.org/10.1016/j.poly.2009.12.004
13. C.E. La Rotta, E. D'Elia and E.P.S. Bon, *Electr. J. Biotechnol.*, **10**, 1 (2007); https://doi.org/10.2225/vol10-issue5-fulltext-5
14. C.J. Clarke, W.-C. Tu, O. Levers, A. Brohl and J.P. Hallett, *Chem. Rev.*, **118**, 747 (2018); https://doi.org/10.1021/acs.chemrev.7b00571
15. A. Ariza, E. García-Martín, M. Salas, M.I. Montañez, C. Mayorga, N. Blanca-Lopez, I. Andreu, J. Perkins, M. Blanca, J.A.G. Agúndez and M.J. Torres, *Sci. Rep.*, **6**, 23845 (2016); https://doi.org/10.1038/srep23845
16. P.M. Selvakumar, E. Suresh and P.S. Subramanian, *Polyhedron*, **26**, 749 (2007); https://doi.org/10.1016/j.poly.2006.09.004
17. G.T. Selvan, M. Kumaresan, R. Sivaraj, I.V.M.V. Enoch and P.M. Selvakumar, *Sens. Actuators B Chem.*, **229**, 181 (2016); https://doi.org/10.1016/j.snb.2016.01.097
18. D. Premnath, P.M. Selvakumar, P. Ravichandiran, G. Tamil Selvan, M. Indiraleka and J.J. Vennila, *Spectrochim. Acta A Mol. Biomol. Spectrosc.*, **153**, 118 (2016); https://doi.org/10.1016/j.saa.2015.08.008
19. E. Emerson, *J. Org. Chem.*, **8**, 417 (1943); https://doi.org/10.1021/jo01193a004
20. F. Matemadombo, S. Griveau, F. Bedioui and T. Nyokong, *Electroanalysis*, **20**, 1863 (2008); https://doi.org/10.1002/elan.200804269
21. P.N. Mashazi, P. Westbroek, K.I. Ozoemena and T. Nyokong, *Electrochim. Acta*, **53**, 1858 (2007); https://doi.org/10.1016/j.electacta.2007.08.044
22. N. Sehlotho and T. Nyokong, *J. Electroanal. Chem.*, **595**, 161 (2006); https://doi.org/10.1016/j.jelechem.2006.07.011
23. K. Kasuga, K. Tsuboi, M. Handa, T. Sugimori and K. Sogabe, *Inorg. Chem. Commun.*, **2**, 507 (1999); https://doi.org/10.1016/S1387-7003(99)00135-5
24. N. Chebotareva and T. Nyokong, *Electrochim. Acta*, **42**, 3519 (1997); https://doi.org/10.1016/S0013-4686(97)00033-9
25. T. Wieprecht, J. Xia, U. Heinz, J. Dannacher and G. Schlingloff, *J. Mol. Catal. Chem.*, **203**, 113 (2003); https://doi.org/10.1016/S1381-1169(03)00406-0
26. H.W. Park, S.Y. Lee, J.B. Ahn, J. Suh, B. Kim, K. Lee and W.J. Kim, *J. Surfactants Deterg.*, **9**, 385 (2006); https://doi.org/10.1007/s11743-006-5017-9
27. Mounesh and K.R. Venugopala Reddy, *Anal. Chim. Acta*, **1108**, 98 (2020); https://doi.org/10.1016/j.aca.2020.02.057
28. M. Pari and K.R. Venugopala Reddy, *Anal. Bioanal. Electrochem.*, **11**, 1383 (2019).
29. M.N.K. Harish, J. Keshavayya, K.R.V. Reddy and H.R. Mallikarjuna, *J. Coord. Chem.*, **64**, 2075 (2011); https://doi.org/10.1080/00958972.2011.588705
30. Mounesh, K.R. Venugopala Reddy and Fasiulla, *Anal. Chem. Lett.*, **10**, 137 (2020); https://doi.org/10.1080/22297928.2020.1760132

31. Mounesh, P. Malathesh, N.Y. Praveen Kumara, B.S. Jilani, C.D. Mruthyunjayachari and K.R. Venugopala Reddy, *Heliyon*, **5**, e01946 (2015); https://doi.org/10.1016/j.heliyon.2019.e01946
32. M. Pari and K.R. Venugopala Reddy, *J. Inorg. Organomet. Polym.*, **30**, 3511 (2020); https://doi.org/10.1007/s10904-020-01515-8
33. K.R. Venugopala Reddy, N.Y. Praveenkumar, T.M. Sharanakumar, Mounesh and S.K. Ganiger, *Asian J. Chem.*, **32**, 2722 (2020); https://doi.org/10.14233/ajchem.2020.22803
34. N.Y. Praveen Kumar, Mounesh, T M. Sharanakumar and K R. Venugopala Reddy, *Chem. Pap.*, **75**, 2683 (2021); https://doi.org/10.1007/s11696-021-01523-z
35. Mounesh, T.M. Sharan Kumar, N.Y. Praveen Kumar and K.R. Venugopal Reddy, *Anal. Chem. Lett.*, **10**, 620 (2020); https://doi.org/10.1080/22297928.2020.1857835
36. T.M. Sharanakumar, N.Y. Mounesh, N.Y.P. Kumar, K.R.V. Reddy and Suresh, *Rasayan J. Chem.*, **13**, 2133 (2020); https://doi.org/10.31788/RJC.2020.1345876
37. N. Rajendiran and J. Santhanalakshmi, *J. Mol. Catal. Chem.*, **245**, 185 (2006); https://doi.org/10.1016/j.molcata.2005.09.045
38. B. Agboola, K.I. Ozoemena and T. Nyokong, *J. Mol. Catal. Chem.*, **227**, 209 (2005); https://doi.org/10.1016/j.molcata.2004.10.041
39. W.J. Li, D.Z. Li, J.J. Xian, W. Chen, Y. Hu, Y. Shao and X.Z. Fu, *J. Phys. Chem. C*, **114**, 21482 (2010); https://doi.org/10.1021/jp106659g
40. E.T. Saka, G. Sarki, H. Kantekin and A. Koca, *Synth. Met.*, **214**, 82 (2016); https://doi.org/10.1016/j.synthmet.2016.01.012

Journal of the Indian Chemical Society 98 (2021) 100139

Contents lists available at ScienceDirect

Journal of the Indian Chemical Society

journal homepage: www.editorialmanager.com/JINCS/default.aspx

Investigated aerobic oxidation of aminochlorophenol catalyzed by phthalocyanine complexes

T.M. Sharanakumar [a,b,1], K.R. Venugopala Reddy [a,*], Mounesh [a], N.Y. Praveen Kumar [a], Suresh [b], N.H.M. Nandinibaby [c]

[a] Department of Studies and Research in Chemistry, Vijayanagara Sri Krishnadevaraya University, Bellary, 583105, Karnataka, India
[b] Department of Chemistry, BITM, Jnana Gangotri Campus, Bellary, 583104, Karnataka, India
[c] Department of Physics, BITM, Jnana Gangotri Campus, Bellary, 583104, Karnataka, India

ARTICLE INFO

Keywords:
Phthalocyanine
Catalytic activity
UV-Studies
Chloroaminphenol
Catalytic oxidation

ABSTRACT

The synthesis of 9-Octadecenamide substituted Fe(II) phthalocyanine (ODAFePc) and Ni(II) phthalocyanine (ODANiPc) complexes from Fe(II) tetracarboxylic acid phthalocyanine (FeTcPc) and Ni(II) tetracarboxylic acid phthalocyanine (NiTcPc) with 9-Octadecenamide. These complexes have high molecular weight and soluble in organic solvents. The complexes have been confirmed by FTIR, Mass spectroscopy, UV–Visible X-ray diffraction, and thermogravimetric analysis. The synthesized complexes exhibit excellent stability and are catalytically active in 2-amino-4-chlorophenol (ACP) oxidation. The new method was used for the determination of the oxidation of phenol by applying different experimental parameters like concentration, catalytic quantity, temperature, and pH to get a good yield and catalytic activity of ODAFePc and ODANiPc were studied. ACP was oxidized by dissolved oxygen with ODAFePc and ODANiPc as a catalyst and immediately combined with 4-aminoantipyrine (4-AAP) to form a pink dye and was determined by appearance of absorption intensity at 580 nm. All the experimental results show that ODAFePc and ODANiPc complexes exhibit good catalytic behavior on oxidation of 2-amino-4-chlorophenol.

1. Introduction

Metallophthalocyanine (MPc) is a splendid chemical, thermal stability, and stable metal complex of macrocyclic tetraazoporphyrin. This complex was used in medical, scientific, and industrial areas such as gas sensors, chemical sensors, catalytic systems, molecule solar cells, electrochromic devices, optical materials, nano technology, light-emitting instruments [1], sensors [2–4]. Catalyst [5–9], organic field-effect transistors [10], nonlinear optical materials [11], and laser dyes [12]. The iron and nickel phthalocyanine react with oxidant and transfer oxygen to reactants such as alcohol, alkenes, thiols, phenols, etc. It is highly used as a catalyst in the oxidation process [13–17]. They oxidize various phenolic compounds to quinines and major product as aldehydes.

The disposal of phenol compounds may be contaminated in soil and water, it is a prerequisite to removing the phenolic compounds concerned to public health. Over 70 new methods were used for removing these compounds from wastewater [18–20]. The reported method was used to remove phenolic compounds from waste water [21]. 4-AAP was the broaden used analytical reagent for the estimation of phenol. 4-AAP forms schiff bases when treated with aldehydes/ketones, which are used in chemosensing applications [22]. Its derivatives were developed as an effective chemosensor for the detection of cation and anion [23,24].

ACP is a synthetic precursor of the skeletal muscle relaxant; chlorzoxazone. ACP is a brown colored crystalline powder, and/or chunks [25], soluble in water [26], ACP is also considered by the united states environmental protection agency as toxic environmental water pollutants [27]. Pharmacologically, ACP is labeled in the Sigma-Aldrich catalog as a harmful substance irritating to the eyes, respiratory system, and skin [25]. The new jersey department of health and senior services classifies ACP as a hazardous substance, because acute health effects may occur suddenly or shortly after exposure, including the interference with the ability of the blood to carry oxygen causing headaches, dizziness, and blue color of the lips and skin. At very higher levels cause trouble breathing, collapse, and even death [28].

The various methods are developed for the determination of phenol in water such as capillary electrophoresis, spectroscopy, etc. [29]. The

* Corresponding author.
E-mail addresses: sharanbkl99@gmail.com (T.M. Sharanakumar), venurashmi30@gmail.com (K.R. Venugopala Reddy).
[1] Main author.

https://doi.org/10.1016/j.jics.2021.100139
Received 6 July 2021; Received in revised form 20 August 2021; Accepted 23 August 2021

disadvantages of these methods are: time-consuming sample pretreatment process, demands expensive instruments.These are not suitable for regular analysis, therefore electrochemical methods overcome these limitations because of their good reliability, high accuracy, and inexpensive instruments. The only disadvantage of electrochemical methods is; it produces overpotential and detects poor selectivity when conventional electrode would be used as an electrochemical detector [30–33].

In this work we are reporting the synthesis of 9-octadecenamide substituted iron(II) phthalocyanine and nickel (II) phthalocyanine were characterized by FTIR spectroscopy, UV–Vis spectroscopy, XRD analysis, and TGA analysis. These complexes are catalytically active in ACP oxidation. The new method was used for the determination of oxidation of phenol by applying different experimental parameters to get a good yield and catalytic activity of ODAFePc and ODANiPc were studied. ACP is oxidized by dissolved oxygen using ODAFePc and ODANiPc as a catalyst and immediately combined with 4-AAP to form a pink dye. The intensity of absorption peak increases at 580 nm, which denotes the increase of dye formation, from the all results ODAFePc and ODANiPc complexes exhibit good catalytic behavior on oxidation of 2-amino-4-chlorophenol.

2. Experimental

2.1. Materials and methods

All chemical compounds, solvents, and reagents used were reagent grade and used without purification (Sigma Aldrich CGmbH, Sternheim, Germany). The synthetic reaction was performed under a nitrogen environment. All the solutions were prepared with double-distilled water. FeTcPc and NiTcPc were prepared according to the literature survey [34,35].

FTIR spectra have been recorded on a PerkinElmer 1600 FT-IR spectrophotometer using KBr pellets. Electronic spectra were recorded with a PerkinElmer Lambda 25 spectrophotometer in DMF. Thermal stability was studied by the TGA method by way of the STA6000 system in the temperature range of 25–1100 ^{o}C with the scan rate of 15 ^{o}C min^{-1} under the blowing rate of 40 mL.Min^{-1} oxygen. Elemental analysis for carbon, hydrogen, and nitrogen was done by Vario EL (III) CHNS analyzer. XRD was measured by Bruker D8 diffractometer Co-Kα-radiation source.

2.2. Synthesis of 9-octadecenamide substituted M(II) phthalocyanine complexes

A mixture of 9-octadecenamide (0.05 mmol), tetracarboxylic-M(II)-phthalocyanine (0.015 mmol), potassium carbonate (0.05 mmol) and N, N-dichlorohexylcarbodiimide (catalytic quantities, in dimethylformamide 40 mL) was stirred under nitrogen atmosphere for 30 h at 28 $^{\circ}$C. The green color product was obtained. It was washed with warm water after being washed with methanol followed by NaOH, hydrochloric acid, and distilled water. The product was dried in the oven for 45 min at 40–50 ^{o}C (Scheme 1). Yield = 60% [36,37]. Anal. For ODAFePc with molecular weight and molecular formula 1799.01 (Experimental): $C_{108}H_{150}FeN_{12}O_8$ calc. (%) C-72.053, H-8.3974, N-9.3364, O-7.1096, Fe; 3.102 found: C-71.932, H-8.301, N-9.301, O-7.001, Fe-3.010%. Anal. For ODANiPc with molecular weight and molecular formula 1799.9178

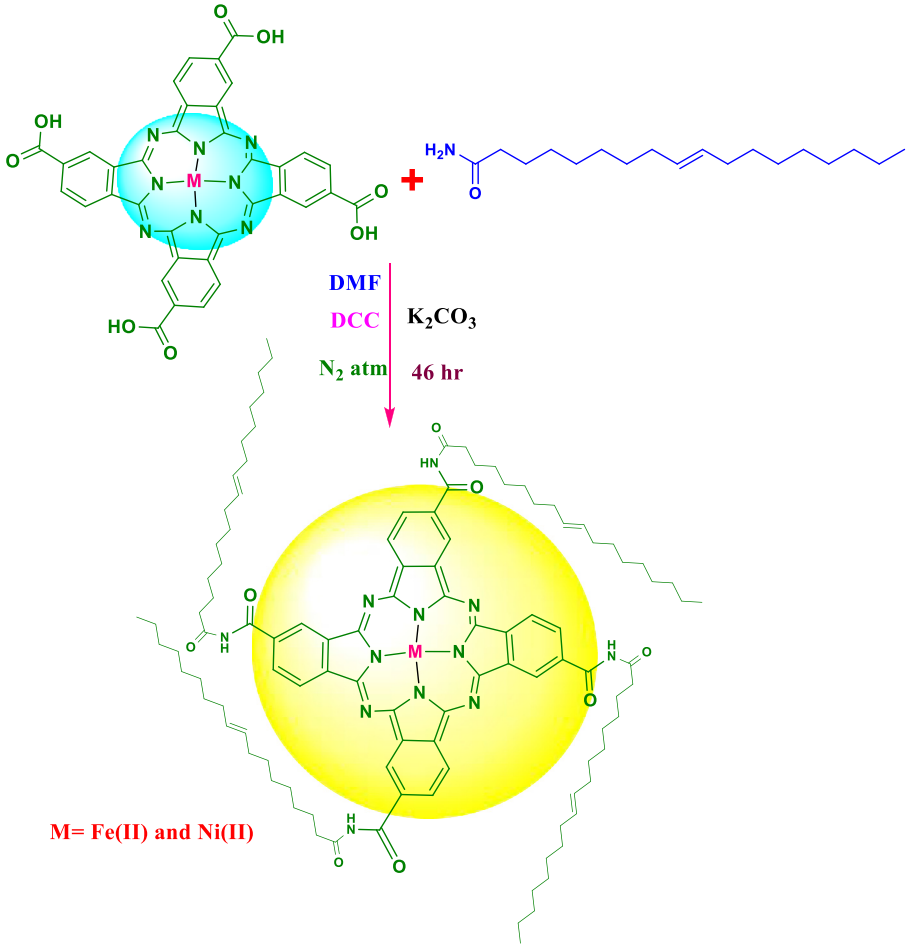

Scheme 1. 9-Octadecenamide substituted-M(II)-phthalocyanine complex synthesis.

(Experimental): $C_{108}H_{150}NiN_{12}O_8$ calc. (%) C-72.053, H-8.3974, N-9.3364, O-7.1096, Ni; 3.260 found: C-71.900, H-8.300, N-9.291, O-7.101, Ni-3.200%.

2.3. Catalytic oxidation of 2-amino-4-chlorophenol by MPc (M = Fe & Ni) ODAFePc and ODANiPc

A 30 mL of 0.05 mol/L phosphate buffer solution, 6 mL of 4-AAP (0.005 mol/L), 6 mL of ACP (0.005 mol/L), and 20 mL ethyl alcohol were added into a 100 mL beaker. The reaction was performed by the addition of a 20 mg MPc catalyst into the reaction vessel and it is ultrasonicated for 3 min and continues magnetic stirring at 35 °C. The reaction solution was filtered (20 mM) to remove MPc particles (Scheme 2). The absorbance of filtrates from 300 to 800 nm was recorded by a UV–Vis spectrophotometer, and the pure distilled water was used for reference solution. In the optimization experiments, the variables, such as the dosage of catalyst, pH, and temperature were adjusted according to the experimental parameters of a typical chromogenic reaction.

The recovery of the catalyst was carried out by centrifugation followed by thoroughly washed with distilled water until the disappearance of pink color then filter and dry. The MPc powder was transferred to hot water for 60 min to the removal of catalyst from organic compounds. Finally, the MPc was obtained and dried at 90 °C in the oven.

3. Results and discussion

3.1. FTIR-spectra

The FTIR (cm^{-1}) spectrum in Fig. 1S (A & B) shows intense and broad absorption bands in the region of 3680–3400 cm^{-1} (-OH and $–NH_2$). In the spectrum shows in Fig. 1S (red) the peak corresponds to the carboxylic acid group of FeTCPc and NiTCPc appears in the range of 3700–3200 cm-1. However, in Fig. 1S (block & blue), the peak for the –COOH group disappears with the appearance of a peak corresponding to a substituted amide group (ODAFePC and ODANiPc) at 3326 cm-1 (-CONH), a peak in the rgion of 2933–2662 cm-1 (Ar-CH), and peaks for the vibrations caused by the stretching of the (C═N) and (C═C) at around 1630-1605 cm-1. The sharp peak in the region of 1564–1522 cm-1 corresponds to C═O, and the sharp peak at 743 cm-1is attributed to C–Br, thus, the vibrational bands at 1498, 1456, 1432, 1391, 1308, 1244, 1227, 1112, 1031, 883, 846, 843, 645, and 604 cm-1 support the presence of functional groups in the ODAFePC and ODANiPc ring [8,9,41].

3.2. UV–Vis spectroscopy

UV–Visible spectroscopy is the most widely used characteristic method to identify the compounds. Phthalocyanine complexes exhibit good spectral properties in the 300–800 nm range [19,20], i.e. the Q-band [$a1u \rightarrow eg$] and the other being the B or Soret band [$a2u \rightarrow eg^*$]. The Q-band region at 600–750 nm and B or Soret band region at 300–400 nm Fig.2S. Electronic spectra of compounds MPc (M= Fe & Ni) show the Soret bands (B bands) are quite similar in the range 300–400 nm and characteristic Q-bands exist in the range 600–750 nm. Both the bands are obtained due to π-π* transitions in the ODAFePc and ODANiPc molecules. The optical band gap was determined from the analysis of the absorption spectrum as described by the Tauc plot using the formula (EI-Nhass et al., 2001).

$$\alpha h\nu = \alpha_0 (h\nu - E_g)^n \quad (1)$$

The value of the energy band gaps for the ODAFePc and ODANiPc was shown in one region (Q-band) as shown in Fig.3S.

3.3. Mass spectroscopy

Mass spectroscopy (MS) is an analytical technique that measures the mass to charge ratio [M+2] of ions. The results are typically presented as a mass spectrum, plot intensity as a function of the mass to charge ratio. The theoretical observation of mass spectra of the ODAFePc complex is 1801.56 and experimental mass of the ODAFePc exhibits molecular ion peak at 1799.01 Fig. 4(S1) and the theoretical observation of mass spectra of the ODANiPc complex is 1803.11 and experimental mass of the ODANiPc exhibits molecular ion peak at 1799.9178 Fig. 4(S2). It indicates that the confirmation of the formation of proposed complexes.

3.4. Thermogravimetric analysis

Fig.5S and Fig.6S shows thermal stability and derivative (Wt %) of the ODAFePc and ODANiPc complexes. The ODAFePc is stable up to 245.45 °C and ODANiPc is stable up to 205.15 C. It involves three-step reactions, in the first step process small content of evaporation of water take place, second step complexes undergo degradation and breaking of substituents with 36.45% of weight loss take place at 391.81 °C, and in the third step the phthalocyanine ring breaking take place with 9% of weight loss, finally metal was converted into metal oxide 38.82% of weight loss at 451.51 C and 447.87 C [37,40,42]. These results have given evidence for the high thermal stability of ODAFePc and ODANiPc complexes nearly 200–250 C. It indicates that the melting point and stability of the ODAFePc and ODANiPc were very high ≥450 C, therefore these complexes are used for chemical oxidation of 2-amino-4-chlorophenol.

3.5. XRD analysis

The powder X-ray diffraction study (PXRD) of ODAFePC and ODANiPc were done in the 2θ angle range of 0–100°, inset curve ((a) TCPc (b) ODAFePc (c) ODANiPc). The PXRD analysis was performed to elucidate the crystal nature and size of the QDs. The parent Pcs and substituted complex exhibit the same patterns. However, the patterns vary in

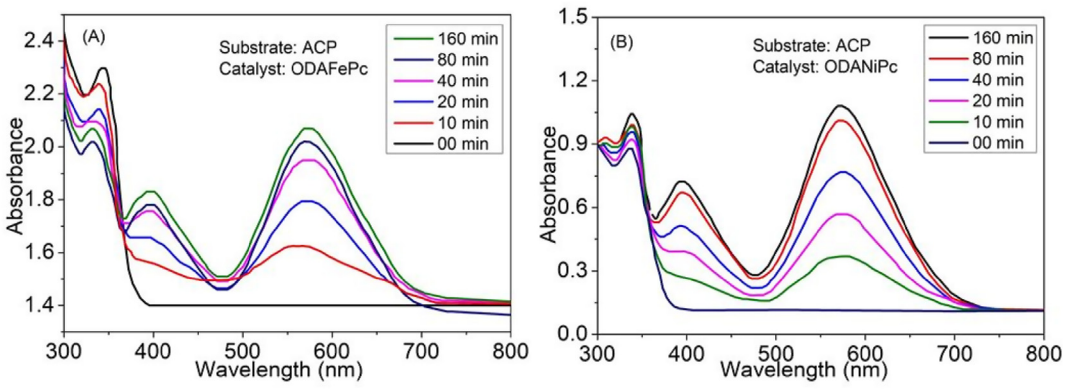

Fig. 1. Catalytic oxidation of ACP substrate with 4-AAP in the existence of O_2 (A) ODAFePc catalyst (B) ODANiPc catalyst.

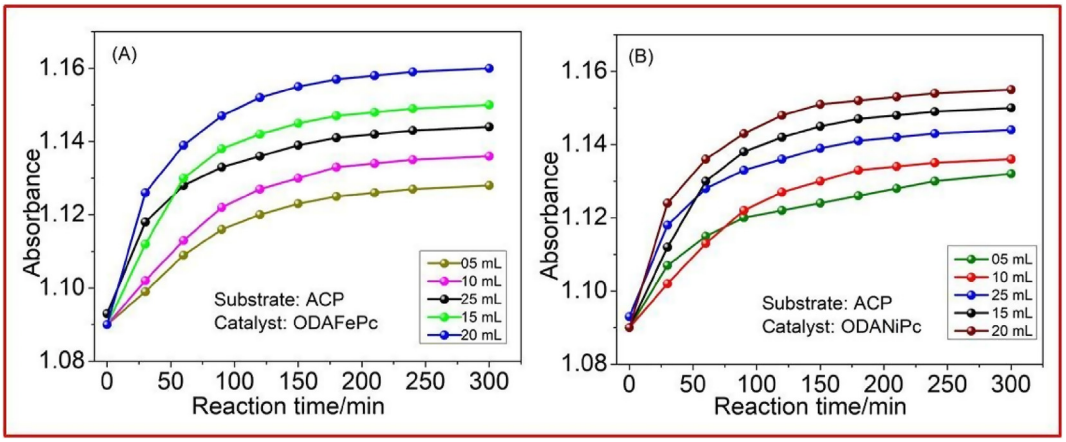

Fig. 2. Effect of concentration for oxidation of ACP (A) Different volume of ethanol in presence of ODAFePc catalyst (B) Different volume of ethanol in presence of ODAFePc catalyst.

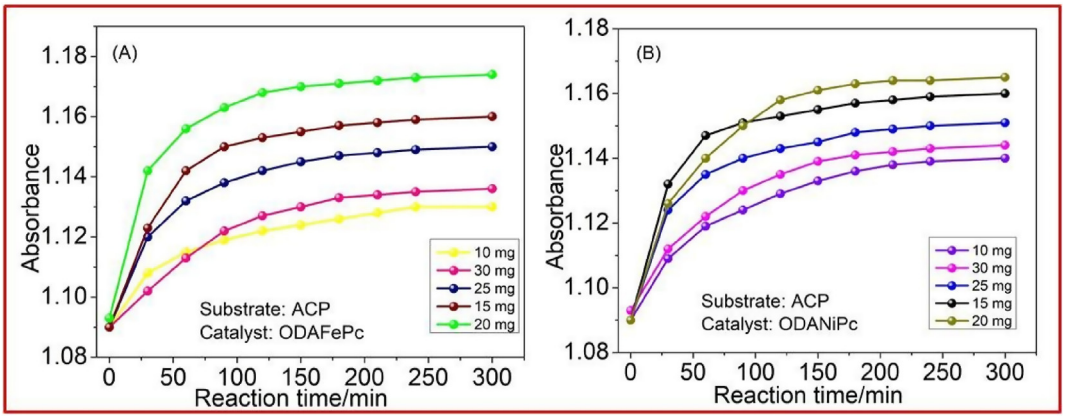

Fig. 3. Effect of a catalytic quantity for an oxidation of 2-amino-4-chlorophenol (A) Different quantity of ODAFePc catalyst (B) Different quantity of ODANiPc catalyst.

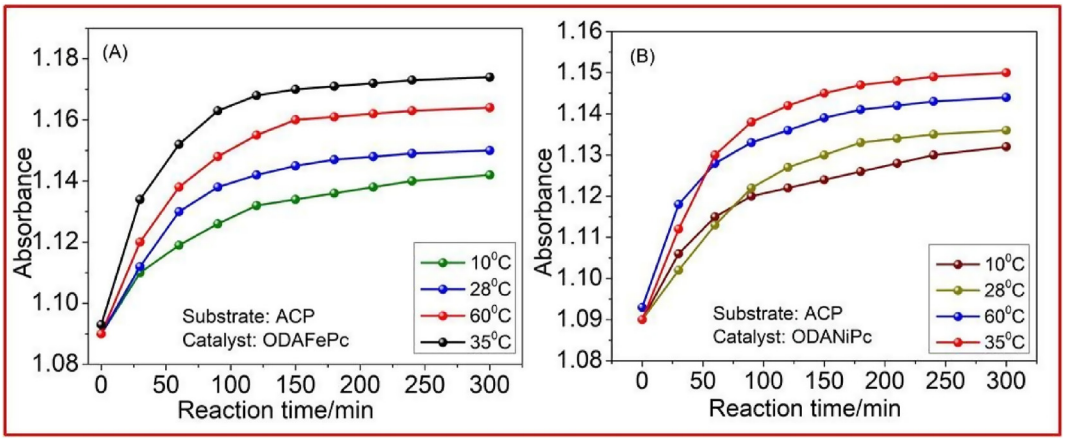

Fig. 4. Effect of temperature on oxidation of ACP (A) Apply different temperature in presence of ODAFePc catalyst (B) Apply different temperature in presence of ODANiPc catalyst.

intensity for the complex compared to the corresponding metal Pcs. The PXRD patterns are used to describe the crystalinity of materials [18, 37–39]. The diffraction patterns of ODAFePc and ODANiPc shows sharp peaks at 08.08°, 13.00°, 15.12°, 30.39°, 31.20°, 32.00°, 52.39° and 55.20° for ODAFePc complex Fig. 7S(A) and 06.08°, 10.00°, 11.12°, 12.39°, 13.20°, 25.00°, 32.39°,45.20°, 46.39°, 48.20°, 58.00° and 59.39° for ODANiPc complex Fig. 7S(B) with low intensity and 09.82°, 10.05°, 11.15°, 16.65°, 20.05°, 25.82° and 42.05° for ODAFePc and 03.15°, 22.65°, 40.05° and 56.02° for ODANiPc with high intensity, indicating that ODAFePc and ODANiPc are crystalline nature. Furthermore, the shapes of the X-ray diffraction patterns indicates that FePc and NiPc were crystalline in nature. The XRD also shows the good microstrain and dislocation density of the ODAFePc and ODANiPc complexes (Table- 1S & Table- 2S).

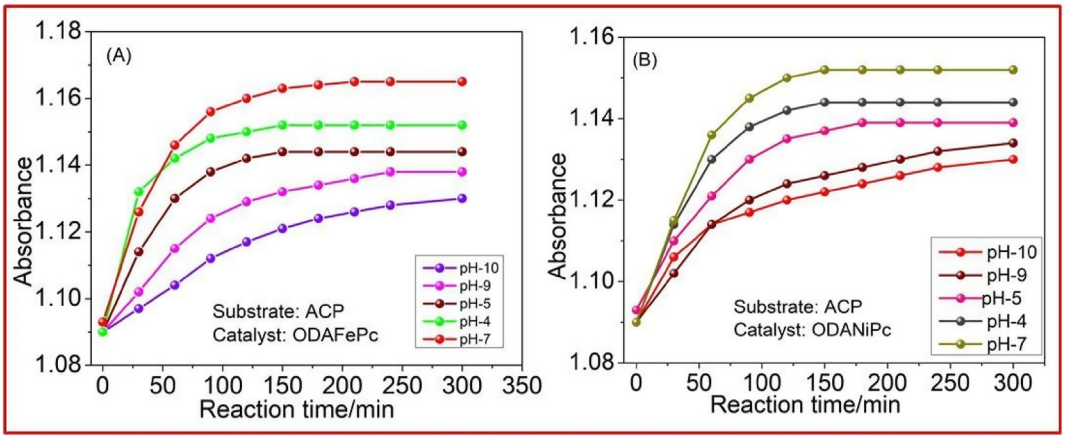

Fig. 5. Effect of pH on oxidation of ACP in presence of (A) ODAFePc catalyst (B) ODANiPc catalyst.

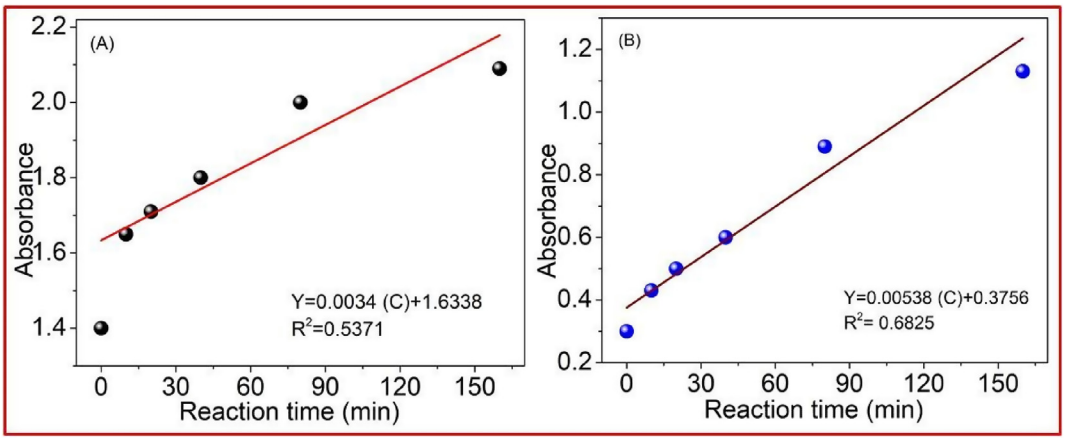

Fig. 6. A calibration curve between absorbance vs reaction time/min (0–160 min) (A) ODAFePc (B) ODANiPc.

3.6. Catalytic oxidation reaction of 2-amino-4-chlorophenol by using ODAFePc and ODANiPc catalysts

In the present work, the catalytic oxidation of 2-amino-4-chlorophenol was carried out by UV–Vis method by using ODAFePc and ODANiPc catalyst in different parameters. Fig.(1) shows a time-dependent UV–Vis absorption spectra of ACP with 4-AAP in the presence of ODAFePc and ODANiPc catalyst in pH-7 (PBS) solution at 35 °C. The 2-amino-4-chlorophenol which oxidized by dissolved oxygen using ODAFePc and ODANiPc, and immediately combined with 4-AAP to form a pink color antipyrilquinoneimine dye (Scheme- 2). The intensity of absorption peak was observed at 580 nm, which denotes the formation of antipyrilquinoneimine dye [6,7]. When the reaction is carried out by passing excess nitrogen to eliminate the dissolved oxygen in the solution.

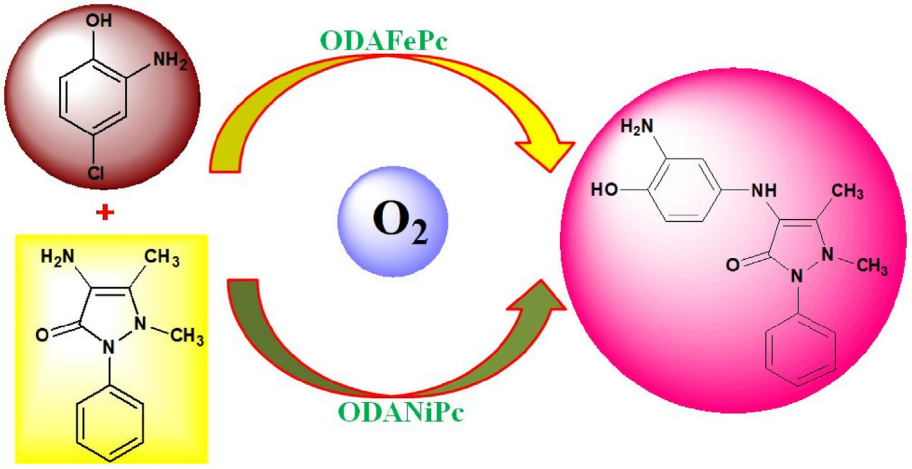

Scheme 2. Mechanism of oxidation of 2-Amino-4 chlorophenol by ODAFePc and ODANiPc complexes.

It observed that the dye formation reduces rapidly, which gives evidence for the oxidation of ACP the dissolved oxygen must be required and ODAFePc and ODANiPc catalysts are very important for the formation of dye.

The experiment was carried out in a different time interval (0–160 min). The absorption was observed at 580 nm. The intensity of absorption increases with time because of more dye formation. This denotes that the catalytic effect is involved in the formation of dye in the chemical reaction.

3.7. Apply of various experimental conditions

3.7.1. Effect of volumes of ethanol for oxidation of ACP

The experiment was carried out using ethyl alcohol solvent with different volumes in presence of ODAFePc and ODANiPc catalysts. The different volumes of 5 mL, 10 mL, 15 mL, 20 mL, and 25 mL of ethanol was used to carried out the experiment Fig.(2). It shows good results and it was observed that at 20 mL volume the reaction rate was good compared with 5 mL, 10 mL, 15 mL, and 25 mL. However, more ethanol could not contribute to more production of dye. It indicates that the maximum absorbance of dye formed within 300 min corresponded to the addition of 20 mL of ethyl alcohol so that 20 mL is the optimum volume requred for carriedout the reactions.

3.7.2. Effect of a catalytic quantity for an oxidation of ACP

The catalytic quantity is also one of the parameter for affecting rate of reaction. The rate of reaction increases by the addition of a catalyst. The ODAFePc and ODANiPc dosage of 10 mg, 15 mg, 20 mg, 25 mg, and 30 mg were used for carrying the reaction, the maximum absorption was monitored within 300 min as shown in Fig.(3). The results show that 20 mg of ODAFePc and ODANiPc catalysts should contribute to the formation of more dye. But excess of catalyst 30 mg did not show the best catalytic efficiency because of the dye deposited on the catalytic site so that the 20 mg of ODAFePc and ODANiPc catalysts are well in the formation of dye. Therefore 20 mg was good for the optimum catalytic quantity for carrying out the reaction.

3.7.3. Effect of temperature on oxidation of ACP

The reaction rate had increased by applying temperature. The catalytic oxidation reaction (COR) of ACP in presence of ODAFePc and ODANiPc catalysts was performed at different temperatures of 10 °C, 28 °C, 35 °C, and 60 °C, the maximum absorption was monitored within 300 min. The results revealed that at 35 °C the rate of reaction was faster due to the faster COR of ACP related to the fast concussion of radical species, therefore more dye formation takes place as shown in Fig.(4). At 60 °C the less dye formed due to the small effect of rate of reaction on COR and it involved pseudo-first-order reaction [3], by the arrhenius theory, the rate of side reactions depends upon the less yielding of dye. At 10 °C and 28 °C the rate of reaction was slow so that less yield formed at low temperature. The above data indicates that the temperatre is also affected by the COR of ACP.

3.7.4. Effect of pH of the solution on oxidation of ACP

The pH is one of the parameters for the formation of dye. The COR of ACP with 4-AAP was carried out with different pH conditions [25]. The various buffer solutions were used for conducting the reaction to the measurement of absorption. The phosphate buffer solution (PBS, pH-7, 9, and 10) and acetic acid solution (CH_3COOH, pH-4, 5), as well as demineralized water, were employed to study the catalytic reactions. Fig.(5) shows the dye formation process in ACP at various pH on the plot of UV–Vis absorption ($\lambda = 580$ nm) v/s reaction time. In the ACP system, the catalytic reaction in presence of ODAFePc Fig. 5A was over after 2 h at pH-7.0 and 2.5 h at pH-4 and 5, while the reaction was continued after 4 h at pH 9 and 10. From these results the COR of ACP in demineralized water, more dye formed at pH-7.0 ($\geq$120) was required. The concentration of dye at pH-4 and 5 after 150 min, and at pH-9 and 10 after 240 min.

In the presence of ODANiPc Fig. 5B, the reaction was over after 2.5 h at pH-7.0 and 3.0 h at pH-4 and 5, while the reaction proceeded after 5 h at pH-9 and 10. From these results the COR of ACP in demineralized water, more percentage of dye yields at pH-7.0 ($\geq$150) was needed. The concentration of dye at pH-4 and 5 after 300 min, and at pH-9 and 10 after 300 min. All the results show that the pH-7 is good for the optimal experimental parameter.

3.7.5. Concentration vs. reaction time

The reaction was carried out at room temperature within 160 min at pH-7 using 20 mg ODAFePc and ODAFePc catalyst, observing that as the oxygen concentration increased with an increase of oxidation process observed within 160 min. The calibration plot of 2-amino-4-chlorophenol detection could be determined in Fig.(6). The dye formation at 580 nm was proportional to the concentration of 2-amino-4-chlorophenol from 2.15×10^{-5} to 10.15×10^{-4} mol/L. It indicates that the temperature, pH, catalyst are very important parameters for the formation of dye. A calibration curve drawn between absorbance and reaction time/min, with correlation coefficient of 0.5371 and 0.6825 with linear regression equation $Y = 0.0034\ (C)+1.6338$ Fig. 6A and $Y = 0.00538\ (C)+0.3756$ Fig. 6B.

3.8. Reaction mechanism

Step-I: Formation of p-quinoid radical by treating with ACP and oxygen
Step-II: Formation of antipyrine-NH^+
Step-III: Formation of antipyrilquinoneimine dye

From the point of Meunier and Sorokin, the proposed active iron–oxygen/nickel-oxygen species was responsible for ACP oxidation, which also illuminated the acceptor-donor interactions existed in substrate, catalyst [7,38,39]. In the ODAFe(II)Pc/ODANi(II)Pc catalytic reaction system, the interactions among substrate, catalyst and O_2 should result in the coordination structures of aminochlorophenol–ODAFe(II)Pc-O_2/ODANi(II)Pc. Then the successive single electron transfer from hydroxyl oxygen (donor) of chlorophenol to O_2 (acceptor) via the axis of ODAFe(II)Pc/ODANi(II)Pc macrocycle realized the fast oxidation of chlorophenol (Scheme- 3, a case of ACP), which was responsible for the succeeding generation of p-quinoid radical and $O_2^{\bullet-}$ (step-I). In turn, the resulting $O_2^{\bullet-}$ could further oxidize the amino group of 4-AAP to produce the Antipyrine-$NH^{\bullet}$ (step-II). Immediately, p-quinoid radical and Antipyrine-$NH^{\bullet}$ could combine to generate the final products of pink antipyrilquinoneimine dye (step-III). This is the possible mechanism for the generation of $O_2^{\bullet-}$ and dye formation via radical coupling. For the ACP oxidation, the resulting pink dye should be antipyrilquinoneimine (Scheme- 2). In this mechanim, the Ni(II) is converted to Ni(III) and Fe(II) is converted to Fe(III) because phenol is oxidized and Metallophthalocyanne is reduced [43].

4. Conclusion

In the present work, we have synthesized ODAFePc and ODANiPc macromolecule complexes, and their characterization was done by various spectral methods like FTIR, UV–Vis spectra, XRD, TGA, and Mass spectroscopy. It exhibits good thermal stability and solubility. The catalytic activity of ACP was carried by simple UV–Vis absorption method and it gives excellent results and measured absorption at 300–800 nm. The ODAFePc and ODANiPc were catalytically active in 2-amino-4-chlorophenol (ACP) oxidation. Different experimental parameters affecting the formation of the reaction product were studied. ACP which is

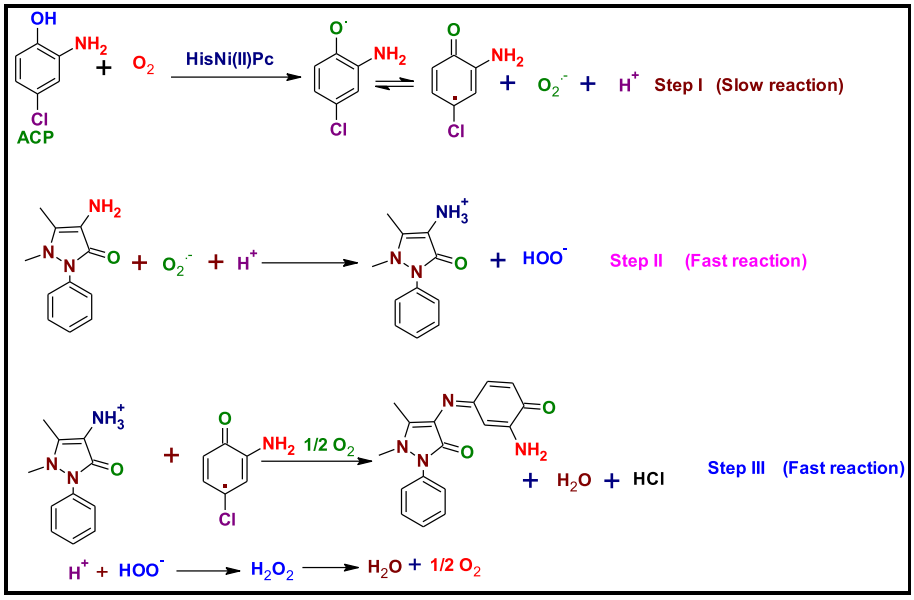

Scheme 3. Reaction mechanism.

oxidized by dissolved oxygen in presence of ODAFePc and ODANiPc catalysts reacted with 4-AAP to form a pink dye. The intensity of the absorption peak was observed at 580 nm. From all the results we conclude that the ODAFePc and ODANiPc is an excellent catalyst for the oxidation of 2-amino-4-chlorophenol.

Declaration of competing interest

The authors declare that they have no known competing financial interests or personal relationships that could have appeared to influence the work reported in this paper.

Acknowledgment

One of the authors Sharanakumar T. M thanks VSK University, Ballari Institute of Technology and Management, Ballari for facilities and encouragement.

Appendix A. Supplementary data

Supplementary data to this article can be found online at https://doi.org/10.1016/j.jics.2021.100139.

References

[1] Selçukoglu M, Hamuryudan E. Dyes Pigments 2007;74:17. https://doi.org/10.1016/j.dyepig.2006.01.009.
[2] Moser FH, Thomas AL. *American Chemical Society* MonograpH Series. New York: Reinhold Publishing Corporation; 1963. https://doi.org/10.1039/PS9630000229.
[3] Parra V, Bouvet M, Brunet J, Rodríguez-Méndez ML, Saja JA. Thin Solid Films 2008; 516. https://doi.org/10.1016/j.tsf.2007.11.092. 9012.
[4] Bouvet M. Anal. Bioanal. Chem. 2006;384:366. https://doi.org/10.1007/s00216-005-3257-6.
[5] Yılmaz F, Özer M, Kani I, Bekaroğlu O. Catal. Lett. 2009;130:642. https://doi.org/10.1007/s10562-009-9959-1.
[6] Saka ET, Uzun S, Çağlar Y. Organomet J Chem 2016;810:25. https://doi.org/10.1016/j.jorganchem.2016.03.005.
[7] Saka ET, Sarki G, Kantekin H, Koca A. Synth. Met. 2016;214:82. https://doi.org/10.1016/j.synthmet.2016.01.012.
[8] Mounesh, malathesh pari, Praveen kumara NY, Bhvimane jilani, Mruthynjayachari CD, Venugopala Reddy KR. Heliyon 2019;5:e01946. https://doi.org/10.1016/j.heliyon.2019.e01946.
[9] sanna jilani Bhvimane, Mruthyunjayachari CD, Malatesh P, Mounesh, Sharanakumar TM, Venugopala Reddy KR. Sensor. Actuator. B Chem. 2019;301: 127078. https://doi.org/10.1016/j.snb.2019.127078.
[10] Kim DK, Oh JD, Shin ES, Seo HS, Choi JH. J. Appl. Phys. 2014;115:164503. https://doi.org/10.1063/1.4873299.
[11] De La Torre G, Vazquez P, Agullo-Lopez F, Torres T. J. Mater. Chem. 1998;8:1671. https://doi.org/10.1039/A803533D.
[12] Leznoff CC, Lever ABP, editors. New York: Book); 1996. https://doi.org/10.1021/ja965771a.
[13] Teng HS, Hsieh CT. Ind. Eng. Chem. Res. 1998;37:3618. https://doi.org/10.1021/ie970796j.
[14] Saka ET, Biyiklioglu Z, kantekin H, Kani I. Applorgano met chem 2013;27:45.
[15] Sorokin AB, Tuel A. Catal. Today 2000;57:45. https://doi.org/10.1016/S0920-5861(99)00312-0.
[16] Sorokin AB, Kudrik EV. Catal. Today 2011;159:37. https://doi.org/10.1016/j.cattod.2010.06.020.
[17] ISCI U, Dumoulin F, Sorokin AB. Absen.V., *turk. J Chem.* 2014;38:923. https://doi.org/10.3906/kim-1407-47.
[18] Mounesh JilaniBS, Malatesh P, Venugopala Reddy KR, Lokesh KS. Microchem. J. 2019;147:755–63. https://doi.org/10.1016/j.microc.2019.03.090.
[19] Mounesh Venugopala ReddyKR. Anal. Chim. Acta 2020;1108:98–107. https://doi.org/10.1016/j.aca.2020.02.057.
[20] Mounesh Venugopala ReddyKR. New J. Chem. 2020;44(8):3330–40. https://doi.org/10.1039/C9NJ05807A.
[21] Sabhi S, Kiwi J. Water Res. 2001;35. https://doi.org/10.1016/S0043-1354(00)00460-7. 1994.
[22] Selvakumar PM, Suresh E, Subramanian PS, Subramanian. Polyhedron 2007;26(4): 749–756S. https://doi.org/10.1016/j.poly.2006.09.004.
[23] Rosatto, Freire RS, Duran N, Kubota LT. Nova 2001;24:77. https://doi.org/10.1590/S0100-40422001000100014.
[24] Selvan GT, Kumaresan M, Sivaraj R, Enoch IVMV, Selvakumar PM. Sensor. Actuator. B 2016;229:181–9. https://doi.org/10.1016/j.snb.2016.01.097.
[25] Premnath D, Selvakumar PM, Ravichandriran P, Selvan GT, Indiraleka M, et al. spectrochem Acta:A Mol Biomol Spectrosc 2016;153:118–23. https://doi.org/10.1016/j.molstruc.2016.10.053.
[26] Sigma-Aldrich Catalogue.
[27] www.Chemicalland21.com.
[28] United states Environmental protection Agency. www.epa.gov.
[29] Cruz Iolanda, Orlando Vieira, Fatibello-Filho. Talanta 2000;52(4):681–9. https://doi.org/10.1016/S0039-9140(00)00420-3.
[30] Han L, Zhang X. Electroanalysis 2009;21:124–9. https://doi.org/10.1002/elan.200804403.
[31] Chen L, Tang Y, Wang K, Liu C, Luo S. Electrochem. Commun. 2011;13:133–7. 978-1-119-46965-0.
[32] Zhao DM, Zhang XH, Feng LJ, Jia L, Wang SF. Colloids Surf. B Biointerfaces 2009; 74:317–21. https://doi.org/10.1016/j.colsurfb.2009.07.044.
[33] Ece Tugba Saka1karl peters. J. Inclusion Phenom. Macrocycl. Chem. 2018. https://doi.org/10.1007/s10847-018-0800-6.
[34] Reddy KRV, Harish MNK, Fassiulla MH, Khan Moinuddin. Keshavayya.J., *Fluor. Chem.* 2007;128:1019–25. https://doi.org/10.1016/j.jfluchem.2007.05.001.
[35] Harish MNK, Keshavayya J, Venugopeda Reddy KR, Mallikarjuna HR. J. Coord. Chem. 2011;64(12):2075. https://doi.org/10.1080/00958972.2010.529902.
[36] Mounesh, Venugopala Reddy KR. Analytical Chemistry Letters 2020;10(1):33–48. https://doi.org/10.1080/22297928.2020.1745683.
[37] Sharanakumar TM, Mounesh, Praveen Kumar NY, Venugopala Reddy KR, Suresh. Rasayan J. Chem. 2020;13(4):2133–42. https://doi.org/10.31788/RJC.2020.1345876.

[38] Mounesh, Sharan Kumar TM, Praveen Kumar NY, Venugopal Reddy KR. Analytical chemical letters 2020;10(5):620–35. https://doi.org/10.1080/22297928.2020.1857835.
[39] Praveen Kumar NY, Mounesh, Sharanakumar TM, Venugopal Reddy KR. Chem. Pap. 2021;75:2683–94. https://doi.org/10.1007/s11696-021-01523-z.
[40] Praveen Kumar NY, Mounesh, Sharanakumar TM, Venugopal Reddy KR, Ganiger Sangappa K. Asian J. Chem. 2020;32(11):2722–30. https://doi.org/10.14233/ajchem.2020.22803.
[41] Mounesh, Sharanakumar TM, Praveenkumar NY, Venugopal Reddy KR, Chandrakala K, Arunkumar L, Vidyasagar CC. RSC Adv. 2021;11:16736–46. https://doi.org/10.1039/d1ra01815a.
[42] Mounesh, Praveen Kumar NY, Sharanakumar TM, Venugopal Reddy KR. Electrochemical Science Advances 2021;1–11. https://doi.org/10.1002/elsa.202100006.
[43] Cárdenas-Jirón Gloria I, Berríos Cristhian. Int. J. Quant. Chem. 2008;108:2586–94. https://doi.org/10.1002/qua.21732.

RJC

RASĀYAN *J. Chem.*
Vol. 14 | No. 3 |1761-1772| July - September | 2021
ISSN: 0974-1496 | e-ISSN: 0976-0083 | CODEN: RJCABP
http://www.rasayanjournal.com
http://www.rasayanjournal.co.in

INVESTIGATING CATALYTIC OXIDATION OF CYCLOHEXENE USING Fe(II) AND Co(II)PHTHALOCYANINE COMPLEXES

T.M. Sharanakumar[1,2], N.Y. Praveen Kumar[2], Mounesh[2], R. Vindhya[3] and K.R. Venugopal Reddy[2,✉]

[1]Department of Chemistry Ballari Institute of Technology and Management, Ballari-583104, Karnataka (INDIA)

[2]Department of Studies and Research in Chemistry, Vijayanagara Sri Krishnadevaraya University, Ballari–583105, Karnataka (INDIA)

[3]Department of Chemistry, Ballari Institute of Technology and Management, Ballari-583104, Karnataka (INDIA)

✉Corresponding Author: venurashmi30@gmail.com

ABSTRACT

The Carbutamide substituted Fe(II) phthalocyanine (CBTAFePc) and Co(II) phthalocyanine (CBTACoPc) complex was synthesized from tetra carboxylic acid Fe(II) phthalocyanine (FeTcPc) and tetra carboxylic acid Co(II) phthalocyanine (CoTcPc) with Carbutamide (CBTA) by linkage of amide has been developed. The macrocyclic molecules have high molecular weight and the molecule is completely soluble in Dimethylformamide and Dimethylsulfoxide. The synthesized complexes were confirmed by FTIR, Ultraviolet-Visible, PXRD, Mass, C,H,N and Thermo-gravimetric techniques. The catalytic activity of CBTAFePc and CBTAFePc were analyzed in the oxidation of Cyclohexene with various parameters like temperature, types of oxidants, oxidant/cat ratio, and subs/catalyst ratio affect the oxidation reactions were investigate the optimum conditions of catalysts. CBTAFePc shows excellent catalytic results on oxidation of Cyclohexene with the highest yield with good selectivity. The overall results show that the CBTAFePc complex exhibits an excellent catalyst compared with the CBTACoPc complex for investigation of the oxidation of Cyclohexene.

Keywords: CBTAFePc, CBTACoPc, Carbutamide, Cyclohexene and Gas Chromatography

RASĀYAN *J. Chem.*, Vol. 14, No.3, 2021

INTRODUCTION

The industries and atmospheric pre-occupations need a common and more effective and low-cost catalyst. The degradation of pollutants was carried out by using an effective catalyst and the catalyst is a very important role in the synthesis of organic compounds and their derivatives. The oxidation of various molecules like alkenes, aromatics and alcohols are very important starting materials for the synthesis of bulk compounds for the production of chemicals in pharmaceuticals, cosmetics and polymerization of organic compounds. In the chemical reaction system, the selectivity of the catalyst was very important.[1] In recent years the researcher mainly concentrates on the catalytic oxidation of Cyclohexene and its derivatives by using transition metal complexes as a catalyst.[2]

Carbutamide under the brand name glucidoral was used as the anti-diabetic drug to treat diabetes in France. Carbutamide belongs to the family of sulphonyl ureas and reduces the excess sugar in the blood by promoting the secretion of insulin. carbutamide promotes increased insulin secretion or it may potentiate the action of insulin. The carbutamide was useful for both acute and chronic treatments on both obese-hyperglycemic and their normal littermates. Metallo phthalocyanine (MPc) molecules exhibit good chemical and physical properties. They show high resistance to thermal and light radiations[3], most of the phthalocyanine is insoluble in organic solvents.[4] The macrocyclic compound of MPc formed by four iso-indole groups connected with azomethine bridges was reported by Kadish K.M. et al.[5-6] Physical, chemical and optical properties of MPc changes with central metal ions have been used in biomedical and industry[7-10]. MPcs are important excellent materials used in scientific areas such as sensors,[11-14]

http://doi.org/10.31788/RJC.2021.1436386

semiconductor[15], dye-based solar cells, molecular electronics[16-17], liquid crystals[18], laser dyes[19], nonlinear optics materials[20], electro chromic[21], photosensitizers for photodynamic therapy of cancer[22-24], electro-catalytic[25]and catalytic activities.[26]

In this present work, CBTAFePc and CBTACoPc complex was synthesized from tetracarboxylic acid Fe(II) and Co(II) phthalocyanines with carbutamide (CBTA). The CBTACoPc has been characterized by FTIR, Ultraviolet-Visible, PXRD, Mass, C,H,N and Thermo-gravimetric techniques. A new method used for catalytic oxidation of Cyclohexene is reported for the first time. The catalytic activity (CA) of CBTAFePc and CBTACoPc were performed in the oxidation of Cyclohexene with various oxidants and parameters like temperature, oxidant/cat ratio, and subs/catalyst ratio affect the oxidation reactions were investigate the optimum conditions of catalysts. CBTAFePc shows excellent catalytic results on oxidation of Cyclohexene with the highest yield with good selectivity. The overall result shows that the CBTAFePc complex exhibits an excellent catalyst compared with the CBTACoPc complex for investigation of the oxidation of Cyclohexene.

EXPERIMENTAL

Materials and Methods

The high-grade solvents, reagents and chemicals are used without refinement (Sigma Aldrich CGmbH, Sternheim, Germany). The reaction was performed in presence of an oxygen environment. All the chemicals were prepared by using distilled water. Iron and cobalt phthalocyanine prepared by literature.[27-29]

FTIR spectra have been recorded by Perkin Elmmer 1600 FT-IR spectrophotometer using KBr pellets. Micromass Quatro LC/MSD was used to measure the mass spectra. A Perkin Elmer Lambda 25 spectrophotometer in DMF was used to measure UV-Vis spectra. C, H and N analysis was done by Vario EL (III) CHNS analyzer. GC Agilent technologies 7820A equipment was used as GC measurement. Thermogravimetric analysis of the synthesized complexes was studied by the STA6000 system in the temperature range of 25 to 900 °C under the blowing rate of 20 mL.min^{-1} oxygen.

Synthesis of Carbutamide Substituted Fe(II) phthalocyanine (CBTAFePc) Complex

A mixture of carbutamide (0.05 mmol), tetra carboxy-Fe(II)-phthalocyanine (0.015 mmol), Potassium carbonate (0.05 mmol) and DCC (catalytic quantities, in Dimethylformamide 40 mL) was agitated under N_2atm for 30 h at 28 °C. The greenish color compound formed. It was soaking with warm water after washing with methanol followed by NaOH, HCl and double-distilled water. The obtained compound was dehydrated in an oven for nearly 45 min at 40-50 °C (Scheme-1). Yield=60%[30]. Anal. For CBTAFePc with molecular weight and molecular formula 1759.70 (Experimental): $C_{80}H_{78}FeN_{20}O_{16}S_4$ calc. (%) C-54.60, H-4.432, N-15.91, O-14.53, S-7.28, Fe; 3.17 found: C-54.51, H-4.32, N-15.80, O-14.61, S-7.20, Fe; 3.15.

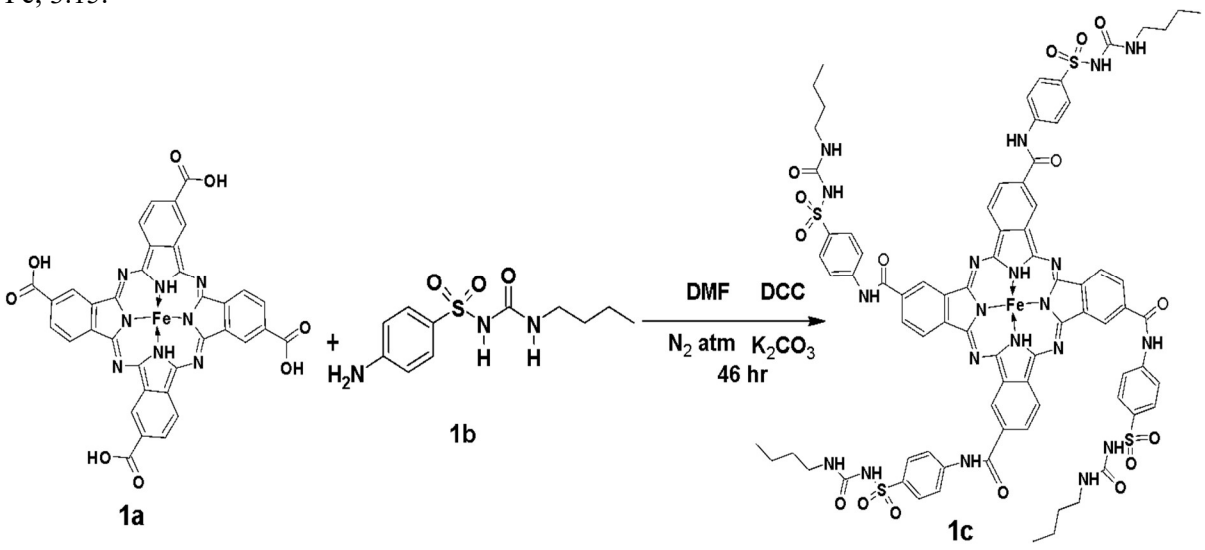

Scheme-1: Carbutamide Substituted-Fe(II)- phthalocyanine Complex Synthesis

Synthesis of Carbutamide Substituted Co(II) phthalocyanine (ODACoPc) Complex

A mixture of carbutamide (0.05 mmol), tetra carboxy-Co(II)-phthalocyanine (0.015 mmol), Potassium carbonate (0.05 mmol) and DCC (catalytic quantities, in Dimethylformamide 40 mL) was agitated under N_2atmosphere for 30 h at 28 °C. The greenish color compound formed. It was soaking with warm water after washing with methanol followed by NaOH, HCl and double-distilled water. The obtained compound was dehydrated in an oven for nearly 45 min at 40-50 °C (Scheme-2). Yield=65%[30]. Anal. For CBTACoPc with molecular weight and molecular formula 1762.79 (Experimental): $C_{80}H_{78}CoN_{20}O_{16}S_4$ calc. (%) C-54.60, H-4.432, N-15.91, O-14.53, S-7.28, Co; 3.34 found: C-54.49, H-4.38, N-15.86, O-14.63, S-7.22, Co; 3.30.

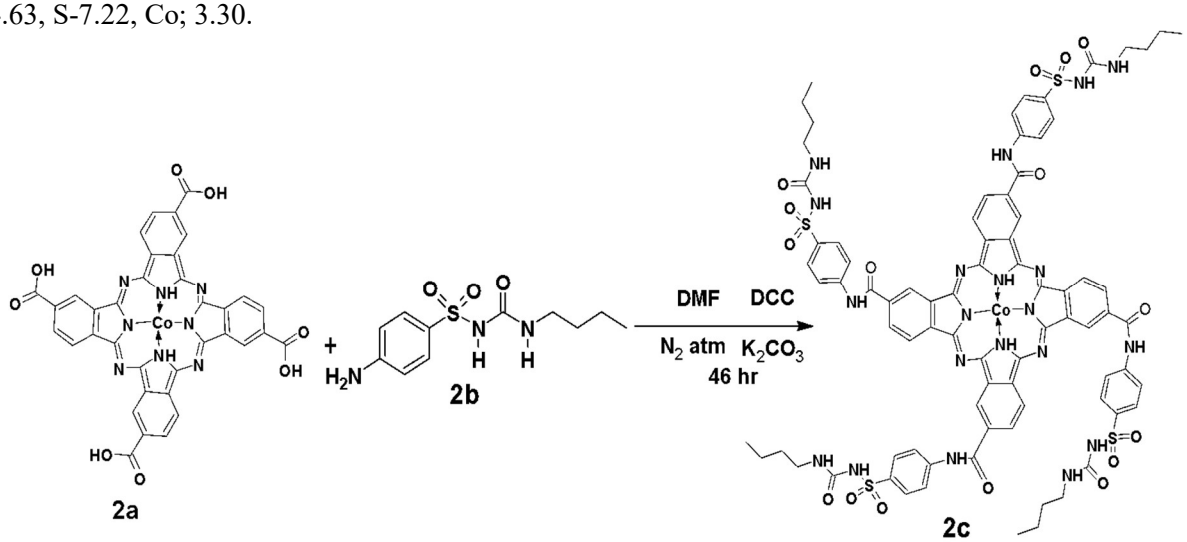

Scheme-2: Carbutamide Substituted-Co(II)- phthalocyanine Complex Synthesis

Mechanism of Cyclohexene Oxidation

The experiment was performed by a thermostated schlenk vessel fixed with a stirrer and condenser. The mixture of Cyclohexene, catalyst and desirable solvent were refining by passing N_2 gas to the removal of oxygen. The mixture of Cyclohexene (0.71×10^{-3} mol), catalyst (3.57×10^{-6} mol) and solvent (0.01 L) was agitated in a vessel for 20 min at 28 °C, and then add m-CPBA oxidant (1.78×10^{-3} mol) into the vessel. The whole mixture was agitated for the proper time. For each interval of time, the sample (0.006 L) was taken and each 1 µL sample was injected into the GC at least two times. The formation of desired products was monitored by GC.

RESULTS AND DISCUSSION

FTIR-Spectra

The infrared spectroscopy was used for studying functional groups. The expected bands assignable to CBTAFePc and CBTACoPc complexes are found at 670-700, 750-790, 840-850, 940-945, 1090-1120, 1140-1147,1200-1210, 1240-1290, 1305-1320, 1400-1430, 1490-1540 and 1600-1625 cm^{-1}. The IR bands of CBTAFePc (KBr pellet), υ/cm^{-1}: 1622-1644 (C=C), 2812-3013 (C=N), 3212-3424 (amide peak), 1492-1575 (-C=C-N=), 1318, 1336, 1258, 1282, 1232, 1252, 1152, 1148 (C-O), 1062, 922, 846, 766, 735 Fig.-1(A). The IR of CBTACoPc (KBr pellet), υ/cm^{-1}: 1624-1648 (C=C), 2814-3016 (C=N), 3216-3433 (amide peak), 1494-1578 (-C=C-N=), 1319, 1336, 1258, 1296, 1234, 1255, 1152, 1144 (C-O), 1062, 924, 847, 769, 731 Fig.-1(B).[31]

UV-Vis Spectroscopy

The electronic spectra of CBTAFePc and CBTACoPc complex solutions are shown in Fig.-2. The absorption shows two intense peaks. The intense absorption peak at 650-750 nm was assigned for Q-Band [a1u→ eg(*)] for the π-π* transitions from the HUMO to the LUMO and 300-500 nm is B-band of CBTAFePc and CBTACoPc complexes[32]. The UV spectra of MPc (M=Fe and Co) are observed in the range of 650-750 nm. This indicates the formation of CBTAFePc and CBTACoPc complexes.

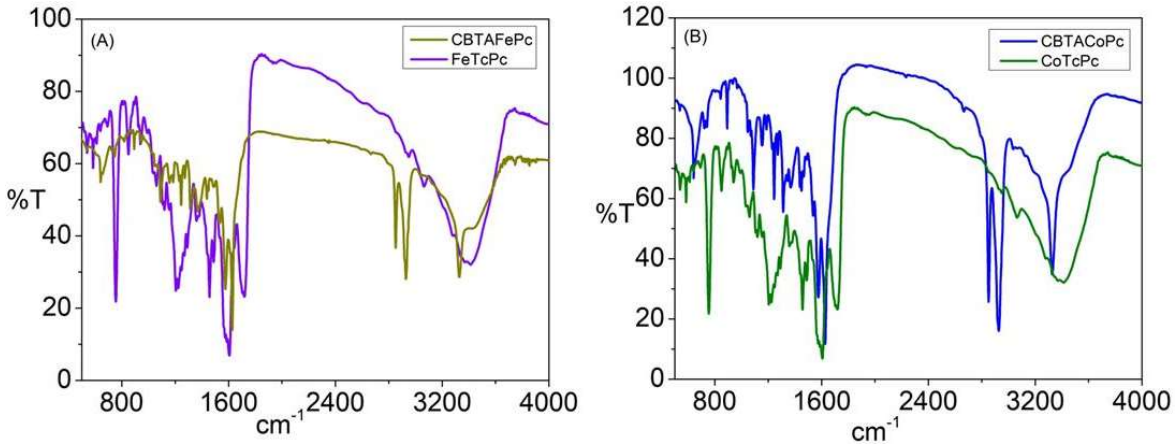

Fig.-1: IR Absorption Spectra of (A) CBTAFePc with FeTcPc (B) CBTACoPc with CoTcPc

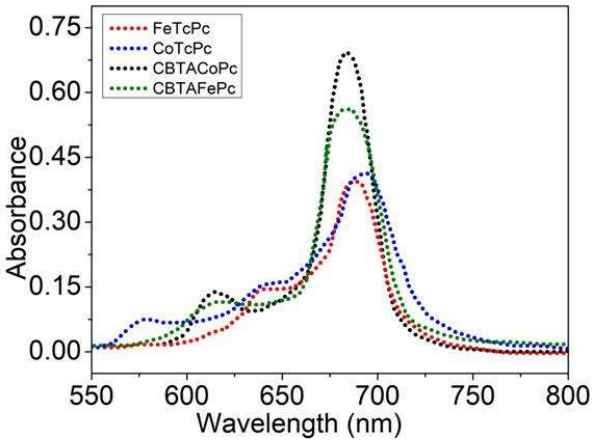

Fig.-2: UV-Vis Spectrum of CBTAFePc with FeTcPc and CBTACoPc with CoTcPc Complexes

Thermogravimetric Analysis

The Thermogram of CBTAFePc and CBTACoPc complexes Fig.-3 shows the stability of the molecule. The CBTAFePc and CBTACoPc show two-step degradation, one at 200 ºC and the other at 300 ºC. Degradation at 200 ºC corresponds to a loss of carbutamide and at 300 ºC loss of phthalocyanine ring and weight loss at 550 ºC is due to complete degradation to form metal oxide. The presence of the substituted group improves the thermal stability of the CBTAFePc and CBTACoPc complexes. The melting point of the molecule is very high ≥ 550 ºC[33]. Therefore, the CBTAFePc and CBTACoPc complexes are used in the determination of oxidation of Cyclohexene.

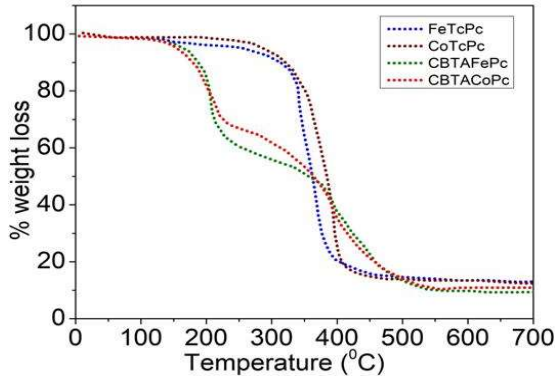

Fig.-3: Thermogravimetric Analysis of CBTAFePc with FeTcPc and CBTACoPc with CoTcPc Complexes

XRD Analysis

The powder XRD of CBTAFePc and CBTACoPc complexes are attained by Co-kα radiation (λ= 1.540 A°). It denotes that the CBTAFePc and CBTACoPc complexes are amorphous. The diffraction pattern of these complexes exhibits broad peaks with various diffused intensities. The peak intensity slowly increased by an increase in carbutamide groups. XRD patterns for the synthesized complexes were noted in the 2θ angle range of 0-60 °C as shown in Fig.-4. The less intensity peaks were observed at 2θ values of less intensity peaks at 11.50°, 12.65°, 23.12°, 24.40°, 32.04°, 46.55°, 47.42°, 58.02° and 59.85° for CBTAFePc complex and 07.06°, 11.20°, 17.52°, 18.39°, 19.20°, 20.00°, 30.39°, 31.20° and 40.39° for CBTACoPc complex, at 2θ values of high intensity peaks at 6.50°, 21.65°, 39.12°, 40.39°, and 55.85° for CBTAFePc complex and 07.08°, 8.00°, 09.12°, 10.39°, 11.50°, 15.65°, 21.12°, 25.39° and 41.39° for CBTACoPc complex. This indicates CBTAFePc and CBTACoPc complexes are amorphous.[34]

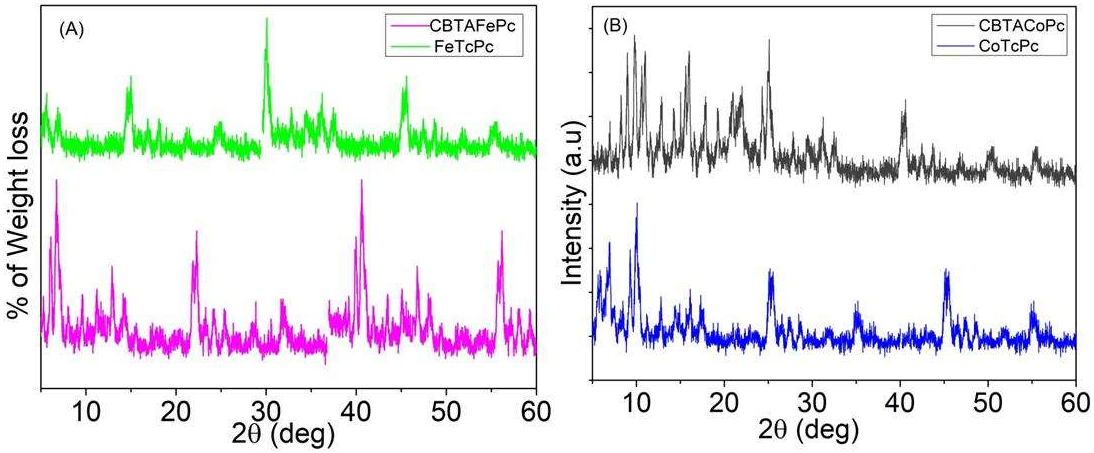

Fig.-4: XRD Analysis of (A) CBTAFePc with FeTcPc (B) CBTACoPc with CoTcPc Complexes

Elemental Analysis of CBTAFePc and CBTACoPc Complexes

Elemental analysis for C, H and N was done by Vario EL (III) C.H.N.S analyzer. The CBTAFePc and CBTACoPc were examined by a known quantity of the complexes with H_2SO_4 and HNO_3 mixture, followed by careful evaporation and calcinations.[31-32] Anal. For CBTAFePc with molecular weight and molecular formula 1759.7026 (Experimental): $C_{80}H_{78}FeN_{20}O_{16}S_4$ calc. (%) C-54.60, H-4.432, N-15.91, O-14.53, S-7.28, Fe; 3.17 found: C-54.51, H-4.32, N-15.80, O-14.61, S-7.20, Fe; 3.15. Anal. For CBTACoPc with molecular weight and molecular formula 1762.79 (Experimental): $C_{80}H_{78}CoN_{20}O_{16}S_4$ calc. (%) C-54.60, H-4.432, N-15.91, O-14.53, S-7.28, Co; 3.34 found: C-54.49, H-4.38, N-15.86, O-14.63, S-7.22, Co; 3.30.

Mass Spectrum

Mass spectroscopy (MS) is used to measure the mass to charge ratio [M+2] of compounds. The theoretical observation of mass spectra of the CBTAFePc complex is 1759.7026 and the experimental mass of the CBTAFePc exhibits a molecular ion peak at 1761.63 Fig.-5. It indicates the conformation of the formation of proposed complex.

Aggregation Behavior of CBTAFePc Complex

The aggregation property of CBTAFePc was analyzed by the UV-Vis method. The synthesized complex has 18 π-electron systems so that it shows aggregation behavior. The aggregation mainly depends on temperature, substituents, concentration and solubility. The CBTAFePc complex shows H-type and J-type aggregation that depends on the position of the substituents. Majorly the Fe-Pc showed H-type aggregation more in solvents and rarely observing J-type aggregation[30]. For measurement of aggregation behavior, we used Beer-Lambert law in the concentration range from 30×10^{-5} to 5×10^{-5} mol dm^{-3}.

In the present work aggregation property of the CBTAFePc complex was performed by different solvents such as DMF, DMSO, CCL_4 and $CHCl_3$ Fig.-6A. it shows that more aggregation takes place in DMF and

DMSO solvent due to the high solubility of the compound and less aggregation in CCL_4 and $CHCl_3$. The aggregation property of the CBTAFePc complex was also studied by using various concentrations of DMF solvent Fig.-6B, as the concentration of the DMF solvent increases the absorption peak intensity (Q-band) also increases. All the above results show that the aggregation behavior of the CBTAFePc was high in DMF solvent with high concentration.

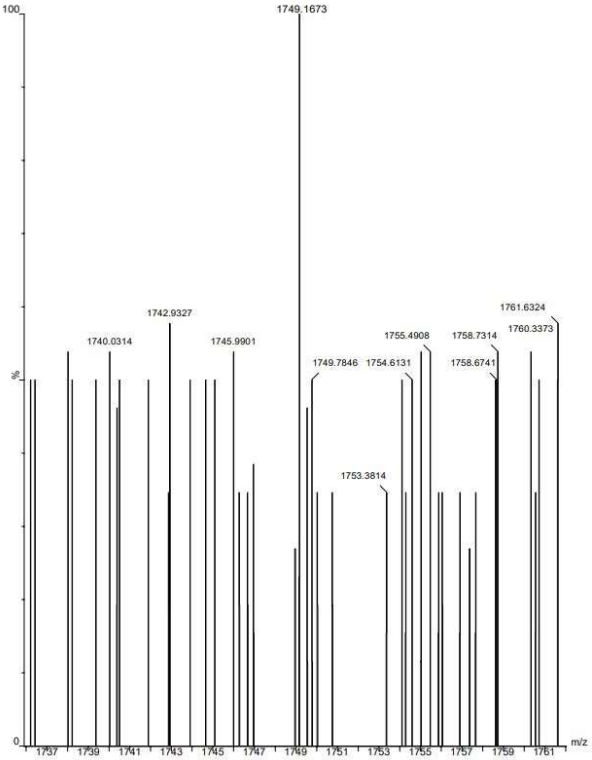

Fig.-5: Mass Spectra of CBTAFePc Complex

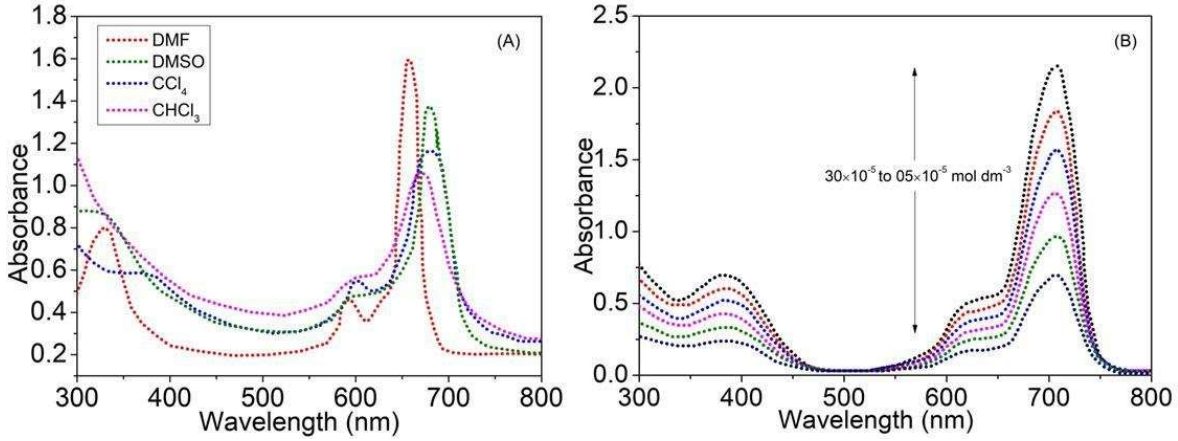

Fig.-6: Aggregation Property of CBTAFePc (A) Different Solvents of DMF, DMSO, CCL_4 and $CHCl_3$, (B) Different Concentrations of DMF Solvents

Catalytic Investigation

Cyclohexene Oxidation with CBTAFePc and CBTACoPc

The selectivity and catalytic activity (CA) of CBTAFePc and CBTACoPc complexes were studied by simple Cyclohexene oxidation method with m-CPBA as the model compound in experimental parameters in DMF (Tables-1 to 4), the oxidation of Cyclohexene was carried out by Cyclohexene (0.71×10^{-4} mol), CBTAFePc (3.58×10^{-7} mol) or CBTACoPc (3.57×10^{-7} mol) and m-CPBA (1.78×10^{-4} mol) and DMF (001 L) in a vessel and refluxed at 90 °C with stirring 800 rpm. The experiment was also performed by various

oxidants like TBHP, H_2O_2 and m-CPBA in absence of catalyst, the results give evidence for the oxidation of Cyclohexene, the catalyst is very important for the completion of the reaction. Therefore the catalyst is playing an important role in the oxidation of Cyclohexene seen in Tables-1 to 4. The comparative studies of CBTAFePc and CBTACoPc for Cyclohexene oxidation exhibits both the compounds are active catalysts in DMF solvents, which gives Cyclohexenol as the major product and Cyclohexene epoxide and 2-cyclohexen-1-one is a minor product, these are analyzed by GC for both penetrate and comparison with standards Scheme-3. The reaction rate increased by varying the oxidants, sub/cat. ratio and temperature.

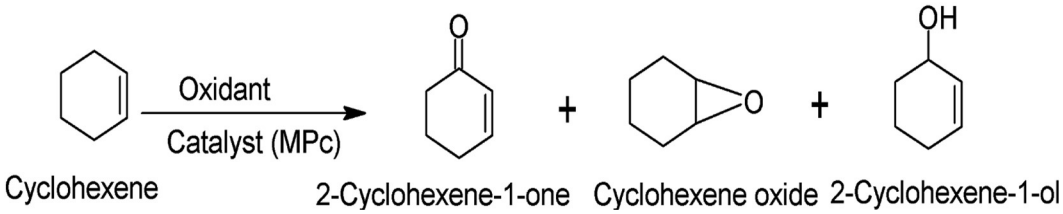

Scheme-3: Mechanism of Oxidation of Cyclohexene

The results of Cyclohexene oxidation by m-CPBA in presence of CBTAFePc and CBTACoPc as seen in Fig.-7A and Fig.-7B, indicates that the product yield is varied with reaction time. High yield was formed that is 2-cyclohexen-1-ol as the major product and Cyclohexene epoxide and 2-cyclohexen-1-one is a minor product for both catalysts. The yields for Cyclohexeneepoxide and Cyclohexenone were nearly similar to the catalysts CBTAFePc and CBTACoPc. The three product yields increased by the same level of time. This level off is most likely due to degradation of the Fe-Pc and Co-Pc catalyst by oxidant with time.

The substrate to catalytic molar ratio effect was examined in the range of 200-1200 and kept other parameters constants. The experimental conditions were 90 ^oC, 1.78×10^{-4} mol m-CPBA, 0.01 L DMF for 3h. the results are seen in Table-1. It gives clear evidence, as the substrate catalytic ratio decreases the increase of conversion. For each various substrate/catalyst ratio the Cyclohexene oxidation gives the same [a]2-Cyclohexene-1-ol as the major product and [c]Cyclohexene epoxide and [b]2-cyclohexen-1-one is a minor product. The major product gives a good selectivity of 60% and 57% for CBTAFePc and CBTACoPc.

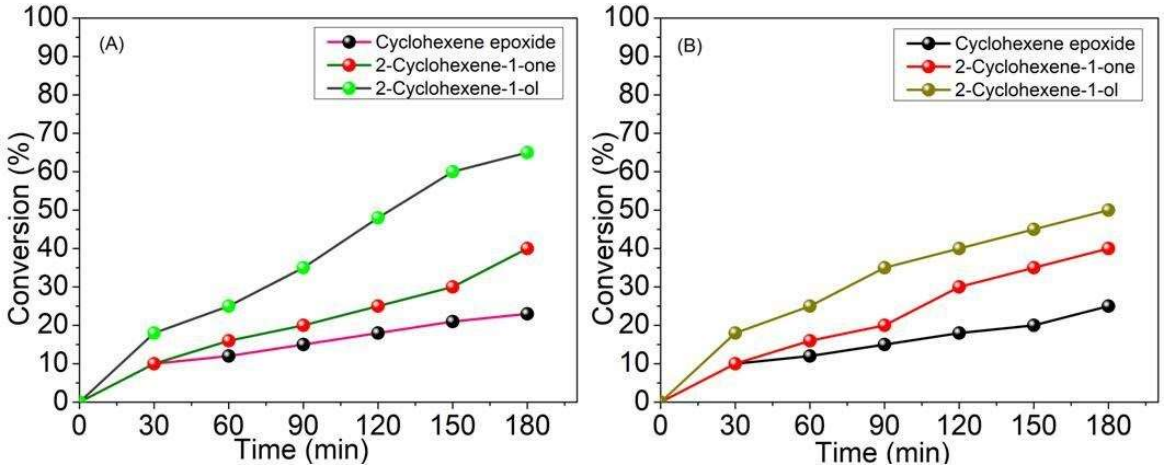

Fig.-7: Cyclohexene Oxidation (Time dependent) with (A) CBTAFePc (B) CBTACoPc

The oxygen source effect on the oxidation of Cyclohexene reaction was scrutinized for m-CPBA, aerobic oxygen, TBHP and H_2O_2, remaining all the experimental parameters kept constant. The obtained results are as shown in Table-2 and Fig.-8. In aerobic oxygen conditions, both complexes are not converted. In this experiment, the Cyclohexene oxidation is more effective in the m-CPBA oxidant with CBTAFePc and CBTACoPc. The same experiment was performed without m-CPBA oxidant; the oxidation reaction of Cyclohexene does not take place. Therefore m-CPBA shows a good oxidant effect on the oxidation of

Cyclohexene. The other oxidants like TBHP and H_2O_2 are not suitable oxidants for the catalytic system. The main reason we observed in the process is that the lower conversion of H_2O_2 undergoes degradized the CBTAFePc and CBTACoPc ring.

Table-1: Effect of Substrate to Catalytic Ratio on Cyclohexene Oxidation with CBTAFePc and CBTACoPc

Catalyst	Subs/Cat	[a]Alcohol	[b]Ketone	[c]Epoxide	Tot. Conv. (%)	TON mole of product/mole of catalyst	TOF (h^{-1}) mole of product/mole of catalyst×time
1c	200/1	60	20	19	99	195	64
2c		57	17	12	85	168	55
1c	400/1	58	18	14	90	355	118
2c		54	15	09	78	310	102
1c	600/1	53	14	12	79	369	155
2c		50	10	05	65	386	128
1c	800/1	48	12	07	67	530	176
2c		44	06	03	53	420	139
1c	1000/1	39	10	07	56	554	184
2c		36	05	04	45	446	148
1c	1200/1	33	10	06	49	582	193
2c		28	06	04	38	452	150

Then the color of the solution immediately turns colorless from blue-green color. Therefore the CBTAFePc and CBTACoPc do not involve effectively as a catalyst in the oxidation process. The same experiment is performed by TBHP. It shows more degradation compared with H_2O_2. All the above results show that the highest activity of CBTAFePc and CBTACoPc takes place in the presence of m-CPBA (TOF: 98 and 90) and other oxidant activity as shown in Table-2.

Table-2: Oxygen Source Effect on Cyclohexene Oxidation with CBTAFePc and CBTACoPc

Catalyst	Subs/Cat	[a]Alcohol	[b]Ketone	[c]Epoxide	Tot. Conv. (%)	TON mole of product/mole of catalyst	TOF (h^{-1}) mole of product/mole of catalyst×time
1c	m-CPBA	69	16	12	98	354	118
2c		64	15	11	90	312	101
1c	H_2O_2	27	16	07	50	184	60
2c		24	13	09	46	170	55
1c	TBHP	50	17	11	78	295	98
2c		46	10	07	63	241	81
1c	Free oxidant		-	-	-	-	-
2c			-	-	-	-	-

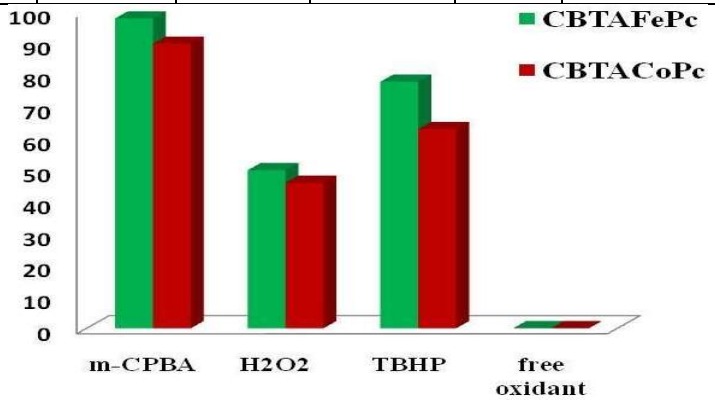

Fig.-8: The Oxidant Effect on the Oxidation of Cyclohexene

The other important parameter involving the oxidation reaction is a substrate to oxidant ratio, the reaction was performed in the range of 300/1-900/1 as seen in Table-3. The rate of oxidation reaction enhances with increasing oxidant/cat. ratio up to 500/1. Further increasing the ratio, the catalytic conversion decreases. It is very difficult to conclude the effect of oxidant at the present stage, but it is possible that the coordination around the iron and cobalt, iron may change and produce in-active intermediate species.

Table-3: Effect of Substrate to Oxidant Ratio on Cyclohexene Oxidation with CBTAFePc and CBTACoPc

Catalyst	Subs/Cat	[a]Alcohol	[b]Ketone	[c]Epoxide	Tot. Conv. (%)	TON mole of product/mole of catalyst	TOF (h^{-1}) mole of product/mole of catalyst×time
1c	300/1	34	18	15	66	258	87
2c		30	15	10	55	215	73
1c	400/1	43	21	16	80	314	106
2c		40	18	14	70	279	94
1c	500/1	64	16	10	90	357	120
2c		58	12	08	78	311	105
1c	600/1	36	18	15	69	370	90
2c		32	18	11	59	228	76
1c	900/1	26	11	05	42	168	57
2c		21	08	06	35	140	47

The temperature is also one of the critical parameters for catalytic oxidation of Cyclohexene with CBTAFePc and CBTACoPc. The CA increases by increasing the temperature. The experiment was performed in the range of 20-90 ºC with ox./subst./cat=500/200/1 and m-CPBA in DMF for 3 h as seen in Table-4. The overall conversion was increased 61% for CBTAFePc and 53% for CBTACoPc, when the temperature was increased from 20 to 90 ºC. The highest conversion (99%) was obtained with TOF=65 for complex CBTAFePc and (85%) was obtained with TOF=56 for complex CBTACoPc at 90 ºC.

Table-4: Effect of Temperature on Cyclohexene Oxidation with CBTAFePc and CBTACoPc

Catalyst	Subs/Cat	[a]Alcohol	[b]Ketone	[c]Epoxide	Tot. Conv. (%)	TON mole of product/mole of catalyst	TOF (h^{-1}) mole of product/mole of catalyst×time
1c	25	26	14	09	49	95	31
2c		23	12	09	44	83	27
1c	50	42	16	10	68	134	44
2c		39	12	09	60	117	39
1c	70	53	18	12	83	164	54
2c		50	13	10	73	141	47
1c	90	69	23	19	99	196	65
2c		60	19	16	85	169	56

The performance of CBTAFePc and CBTACoPc catalytic activity on oxidation of Cyclohexene was compared with other M-porphyrin and MPc catalysts (like Fe, Mn and Co). We get the best results in the form of TOF in Cyclohexene oxidation. We have also noted that the CBTAFePc was acting as the best catalyst compared with CBTACoPc.

The oxidation reaction system was monitoring by absorption spectroscopy in the 300 to 800 nm range of CBTAFePc and CBTACoPc, shows two strong absorptions bands assigned to the transition n- p* and p-p*. The intense absorption peak observed at 650-750 nm is assigned for Q-Band and one more absorption peak at 300-450 nm is assigned for B-band.[30-32] These bands are also found in the CBTAFePc and

CBTACoPc. But they shift and broadens due to m-oxo dimeric species of Fe(II)-Pc to Fe(III)-Pc and Co(II)-Pc to Co(III)-Pc.[33-35]

Table-5: The Homogeneous Catalytic Oxidation of Cyclohexene by the previously reported Catalysts

Catalyst	Reaction time (h)	Reaction Temp. (^{0}C)	Oxidant	Conv. (%)	Ref.
CoPc	8	60	TBHP	45.3	[37]
[Co(Me$_2$salpnMe$_2$)]	8	75	H_2O_2	27.6	[38]
CoPc	3	90	m-CPBA	61	[39]
[Mn(Me$_2$salpnMe$_2$)]	8	40	TBHP	50.9	[40]
Fe(TMP)Cl	10 min	25	m-CPBA	89	[41]
Co[NO]$_2$ Cu[NO]$_2$	8	75	H_2O_2	27.6	[42]
CBTAFePc	3	90	m-CPBA	99	Present work
CBTACoPc	3	90	m-CPBA	85	

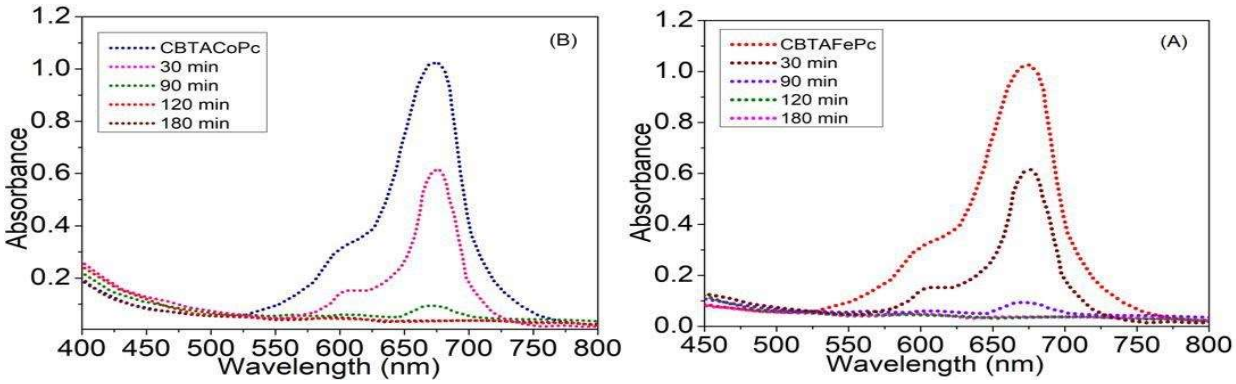

Fig.-9: Time Dependent Variation in the Visible Spectrum of the Oxidized Complex (A) CBTAFePc (B) CBTACoPc

Figures-9A and 9B show changes in the spectrum of CBTAFePc and CBTACoPc during the oxidation reaction with m-CPBA. The monomeric form of MPc is shown in Fig.-2 before the start of the catalytic reactions. The Q-band was observed at 670 nm for both the complexes CBTAFePc and CBTACoPc respectively. With oxidants (TBHP, m-CPBA, or H_2O_2), the decrease of intensity and broadens Q-band peaks at 657 and 665 nm. In the B-band region, there is no peak observed. Thus the addition of m-CPBA to the solutions of Fe (II) and Co(II) complexes resulted in only metal and not ring oxidation of Fe-Pc and Co-Pc. As the process of catalytic activity increases there is a decrease in the intensity of Q-band of the CBTAFePc and CBTACoPc, suggesting catalyst degradation is typical of MPc catalysts in homogeneous catalysis.[36] The m-CPBA produces alkylperoxide and alkoxy radicals, these radicals degradized the MPc ring and were observed by the change in the color of the solution from blue to green by continuing the catalytic reaction. If the reaction is continued the catalyst is turned to yellow color, which gives the formation of intermediate in the reaction. The process is continued and the MPcs undergo degradized by the oxidant. The UV Vis method is used for the determination of the degradation of the compounds. The overall results suggest that the CBTAFePc and CBTACoPc exists a long durable reaction time with effective catalytic activity without degradation of oxidation of Cyclohexene.

CONCLUSION

The Carbutamide substituted Fe(II) phthalocyanine (CBTAFePc) and Co(II) phthalocyanine (CBTACoPc) complex was synthesized from tetracarboxylic acid Fe(II) phthalocyanine (FeTcPc) and tetracarboxylic acid Co(II) phthalocyanine (CoTcPc) with Carbutamide (CBTA) by linkage of an amide has been developed. The macrocyclic molecules have high molecular weight and the molecule is completely soluble in Dimethylformamide and Dimethylsulfoxide. The CBTAFePc and CBTACoPc were confirmed by FTIR, Ultraviolet-Visible, PXRD and Thermo-gravimetric techniques. The catalytic activity

of CBTAFePc and CBTACoPc complexes were analyzed in the oxidation of Cyclohexene with various parameters like temperature, types of oxidants, oxidant/cat ratio, and subs/catalyst ratio affect the oxidation reactions were investigate the optimum conditions of catalysts. CBTAFePc shows excellent catalytic results on oxidation of Cyclohexene with the highest yield with good selectivity. The overall results show that the CBTAFePc complex exhibits an excellent catalyst compared with the CBTACoPc complex for investigation of the oxidation of Cyclohexene.

ACKNOWLEDGMENT

One of the author's T.M. Sharanakumar thanks Vijayanagara Srikrishnadevaraya University, Ballari, BITM College, Ballari for facilities and encouragement.

REFERENCES

1. I. Umit, Ph.D. thesis, Gebze Instıtue of Technology, (2007). https://doi.org/10.1016/j.jorganchem.2013.07.013
2. P. Wu, T. Tatsumi, T. Komatsu, T. Yashima, *Journal of Catalysis*, 202, **245** (2001). https://doi.org/10.1006/jcat.2001.3278
3. M.J. Cook, N.B.Mc. Keown J.M. Simmons A.J. Thomson M.F. Daniel. K.J. Harrison, R.M. Richsrdson, S.J. Roser, *Journal of Material Chemistry,***1**, 11(1991).
4. Z. Odabas, A. Altindal, A. R Ozkaya, M. Bulut, *Polyhedran,* **26**, 3505(2007), https://doi.org/10.1016/j.poly.2007.03.047
5. K.M. Kadish, K.M. Smith, R.Guilard (Eds.), the Porhyrine, Phthalocyanine: Synthesis of Phthalocyanine Precursors, Vol.15 (Chap.97), California (2003), https://doi.org/10.1080/00958972.2018.1423560
6. J. Cynthia M, Allen, Wesley M, Sharman and Johan E, Van Lier, *Journal of Porphyrins and Phthalocyanines*, **5(2),** 161(2001), https://doi.org/10.1002/jpp.324
7. Qiwen Lai, Md Zakaria Quadir and Kondo-Francois Aguey-Zinsou, *ACS Applied Energy Materials,* **12(1)**, 6824(2018), https://doi.org/10.1021/acsaem.8b01087
8. Nana Wang, Junsheng Yu, Yue Zang, Jiang Huang, Yadong Jiang, *Solar Energy Materials and Solar Cells*, **94(2)**, 263(2010), https://doi.org/10.1016/j.solmat.2009.09.012
9. C.C. Lenzoff, A.B.P. Lever (Eds.), Phthalocyanine: Properties and Applications, Vol.1, VCH Publisher, New York (1989), https://doi.org/10.1002/adma.19930051217
10. C.C. Lenzoff, A.B.P. Lever (Eds.), Phthalocyanine: Properties and Applications, Vol.2, VCH Publisher, New York (1993).
11. I. Ozcesmeci, S. Guner, A. I. Okur, A. Gul. *Journal of Porphyrins Phthalocyanine*, **11**,531(2007), https://doi.org/10.1142/S108842460700062X
12. Mounesh, Pari Malathesh, N.Y.Praveen Kumara, Bhvimane Jilani, C.D. Mruthynjayachari, K.R. Venugopala Reddy, *Heliyon,* **5(7)**, E01946(2019), https://doi.org/10.1016/j.heliyon.2019.e01946
13. Mounesh Nayaka, Bhvimane Sanna Jilani, Malatesh Pari, K.R Venugopala Reddy, K.S Lokesh, *Microchemical Journal*, **147**, 755(2019), https://doi.org/10.1016/j.microc.2019.03.090
14. K.R.V. Reddy, M.N.K. Harish, M.H. Fassiulla, Moinuddin Khan, J. Keshavayya, *Journal of Fluorine Chemistry*, **128**, 1019(2007), https://doi.org/10.1016/j.jfluchem.2007.05.001
15. Bhvimane Sanna Jilani, C.D. Mruthyunjayachari, P. Malatesh, Mounesh, T.M. Sharanakumar, K. R. Venugopala Reddy, *Sensors & Actuators: B, Chemical,* **301**, 127078(2019), https://doi.org/10.1016/j.snb.2019.127078
16. S. Nagel, M. Lener, C. Keil, R. Gerdes, L. Lukasz, S.M. Gorun. *The journal of Physical Chemistry C*, **115**, 8779 (2011), https://doi.org/10.1021/jp2010748
17. F. Yang, S.R. Forrest, *ACS nano*, **2**, 1022 (2008).
18. S.R. Forrest, *Chemical Reviews*, **97**, 1793(1997), https://doi.org/10.1021/cr941014o
19. C.C. Lenzoff, A.B.P. Lever (Eds.), Phthalocyanine: Properties and Applications, Vol.3, VCH Publisher, New York (1993).

20. C.C. Lenzoff, A.B.P. Lever (Eds.), Phthalocyanine: Properties and Applications, Vol.4, VCH Publisher, New York (1996).
21. G. De La Torre, P.Vazquez, F. Agullo-Lopez, T. Torres, *Journal of Material Chemistry*, **8**, 1671 (1998).
22. Mounesh, K.R. Venugopala Reddy, *Microchemical Journal*, **160**, 105610(2021), https://doi.org/10.1016/j.microc.2020.105610
23. R.R. Allison, C.H. Sibada Photodiagn, *Photodiagnosis Photodyn Ther*, **7(2)**, 61, (2010).
24. Yilin Tong, Dapeng Li, Jun Huang, Kun Li, Liyun Ding, Tianxia Wang, Jingjing Gong, *Journal of Wuhan University of Technology-Mater. Sci. Ed.,* **29**, 567(2014), https://doi.org/10.1007/s11595-014-0958-8
25. E.J. Denisov, I.B Atanas, pp. 448-500, CRC Press, Taylor and Francis(2005).
26. M.S Dieckmann, K.A Gray, *Water Research,* **30**, 1169(1996), https://doi.org/10.1016/0043-1354(95)00240-5
27. M. H. Moinuddin Khan, Fasiulla, J. Keshavayya and K. R. Venugopala Reddy, *Russian Journal of Inorganic Chemistry*, **53(1)**, 66 (2009), https://doi.org/10.1080/17518250903042414
28. Mounesh, T.M. Sharanakumar, N.Y. Praveen Kumar, K.R. Venugopala Reddy, *Analytical Chemistry Letters*, **10 (5)** (2020), https://doi.org/10.1080/22297928.2020.1857835
29. Mounesh, K.R. Venugopala Reddy, *Analytical Chimca Acta*, **1108**, 98(2020), https://doi.org/10.1016/j.aca.2020.02.057
30. T.M. Sharanakumar, Mounesh, N.Y. Praveen Kumar, K.R. Venugopala Reddy, Suresh, *Rasayan Journal of Chemistry,***13(4)**, 2133(2020), http://dx.doi.org/10.31788/RJC.2020.1345876
31. Mounesh, K.R. Venugopala Reddy, *Analytical Chemistry Letters,* **10(1)**, 33(2020), https://doi.org/10.1080/22297928.2020.1745683
32. Mounesh, K.R. Venugopala Reddy, *New Journal of Chemistry*, **44(8)**, 3330(2020), https://doi.org/10.1039/C9NJ05807A
33. Mounesh, K.R. Venugopala Reddy, *Analytical Chimca Acta,* **1108**, 98(2020), https://doi.org/10.1016/j.aca.2020.02.057
34. Mounesh, B.S. Jilani, P. Malatesh, K.R. Venugopala Reddy, K.S. Lokesh, *Microchemical Journal,* **147**, 755(2019), https://doi.org/10.1016/j.microc.2019.03.090
35. N.Y. Praveen Kumar, Mounesh, T.M. Sharan Kumar, K.R. Venugopal Reddy, Sangappa K. Ganiger, *Asian Journal of Chemistry*, **32(11)**, 2722(2020), http://doi.org/10.14233/ajchem.2020.22803
36. V.N. Nemykin, V.Ya. Chernii, S.V. Volkov, N.I. Bundina, O.L. Kaliya, V.D. Li, E.A. Lukyanets, *Journal Porphyrins Phthalocyanines*, **3(2)**, 87(1999), https://doi.org/10.1002/(SICI)1099-1409(199902)3:2<87::AID-JPP108>3.0.CO;2-G
37. N. Sehlotho, T. Nyokong, *Journal of Molecular Catalysis A: Chemical,* **219**, 201(2004), https://doi.org/10.1016/j.molcata.2004.05.010
38. M.H. Lim, S.W. Jin, Y.J. Lee, G.J. Jhon, W. Nam, C. Kim, *Bulletine of Korean Chemical Society*, **22**, 93(2001).
39. E.T. Saka, D. Çakır, Z. Bıyıklıoglu, H. Kantekin, *Dyes and Pigments*. **98**, 255(2013), https://doi.org/10.1016/j.dyepig.2013.02.021
40. M. Salavati-Niasari, P. Salemi, F. Davar, *Journal of Molecular Catalysis A: Chemical*, **238**, 215(2005), https://doi.org/10.1016/j.molcata.2005.05.026
41. C. Pratap, K. Shigeru, K. Toshinori, S. Shigeo, *Polyhedron*, **28**, 370 (2009).
42. Mounesh, T.M Sharanakumar, N.Y Praveenkumar, K.R Venugopal Reddy, K. Chandrakala, L Arunkumar, C.C Vidyasagar, *RSC Advances*, **11**, 16736(2021), https://doi.org/10.1039/d1ra01815a
43. Mounesh, N.Y Praveen Kumar, T.M Sharanakumar, K.R Venugopal Reddy, *Electrochemical Science Advances,* **27(11)**, 16736(2021), https://doi.org/10.1002/elsa.202100006

[RJC-6386/2021]

RSC Advances

PAPER

View Article Online
View Journal | View Issue

Cite this: *RSC Adv.*, 2021, **11**, 16736

Novel Schiff base cobalt(II) phthalocyanine with appliance of MWCNTs on GCE: enhanced electrocatalytic activity behaviour of α-amino acids†

Mounesh, *[a] T. M. Sharan Kumar,[b] N. Y. Praveen Kumar,[a] K. R. Venugopala Reddy,[a] K. B. Chandrakala,[a] L. Arunkumar[a] and C. C. Vidyasagar[c]

Received 8th March 2021
Accepted 11th April 2021

DOI: 10.1039/d1ra01815a

rsc.li/rsc-advances

A novel tetra-4-{(*E*)-[(8-aminonaphthalen-1-yl)imino]methyl}-2-methoxyphenol Co(II) phthalocyanine (CoTANImMMPPc) was synthesized using a precursor protocol and characterized *via* electroanalytical and spectroscopic techniques. The FT-IR spectra of the synthesized compounds showed significant peaks corresponding to the functional groups of the precursors and phthalocyanine (Pc) compound. The mass and NMR spectra confirmed the formation of the target precursor compounds. A film of CoTANImMMPPc was deposited on the surface of an electrode and applied for the detection and monitoring of L-alanine and L-arginine. The cyclic voltammetric studies of L-alanine and L-arginine using the (CoTANImMMPPc/MWCNTs/GC) electrode showed a linear response in the range of 50–500 nM and the limit of detection was found to be 1.5 and 1.2 nM, respectively. Differential pulse voltammetry and chronoamperometry showed that the catalytic response for L-alanine and L-arginine is in the range of 50–500 nM with an LoD of 1.8 and 2.3 nM, respectively. The oxidation-active CoTANImMMPPc film significantly enhanced the current response in the chronoamperometric method and displayed a selective and sensitive response towards L-alanine and L-arginine in the presence of various other biomolecules. The developed electrode showed good working stability and was applied for the analysis of real samples, which yielded satisfactory results. Therefore, CoTANImMMPPc-MWCNTs/GCE shows good analytical performance, is economical and produced *via* a simple synthetic method and can be applied as a sensor for the detection of L-alanine and L-arginine.

1. Introduction

Amino acids are an important class of organic compounds, which are required in numerous processes in biological systems and used as medicine and in food and beverages. Among them, alanine and arginine play very important roles in many biological functions. L-Alanine (L-Ala) is an amino acid used in the conversion of tryptophan and vitamin B6 into proteins, which provide energy for the muscles and increase immunity in the human body. As another amino acid, L-arginine (L-Arg) is transformed in the body into nitric acid, which acts as a neurotransmitter and makes the circulation of blood very easy by relaxing the blood vessels. Thus, considering the above-mentioned importance of alanine and arginine, it is essential to study their electrochemical behavior and sensitive detection. Electrochemical investigations employing phthalocyanines have been reported by researchers, leading to an enhancement in the electrochemical process by changing their functional groups and forming composites with carbon materials such as graphite and carbon nanotubes.

The electrochemical oxidation of L-Ala and L-Arg on substituted phthalocyanines has been reported earlier.[1–6] However, the electrochemical sensing is not satisfactory due to the slow movement of electrons at the electrode interface.[7–13] Accordingly, it has been reported that the efficiency of phthalocyanines can be enhanced by forming composites with carbon particles such as graphite and carbon nanotubes. The modified electrodes can be used for oxidation and the determination of the adsorption behavior of amino acids. Many researchers have focused on the development of the electrocatalytic process, mainly enhancing the overpotential and faradaic current

[a]*Department of Studies and Research in Chemistry, Vijayanagara Srikrishnadevaraya University, Ballari-583105, Karnataka, India. E-mail: mounesh.m.nayak@gmail.com; Tel: +91-8197546693*

[b]*Department of Studies and Research in Chemistry, Ballari Institute of Technology and Management, Ballari-583104, Karnataka, India*

[c]*Department of Studies and Research in Chemistry, Rani Channamma University, Belagavi-591156, Karnataka, India*

† Electronic supplementary information (ESI) available. See DOI: 10.1039/d1ra01815a

encountered in the electrooxidation of molecules using macrocyclic transition metal complexes.[14–18]

A cobalt tetracarboxylic acid phthalocyanine (CoTCAPc) was immobilized on a gold electrode for the oxidative and reductive detection of H_2O_2 at the physiological pH. We also reported the fabrication of glucose oxidase (GOx) enzyme on a gold electrode modified with an electrocatalyst CoTCAPc,[19] cobalt phthalocyanine tetracarboxylic acid (CoPc-COOH) by H_2O_2,[20] tetra chlorobenzoxazolamine nickel(II) phthalocyanine (NiTCBPc),[21] novel *n*-octadecylcarboxamide CoPc for the amperometric detection of bioanalytes using a modified GCE (CoODAPc),[22] cobalt(II) tetrasulfanilamide phthalocyanine,[23] cobalt phthalocyanine tetracarboxylic acid-functionalized polymer monolith for the selective enrichment of glycopeptides and glycans,[24] and the importance of electrochemical methods in biological and environmental analyses for the determination biomolecules.[25–27]

In this work, we focused on the synthesis of a CoTCAPc complex substituted with the Schiff ligand 4-{*E*-[(8-aminonaphthalen-1-yl)imino]methyl}-2-methoxyphenol (ANImMMP). The structure of the compound was confirmed *via* FTIR, UV-visible, XRD, TGA, mass spectroscopy, and elemental analysis. The Pc complex was used to form a composite with MWCNTs and employed for the detection of nanomolar concentrations of L-Ala and L-Arg *via* the cyclic voltammetry (CV), differential pulse voltammetry (DPV) and chronoamperometry (CA) techniques. Specifically, the modified CoTANImMMPPc/GCE with multiwalled carbon nanotubes (MWCNTs/CNTs) was employed for the detection of nanomolar concentrations of L-Ala and L-Arg *via* the CVs, DPV and CA techniques. The selectivity studies in the presence of some biomolecules including ascorbic acid, dopamine, L-cysteine, L-asparagine (L-Asp), glucose and hydrogen peroxide showed negligible current responses by L-Ala and L-Arg at nM concentrations. In the present work, the oxidation of the L-Ala and L-Arg analytes exhibited well separated and defined peaks. Also, we focused on the surface modification technique in the electrochemical system, which is significant for experimental design, to build an electrochemical sensor with high selectivity, low detection limit, excellent linear concentration responses, reproducibility and sensitivity for the simultaneous detection of individual analytes and L-Ala in the presence of L-Arg.

2. Experimental

2.1 Materials

1,8-Diaminonaphthalene, *m*-vanillin, methanol, L-Ala, L-Arg, L-asparagine (L-Asp), L-cysteine (L-Cys), glucose (GOx), hydrogen peroxide (H_2O_2), ascorbic acid (AA), dopamine (DA), anhydrous potassium carbonate (K_2CO_3), hexane, tetrahydrofuran (THF) and *N*,*N*′-dicyclohexylcarbodiimide (DCC), dimethyl sulfoxide (DMSO) were supplied by Sigma Aldrich. *N*,*N*′-Dimethylformamide (DMF) was obtained from M-Tedia (USA) and used without further purification.

2.2 Preparation of ANImMMP and CoTANImMMPPc

The novel Schiff base ligand was synthesized by adding *m*-vanillin (1 g, 0.0055 M), diaminonaphthalene (1.05 g, 0.0055 M)

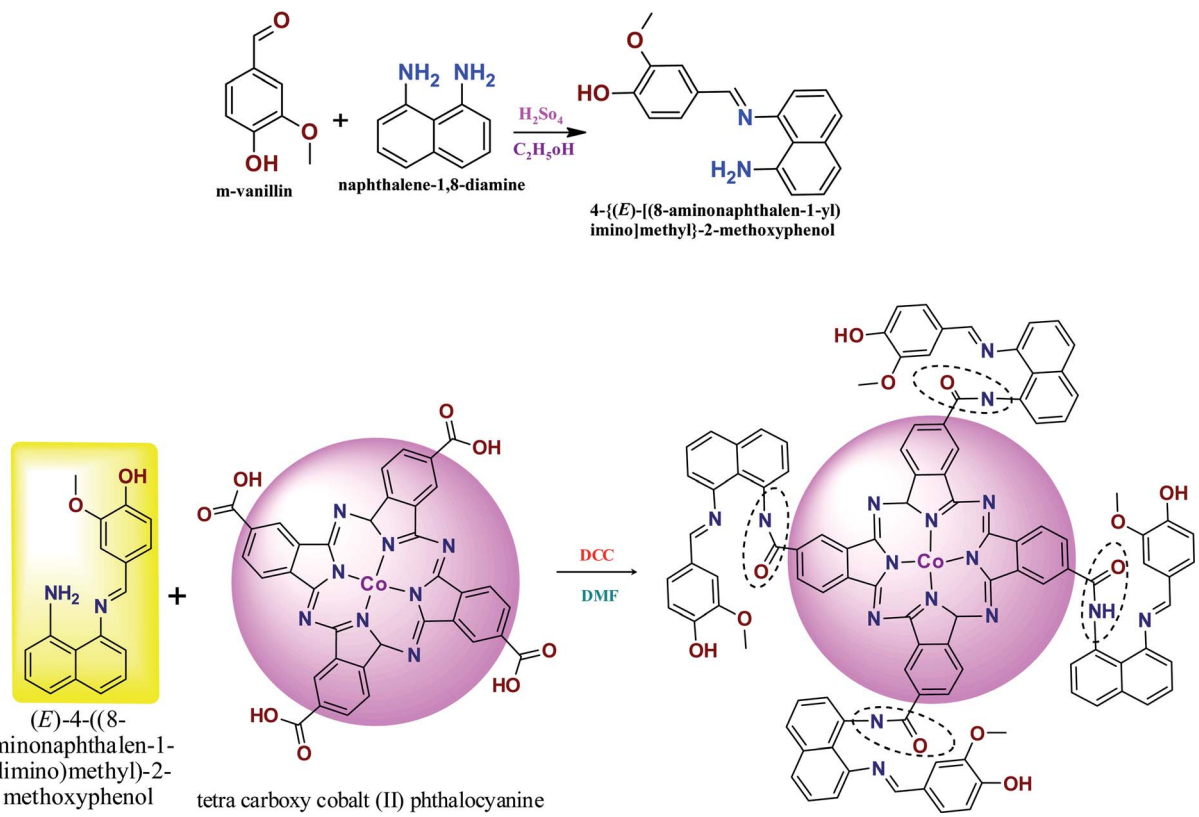

Scheme 1 Preparation of ANImMMP and CoTANImMMPPc.

and 20 mL of methanol to a round-bottom flask. The mixture was stirred under a nitrogen atmosphere, and subsequently 1–2 mL of H_2SO_4 was added dropwise. The chemical mixture was stirred for 6 h at 45–50 °C to obtain a bright gray precipitate. The chemical mixture was refluxed under vacuum and washed with water and recrystallized by methanol and purified by column chromatography using hexane and ethyl acetate as the solvent. Yield (1.298 g, 78.1%). Melting point: 197–200 °C of ANImMMP (Scheme 1).[28,29]

The CoTANImMMPPc complex was synthesized by adding CoTCAPc (0.52 g, 0.00069 M), K_2CO_3 (0.48 g, 0.00345 M) and DCC catalyst dissolved in DMF (25 mL) to an RB flask. The reaction mixture was stirred for 25 min, then ANImMMP (1.5 g, 0.00343 M) was added to the reaction mixture and the solution was stirred for 46 h at 28 °C. A dark green precipitate was formed, and then the product was filtered and washed with cold water and hot water followed by hexane to give CoTANImMMPPc in a yield of 95% (Scheme 1).[1,30]

2.3 Characterization methods

A Shimadzu UV-2550 spectrophotometer is used to measure the UV-visible absorption spectra and the FTIR spectra were measured using a PerkinElmer spectrum 100 FTIR spectrometer. ^{1}H-NMR spectra were recorded at 300 MHz on a Bruker spectrometer and the chemical shift values are expressed in δ ppm with respect to TMS as an internal standard. X-ray diffraction (XRD) (CuKα radiation) patterns were measured using a Bruker Advanced D8-diffractometer. The mass spectrum of the synthesized compound was confirmed using an ESI-MS MALDI-Micro mass Q-TOF2 instrument. Thermogravimetric analyses (TGA) were performed on a Mettler-Toledo instrument at a heating rate of 25 °C min^{-1} and nitrogen flow rate of 40 mL min^{-1}. All electrochemical analyses were performed on a CHI620E electrochemical workstation USA with a conventional 3-electrode system (glassy carbon electrode (GCE), Ag/AgCl electrode and platinum electrode).

2.4 GCE surface modification technique

The surface of the GCE was rubbed with a 0.6 mm alumina slurry and then completely washed with distilled water and sonicated in water followed by acetone for about 5 min followed by drying in an oven at 25 °C. Then 5 mg of CoTANImMMPPc and Nafion binder were ultrasonicated for 30 min for their dispersion in DMF. Using the drop-coating method, the CoTANImMMPPc material was deposited on the GCE electrode. Then the electrode was dried at 25 °C. The same procedure used for the preparation of the CoTANImMMPPc-MWCNT electrode using MWCNTs/CNTs. These modified electrodes were used for the electrochemical detection of L-Ala and L-Arg.

3. Results and discussion

The preparation of the ANImMMP and CoTANImMMPPc complex is presented in Scheme 1. Specifically, vanillin reacts with diaminonaphthalene to form an imine bond. The ligand and complex were obtained with high purity and good yield and were characterized using different spectral techniques including FT-IR, ^{1}H NMR, TGA, MASS, P-XRD and UV-visible spectroscopy. The carboxylic group of the CoTCAPc amine group reacted with the ligand to produce the amide-bridged CoTANImMMPPc complex. The elemental analysis of the synthesized complex gives evidence for the purity of the complex and the experimental values are consistent with the theoretical values, as shown in Table S1.† The CoTANImMMPPc complex is dark green in color and completely soluble in concentrated sulfuric acid (H_2SO_4) and DMSO.

3.1 FT-IR spectra

The FT-IR (cm^{-1}) spectrum in Fig. S1a† shows intense and broad absorption bands in the region of 3680–3400 cm^{-1} (–OH and –NH_2). In the spectrum shown in Fig. S1b,† the peak corresponding to the carboxylic acid group of CoTCAPc appears in the range of 3700–3200 cm^{-1}. However, in Fig. S1c,† the peak for the –COOH group disappears with the appearance of a peak corresponding to a substituted amide group (CoTANImMMPPc) at 3327 cm^{-1} (–CONH), a peak in the region of 2934–2663 cm^{-1} (Ar-CH), and peaks for the vibrations caused by the stretching of the (C=N) and (C=C) at around 1631–1606 cm^{-1}. The sharp peak in the region of 1565–1523 cm^{-1} corresponds to C=O, and the sharp peak at 744 cm^{-1} is attributed to C–Br. Thus, the vibrational bands at 1499, 1457, 1433, 1392, 1309, 1245, 1228, 1113, 1032, 884, 847, 844, 647, and 605 cm^{-1} support the presence of functional groups in the CoTANImMMPPc ring.

3.2 ^{1}H NMR spectra

^{1}H-NMR (300 MHz, DMSO-d_6): δ 2.50 (3H, s), 6.68 (1H, dd, J = 7.8, 1.6 Hz), 6.80 (1H, dd, J = 8.4, 0.5 Hz), 6.91 (1H, dd, J = 7.8, 1.3 Hz), 6.99 (1H, dd, J = 1.7, 0.5 Hz), 7.20 (5H, 7.48 dd, J = 8.4,1.7 Hz), 7.30 (td, J = 7.8, 0.5 Hz), 7.96 (ddd, J = 8.1, 7.8, 0.5 Hz), 8.12 (dddd, J = 8.1,2.0,1.3, 0.5 Hz), 8.43 (1H, s), 4.10 (1H, s) and 2.0 (base line), as shown in Fig. S2.†

3.3 UV-visible spectra

The UV-Vis spectra of the ANImMMP, CoTCAPc and CoTANImMMPPc systems show distinct B and Q bands. ANImMMP shows the Q-band at 300–500 nm and B-band at 200–260 nm (Fig. S3† inset a curve). The UV studies of the phthalocyanine exhibit two strong absorption curves, where one appears in the range of 550–720 nm (Q band), which represents the π–π* transition from the HOMO to the LUMO within the Pc ring. The second curve in the wavelength range of 300–450 nm corresponds to the B band (Fig. S3,† inset curves b and c), arising from the deeper π-levels/LUMO transition.[31,32] The UV-Vis spectrum of the compound shown in Scheme 1 in DMSO at 28 °C is presented in Fig. S3.† The red and green color of the complexes show a peak in the Q-band region and a shoulder peak was observed in the range of 550–700 nm, indicating the good aggregation of Pcs.

3.4 PXRD analysis

The powder X-ray diffraction study (PXRD) of CoTANImMMPPc was done in the 2θ range of 10–100°, as shown in Fig. S4,† inset

curve ((a) ANImMMP, (b) CoTCAPc and (c) CoTANImMMPPc). The PXRD analysis was performed to elucidate the crystal nature and size of the QDs. The parent Pcs and substituted complex exhibit the same patterns. However, the patterns vary in intensity for the complex compared to the corresponding metal Pcs. The PXRD patterns are used to describe the crystallinity of materials.[33,34] The diffraction pattern of CoTANImMMPPc shows sharp peaks at 9°, 20°, 21°, 25°, 49°, 60°, and 70° with a low intensity, indicating that CoTANImMMPPc is crystalline in nature. Furthermore, the shapes of the X-ray diffraction patterns indicate that ANImMMP, CoTCAPc and CoTANImMMPPc were crystalline in nature.

3.5 Thermogravimetric analysis

Fig. S5† shows the thermal stability and decomposition behavior of the CoTANImMMPPc and CoTCAPc complexes at various temperatures (inset (a) CoTCAPc and (b) CoTANImMMPPc). The TGA data shows that CoTANImMMPPc and CoTCAPc degraded mainly in three ways in a nitrogen environment. The first step revealed that the initial weight loss of 0% corresponds to the moisture of volatile species. In the second step, the substituent gets isolated in the temperature range of 0–386 °C, leading to 55.14% weight loss due to the degradation of the substituted ligand. The third step occurs readily in the oxidizing environment and leads to the degradation of the Pc structure in the temperature range of 386–580 °C and 24.46% weight loss. Finally, the cobalt oxide (CoO) product is formed, and the cobalt oxide corresponds to 21.42% weight loss. Thus, all these results show that the substituted CoTANImMMPPc has greater stability compared to other substituted metal phthalocyanines.[35–38]

3.6 Mass spectra

LC-mass spectrum (LCMS) analysis: *m*/*z* [M] calcd. 292 for $C_{18}H_{16}N_2O_2$: found [M + Z] +293, as shown in Fig. S6† for ANImMMP. The mass spectrum of CoTANImMMPPc shown in Scheme 1 confirms the desired structure: *m*/*z* [M] calcd. 1851 for $C_{108}H_{79}CoN_{16}O_{12}$: found [M + Z] +1853, as shown in Fig. S7.†

4. Electrochemical studies

Fig. 1A shows the charge transfer behavior of the CoTANImMMPPc/GCE and CoTANImMMPPc-CNTs/GCE electrodes, where in the CVs plot no peak can be observed at the bare GCE in pH 7 PBS solution (inset curve a). Conversely, when the same reaction was carried out in the presence of the $K_4Fe(CN)_6$ system in 100 nM, a peak corresponding to the $[Fe(CN)_6^{3-}]/[Fe(CN)_6^{4-}]$ redox was observed (Fig. 1A, inset curve b). Then the GCE surface was well-coated with CoTANImMMPPc and CoTANImMMPPc-CNTs, and the modified GCE electrodes were immersed in PBS containing 100 nM $K_4Fe(CN)_6$ (Fig. 1A, inset curve c). The modified GCE and with CNTs exhibited the fast movement of electrons in the $[Fe(CN)_6^{3-}]/[Fe(CN)_6^{4-}]$ redox couple system, which was not inhibited by the CoTANImMMPPc/CNTs. The lack of inhibition of the redox couple was observed even before the substituted CoPc was deposited on the GCE; however, both CoTANImMMPPc/GCE and CoTANImMMPPc/CNTs/GCE show high peak current intensities and the same redox potential for the $[Fe(CN)_6^{3-}]/[Fe(CN)_6^{4-}]$ system at the scan rate of 50 mV s^{-1} because the modified GCE acts as a current carrying conductor and it allows rapid electron transfer in solution. The modified CoTANImMMPPc-CNTs/GCE was scanned at various scan rates, and a linear increase in the peak current was observed in both the anodic and cathodic peak currents, showing a positive potential at 240 and 130 mV with an increase in the scan rate (10–250 mV s^{-1}), respectively, as shown in Fig. 1B. Thus, the increase in peak current observed in the CV plot with the square root of scan rate indicates a diffusion-controlled mass transfer process.[39,40]

4.1 Electrochemical characterization

The electrochemical investigation of the CoTANImMMPPc-modified electrode was carried out in the presence of (pH 7) PBS, bare GCE (inset Fig. S8A†). CoTANImMMPPc/GCE exhibited a cathodic peak potential of 25 mV with low current responses (Fig. S8A,† inset curve a), and CoTANImMMPPc/CNTs/GCE exhibited an enhanced peak current, as shown by the cathodic peak potential (Fig. S8A,† inset curve b) at the scan

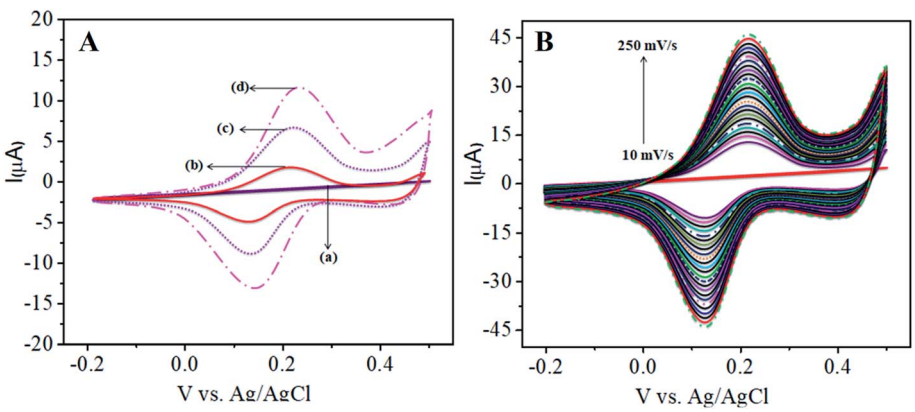

Fig. 1 Cyclic voltammetric curves in (pH 7) PBS for 100 nM $K_4Fe(CN)_6$: (A) inset curves (a) bare GCE without $K_4Fe(CN)_6$ in (pH 7) PBS, (b) bare GCE, (c) CoTANImMMPPc/GCE, (d) CoTANImMMPPc/CNTs/GCE at a scan rate of 50 mV s^{-1} and (B) various scan rates for CoTANImMMPPc/CNTs/GCE/mV s^{-1}.

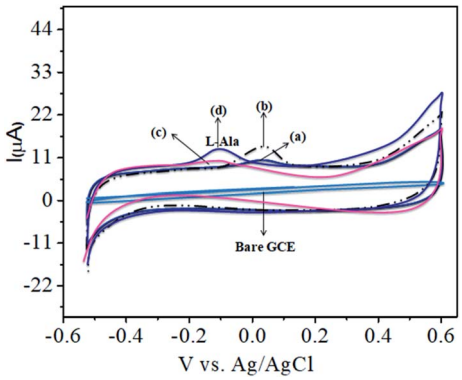

Fig. 2 Experimental CVs of modified GCE in (pH 7) PBS at peaks: inset bare GCE, (a) CoTANImMMPPc, (b) CoTANImMMPPc/CNTs, (c) 100 nM of L-Ala by CoTANImMMPPc and (d) L-Ala by CoTANImMMPPc/CNTs at a scan rate of 50 mV s^{-1}.

rate of 50 mV s^{-1}. The electrons transfer to the CNTs absorbed on the hydrophobic surface of the GCE by Co^{III}/Co^{II}. On the CoPc–CNTs-modified GCE, the oxidation of CoTANImMMPPc-CNTs/GCE in pH 7 PBS occurs in the one-step electrocatalytic oxidation of Co(II)Pc to Co(III)Pc according to eqn (1) as follows:

$$Co^{II}PC \rightarrow Co^{III}PC + e^{-} \quad (1)$$

The oxidation of the CoTANImMMPPc/CNT electrode was observed using the cathodic peak potential by applying different scan rates in the range of 10–100 mV s^{-1} with an increase in the high positive current response by CoTANImMMPPc/CNTs. The linear regression curve determined using I_p *vs.* different scan rates was $Y = 0.224x + 25.610$ with a correlation coefficient of $R^2 = 0.998$ (inset Fig. S8B†).

4.2 Nanomolar detection of L-alanine (L-Ala)

The CoTANImMMPPc complex was used for analytical applications, where both CoTANImMMPPc/GCE and CoTANImMMPPc/CNTs/GCE showed high peak current intensities due to the fast electron transfer, as discussed above (Fig. S8A and S2A,† inset curves a and b). The electrocatalytic ability of CoTANImMMPPc/CNTs was evaluated for the electrooxidation of L-Ala. Fig. 2 shows the cyclic voltammograms of CoTANImMMPPc (inset c curve) and CoTANImMMPPc/CNTs (inset d curve) in the presence of 100 nM L-Ala, where a strong oxidation peak was observed at −120 mV due to the high positive peak current of CoTANImMMPPc/CNTs and an increase in oxidation peak current was achieved for the oxidation of L-Ala. The well-defined anodic peak potential at −120 mV shows its significant electrocatalytic effect and good electrochemical response for detection of L-Ala.[41] Thus, according to the results, in the presence of CNTs, a greater enhancement in peak potential was observed compared with CoTANImMMPPc.

In our present work, the CoTANImMMPPc/CNT complex exhibits excellent electrocatalytic activity and it can facilitate the transfer of electrons in L-Ala, where the CoTANImMMPPc/GCE surface modulates the electrochemical reactions in a controlled fashion. In addition, the high density and well distributed CoTANImMMPPc on the surface of the CNTs can induce the exposure of more active sites for the catalytic oxidation reaction and result in efficient electrical behavior through direct binding with the CNTs, which enhances the electrocatalytic activity. Overall, the results show that both CNTs and CoTANImMMPPc play an important role and exhibit a synergistic effect in the oxidation of L-Ala in PBS (pH 7) solution. Fig. 3A shows the detection of L-Ala with different concentrations in the range of 50–400 nM at the anodic peak potential (−120 mV) with a high positive current, which indicates the excellent electrocatalytic oxidation of L-Ala by the modified GCE. The linear concentration range was determined to be 50–400 nmol L^{-1} using I_p *vs.* different concentration: $Y = 0.097$ (L-Ala) + 22.144 with $R^2 = 0.999$ (inset Fig. 3A) at different scan rates for the detection of 200 nM L-Ala at the anodic potential. With an enhancement in the scan rate (10–100 mV s^{-1}) with a high positive peak current (Fig. 3B), the linearity was determined using I_p *vs.* different scan rates: $Y = 0.489x + 30.750$ with the correlation coefficient of $R^2 = 0.9998$ (inset Fig. 3B).[13] Thus, the modified electrode exhibits a low detection limit and limit of quantification and high sensitivity, as shown in Table 1.

4.3 Detection of L-Ala in the presence of L-Arg

The analytical applicability of the CoTANImMMPPc/CNTs/GCE at +25 mV (Fig. 4, inset curve a) for the detection of L-Ala at

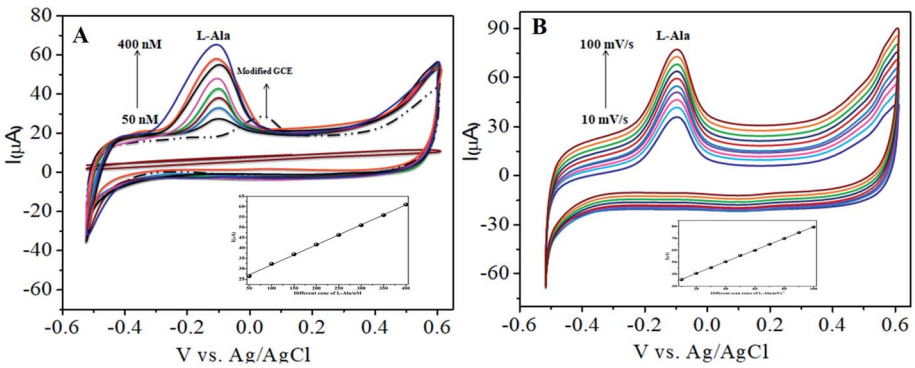

Fig. 3 Experimental CVs of modified GCE in (pH 7) PBS electrolyte: (A) inset modified CoTANImMMPPc, various concentrations of 50–400 nM of L-Ala by CoTANImMMPPc/CNTs at scan rate 50 mV s^{-1} and (B) various scan rates (10–100 mV s^{-1}) for the detection of L-Ala by CoTANImMMPPc/CNT electrode.

Table 1 Analytical parameters observed for the detection of L-alanine and L-arginine[a]

Method	Analyte	Detection methods	[a]Potential (E_p)	[b]LOD	[c]LOQ	[d]R^2	Sensitivity ($\mu A\ nM^{-1}\ cm^{-2}$)	Linear range	Ref.
MWCNT-HF/QD modified PGE		DPV	−540	0.158 μM	0.610 μM	0.994	—	0.561–33 670 μM	43
Acid co-injection		Anion-exchange column	—	10.4 μM	—	0.999	—	0.5 to 20 μM	48
MWCNT-Cu_2O CPE		CA	—	0.17 μM	—	—	—	5–400 μM	49
NiONPs/GCE		CA	0.42 V (AP)				0.4 nA $\mu M^{-1}\ cm^{-2}$	30–200 μM	51
CoTANImMMPPc/		CVs	−0.120 V	1.5 nM	4.5 nM	0.999	0.097	50 to 400 nM	This work
CNTs/GCE		DPV	−0.120 V	1.8 nM	5.4 nM	0.997	0.081	50 to 500 nM	
		CA	−0.130 V (AP)	3.1 nM	9.3 nM	0.997	0.068	50 to 500 nM	
MWCNT-HF/QD modified PGE		DPV	−0.150 V	0.081 μM	0.312 μM	0.988	—	0.287–17 220 μM	43
Acid co-injection		Anion-exchange column	—	15.4 μM	—	0.992	—	0.5 to 8 μM	48
Iridium nano-CPE		CV, CA	—	19.7	—	—	—	0–544	50
CoTANImMMPPc/		CVs	+0.140 V	1.2 nM	3.6 nM	0.998	0.054	50 to 500 nM	This work
CNTs/GCE		DPV	+0.140 V	2.3 nM	6.9 nM	0.999	0.104	50 to 500 nM	
		CA	+0.150 V (AP)	3.5 nM	10.5 nM	0.997	0.105	50 to 500 nM	

[a] a = peak potential, b = limit of detection, c= limit of quantification, d = correlation coefficient, CV = cyclic voltammetry, DPV = differential pulse voltammetry, CA = chronoamperometry, AP = applied potential/fixed potential.

−120 mV (Fig. 4, inset curve b) was investigated with the continuous addition of 100 nM L-Arg in the same electrolyte cell. The detected cathodic peak potential was +140 mV by CoTANImMMPPc (Fig. 4, inset curve c), whereas the CoTANImMMPPc/CNT electrode exhibited a high positive current at the oxidation peak potential compared to CNTs due to the good electrocatalytic activity of the material (Fig. 4, inset curve d). Initially, the electrochemistry for L-Ala and L-Arg on the surface of the modified GCE was studied *via* CV. A well-defined cathodic peak potential was observed at +140 mV with a remarkable increase in peak current due to the oxidation of L-Arg when the electrode surface was modified with the CoTANImMMPPc/CNT complex, which indicates its significant electrocatalytic effect and good electrochemical response for the oxidation of L-Arg in the presence of L-Ala.[42]

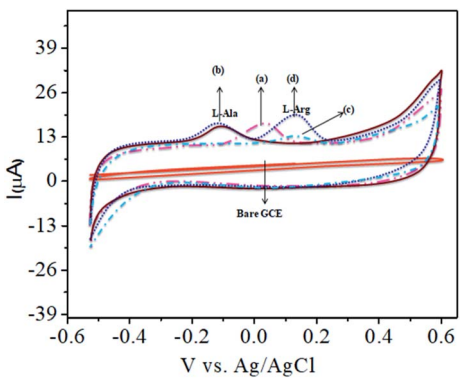

Fig. 4 Experimental CVs of modified GCE in (pH 7) PBS: inset bare GCE, (a) CoTANImMMPPc/CNTs, (b) 100 nM of L-Ala by CoTANImMMPPc/CNT/GCE, (c) 100 nM of L-Arg by CoTANImMMPPc and (d) L-Ala in the presence of 100 nM of L-Arg by CoTANImMMPPc/CNTs at the scan rate of 50 mV s^{-1}.

The CoTANImMMPPc/CNT electrode plays an important role and has a synergistic effect in the oxidation of L-Ala in presence of L-Arg in PBS (pH 7) solution. With a fixed concentration of L-Ala in the same cell and the addition of different concentrations in the range of 50–400 nM for the detection of L-Arg at the cathodic peak potential (+140 mV), the high positive current, as shown in Fig. 5A, indicates the excellent electrocatalytic oxidation of L-Ala simultaneously in the presence of L-Arg by the modified electrode, and the linear regression curve determined using I_p *vs.* different concentration/nM was $Y = 0.135$ (L-Arg) + 28.432 with $R^2 = 0.99982$ (inset Fig. 5A) at different scan rates for the detection of 200 nM L-Arg at the cathodic potential. With an enhancement in the scan rate (10–150 mV s^{-1}) with a high positive current (Fig. 5B), the linearity I_p *vs.* different scan rates was determined to be $Y = 0.424x + 31.909$ with $R^2 = 0.99986$ (inset Fig. 5B). Thus, the CoTANImMMPPc-CNT electrode exhibits good electrocatalytic activity, reproducibility and stability.

4.3.1 Individual detection of L-arginine. The electrocatalytic activity of CoTANImMMPPc/CNTs was examined *via* CV. Fig. 6 shows the CV responses for various concentrations of L-Arg in the range of 50–500 nM and CoTANImMMPPc/CNTs in

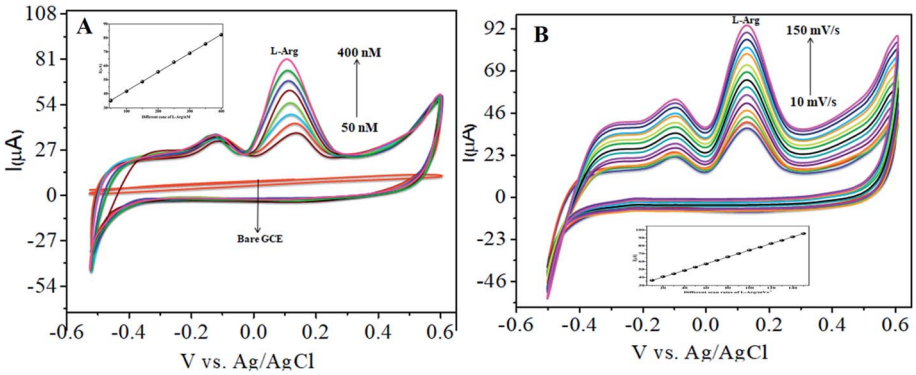

Fig. 5 Experimental CVs of modified GCE in (pH-7) PBS: (A) inset bare GCE, L-Ala in the presence of various concentrations in the range of 50–400 nM of L-Arg by CoTANImMMPPc/CNTs at a scan rate of 50 mV s^{-1} and (B) various scan rates for the detection of L-Arg.

(pH 7) PBS at a scan rate of 50 mV s^{-1} (Fig. 6A). The modified GCE electrode shows significant oxidation currents at +140 mV *vs.* Ag/AgCl and a reduction peak was not observed in the reverse scan. The substantial positive shift in the peak potential and enhancement in the current indicate the significant electrocatalytic ability of CoTANImMMPPc-CNTs for the oxidation of L-Arg, which can be attributed to the high surface area to volume ratio of the CoTANImMMPPc-CNT electrode, where L-Arg can easily penetrate the conductive porous channels of the electrode, leading to good sensitivity. The modified GCE was predicted to show a high cathodic peak current with an increase in the concentration of L-Arg in the range of 50–500 nM L^{-1} and the linearity I_p *vs.* different concentrations of L-Arg was determined to be $Y = 0.054$ (L-Arg) + 8.008 with $R^2 = 0.998$ (inset Fig. 6A). The CVs of 50 nM L-Arg solution at different scan rates (10–150 mV s^{-1}) were recorded, as shown in Fig. 6B, and current function was smoothly enhanced with the potential sweep rate, confirming the electrocatalytic nature of the electrooxidation process, with the linear equation $Y = 0.323x + 19.850$ with $R^2 = 0.999$. Thus, the modified GCE was exhibited good electrocatalytic activity and excellent analytical performance, as shown in Table 1.

4.4 DPV studies for L-Ala and L-Arg

The various parameters were studied in the DPV method by analyzing the peak currents and standard concentrations of the two analytes. For the simultaneous detection of L-Arg and L-Ala in PBS (pH 7) at a scan rate 50 mV s^{-1} in the presence of CoTANImMMPPc/CNTs, well-defined peaks were observed with a variation in the concentration, clearly indicating the effect of concentration. The simultaneous and individual voltammetric detection of L-Arg (Fig. 7A), and different concentrations of L-Ala (50–500 nM) using the CoTANImMMPPc/CNTs electrode was investigated at the anodic peak potential (−130 mV) by DPV, and the linear equation was determined to be $Y = 0.081$ (L-Ala) + 8.40 with $R^2 = 0.997$ (inset Fig. 7A). When the concentration of one species changed, the concentration of L-Ala remained constant. Fig. 7B shows the various DPV of L-Ala with various concentrations in the presence of L-Arg analyte, where the peak currents for L-Arg increased linearly with an increase in L-Arg concentration in the range of 50–500 nM with the related regression equation $Y = 0.120$ (L-Arg) + 7.354 with $R^2 = 0.999$, as shown in the inset of Fig. 7B.[43,44]

Similarly, Fig. 8A and B show that the peak current was enhanced linearly with an increase in the concentration of L-Arg and L-Ala, and with a fixed concentration of L-Arg analyte constant. The results show that the electrochemical signals of L-Arg and L-Ala are not dependent on each other at the CoTANImMMPPc/CNTs electrode, where different concentrations (50–500 nM) of L-Arg, as shown in Fig. 8A, were detected at a constant cathodic peak potential (+140 mV), and as shown in Fig. 8B, L-Ala in the presence of a fixed concentration of L-Arg was detected at the anodic peak potential (−140 mV). Therefore,

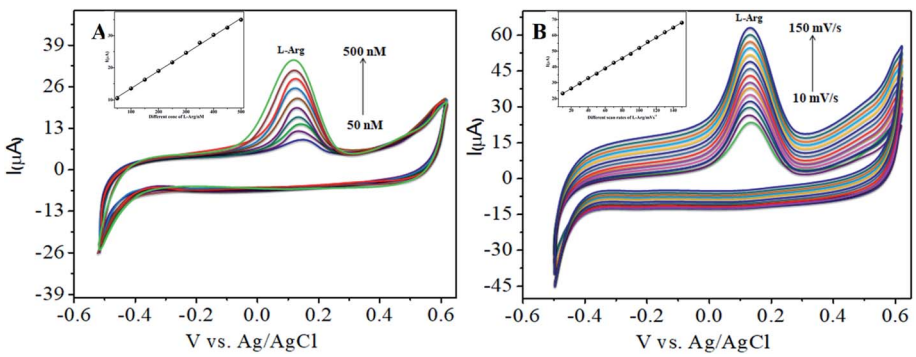

Fig. 6 Experimental CVs of modified GCE in (pH 7) PBS: (A) inset bare GCE, various concentrations of L-Arg in the range of 50–500 nM by CoTANImMMPPc/CNTs at a scan rate of 50 mV s^{-1} and (B) various scan rates for the detection of L-Arg.

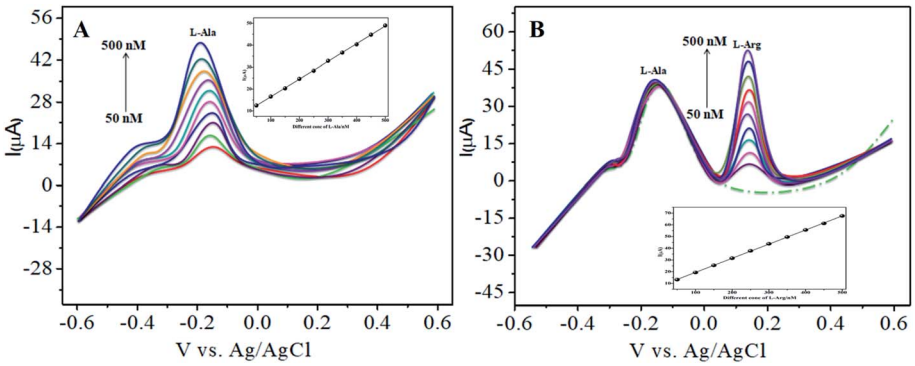

Fig. 7 Experimental DPV for CoTANImMMPPc/CNT/GCE in (pH 7) PBS: (A) various concentrations of L-Ala in the range of 50–400 nM and (B) in the presence of different concentrations of L-Arg at a scan rate of 50 mV s^{-1}.

the selective determination of each amino acid in the presence of each other is possible and a well-distinguished anodic peak and cathodic peak corresponding to L-Arg and L-Ala oxidation can obtained at CoTANImMMPPc/CNTs, respectively. For the pre-concentration factor, the corresponding regression equation is $Y = 0.104$ (L-Arg) + 0.889, as shown in the inset of Fig. 8A, and $Y = 0.112$ (L-Ala) + 7.477, as shown in the inset of Fig. 8B with the correlation coefficient of 0.9998 and 0.999, respectively. Furthermore, the experimental limit of detection (LOD),[43,44] quantification (LOQ), and linear dynamic range (LDR) were studied under the optimum conditions to evaluate the practical applicability of the sensor, as shown in Table 1.

4.5 Amperometric responses for L-Ala and L-Arg

The amperometric determination of L-Ala and L-Arg in flow systems and the hydrodynamic behavior of different concentrations in the range of 50–500 nM of L-Ala and L-Arg were investigated at the CoTANImMMPPc/CNT electrode, and the applied potential for L-Ala and L-Arg (±150 mV) is shown in the inset of Fig. 9A. For the detection of L-Arg, low current responses to L-Ala were observed, indicating that the oxidation of L-Ala readily increases at the modified GCE electrode due to electrocatalysis.[45,46] Hence, a potential of −150 mV and +150 mV were selected as the working potential for the amperometry determination of L-Ala and L-Arg using CoTANImMMPPc/CNTs under hydrodynamic conditions, respectively. Fig. 9A shows the typical current–time responses of CoTANImMMPPc/CNTs during the successive addition of L-Ala and L-Arg separately to a continuous stirring PBS solution under the optimized experimental conditions (pH 7, applied potential of +150 and −150 mV *vs.* Ag|AgCl). It was observed that the sensor exhibited a response within 5 s (inset Fig. 9A). The sensor showed a linear response in the L-Ala and L-Arg concentration range of 50 to 500 nM L^{-1} with the linear equation $Y = 0.068$ (L-Ala) + 3.164 and $Y = 0.105$ (L-Arg) − 5.847 with a correlation coefficient of 0.997 and 0.997, respectively, as shown in Fig. 9B. Furthermore, the detection limit (signal/noise ratio [S/N] = 3) was found to be 120 and 100 nM L^{-1}, respectively. Thus, the results indicate that our proposed sensor has a low detection limit and good sensitivity, as shown in Table 1.

4.5.1 Interference and selectivity. Difficulties in the accurate measurement of the concentration of L-Ala (Fig. S9A†) and L-Arg (Fig. S9B†) can arise from electroactive interfering amino acids such as histidine, lysine, glycine, methionine, L-asparagine (L-Asp), L-cysteine, and tyrosine, which are normally present in physiological samples. Thus, we tested the selectivity of the above biosensor design by adding the abovementioned seven interfering compounds at their typical concentrations

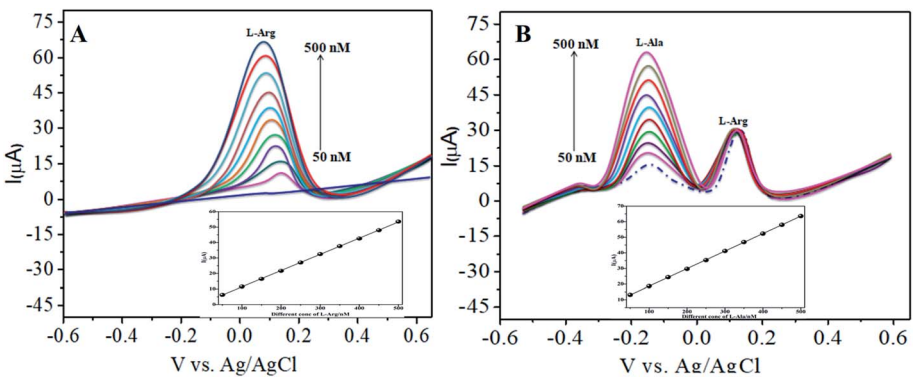

Fig. 8 Experimental DPV of CoTANImMMPPc/CNTs in (pH 7) PBS: (A) various concentrations of L-Arg and (B) in the presence of different concentrations of L-Ala at a scan rate of 50 mV s^{-1}.

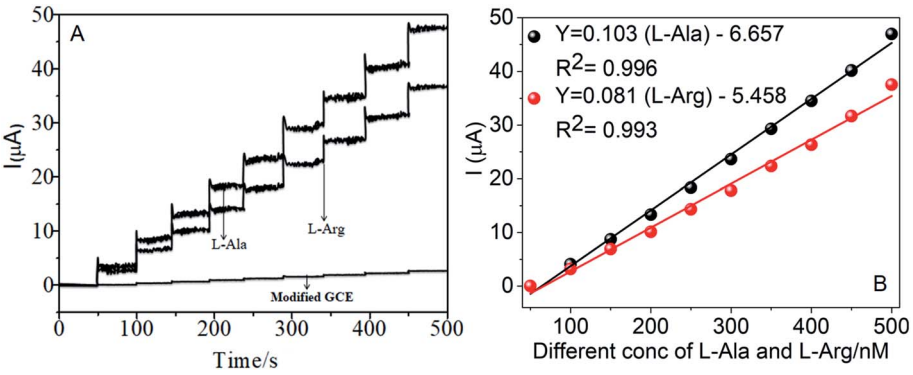

Fig. 9 Individual amperometry responses of CoTANImMMPPc/CNT electrode in (pH 7) PBS: (A) inset modified GCE, various concentrations of L-Ala & L-Arg in the range of 50–500 nM and (B) linear plot of various concentrations of L-Ala and L-Arg/nM *vs.* peak current at the applied potential of ±150 mV.

(200 nM of the abovementioned interfering molecules). The introduction of CNTs deposited on the electrode surface dramatically reduced the sensitivity to the interfering compounds, while retaining the sensitivity for L-Ala and L-Arg. Furthermore, the compounds usually present in matrices where L-Ala and L-Arg are determined such as histidine, lysine, glycine, methionine, L-asparagine (L-Asp), L-cysteine, and tyrosine were tested for their ability as potential interferences, either directly electrochemically active at the potential used or indirectly as matrix components at the fixed potential of ±150 mV. Fig. S9† shows the amperogram recorded at the CoTANImMMPPc-CNTs/GCE composite biosensor under the experimental parameters employed for the detection of L-Ala and L-Arg. It can be observed that the newly developed biosensor did not exhibit any interference for the detection of the tested analytes, with negligible/minimal current responses for the interfering biomolecules, as shown in Fig. S9.†

4.6 Repeatability, reproducibility and stability of the CoTANImMMPPc/CNT electrode L-alanine and L-arginine sensors

The repeatability of the sensor was analyzed using the peak current values in the CV curves of the CoTANImMMPPc/CNT-GC electrode for the detection of 200 nM L-alanine and L-arginine in PBS (pH 7) for five successive measurements. The relative standard deviation (RSD) was less than 2.5%, indicating that there was no blocking effect on the oxidation products on the electrode surface. The fabrication reproducibility of six sensors, which were prepared using the same procedure, demonstrated acceptable reproducibility with an RSD of 1.9%. The stability of the L-alanine and L-arginine sensors was recorded using CV curves for 200 nM L-alanine and L-arginine in PBS (pH 7). It should be noted that the fabricated sensor was stored under ambient conditions. The peak current value was obtained at 7 day intervals. The results show that the current maintained about 95% of its initial value after 60 days, indicating the long-term stability of the sensor.

4.6.1 Real sample analysis. Amperometric detection curves were obtained (inset in Fig. S10†) for the determination of L-arginine and L-alanine in peanuts and almonds (A) and egg and green beans (B) using CoTANImMMPPc/CNTs-GCE. During the amperometric detection, PBS (pH 7) electrolyte was added for each analysis. The current response observed was up to 95% within the 5–7 s after the sample was added and resultant amperogram was consistent with the lab sample results. The linearity was obtained from the concentration-dependent linear calibration plots, as shown in Fig. S10† ((A) peanuts and almonds and (B) eggs and green beans). The sensor parameters such as working range were calculated, and finally, it was found that it exhibited a more extensive linear range for the milk sample between 100 to 1800 nM (Fig. S10C and D†), and sensitivity and detection limit obtained for the seeds, eggs and vegetables were calculated. The linear range, LOD and sensitivity for L-arginine in the peanut and almond samples were determined to be 3 nM, 100 to 1800 nM, and 0.038 and 0.034 μA nM cm^{-2}, respectively. For L-alanine in the egg and green bean samples, the LOD and sensitivity were 5 nM, and 0.032 and 0.029 μA nM cm^{-2}, respectively. Thus, satisfying the requirements of a cheap and responsive electrochemical device, herein, an advantageous and instantaneous analytical device for the detection of L-arginine and L-alanine in peanut, almond, egg, and green bean samples was developed.

4.7 Electronic impedance spectroscopy

To study the nature of the electrode–electrolyte interface at the bare surface and modified electrodes, electrochemical impedance spectroscopy (EIS) is a suitable technique. The electron transfer resistance (R_{ct}) at the electrode surface, which determines the electron transfer kinetics of the redox probe, can be calculated using the diameter of the semi-circle in the impedance spectrum.[47] The present impedance spectra were compiled using an aqueous electrolyte solution of 0.1 M KCl. The obtained Nyquist plots for the CoTANImMMPPc/CNT-GC electrode (Fig. S11A†) and bare GCE (Fig. S11B†) show a significant difference in their response, as shown in Fig. S11A.† A semi-circle with a larger diameter was observed for the CoTANImMMPPc/CNT-GC electrode in the frequency range of 100 kHz to 0.01 Hz. The charge transfer resistance (R_{ct}) values

obtained using the plots in Fig. S11† for the CoTANImMMPPc/MWCNT/GCE and bare GCE are 298 and 418, respectively.

5. Conclusion

Herein, a novel CoTANImMMPPc complex was synthesized and its structure was confirmed using various spectroscopic techniques. Also, an electrochemical investigation was performed using the CoTANImMMPPc/CNTs/GC electrode for the detection of L-alanine in the presence of L-arginine with the individual determination of two well-defined peaks by CV and DPV. These two amino acid analytes were detected at nanomolar concentrations, and the amperometry detection of the individual analytes and the selectivity of the electrode in the presence of other biomolecules such as L-cysteine, L-asparagine, ascorbic acid, dopamine, glucose and hydrogen peroxide were investigated, showing a negligible current response during the detection of L-alanine and L-arginine. The CoTANImMMPPc/MWCNT-GC electrode exhibits good analytical performances including low detection limit, repeatability, reproducibility, excellent linear dynamic range concentration range, and high selectivity and sensitivity.

Conflicts of interest

The authors declare no conflicts of interest.

Acknowledgements

One of the author Mounesh thanks to Vijayanagara Sri Krishnadevaraya University SC/ST fellowship.

References

1 Mounesh, B. S. Jilani, P. Malatesh, K. R. Venugopala Reddy and K. S. Lokesh, *Microchem. J.*, 2019, **147**, 755–763.
2 K. E. Sekhosana, E. Amuhaya and T. Nyokong, *Polyhedron*, 2016, **105**, 159–169.
3 *The Porphyrin Handbook*, ed. K. Ishii, N. Kobayashi, K. M. Kadish, K. M. Smith and R. Guilard, Academic Press, New York, 2003, 16, pp. 1–40.
4 N. B. McKeown, *Phthalocyanine Materials: Synthesis, Structure and Function*, Cambridge University Press, 1998, vol. xvii, p. 193, ISBN 0-521-49623-3.
5 P. Sen and S. Z. Yildiz, *Inorg. Chim. Acta*, 2017, **462**, 30–39.
6 J. P. Randin, *Electrochim. Acta*, 1974, **19**(2), 83–85.
7 F. Beck, *J. Appl. Electrochem.*, 1977, **7**, 191.
8 R. K. Sen, J. Zagal and E. Yeager, *Inorg. Chem.*, 1977, **16**(12), 3379–3380.
9 J. Zagal, R. K. Sen and E. Yeager, *J. Electroanal. Chem.*, 1977, **83**, 207–213.
10 Mounesh, T. M. Sharan Kumar, N. Y. Praveen Kumar and K. R. Venugopal Reddy, *Anal. Chem. Lett.*, 2020, **10**(5), 620–635.
11 A. V. D. Putten, A. Elzing, W. Visscher and E. Barendrecht, *J. Electroanal. Chem.*, 1987, **221**, 95–104.
12 Y. S. Fung and S. Y. Mo, *J. Anal. Chem.*, 1995, **67**, 1121–1124.
13 S. Majdi, A. Jabbari, H. Heli and A. A. Moosavi-Movahedi, *Electrochim. Acta*, 2007, **52**, 4622–4629.
14 J. Obirai, F. Bedioui and T. Nyokong, *J. Electroanal. Chem.*, 2005, **576**, 323.
15 M. Beley, J. P. Collin, R. Ruppert and J. P. Sauvage, *J. Am. Chem. Soc.*, 1986, **108**, 7461.
16 F. Xu, H. Li, S. J. Cross and T. F. Guarr, *J. Electroanal. Chem.*, 1994, **368**, 221.
17 J. Obirai and T. Nyokong, *Electrochim. Acta*, 2005, **50**, 5427.
18 K. I. Ozoemena, Z. Zhao and T. Nyokong, *Inorg. Chem. Commun.*, 2006, **9**, 223.
19 P. N. Mashaz, K. Ozoemena and T. Nyokong, *Electrochim. Acta*, 2006, **52**, 177–186.
20 I. S. Hosu, Q. Wang, A. Vasilescu, S. F. Peteu, V. Raditoiu, S. Railian, V. Zaitsev, K. Turcheniuk, Q. Wang, M. Li, R. Boukherroub and S. Szunerits, *RSC Adv.*, 2015, **5**, 1474–1484.
21 N. Y. Praveen kumar, Mounesh, T. M. Sharanakumar and K. R. Venugopalreddy, *Chem. Pap.*, 2021, **75**, 2683–2694.
22 Mounesh, K. R. Venugopalreddy and O. Nagaraja, *Chem. Pap.*, 2021, **75**, 2945–2956.
23 K. R. Venugopala Reddy, N. Y. Praveenkumar, Mounesh, T. M. Sharanakumar and S. K. Ganiger, *Asian J. Chem.*, 2020, **32**(11), 2722–2730.
24 W. Zhang, N. Song, H. Zheng, W. Feng and Q. Jia, *Proteomics*, 2018, **18**(20), 1700399.
25 J. Xie, D. Cheng, Z. Zhou, X. Pang, M. Liu, P. Yin, Y. Zhang, H. Li, X. Liu and S. Yao, *Microchim. Acta*, 2020, **187**, 469.
26 I. Mohammed, M. Nemakal, S. Aralekallu, V. A. Sajjan, T. R. Divakara, M. Palanna, C. P. K. Prabu and L. K. Sannegowda, *J. Electroanal. Chem.*, 2020, **871**, 114292.
27 L. Yang, N. Huang, Q. Lu, M. Liu, H. Li, Y. Zhang and S. Yao, *Anal. Chim. Acta*, 2016, **903**, 69–80.
28 M. Saddam Hossain, C. M. Zakaria, M. Kudrat-E-Zahan and B. Zaman, *Chem. Sin.*, 2017, **8**(3), 380–392.
29 H. Karaca, *J. Organomet. Chem.*, 2016, **822**, 39–45.
30 Mounesh, P. Malathesh, N. Y. Praveen Kumara, B. S. Jilani, C. D. Mruthyunjayachari and K. R. Venugopala Reddy, *Heliyon*, 2019, **5**, e01946.
31 Mounesh and K. R. Venugopala Reddy, *Anal. Chem. Lett.*, 2020, **10**(2), 137–151.
32 K. Serbest, I. Degirmencioglu, Y. Unver, M. Er, C. Kantar and K. Sancak, *J. Organomet. Chem.*, 2007, **692**, 5646–5654.
33 K. Sawada, W. Duani, K. Sekitani and K. Satoh, *J. Mol. Liq.*, 2005, **119**, 171–176.
34 Mounesh and K. R. Venugopal Reddy, *Microchem. J.*, 2021, **160**, 105610.
35 J. P. Fan, X. M. Zhang and M. Ying., *S. Afr. J. Chem.*, 2010, **63**, 145–151.
36 Mounesh and K. R. Venugopala Reddy, *Anal. Chem. Lett.*, 2020, **10**(1), 33–48.
37 Mounesh and K. R. Venugopala Reddy, *Anal. Chim. Acta*, 2020, **1108**, 98–107.
38 Mounesh and K. R. Venugopala Reddy, *New J. Chem.*, 2020, **44**(8), 3330–3340.
39 Mounesh and Venugopala Reddy, *New J. Chem.*, 2020, **44**, 16831–16844.

40 P. Mashazi, C. Togo, J. Limson and T. Nyokong, *J. Porphyrins Phthalocyanines*, 2010, **14**, 252–263.
41 X. Qiao, Y. Huanga, X. Lin, S. Zhu and Y. Fu, *Biochem. Eng. J.*, 2016, **113**, 1–6.
42 P. Akhtar, C. O. Too and G. G. Wallace, *Anal. Chim. Acta*, 1997, **339**, 211–223.
43 S. Hooshmand and Z. Es'haghi, *J. Pharm. Biomed. Anal.*, 2017, **146**, 226–235.
44 C. J. Hsueh, J. H. Wang, L. Dai and C. C. Liu, *Biosensors*, 2011, **1**, 107–117.
45 C. H. Kwan Roger, Y. T. Hon Phoebe and R. Renneberg, *Anal. Chim. Acta*, 2004, **523**, 81–88.
46 W. Dai, M. Li, H. Li and B. Yang, *Sens. Actuators, B*, 2014, **201**, 31–36.
47 M. Palanna, S. Aralekallu, C. P. K. Prabhu, V. A. Sajjan, Mounesh and L. K. Sannegowda, *Electrochim. Acta.*, 2021, **367**, 137519.
48 P. Jandik, J. Cheng, D. Jensen, S. Manz and N. Avdalovic, *Anal. Biochem.*, 2000, **287**, 38–44.
49 S. Dong, S. Zhang, L. Chi, P. He, Q. Wang and Y. Fang, *Anal. Biochem.*, 2008, **381**, 199–204.
50 C. J. Hsueh, J. H. Wang, L. Dai and C. C. Liu, *Biosensors*, 2011, **1**, 107–117.
51 M. Roushani, M. Shamsipur and S. M. Pourmortazavi, *J. Appl. Electrochem.*, 2012, **42**, 1005–1011.

South East Asian J. of Mathematics and Mathematical Sciences
Vol. 18, No. 1 (2022), pp. 341-350

ISSN (Online): 2582-0850

ISSN (Print): 0972-7752

DEGREE SEQUENCES ON LINE GRAPH OF R-CORONA GRAPHS

Veeresh S. M., Manjunath Muddalapuram and Pralahad M.

Department of Mathematics,
Ballari Institute of Technology and Management,
Ballari - 583104, Karnataka, INDIA

E-mail : veeresh2010.1155@gmail.com, manju3479@gmail.com,
pralahadm74@gmail.com

(**Received:** *Apr. 12, 2021* **Accepted:** *Apr. 01, 2022* **Published:** *Apr. 30, 2022)*

Abstract: A graph $G = (V, E)$ is a set of vertices, which are connected by edges. In this paper, we study the line graph of R-corona operations of complete, cycle and r-regular graphs in terms of degree sequences(DS).

Keywords and Phrases: Line graph, R- corona operations, complete, cycle and r-regular graphs.

2020 Mathematics Subject Classification: 05C76.

1. Introduction

Let $G = (V, E)$ be a simple connected graph which does not contains loops and multiple edge. The degree of vertex u is the number of vertices are adjacent to u and it is denoted as deg_u or d_u. A graph in which every two vertices are adjacent is called as a complete graph [5]. A closed walk is finite or infinite vertices and no vertex is repeated is called cycle [11]. A graph is said to be r-regular graph in which each vertex degree is r [8].

Tyshkevich et. al., [10, 4] established a correspondence between DSs of graph and some structural properties of the graph in 1981 and Bolloas started the study on DSs on the same year. The degree sequences DSs of a graph G is obtained by degree of vertices x_i of G in ascending or descending order and it is defined as $DS(G) = \{\aleph_1^{\ell_1}, \aleph_2^{\ell_2}, \aleph_3^{\ell_3}, ..., \aleph_n^{\ell_n}\}$ [2, 9].

Definition 1.1. *The line graph of a graph G is another graph $L(G)$ is defined on $V(G)$, if two vertices are adjacent in $L(G)$ if and only if their corresponding edges are adjacent in G* [3].

Definition 1.2. *The semi-total point graph $R(G)$ is obtain from G by adding one vertex($I(G)$ is the set contains additional vertices) to each edge of G and joining each new vertex ($I(G)$) to the end vertices of the corresponding edge* [7].

Definition 1.3. *Let G and H be two graphs with vertices n_1 and n_2 and edges m_1 and m_2 respectively. The R- vertex corona of graphs G and H with $(n_1+m_1+n_1n_2)$ vertices and $(3m_1 + n_1(n_2 + m_2))$ edges and is obtained from one copy $R(G)$ and $|V(G)|$ copies of H, by joining the i^{th} vertex of $V(G)$ to each vertex in the i^{th} copy of H* [1, 6].

Figure 1: K_2 and K_1

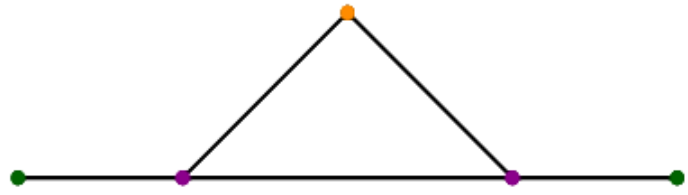

Figure 2: $K_2 \odot_R K_1$

Definition 1.4. *Let G and H be two graphs with vertices n_1 and n_2 and edges m_1 and m_2 respectively. The R- edge corona of graphs G and H with $(n_1+m_1+m_1n_2)$ vertices and $m_1(n_2+m_2+3)$ edges and is obtained from one copy $R(G)$ and $|E(G)|$ copies of H, by joining the i^{th} vertex of $I(G)$ to each vertex in the i^{th} copy of H.*

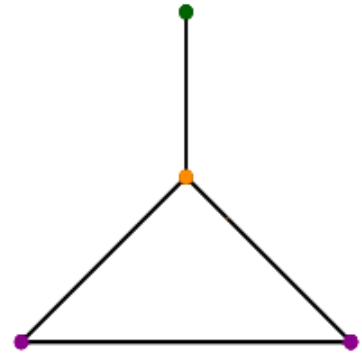

Figure 3: $K_2 \ominus_R K_1$

Definition 1.5. *Let G and H be two graphs with vertices n_1 and n_2 and edges m_1 and m_2 respectively. The R-vertex neighbourhood corona of graphs G and H with $(n_1+m_1+n_1n_2)$ vertices and $(3m_1+n_1m_2+m_1n_2)$ edges and is obtained from one copy $R(G)$ and $|V(G)|$ copies of H, by joining the neighbours of i^{th} vertex of $V(G)$ to each vertex in the i^{th} copy of H.*

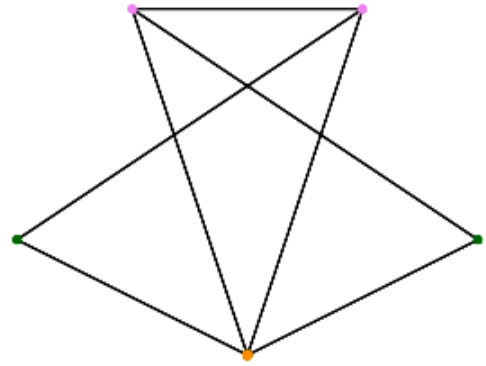

Figure 4: $K_2 \odot_{nR} K_1$

Definition 1.6. *Let G and H be two graphs with vertices n_1 and n_2 and edges m_1 and m_2 respectively. The R-edge neighbourhood corona of graphs G and H with*

$(n_1 + m_1 + m_1n_2)$ vertices and $m_1(2n_2 + m_2 + 3)$ edges and is obtained from one copy $R(G)$ and $|E(G)|$ copies of H, by joining the neighbours of i^{th} vertex of $I(G)$ to each vertex in the i^{th} copy of H.

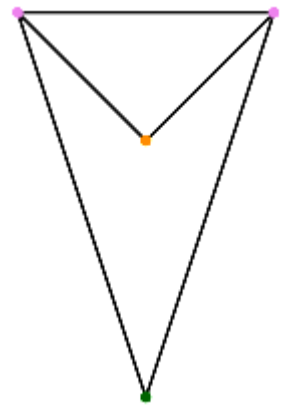

Figure 5: $K_2 \ominus_{nR} K_1$

2. Main Results

In this section, we derive the DSs of line graph of R-corona operations on K_m, C_m and r-regular graphs.

Theorem 2.1. *The DSs of line graph of R-vertex corona of complete, cycle and r-regular graphs.*

Proof. Let G and H be two simple connected graphs with n_1, m_1 and n_2, m_2 are vertex set and edge set respectively. Using the definitions 1.1 and 1.3, we obtain the line graph of R-vertex corona of G and H $[L(G \odot_R H)]$ with $(3m_1 + n_1(n_2 + m_2))$ vertices. There are four type of vertices, in which m_1 vertices having degree $(4d_G + 2n_2 - 2)$, $2m_1$ vertices having degree $(2d_G + n_2)$, n_1m_2 vertices having degree $(2d_H)$ and n_1n_2 vertices having degree $(d_H + 2d_G + n_2 - 1)$.
Therefore,

$$DS[L(G \odot_R H)] = \{(4d_G + 2n_2 - 2)^{m_1}, (2d_G + n_2)^{2m_1}, (2d_H)^{n_1m_2}, (d_H + 2d_G + n_2 - 1)^{n_1n_2}\}$$

Table 1. Degree sequences of line graph R-vertex corona for complete, cycle and r-regular graphs.

G	H	$DS[L(G \odot_R H)]$
K_n	K_m	$\{(4n+2m-6)^{\frac{n(n-1)}{2}}, (2n+m-2)^{n(n-1)}, (2m-2)^{\frac{nm(m-1)}{2}}, (2m+2n-4)^{nm}\}$
K_n	C_m	$\{(4n+2m-6)^{\frac{n(n-1)}{2}}, (2n+m-2)^{n(n-1)}, 4^{mn}, (m+2n-1)^{nm}\}$
K_n	r-regular graph with m-vertices	$\{(4n+2m-6)^{\frac{n(n-1)}{2}}, (2n+m-2)^{n(n-1)}, (2r)^{\frac{nmr}{2}}, (r+2n+m-3)^{nm}\}$
C_n	K_m	$\{(2m+6)^n, (m+4)^{2n}, (2n-2)^{\frac{nm(m-1)}{2}}, (2m+2n-4)^{nm}\}$
C_n	C_m	$\{(2m+6)^n, (m+4)^{2n}, 4^{mn}, (m+5)^{nm}\}$
C_n	r-regular graph with m-vertices	$\{(2m+6)^n, (m+4)^{2n}, (2r)^{\frac{nmr}{2}}, (r+m+3)^{nm}\}$
r-regular graph with n-vertices	K_m	$\{(4r+2m-2)^{\frac{nr}{2}}, (2r+m)^{nr}, (2m-2)^{\frac{nm(m-1)}{2}}, (2m+2r-2)^{nm}\}$
r-regular graph with n-vertices	C_m	$\{(4r+2m-2)^{\frac{nr}{2}}, (2r+m)^{nr}, 4^{nm}, (2r+m-1)^{nm}\}$
r_1-regular graph with n-vertices	r_2-regular graph with m-vertices	$\{(4r_1+2m-2)^{\frac{nr_1}{2}}, (2r_1+m)^{nr_1}, (2r_2)^{\frac{nmr_2}{2}}, (r_2+2r_1+m-1)^{nm}\}$

Theorem 2.2. *The DSs of line graph of R-edge corona of complete, cycle and r-regular graphs.*

Proof. Let G and H be two simple connected graphs with n_1, m_1 and n_2, m_2 are vertex set and edge set respectively. Using the definitions 1.1 and 1.4, we obtain the line graph of R-edge corona of G and H $[L(G \ominus_R H)]$ with $m_1(n_2+m_2+3)$ vertices. There are four type of vertices, in which m_1 vertices having degree $(4d_G-2)$, $2m_1$ vertices having degree $(2d_G+n_2)$, n_2m_1 vertices having degree (d_H+n_2+1) and m_1m_2 vertices having degree $(2d_H)$.
Therefore,

$$DS[L(G \ominus_R H)] = \{(4d_G-2)^{m_1}, (2d_G+n_2)^{2m_1}, (d_H+n_2+1)^{n_2m_1}, (2d_H)^{m_1m_2}\}$$

Table 2. Degree sequences of line graph R-edge corona for complete, cycle and r-regular graphs.

G	H	$DS[L(G \ominus_R H)]$
K_n	K_m	$\left\{(4n-6)^{\frac{n(n-1)}{2}}, (2n+m-2)^{n(n-1)}, (2m)^{\frac{nm(n-1)}{2}}, (2m-2)^{\frac{nm(n-1)(m-1)}{4}}\right\}$
K_n	C_m	$\left\{(4n-6)^{\frac{n(n-1)}{2}}, (2n+m-2)^{n(n-1)}, (m+3)^{\frac{nm(n-1)}{2}}, 4^{\frac{mn(n-1)}{2}}\right\}$
K_n	r-regular graph with m-vertices	$\left\{(4n-6)^{\frac{n(n-1)}{2}}, (2n+m-2)^{n(n-1)}, (r+m+1)^{\frac{nm(n-1)}{2}}, (2r)^{\frac{mnr(n-1)}{4}}\right\}$
C_n	K_m	$\left\{6^n, (m+4)^{2n}, (2m)^{mn}, (2m-2)^{\frac{nm(n-1)}{2}}\right\}$
C_n	C_m	$\left\{6^n, (m+4)^{2n}, (m+3)^{mn}, 4^{mn}\right\}$
C_n	r-regular graph with m-vertices	$\left\{6^n, (m+4)^{2n}, (r+m+1)^{mn}, (2r)^{\frac{mnr}{2}}\right\}$
r-regular graph with n-vertices	K_m	$\left\{(4r-2)^{\frac{nr}{2}}, (2r+m)^{nr}, (2m)^{\frac{mnr}{2}}, (2m-2)^{\frac{mnr(m-1)}{4}}\right\}$
r-regular graph with n-vertices	C_m	$\left\{(4r-2)^{\frac{nr}{2}}, (2r+m)^{nr}, (m+3)^{\frac{mnr}{2}}, 4^{\frac{mnr}{2}}\right\}$
r_1-regular graph with n-vertices	r_2-regular graph with m-vertices	$\left\{(4r_1-2)^{\frac{nr_1}{2}}, (2r_1+m)^{nr_1}, (r_2+m+1)^{\frac{mnr_2}{2}}, (2r_2)^{\frac{mnr_1r_2}{4}}\right\}$

Theorem 2.3. *The DSs of line graph of R-vertex neighbourhood corona of complete, cycle and r-regular graphs.*

Proof. Let G and H be two simple connected graphs with n_1, m_1 and n_2, m_2 are vertex set and edge set respectively. Using the definitions 1.1 and 1.5, we obtain the line graph of R-vertex neighbourhood corona of G and H $[L(G \odot_{nR} H)]$ with $m_1(2n_2+3)+n_1(n_2+m_2)$ vertices. There are five type of vertices, in which m_1 vertices having degree $(2d_G(2+n_2)-2)$, $2m_1$ vertices having degree $(d_G(2+n_2)+2n_2)$, $2n_2m_1$ vertices having degree $(d_H + 2d_G + 2n_2)$, n_1m_2 vertices having degree $(2(d_H + 2d_G - 1))$ and n_1n_2 vertices having degree $(4d_G + d_H + d_Gn_2 - 2)$.
Therefore,

$$DS[L(G \odot_{nR} H)] = \{(2d_G(2+n_2)-2)^{m_1}, (d_G(2+n_2)+2n_2)^{2m_1}, (d_H + 2d_G + 2n_2)^{2n_2m_1}, (2(d_H + 2d_G - 1))^{n_1m_2}, (4d_G + d_H + d_Gn_2 - 2)^{n_1n_2}\}$$

Table 3. Degree sequences of line graph R-vertex neighbourhood corona for complete, cycle and r-regular graphs.

G	H	$DS[L(G \odot_{nR} H)]$
K_n	K_m	$\Big\{(2(n-1)(m+2)-2)^{\frac{n(n-1)}{2}}, (mn+2n+m-2)^{n(n-1)}, (2n+3m-3)^{mn(n-1)}, (mn+4n-7)^{mn}, (2[m+2n-4])^{\frac{mn(m-1)}{2}}\Big\}$
K_n	C_m	$\Big\{(2(n-1)(m+2)-2)^{\frac{n(n-1)}{2}}, (mn+2n+m-2)^{n(n-1)}, (2(m+n)^{mn(n-1)}, (mn+4n-m-4)^{mn}, (2[2n-1])^{mn}\}$
K_n	r-regular graph with m-vertices	$\Big\{(2(n-1)(m+2)-2)^{\frac{n(n-1)}{2}}, (mn+2n+m-2)^{n(n-1)}, (r+2(n+m-1))^{mn(n-1)}, (r+4n+mn-m-6)^{mn}, (2[r+2n-3])^{\frac{mnr}{2}}\Big\}$
C_n	K_m	$\Big\{(4m+6)^n, (4m+4)^{2n}, (3m-3)^{2mn}, (2m+4)^{\frac{mn(m-1)}{2}}, (3m-5)^{mn}\Big\}$
C_n	C_m	$\Big\{(4m+6)^n, (4m+4)^{2n}, (2m+6)^{2mn}, (10)^{mn}, (2m+8)^{mn}\Big\}$
C_n	r-regular graph with m-vertices	$\Big\{(4m+6)^n, (4m+4)^{2n}, (2m+r+4)^{2mn}, (2r-6)^{\frac{mnr}{2}}, (r+2m-6)^{mn}\Big\}$
r-regular graph with n-vertices	K_m	$\Big\{(2r(m+2)-2)^{\frac{nr}{2}}, (r(m+2)+2m)^{nr}, (2r+3m-1)^{mnr}, (2m+4r-4)^{\frac{mn(m-1)}{2}}, (4r+m(r+1)-3)^{mn}\Big\}$
r-regular graph with n-vertices	C_m	$\Big\{(2r(m+2)-2)^{\frac{nr}{2}}, (r(m+2)+2m)^{nr}, (2m+2r+2)^{mnr}, (4r+2)^{mn}, (rm+4r)^{mn}\Big\}$
r_1-regular graph with n-vertices	r_2-regular graph with m-vertices	$\Big\{(2r_1(m+2)-2)^{\frac{nr_1}{2}}, (r_1(m+2)+2m)^{nr_1}, (2m+2r_1+r_2)^{mnr_1}, (4r_1+2r_2-2)^{\frac{mnr_2}{2}}, (4r_1+r_2+r_1m-2)^{mn}\}$

Theorem 2.4. *The DSs of line graph of R-edge neighbourhood corona of complete, cycle and r-regular graphs.*

Proof. Let G and H be two simple connected graphs with n_1, m_1 and n_2, m_2 are vertex set and edge set respectively. Using the definitions 1.1 and 1.6, we obtain the line graph of R-edge neighbourhood corona of G and H $[L(G \ominus_{nR} H)]$ with $m_1(2n_2 + m_2 + 3)$ vertices. There are four type of vertices, in which m_1 vertices

having degree $(2d_G(2+n_2)-2)$, $2m_1$ vertices having degree $(d_G(2+n_2))$, m_1m_2 vertices having degree $(2d_H+2)$ and $2n_2m_1$ vertices having degree $(2d_G+d_H+n_2)$. Therefore,

$$DS[L(G \ominus_{nR} H)] = \{(2d_G(2+n_2)-2)^{m_1}, (d_G(2+n_2))^{2m_1}, (2d_H+2)^{m_1m_2}, (2d_G+d_H+n_2)^{2n_2m_1}\}$$

Table 4. Degree sequences of line graph R-edge neighbourhood corona for complete, cycle and r-regular graphs.

G	H	$DS[L(G \ominus_{nR} H)]$
K_n	K_m	$\Big\{(2(n-1)(m+2)-2)^{\frac{n(n-1)}{2}}, ((n-1)(m+2))^{n(n-1)}, (2m)^{\frac{mn(n-1)(m-1)}{4}}, (2m+2n-3)^{mn(n-1)}\Big\}$
K_n	C_m	$\Big\{(2(n-1)(m+2)-2)^{\frac{n(n-1)}{2}}, ((n-1)(m+2))^{n(n-1)}, (6)^{\frac{mn(n-1)}{2}}, (2n+m)^{mn(n-1)}\Big\}$
K_n	r-regular graph with m-vertices	$\Big\{(2(n-1)(m+2)-2)^{\frac{n(n-1)}{2}}, ((n-1)(m+2))^{n(n-1)}, (2r+2)^{\frac{mnr(n-1)}{4}}, (2(n-1)+r+m)^{mn(n-1)}\Big\}$
C_n	K_m	$\Big\{(4m+6)^n, (2m+4)^{2n}, (2m)^{\frac{mn(m-1)}{2}}, (2m+3)^{2mn}\Big\}$
C_n	C_m	$\{(4m+6)^n, (2m+4)^{2n}, (6)^{mn}, (m+6)^{2mn}\}$
C_n	r-regular graph with m-vertices	$\Big\{(4m+6)^n, (2m+4)^{2n}, (2r+2)^{\frac{mnr}{2}}, (m+r+4)^{2mn}\Big\}$
r-regular graph with n-vertices	K_m	$\Big\{(2r(m+2)-2)^{\frac{nr}{2}}, (r(m+2))^{nr}, (2m)^{\frac{mnr(m-1)}{4}}, (2r+2m-1)^{mnr}\Big\}$
r-regular graph with n-vertices	C_m	$\Big\{(2r(m+2)-2)^{\frac{nr}{2}}, (r(m+2))^{nr}, (6)^{\frac{mnr}{2}}, (2r+m+2)^{mnr}\Big\}$
r_1-regular graph with n-vertices	r_2-regular graph with m-vertices	$\Big\{(2r_1(m+2)-2)^{\frac{nr_1}{2}}, (r_1(m+2))^{nr_1}, (2r_2+2)^{\frac{mnr_1r_2}{4}}, (2r_1+r_2+m)^{mnr_1}\Big\}$

3. Conclusion

In this article, we have established the degree sequences for line graph of R-vertex(edge), R-vertex(edge) neighbourhood corona of complete, cycle and r-regular graphs.

References

[1] Adiga Chandrashekar and Rakshith B. R, Spectra of graph operations based on corona and neighborhood corona of graph G and K1, Journal of the international mathematical virtual institute, 5(1), (2015), 55-69.

[2] Ananda N., Lokesha V., Ranjini P. S. and Kumar Sandeep, Degree sequence of graph operator for some standard graphs, Applied Mathematics and Nonlinear Sciences (Accepted), Preprint.

[3] Beineke L. W., Characterizations of derived graphs, Journal of combinatorial theory, 9(2), (1970), 129-135.

[4] Bollobas B., Degree Sequences of Random Graphs, Discrete Mathematics, 33, (1981), 1-19.

[5] Gries David and Schneide Fred Barry, A logical approach to discrete Math, Springer-Verlag.

[6] Gupta C. K., Lokesha V., Shetty S. B. and Ranjini P. S., Graph Operations on Symmetric Division Deg Index of Graphs, Palestine Journal of Mathematics, 6(1), (2017), 280-286.

[7] Kulli V. R., Lokesha V., Jain Sushmitha and Manjunath. M, The Gourava index of four operations on Graphs, International Journal of Mathematical Combinatorics, 4(1), (2018), 65-76.

[8] Lokesha V., Manjunath M., Chaluvaraju B., Devendraiah K. M., Cangul I. N. and Cevik A. S., Computation of Adriatic indices of certain operators of regular and complete Bipartite graphs, Advanced studies in contemporary Mathematics, 28(2), (2018), 231-244.

[9] Mishra Vishnu Narayan, Delen Sadik and Cangul Ismail Naci, Degree sequences of join and corona products of graphs, Electronic Journal of Mathematical Analysis and Applications, 7(1), (2019), 5-13.

[10] Tyshkevich R. I., Mel'nikov O. I., Kotov V. M., On graphs and degree sequences: Canonical decomposition, Kibernetika, 6(1), (1981), 05-08.

[11] Wilson R. J., Introduction to graph theory, Prentice Hall.

Eur. Phys. J. Plus (2021) 136:1074
https://doi.org/10.1140/epjp/s13360-021-02022-6

THE EUROPEAN PHYSICAL JOURNAL PLUS

Regular Article

Energy dissipation and Hall effect on MHD convective flow of nanofluid within an asymmetric channel with arbitrary wall thickness and conductance

Jitendra Kumar Singh[1,a], **Suneetha Kolasani**[1,2]

[1] Department of Mathematics, Vijayanagara Sri Krishnadevaraya University, Ballari 583105, India
[2] Department of Mathematics, Ballari Institute of Technology and Management, Ballari 583105, India

Received: 15 June 2021 / Accepted: 1 October 2021

Abstract The current study examines the consequences of viscous and Joule dissipations, and Hall current on steady buoyancy-driven MHD flow of Ti_6Al_4V-H_2O-based nanofluid within an asymmetric channel with arbitrary wall thickness and conductance in the presence of a highly intense magnetic field. The boundary conditions for the induced magnetic field are also derived. The closed-form solutions for velocity field, induced magnetic field, temperature field, surface skin friction, mass flow rate and critical Grashof number are extracted from non-dimensional flow model analytically, while the numerical values of heat transport rate are obtained by mathematical computations using MATLAB software. The results of the study are thoroughly discussed with the assistance of graphs and tables. Such study has great importance in analyzing the heat transport behavior of the highly electrically conducting nanofluids. A special feature observed from this investigation is that, on incrementing the wall electrical conductivity, the fluid velocity reduces due to induction of magnetic drag. On raising the volumetric concentration of nanoparticles in the fluid, the fluid temperature raises and hence the fluid velocity rises due to generation of more thermal buoyancy force. The viscous dissipation leads to rise the fluid temperature due to rise in internal energy of the system.

List of symbols

C_p	Specific heat at constant pressure
$\vec{E}$	Electric field
Er	Eckert number
g	Acceleration due to gravity
g_Θ	Thermal Grashof number
Gc	Critical Grashof number
$\vec{h}$	Magnetic field vector
Hc	Hall current parameter
H_0	Applied magnetic field
$(h_1,\ h_2,\ h_3)$	Components of induced magnetic field along the coordinate axes

[a] e-mail: s.jitendrak@yahoo.com (corresponding author)

Published online: 26 October 2021

$\vec{J}$	Current density
k	Thermal conductivity
M	Mass flow rate
Mg	Magnetic parameter
Pr	Prandtl number
Ro	Rotation parameter
$\vec{u}$	Fluid velocity
$(u_1,\ u_2,\ u_3)$	Components of velocity along the coordinate axes
w	Thickness of the wall of the channel
w_0	Separation of the walls of the channel
(x_1, x_2, x_3)	Rectangular Cartesian coordinate

Greek symbols

β	Volumetric thermal expansion coefficient
μ	Dynamic viscosity
μ_e	Magnetic permeability
υ	Coefficient of viscosity
$\vec{\Omega}$	Angular velocity of the gyration
ϕ	Wall conductance constants
ρ	Fluid density
σ	Electrical conductivity
θ	Fluid temperature
Θ	Non-dimensional fluid temperature
τ	Non-dimensional skin friction
ϑ	Volume fraction constant of nanofluid

Subscripts

f	Quantities for base fluid
l	Quantities at the lower wall of the channel
nf	Quantities for nanofluid
s	Quantities for suspended nanoparticles
u	Quantities at the upper wall of the channel

1 Introduction

The engineers and scientists are continuously exploring the magnetohydrodynamic (MHD) fluid flow problems within symmetric/asymmetric channels and rectangular ducts under various flow circumstances since last few decades because of its direct or indirect involvement in several physical phenomena and development of devices. Hartmann [1] was first who experimentally studied the behavior of an electrically conducting fluid flow within a channel in the presence of a transverse magnetic field domain and reported that the presence of magnetic field domain flattens the velocity profile due to magnetic drag. It also causes the formation of a boundary layer adjacent to the channel wall called Hartmann boundary layer. This classical problem is known as Hartmann problem. The MHD flow within a rectangular duct with

a combination of non-conducting, perfectly conducting and arbitrarily conducting walls is analytically investigated by Hunt [2]. Thereafter, a series of research papers are presented by researches on MHD channel/duct flows and the outcomes of the research reports are used in development of several MHD devices. A deep review of literature on MHD channel/duct flow reports that in most of the research works either channel walls are considered to be non-conducting or perfectly conducting or the combination of both for the simplicity of the flow model. Very less numbers of the problems consider the arbitrarily conducting channel walls. Furthermore it is seen that in most of the studies IMF is neglected due to large magnetic viscosity ($\upsilon_m \gg 1$ or $\mathrm{Rm} \ll 1$). But there are many working fluids for which the magnetic viscosity is very small ($\upsilon_m \ll 1$ or $\mathrm{Rm} \gg 1$); in such cases, the effects of IMF cannot be neglected. The wall conductance effect on the flow nature of an electrically conducting fluid through a channel is firstly reported in the paper of Chang and Yen [3]. He observed that, similar to the presence of magnetic field domain, the sum of the wall conductance constants also flatten the velocity profile. Subsequently Snyder [4] and Gold [5] examined the consequences of wall conductance on MHD channel flow with and without heat transfer characteristics, respectively. The wall conductance effect with heat transfer characteristics in a gyratory system is analyzed by Mazumdar [6]. He studied the dependency of VF, current density and TF on sum of the wall conductance constants. The IMF depends on the individual values of conductive constants of each of the walls. The influences of applied magnetic field intensity and wall conductivities on the flow of an electrically conducting fluid in a rectangular channel are nicely presented by Tezer-Sezgin and Dost [7] in their paper. An important remark of their study is that velocity profile flattens on increasing the magnetic field strength or decreasing the conductivity parameter. Moreover, Nagy and Demendy [8] presented the joint impacts of Hall current and gyration of the system on MHD channel flow with variable wall conductivity and thickness. An analytical solution for unsteady oscillatory Hartmann flow within a symmetric channel with finitely conducting walls is obtained by Ansari et al. [9]. They noticed that the wall conductivity leads to decrement in the flow as well as IMF. Seth and Singh [10] and Seth et al. [11] are, respectively, presented the mixed convective Hartmann flow and Hartmann-Couette flow problems within a horizontal asymmetric channel with arbitrary wall conductivity parameters, Hall current and rotation. Seth and Singh [9] also approved the results of Mazumdar [6] through their investigation. The effect of the permeability of the flow medium to the buoyancy-driven Couette-Hartmann flow within an asymmetric channel with random wall conductance and thickness with gyratory action and Hall current is well examined in the research article of Singh et al. [12]. They found that in the small permeable regime there occurs the reverse flow in the direction of the normal flow. In particular for Poiseuille flow within a non-porous channel, Borrelli et al. [13] scrutinized that the reverse flow arise due to the buoyancy action and its direction is parallel to the main flow. The consequences of IMF on the unsteady MHD oscillatory flow within a channel with the magnetized walls are presented in the collaborative research works of Seth et al. [14] and Singh et al. [15, 16]. They examined that the magnetic diffusion raises the main flow and lessens the normal flow. Some noteworthy recent investigations of IMF effect on MHD flows are due to Kumar et al. [17], Hayat et al. [18], Rashid et al. [19], Kumar et al. [20] and Raza et al. [21]. In electrodynamics, the Hall and ion-slip phenomena occur due to drifting of charge particles and ions about the lines of a strong electromagnetic magnetic field domain. Since the mass of the ions is much larger than the mass of the electrons and their velocity is much smaller than the velocity of electrons, the ion-slip phenomenon may be neglected in many of the cases. The Hall phenomenon found enormous applications in the study of plasma flow and generation of sensors. These phenomena place a prominent role in deciding the flow features of many problems. Hall phenomenon for the flow of ionized

gases within a parallel plate channel was firstly examined by Sato [22]. Soon after this study the research scientists started to explore the phenomenon of Hall current in connection with MHD. Recently many eminent researchers [23–32] excellently examined the Hall phenomena for the MHD flow within symmetric/asymmetric channel by implanting various analytical and numerical computational techniques with diverse flow models.

The theory of gyratory system is the topic which is continuously studied by the researchers in connection with MHD because it is frequently encountered by the scientists and engineers in technology-based systems and MHD devices. The action of the gyratory force is important to study in connection with MHD because order of magnitude of this force is same as order of viscous and magnetic forces. An important feature of this force is to stabilize the main flow and inducing the normal flow. The significances of the gyratory force (Coriolis force) on the hydromagnetic flows are recently scrutinized by Mahanthesh et al. [33], Chamkha et al. [34], Akinshilo [35], Singh et al. [36], Nandi and Kumbhakar [37] and Shoaib et al. [38] in their respective problems. In order to study the heat transfer characteristics in MHD flows, viscous and Joule dissipations play an important role. The viscous and Joule dissipations in MHD flows arise due to viscous and magnetic drags. Due to these drag forces the internal energy of the fluid rises in the form of the heat. The viscous and Joule dissipation impacts on the heat transfer characteristics of MHD buoyancy-driven flow over a stretching sheet are explored by Chien [39]. They found that the viscous and Joule dissipations reduce the heat transfer rate. Gopal et al. [40] scrutinized the heat and mass transfer aspects of MHD flow of Casson fluid over a stretching surface with multiple slips and viscous and Joule dissipations. The energy dissipative effect on the Couette-Hartmann flow of Jeffery fluid within a horizontal symmetric channel is disused in the research paper of Remesh [41]. Some more impactful research works including the viscous and Joule dissipations on the MHD flow are presented in the articles of the eminent researchers, Atif et al. [42], Shamshuddin and Satya Narayana [43] and Swain et al. [44]. During the laboratory experiment Choi [45] found that the emergence on nanosize particles in a base fluid significantly raises its thermal conductivity. Later on Lee et al. [46] and Chon and Kihm [47] developed the techniques to measure the thermal conductivity of the nanofluid. Due to vast thermal engineering applications nowadays this area became the pioneer area of research for the research scientists. Stimulated from widespread applications recently many authors [48–54] published the excellent research works which consider the heat transfer aspects of MHD nanofluid flow under various geometries. Das et al. [55] presented an analytical study to analyze the consequences of Hall current and rotation on MHD Fe_3O_4—water-based nanofluid flow within a channel with IMF and dissipative effects. They examined that the Hall current significantly affects the flow velocity. An important fact noticed in this study is that, at the upper wall of the channel, the heat transfer rate in the nanofluid is larger than the purely base fluid. An analytical approach to examine the effects of heat source and IMF to the MHD free convective nanofluid flow within a vertical channel is applied by Jha and Samaila [56]. This paper reveals that the Hartmann number (magnetic parameter) reduces velocity due to induction of magnetic drag, while it enhances the IMF. Askari et al. [57] implemented both the analytical (LSM) and numerical (FEM) schemes to scrutinize the heat transfer behavior of MHD water graphene-based nanofluid flow within a channel with viscous dissipation and IMF effects. Through the results it is demonstrated that Hartmann number reduces the velocity by up to 50%, while the volumetric concentration of nanoparticles in the fluid enhances the fluid temperature by 20–50%.

The aforementioned research work prepared the base for this study. During the meticulous review of literatures we found that yet no investigations are performed which simultaneously examine the significances of wall conductance and energy dissipation on MHD convective flow of nanofluid within an asymmetric channel. In this research work we examined the

consequences of energy dissipation and Hall current to the MHD mixed convective flow of Ti_6Al_4V-H_2O-based nanofluid within two horizontal parallel walls channel with arbitrary thickness and conductance. The closed-form solution for VF, IMF and TF is obtained analytically. On computing the results, a noteworthy result noted that the wall conductance constants bring decrement in the flow due to generation of the magnetic drag force. The magnetic drag force due to wall conductance enhances the internal energy of the system which causes rise in the fluid temperature. The viscous dissipation leads to rise the fluid temperature due to rise in internal energy of the system.

2 Formulation of flow model and solution scheme

The steady fully developed flow of Ti_6Al_4V-H_2O-based nanofluid within an asymmetric channel of arbitrary wall thickness and conductance is considered. The reference system of the flow is taken as rectangular Cartesian coordinate system such that the walls of the channel are parallel to the x_1x_2-plane, while x_3-axis is normal to the surfaces of the walls. The geometrical consideration of the problem is demonstrated in Fig. 1. The following flow assumptions are implemented in the investigation:

(a) The nanofluid is a dilute suspension of nanosize particles in the base fluid.
(b) The nanofluid is considered to be incompressible, Newtonian, thermally and electrically conducting in nature.
(c) Both the phase of fluid and nanoparticles are considered to be in same thermal equilibrium state.
(d) Induction of Hall current is considered due to the presence of a strong magnetic field domain H_0 along x_3-axis.
(e) The magnetic viscosity of nanofluid is considered to be low. Thus, IMF effect is also considered on the flow field.
(f) Coriolis force effect is considered due to gyratory action of the flow system about x_3-axis with angular velocity $\vec{\Omega}$.
(g) It is considered that the fluid temperature varies linearly with temperature gradient P in the direction of x_1-axis, i.e., $\theta = \theta_0 + Px_1 + f(x_3)$, where $f(x_3)$ is an arbitrary function of x_3.
(h) Further it is assumed that the gravity is sufficiently strong for the flow to generate the buoyancy force and hence Boussinesq approximation is applied.

The system of equations (field and constitutive equations) which mathematically expresses the flow phenomena is the equation of continuity for the flow field

$$\nabla \cdot \vec{u} = 0, \tag{1}$$

The equation of linear momentum

$$(\vec{u} \cdot \nabla)\vec{u} = -\frac{1}{\rho_{\mathrm{nf}}}\nabla p^* + \upsilon_{\mathrm{nf}}\nabla^2\vec{u} + \frac{\mu_e}{\rho_{\mathrm{nf}}}(\vec{h}.\nabla)\vec{h} + 2\vec{u} \times \vec{\Omega}, \tag{2}$$

where $p^* = p + \frac{\mu_e H_0^2}{2}$ is modified pressure includes the magnetic pressure.

The fundamental laws which connect electric and magnetic fields are the law of conservation of charges, Ampere's law, Faraday's law and solenoidal relation. The mathematical forms of these laws are, respectively, expressed as (Sutton and Sherman [58])

$$\nabla \cdot \vec{J} = 0, \quad \nabla \times \vec{h} = \vec{J}, \quad \nabla \times \vec{E} = 0, \quad \nabla \cdot \vec{h} = 0. \tag{3}$$

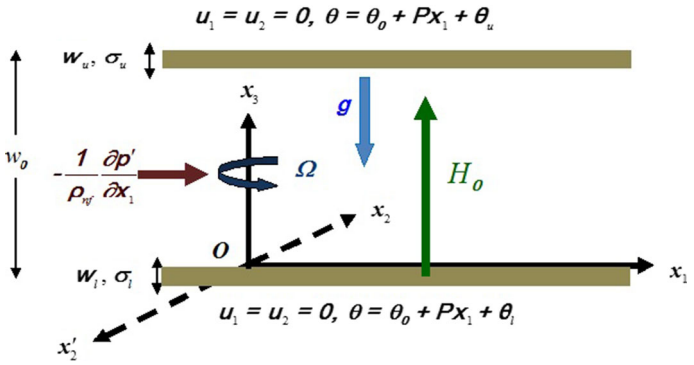

Fig. 1 The geometrical configuration of the physical problem

The Ohm's law in case of a moving conductor with inclusion of Hall term is mathematically presented as (Cramer and Pai [59])

$$\vec{J} = \sigma_{\rm nf}\Big(\vec{E} + \mu_e(\vec{u} \times \vec{h})\Big) + \frac{\rm Hc}{H_0}\Big(\vec{J} \times \vec{h}\Big). \tag{4}$$

The magnetic induction equation is derived on bunching Eqs. (3) and (4), which is expressed in the following form (Singh et al. [12])

$$-\nabla^2\vec{h} = \sigma_{\rm nf}\mu_e\,\nabla \times (\vec{u} \times \vec{h}) - \frac{\rm Hc}{H_0}\,\nabla \times \Big[(\vec{h} \cdot \nabla)\,\vec{h}\Big]. \tag{5}$$

The equation of energy with energy dissipation due to viscous and Joule heating is (Aris [60])

$$(\rho C_p)_{\rm nf}(\vec{u} \cdot \nabla)\,\theta = k_{nf}\nabla^2\theta + \Phi + \frac{J^2}{\sigma_{\rm nf}}, \tag{6}$$

where $\Phi = \mu_{\rm nf}\big[\nabla\vec{u} + (\nabla\vec{u})^T\big]$ is the viscous dissipation term.

In the essence of Eqs. (1) and (3) we have $\vec{u} \equiv (u_1,\ u_2,\ 0)$, $\vec{h} \equiv (h_1,\ h_2,\ H_0)$, $\vec{J} \equiv (J_1,\ J_2,\ 0)$. Since flow is fully developed steady flow and walls are infinitely extended in their plane, all flow functions except temperature and pressure will be function of x_3, but temperature and pressure are functions of x_1 and x_3.

With the use of above-described assumptions, the equation of linear momentum (2), magnetic induction Eq. (5) and the energy equation with dissipation effect (6), in component form, are

$$0 = -\frac{1}{\rho_{\rm nf}}\frac{\partial p^*}{\partial x_1} + \upsilon_{nf}\frac{{\rm d}^2u_1}{{\rm d}x_3^2} + \frac{\mu_e H_0}{\rho_{\rm nf}}\frac{{\rm d}h_1}{{\rm d}x_3} + 2\Omega u_2, \tag{7}$$

$$0 = \upsilon_{\rm nf}\frac{{\rm d}^2u_2}{{\rm d}x_3^2} + \frac{\mu_e H_0}{\rho_{\rm nf}}\frac{{\rm d}h_2}{{\rm d}x_3} - 2\Omega u_1, \tag{8}$$

$$0 = -\frac{1}{\rho_{\rm nf}}\frac{d}{dx_3}\Big[p^* + \frac{\mu_e}{2}\big(h_1^2 + h_2^2\big)\Big] - g\big[1 - (\beta)_{\rm nf}(\theta - \theta_0)\big], \tag{9}$$

$$-\frac{{\rm d}^2h_2}{{\rm d}x_3^2} = \sigma_{\rm nf}\mu_e H_0\frac{{\rm d}u_2}{{\rm d}x_3} - {\rm Hc}\frac{{\rm d}^2h_1}{{\rm d}x_3^2}, \tag{10}$$

$$\frac{\mathrm{d}^2 h_1}{\mathrm{d}x_3^2} = -\sigma_{\mathrm{nf}}\mu_e H_0 \frac{\mathrm{d}u_1}{\mathrm{d}x_3} - \mathrm{Hc}\frac{\mathrm{d}^2 h_2}{\mathrm{d}x_3^2}, \tag{11}$$

$$\begin{aligned}\left(\rho C_p\right)_{\mathrm{nf}} u_1 \frac{\partial(\theta-\theta_0)}{\partial x_1} &= k_{\mathrm{nf}}\frac{\partial^2(\theta-\theta_0)}{\partial x_3^2} + \mu_{\mathrm{nf}}\left[\left(\frac{\mathrm{d}u_1}{\mathrm{d}x_3}\right)^2 + \left(\frac{\mathrm{d}u_2}{\mathrm{d}x_3}\right)^2\right] \\ &+ \frac{1}{\sigma_{\mathrm{nf}}}\left[\left(\frac{\mathrm{d}h_1}{\mathrm{d}x_3}\right)^2 + \left(\frac{\mathrm{d}h_2}{\mathrm{d}x_3}\right)^2\right].\end{aligned} \tag{12}$$

At the surface of contacts the normal velocity of the surface and fluid is the same; thus, BCs for velocity field at the surface of contact are

$$\left.\begin{aligned}&\text{at } x_3 = 0: \qquad u_1 = u_2 = 0,\\ &\text{at } x_3 = w_0: \qquad u_1 = u_2 = 0.\end{aligned}\right\} \tag{13}$$

The BCs for the IMF are derived with the assistance of the continuity of the tangential components of electric and magnetic fields at the interface of the channel walls. These are

$$\left.\begin{aligned}&\text{at } x_3 = 0: \qquad \frac{\mathrm{d}h}{\mathrm{d}x_3} - \frac{\sigma_{\mathrm{nf}} h}{\sigma_l w_l(1-i\mathrm{Hc})} = 0,\\ &\text{at } x_3 = w_0: \qquad \frac{\mathrm{d}h}{\mathrm{d}x_3} + \frac{\sigma_{\mathrm{nf}} h}{\sigma_u w_u(1-i\mathrm{Hc})} = 0,\end{aligned}\right\} \tag{14}$$

where $h = h_1 + ih_2$.

The temperature of the bounding surface varies linearly along x_1-axis; thus, the BCs for temperature field are

$$\left.\begin{aligned}&\text{at } x_3 = 0: \qquad \theta = \theta_0 + Px_1 + \theta_l,\\ &\text{at } x_3 = w_0: \qquad \theta = \theta_0 + Px_1 + \theta_u.\end{aligned}\right\} \tag{15}$$

The mathematical expressions representing the fundamental thermophysical characteristics of the nanofluid are (Khan et al. [52])

$$\left.\begin{aligned}\mu_{\mathrm{nf}} &= \frac{\mu_f}{(1-\vartheta)^{2.5}}, \quad \rho_{\mathrm{nf}} = (1-\vartheta)\rho_f + \vartheta\rho_s, \quad (\rho\beta)_{\mathrm{nf}} = (1-\vartheta)(\rho\beta)_f + \vartheta(\rho\beta)_s,\\ \sigma &= \frac{\sigma_s}{\sigma_f}, \qquad \sigma_{\mathrm{nf}} = \sigma_f\left(1 - \frac{3(1-\sigma)\vartheta}{(2+\sigma)+(1-\sigma)\vartheta}\right),\\ \left(\rho C_p\right)_{\mathrm{nf}} &= (1-\vartheta)(\rho C_P)_f + \vartheta(\rho C_p)_s, \quad \frac{k_{\mathrm{nf}}}{k_f} = \frac{\left(k_s+2k_f\right)+2\vartheta\left(k_s-k_f\right)}{\left(k_s+2k_f\right)-\vartheta\left(k_s-k_f\right)}.\end{aligned}\right\} \tag{16}$$

In order to obtain the modified pressure p^*, integrating Eq. (9) from 0 to x_3 and applying $\theta - \theta_0 = Px_1 + f(x_3)$, we get

$$p^* = -\frac{\mu_e}{2}\left(h_1^2 + h_2^2\right) - \rho_{\mathrm{nf}} g\, x_3 + g(\rho\beta)_{\mathrm{nf}} P\, x_1\, x_3 + g\,(\rho\beta)_{\mathrm{nf}}\int_0^{x_3} f(v)\,dv + \rho_{\mathrm{nf}}\, g(x_1), \tag{17}$$

where $g(x_1)$ is arbitrary function of x_1. If modified pressure p^* is linear function of x_1 with pressure gradient K, then $g(x_1)$ can be regarded as $g(x_1) = Kx_1$. Thus

$$p^* = -\frac{\mu_e}{2}\left(h_1^2 + h_2^2\right) - \rho_{\mathrm{nf}} g\, x_3 + g(\rho\beta)_{\mathrm{nf}} P\, x_1\, x_3 + g\,(\rho\beta)_{\mathrm{nf}}\int_0^{x_3} f(v)\,dv + \rho_{\mathrm{nf}}\, K x_1. \tag{18}$$

Applying Eq. (18) to Eq. (7), we get

$$0 = -g(\beta)_{\mathrm{nf}} P\, x_3 - K + \upsilon_{\mathrm{nf}} \frac{\mathrm{d}^2 u_1}{\mathrm{d}x_3^2} + \frac{\mu_e H_0}{\rho_{\mathrm{nf}}} \frac{\mathrm{d}h_1}{\mathrm{d}x_3} + 2\Omega u_2. \tag{19}$$

For simplifying the solution process combining Eq. (19) to Eqs. (8) and (10) to Eq. (11), the compact equations are

$$\upsilon_{\mathrm{nf}} \frac{\mathrm{d}^2 u}{\mathrm{d}x_3^2} + \frac{\mu_e H_0}{\rho_{\mathrm{nf}}} \frac{\mathrm{d}h}{\mathrm{d}x_3} + 2i\Omega u = -g(\beta)_{\mathrm{nf}} P\, x_3 - K, \tag{20}$$

$$\frac{\mathrm{d}^2 h}{\mathrm{d}x_3^2} + \frac{\sigma_{\mathrm{nf}}}{(1 - i\mathrm{Hc})} \mu_e H_0 \frac{\mathrm{d}u}{\mathrm{d}x_3} = 0, \tag{21}$$

where $u = u_1 + iu_2$.

After combining the BCs for the velocity field at the surface of contact, we get

$$\left.\begin{aligned} &\text{at } x_3 = 0: && u = 0, \\ &\text{at } x_3 = w_0: && u = 0. \end{aligned}\right\} \tag{22}$$

In order to transform the mathematical model to a simplified non-dimensional similar model, we defined the following transformations

$$x_3^* = \frac{x_3}{w_0}, u^* = \frac{u w_0}{\upsilon_f}, h^* = \frac{h}{\sigma_f \mu_e \upsilon_f H_0}, \quad \Theta = \frac{g(\beta)_f w_0^3 (\theta - \theta_l)}{\upsilon_f^2}. \tag{23}$$

Applying the above-defined transformation to the flow governing equations and ignoring asterisk sign which represents the non-dimensional quantities, we have

$$\frac{\mathrm{d}^2 u}{\mathrm{d}x_3^2} + \mathrm{Mg}^2 \gamma_2 \frac{\mathrm{d}h}{\mathrm{d}x_3} - 2i\,\mathrm{Ro}\,\gamma_1 u = \gamma_3 g_\Theta x_3 + K_1 \gamma_1, \tag{24}$$

$$\frac{\mathrm{d}^2 h}{\mathrm{d}x_3^2} + \frac{e_4}{(1 - i\,\mathrm{Hc})} \frac{\mathrm{d}u}{\mathrm{d}x_3} = 0, \tag{25}$$

$$\frac{\mathrm{d}^2 \Theta}{\mathrm{d}x_3^2} = \frac{1}{2} \gamma_4 g_\Theta \mathrm{Pr} \left(\frac{u + \overline{u}}{2} \right) - \mathrm{Er}\,\mathrm{Pr} \left[\gamma_5 \left(\frac{\mathrm{d}u}{\mathrm{d}x_3} \right) \left(\frac{\mathrm{d}\overline{u}}{\mathrm{d}x_3} \right) + \gamma_6 \mathrm{Mg}^2 \left(\frac{\mathrm{d}h}{\mathrm{d}x_3} \right) \left(\frac{\mathrm{d}\overline{h}}{\mathrm{d}x_3} \right) \right], \tag{26}$$

where $\overline{u}$ and $\overline{h}$ are, respectively, complex conjugate of u and h.

$$\mathrm{Mg}^2 = \mu_e^2 H_0^2 w_0^2 (\sigma_f / \upsilon_f \rho_f), \quad \mathrm{Ro} = \Omega w_0^2 / \upsilon_f, \quad g_\Theta = g(\beta)_f P w_0^4 / \upsilon_f^2,$$

$$K_1 = K w_0^3 / \upsilon_f^2, \quad \mathrm{Pr} = \upsilon_f (\rho C_p)_{\mathrm{nf}} / k_f, \quad \mathrm{Er} = g(\rho\beta)_f w_0 / (\rho C_p)_f,$$

$$e_1 = \frac{1}{(1 - \vartheta)^{2.5}}, \quad e_2 = (1 - \vartheta) + \vartheta \left(\rho_s / \rho_f \right), \quad e_3 = (1 - \vartheta) + \vartheta \left((\rho\beta)_s / (\rho\beta)_f \right),$$

$$e_4 = \frac{(1 + 2\vartheta) + 2(1 - \vartheta)(\sigma_f / \sigma_s)}{(1 - \vartheta) + (2 + \vartheta)(\sigma_f / \sigma_s)}, \quad e_5 = (1 - \vartheta) + \vartheta \frac{(\rho C_p)_s}{(\rho C_p)_f},$$

$$e_6 = \frac{1 + 2(k_f / k_s) + 2\vartheta(1 - k_f / k_s)}{1 + 2(k_f / k_s) - \vartheta(1 - k_f / k_s)},$$

$$\gamma_1 = \frac{e_2}{e_1}, \ \gamma_2 = \frac{1}{e_1}, \ \gamma_3 = \frac{e_3}{e_1}, \ \gamma_4 = \frac{e_5}{e_6}, \ \gamma_5 = \frac{e_1}{e_6}, \ \gamma_6 = \frac{1}{e_4 e_6}.$$

Transformation (23) transforms BCs (22), (14) and (15) to the following form

$$\left.\begin{aligned} &\text{at } x_3 = 0: \quad u = 0,\ \frac{\mathrm{d}h}{\mathrm{d}x_3} - \frac{e_4}{\phi_l(1 - i\mathrm{Hc})}h = 0,\ \Theta = 0, \\ &\text{at } x_3 = 1: \quad u = 0,\ \frac{\mathrm{d}h}{\mathrm{d}x_3} + \frac{e_4}{\phi_u(1 - i\mathrm{Hc})}h = 0,\ \Theta = \frac{g(\beta)_f w_0^3(\theta_u - \theta_l)}{\upsilon_f^2} = \Theta_0(\text{say}), \end{aligned}\right\} \tag{27}$$

where $\phi_l = \sigma_l w_l/\sigma_f w_0$ and $\phi_u = \sigma_u w_u/\sigma_f w_0$ are wall conductance constants.Θ_0 is a constant temperature which is regarded as unity during numerical computation.

Simultaneous ODE systems (24) and (25) are solved analytically with the assistance of the suitable BCs given in Eq. (27). The closed-form solutions for VF and IMF are

$$u = A_1 \sinh\xi\, x_3 - B_1(1 - \cosh\xi\, x_3) - \frac{\gamma_3\, g_\Theta\, x_3}{\xi^2}, \tag{28}$$

$$\begin{aligned} h =& \frac{e_4}{\xi(1 - i\mathrm{Hc})}\left[A_1(1 - \cosh\xi x_3) - B_1\left\{\sinh\xi x_3 + \frac{\phi_l(1 - i\mathrm{Hc})\xi}{e_4}\right\} + \frac{\gamma_3 g_\Theta x_3^2}{2\xi}\right] \\ &- \frac{(2i\,\mathrm{Ro}B_1 - K_1)\gamma_1}{\mathrm{Mg}^2\gamma_2}\left\{x_3 + \frac{\phi_l(1 - i\mathrm{Hc})}{e_4}\right\}, \end{aligned} \tag{29}$$

where

$$Y_1 = \frac{\mathrm{Mg}^2\,\gamma_2 e_4}{(1 + \mathrm{Hc}^2)}, \quad Y_2 = 2i\mathrm{Ro}\,\gamma_1 + \frac{\mathrm{HcMg}^2\,\gamma_2\, e_4}{(1 + \mathrm{Hc}^2)}, \quad Z_1,\, Z_2 = \tfrac{1}{\sqrt{2}}\left[\left\{Y_1^2 + Y_2^2\right\}^{1/2} \pm Y_1\right]^{1/2},$$

$$\xi = Z_1 + iZ_2, \quad \phi = \phi_l + \phi_u, \quad \Delta_1 = 1 + \frac{\phi(1 - i\mathrm{Hc})}{e_4}, \quad \Delta_2 = (2i\,\mathrm{Ro}\,\gamma_1 - \xi^2)(1 - \cosh\xi),$$

$$\Delta_3 = \frac{\xi^2\phi(1 - i\mathrm{Hc})}{e_4} + 2i\mathrm{Ro}\gamma_1, \quad \alpha_0 = 2\gamma_1\xi^3\Delta_1\sinh\xi(1 - \cosh\xi),$$

$$\alpha_1 = \gamma_3\Delta_2[(2 + 2\cosh\xi - \xi\sinh\xi) + 2\,\xi\,\Delta_3\sinh\xi], \quad \beta_0 = 2\gamma_1\,\xi^3\Delta_1\sinh\xi,$$

$$\beta_1 = \gamma_3\left[\xi\sinh\xi\left(2i\mathrm{Ro}\,\gamma_1 - \xi^2\right) + 2\Delta_2\right], \quad F = 2\xi^2[2\Delta_2 + \xi\,\Delta_3\sinh\xi],$$

$$A_1 = \frac{\alpha_0 K - \alpha_1}{F\sinh\xi}, \quad B_1 = \frac{\beta_0 K_1 - \beta_1 g_\Theta}{F}.$$

In the case when $\vartheta \to 0$ (purely base fluid) solutions (28) to (29) are in agreement with solutions of Seth and Singh [10]. These solutions further reveal that VF is affected by the sum of wall conductance constants of both the walls, while IMF is affected by the individual values of wall conductance constant of each walls. In the case of the perfectly conducting walls, the VF and IMF can be obtained with the assistance of solutions (28) to (29) by taking the limiting case when $\phi_l,\ \phi_u \to \infty$. In the case of non-conducting walls, these can be obtained by taking $\phi_l,\ \phi_u \to 0$. In case one wall is perfectly conducting and another is non-conducting we can obtain the VF and IMF by taking the limiting case $\phi_l \to 0$, $\phi_u \to \infty$ or $\phi_l \to \infty,\ \phi_u \to 0$. Energy Eq. (26) is solved in accordance with the BCs available in Eq. (27), and the solution for temperature field is presented in the following form

$$\Theta = \Psi(x_3) + (\Theta_0 - \Psi(1))x_3 + (x_3 - 1)\Psi(0), \tag{30}$$

where

$$\Upsilon(x_3) = \frac{1}{2}\gamma_4\, g_\Theta\,\mathrm{Pr}\left(\frac{u + \overline{u}}{2}\right) - \mathrm{Er}\,\mathrm{Pr}\left[\gamma_5\left(\frac{\mathrm{d}u}{\mathrm{d}x_3}\right)\left(\frac{\mathrm{d}\overline{u}}{\mathrm{d}x_3}\right) + \gamma_6\,\mathrm{Mg}^2\left(\frac{\mathrm{d}h}{\mathrm{d}x_3}\right)\left(\frac{\mathrm{d}\overline{h}}{\mathrm{d}x_3}\right)\right],$$

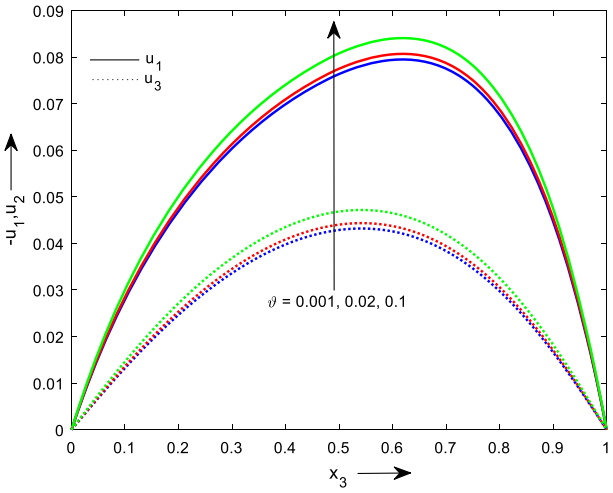

Fig. 2 Velocity field (VF) along the main and normal flow directions for various values of ϑ

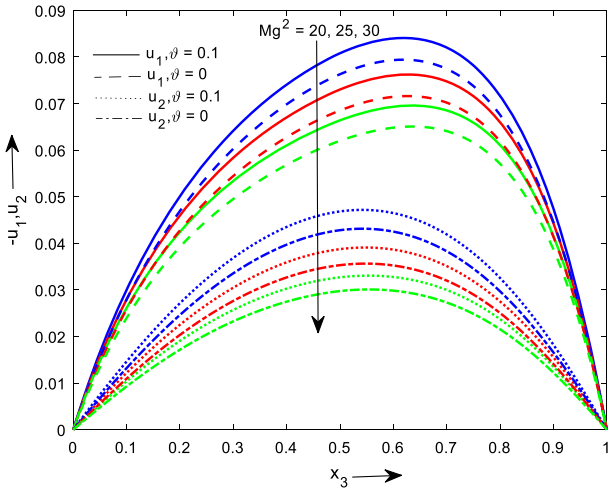

Fig. 3 Velocity field (VF) along the main and normal flow directions for various values of Mg^2

$$\Psi(x_3) = \int_0^{x_3} \left(\int_0^{\zeta} \Upsilon(\varsigma)\, d\varsigma \right) d\zeta.$$

The surface skin friction (SSF), mass flow rate (MFR) and critical Grashof number (CGN) are derived from solution (28) and presented in the following form

$$\tau_l = \tau_{l1} + i\,\tau_{l2} = \frac{1}{\xi^2}\left(A_1\xi^3 - \gamma_3 g_\Theta\right), \tag{31}$$

$$\tau_u = \tau_{u1} + i\,\tau_{u2} = \frac{1}{\xi^2}\left(A_1\xi^3\cosh\xi + B_1\xi^3\sinh\xi - \gamma_3 g_\Theta\right), \tag{32}$$

$$M = M_1 + i\,M_2 = \frac{1}{2\xi^2}\left[2\xi\{A_1(\cosh -1) + B_1(\sinh\xi - 1)\} - \gamma_3 g_\Theta\right], \tag{33}$$

$$\mathrm{Gc}_l = \mathrm{Gc}_{l1} + i\mathrm{Gc}_{l2} = -\frac{\xi\,\Delta_1 K}{(\delta_0 + \delta_1)}, \tag{34}$$

Table 1 Thermophysical constants for Ti_6Al_4V-H_2O nanofluid (Khan et al. [52])

Constants	Ti_6Al_4V	H_2O
$\beta \times 10^{-5}(1/K)$	5.8	21
$\rho(\mathrm{kg}/m^3)$	4420	997.1
$\sigma(S/m)$	5.8×10^5	0.005
$C_p(J/\mathrm{kg}K)$	0.56	4179
$k(W/mK)$	7.2	0.613

Table 2 Surface skin friction (SSF) along the main and normal flow directions at the lower and upper walls of the channel

ϑ	Mg^2	Ro	g_Θ	Hc	ϕ	$-\tau_{l1}$	τ_{l2}	τ_{u1}	$-\tau_{u2}$
0.1	20	5	2	0.25	2	0.3668	0.1521	0.6313	0.1924
0.001						0.3401	0.1367	0.5924	0.1745
0.02						0.3469	0.1410	0.6036	0.1797
	25					0.3479	0.1268	0.6004	0.1645
	30					0.3310	0.1076	0.5731	0.1432
		3				0.4091	0.1112	0.6778	0.1413
		7				0.3223	0.1759	0.5815	0.2255
			0			0.2468	0.0852	0.2468	0.0852
			4			0.4869	0.2190	1.0158	0.2996
			6			0.6070	0.2860	1.4004	0.4068
				0.50		0.3493	0.1604	0.6160	0.2125
				0.75		0.3330	0.1722	0.6047	0.2336
					0	0.5735	0.3953	0.8379	0.4356
					1	0.4213	0.1884	0.6858	0.2287
					3	0.3408	0.1383	0.6052	0.1786
					∞	0.2717	0.1111	0.5362	0.1514

$$\mathrm{Gc}_u = \mathrm{Gc}_{u1} + i\mathrm{Gc}_{u2} - \frac{\xi\,\Delta_1 K}{(\delta_0 - \delta_2 - \delta_3 + \delta_4)}, \tag{35}$$

where

$$\begin{aligned}
\delta_0 =& \gamma_3\Delta_2[(2 + 2\cosh\xi - \xi\sinh\xi)\xi - 4\sinh\xi],\\
\delta_1 =& 2\gamma_3\Delta_3\xi\sinh\xi(\xi - \sinh\xi),\quad \delta_2 = \gamma_3\xi^2\sinh^3\xi\left(2i\mathrm{Ro}\gamma_1 - \xi^2\right),\\
\delta_3 =& \gamma_3\Delta_2\xi^2\cosh\xi\,\sinh\xi,\quad \delta_4 = 2\gamma_3\Delta_3\xi\sinh\xi(\xi\cosh\xi - \sinh\xi).
\end{aligned}$$

3 Results and discussion

In this section we examined the impacts of significant flow-influencing parameters to the fluid properties. For achieving this purpose the numerical values of VF, IMF and TF are computed from the closed-form solutions derived in the previous section and presented in graphical form (Figs. 2, 3, 4, 5, 6, 7, 8, 9, 10, 11, 12, 13, 14, 15, 16, 17, 18, 19, 20, 21, 22, 23). The

Table 3 Mass flow rate (MFR) along the main and normal flow directions

ϑ	Mg^2	Ro	g_Θ	Hc	ϕ	$-M_1$	M_2
0.1	20	5	2	0.25	2	0.0171	0.0014
0.001						0.0166	0.0017
0.02						0.0169	0.0017
	25					0.0150	0.0019
	30					0.0134	0.0022
		3				0.0155	0.0001
		7				0.0177	0.0036
			0			0.0059	0.0088
			4			0.0402	0.0116
			6			0.0633	0.0218
				0.50		0.0180	0.0 041
				0.75		0.0192	0.0066
					0	0.0164	0.0116
					1	0.0162	0.0011
					3	0.0176	0.0025
					∞	0.0192	0.0051

Table 4 Critical Grashof number (CGN) along the main and normal flow directions at the lower and upper walls of the channel

ϑ	Mg^2	Ro	Hc	ϕ	$Gc_{l1} \times e^{12}$	$-Gc_{l2} \times e^{12}$	$-Gc_{u1} \times e^{12}$	$Gc_{u2} \times e^{12}$
0.1	20	5	0.25	2	6.5859	6.4156	0.5039	0.2694
0.001					5.0387	6.3149	0.4914	0.3620
0.02					5.0888	6.3290	0.5388	0.3439
	25				56.229	120.18	0.0466	0.0622
	30				300.91	1455.1	0.0029	0.0078
		3			− 3.8869	1.1340	− 0.2078	8.9972
		7			10.257	20.518	8.8789	− 0.0159
			0.50		300.91	1455.1	0.0029	0.0078
			0.75		671.74	− 5.0961	− 2.6129	− 0.3620
				0	2.9529	2.1233	7.7031	1.2544
				1	4.7694	4.2694	0.2454	0.1045
				3	8.4024	− 8.5617	0.8525	0.5072
				∞	57.448	66.507	0.0044	0.0034

results for SSF, MFR, CGN and HTR are tabulated in tabular from (Tables 2, 3, 4, 5). Unless the flow-influencing parameters are specified these are fixed as $\vartheta = 0.1, Mg^2 = 20, Ro = 5$, $g_\Theta = 2$, Hc $= 0.25$, $\phi = 2$, $\phi_l = 2$, $\phi_u = 2$, Pr $= 7.0$, Er $= 2$, $K = 1$ and $\Theta_0 = 1$ for the computational requirement. For the Ti_6Al_4V-H_2O nanofluid the constants representing the thermophysical characteristics are expressed in Table 1.

Table 5 Heat transport rate (HTR) at the lower and upper walls of the channel

ϑ	Mg^2	Ro	g_Θ	Hc	ϕ_l	ϕ_u	Pr	Er	$\left(\frac{d\Theta}{dx_3}\right)_l$	$-\left(\frac{d\Theta}{dx_3}\right)_u$
0.1	20	5	2	0.25	2	2	7.0	2.0	7.5756	14.1660
0.001									6.1199	10.5799
0.02									6.4519	11.3844
	25								8.0459	15.5645
	30								8.3835	16.6241
		3							8.4968	16.1477
		7							6.6998	12.3147
			0						1.2095	− 0.7905
			4						23.6147	54.7402
			6						49.3267	120.930
				0.50					7.3620	13.8458
				0.75					7.3336	14.0540
					0				7.4469	13.8278
					1				7.5296	14.0460
					3				7.6049	14.2418
					∞				7.7226	14.5427
						0			7.4469	13.8278
						1			7.5296	14.0460
						3			7.6049	14.2418
						∞			7.7226	14.5427
							0.03		1.0282	− 0.9350
							0.71		1.6670	0.5383
							3.0		3.8181	5.4997
								0.50	2.8619	3.0417
								1.0	4.4331	6.7498
								1.5	6.0044	10.4579

3.1 Effects on velocity field (VF)

As Fig. 2 reflects, the velocity profiles grow for incrementing values of ϑ. In general the velocity profile reduces on increasing the volumetric concentration of nanoparticles in the fluid due to rise in the viscosity and hence the flow resisting force. But in our case this trend is opposite due to thermal buoyancy force. The magnetic field intensity leads to bring rigidness in the flow as can be seen in Fig. 3. This rigidness in flow is caused by magnetic drag arising due to the Lorentz force. Figure 4 illustrates the gyratory action of the system to the VF. The gyration of the system about an axis leads to stabilize the main flow due to centripetal force which pulls the fluid in the direction opposite to the main flow, while it brings increment in the normal flow due to action of Coriolis force which pushes the fluid outward in the direction normal to the main flow. The incrementing values of g_Θ grow the velocity profiles as can be noticed in Fig. 5. The flow-impacting parameter g_Θ is the ratio of the thermal buoyancy force to the viscous force. For large thermal buoyancy force, g_Θ is large. Thus we may conclude that thermal buoyancy force leads to grow the fluid velocity. Hall effect

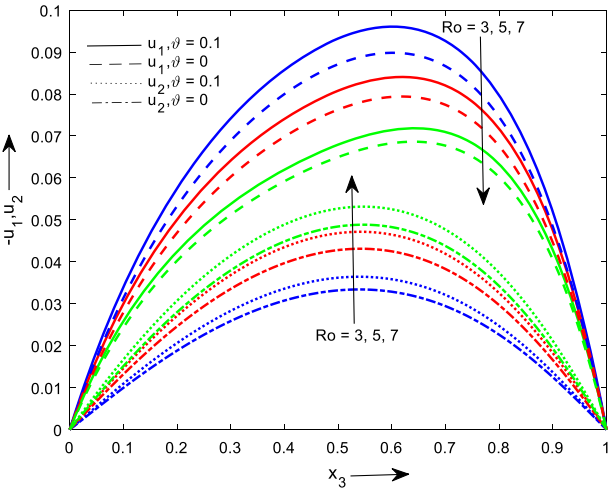

Fig. 4 Velocity field (VF) along the main and normal flow directions for various values of Ro

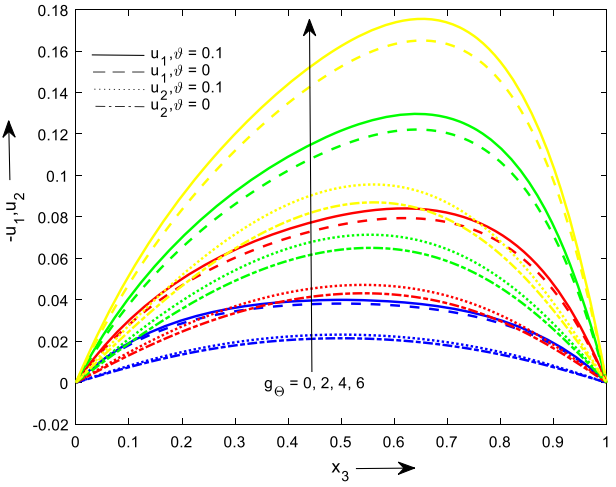

Fig. 5 Velocity field (VF) along the main and normal flow directions for various values of g_Θ

on VF is demonstrated through Fig. 6. Similar to gyratory action Hall effect stabilizes the main flow and rises the normal flow. This is due to the fact that the fluid particles deviated from its linear path due to the presence of a strong magnetic field domain and collision with the other particles. Thus in place on moving on a linear path it starts to move on spiral path about the lines of magnetic field. Figure 7 expresses that the sum of the wall conductance constants ϕ leads to a decrement in the flow. This is happening because on incrementing the wall electrical conductivity, the magnetic drag force enhances due to the induced magnetic field. An impressive result is noticed from Figs. 2, 3, 4, 5, 6, 7 that the velocity of the purely base fluid is lesser than the velocity of the nanofluid due to impacts of thermal buoyancy force.

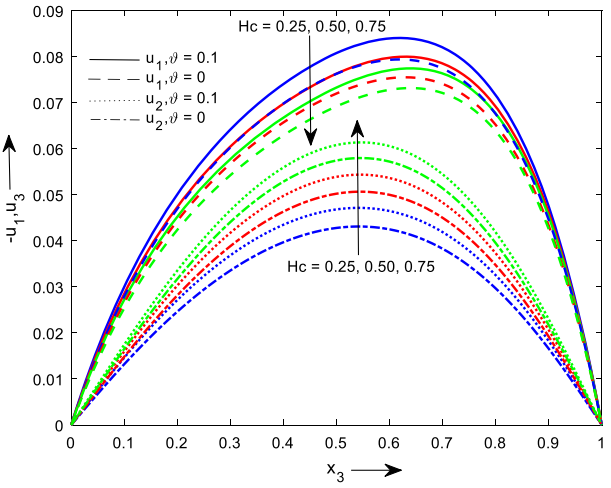

Fig. 6 Velocity field (VF) along the main and normal flow directions for various values of Hc

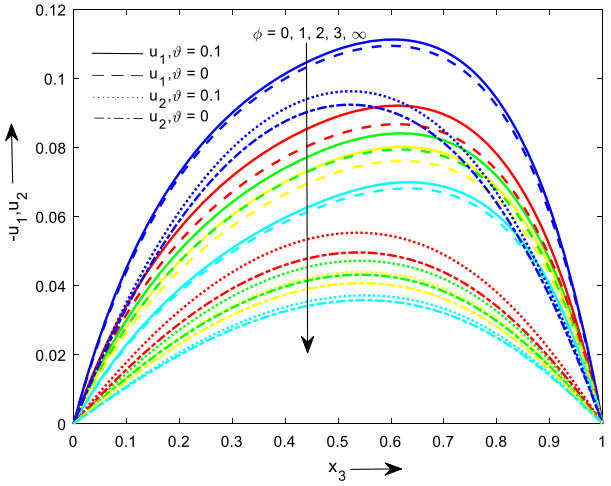

Fig. 7 Velocity field (VF) along the main and normal flow directions for various values of ϕ

3.2 Effects on induced magnetic field (IMF)

The variation in IMF corresponding to ϑ is displayed in Fig. 8. This figure shows that on enhancing the volumetric concentration of nanoparticles in the fluid, the electrical conductivity and flow velocity of the nanofluid also rise and hence a substantial growth in IMF closer to the walls of the channel is noted. As can be viewed from Fig. 9, on strengthening the applied magnetic field intensity the IMF adjacent to both surfaces of the channel significantly reduces due to magnetic drag force which leads to reduce the flow velocity. Figure 10 displays that the gyration of the flow system has IMF reducing tendency near the walls of channel similar to the magnetic field because it also has main flow-stabilizing nature similar to the magnetic field. Figure 11 reflects that the thermal buoyancy force brings the growth in the IMF in the vicinity of both the channel walls due to its flow-accelerating nature. The behavior of Hall current on IMF is exactly similar to the behavior of magnetic field and gyratory action as can be easily seen from Fig. 12. This may be due to the similar main flow-decelerating nature as

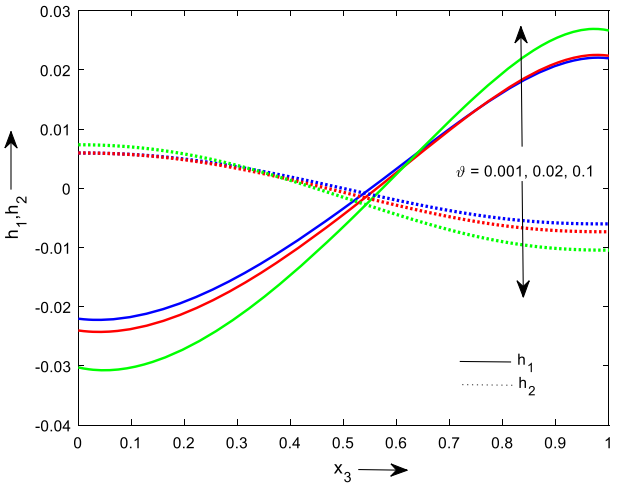

Fig. 8 Induced magnetic field (IMF) along the main and normal flow directions for various values of ϑ

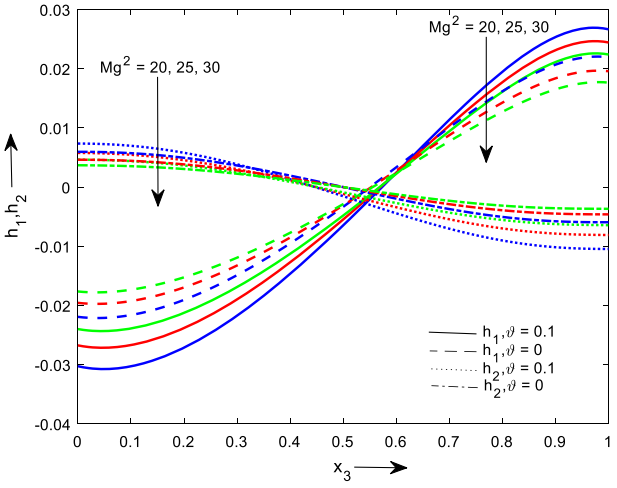

Fig. 9 Induced magnetic field (IMF) along the main and normal flow directions for various values of Mg^2

that of magnetic field and rotation. The consequence of the wall conductance constants of the both the walls of the channel is illustrated in Figs. 13 and 14. A noteworthy observation made from these figures is that on incrementing the wall conductivity of the lower wall the IMF grows up in the region close to lower wall, while it falls down in the area near the upper wall. On incrementing the wall conductivities the flow velocity reduces, this may cause of reduction in IMF near the upper wall. This nature is opposite near the lower wall due to its high wall conductivity. The similar observation is recorded for the wall conductivity of the upper wall, i.e., on incrementing the wall conductivity of the upper wall the IMF grows up in the region close to upper wall, while it falls down in the area near the lower wall. Thus we may conclude that the wall conductance constant has tendency to raise the IMF in the region adjacent to that wall. Further Figs. 7, 8, 9, 10, 11, 12, 13, 14 reflect that the IMF in the purely base fluid is lesser than the IMF in the nanofluid.

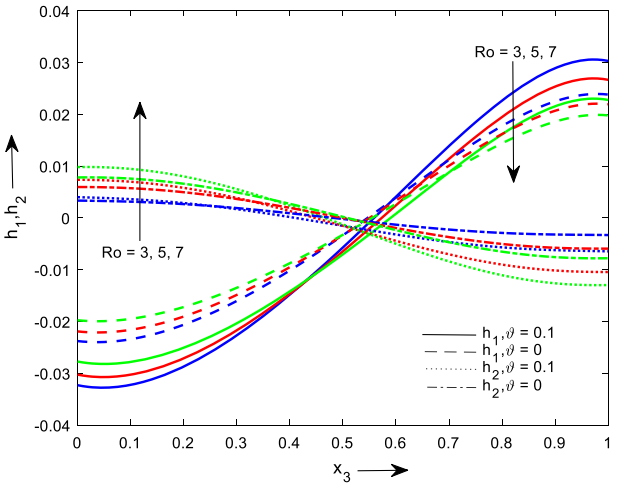

Fig. 10 Induced magnetic field (IMF) along the main and normal flow directions for various values of Ro

Fig. 11 Induced magnetic field (IMF) along the main and normal flow directions for various values of g_Θ

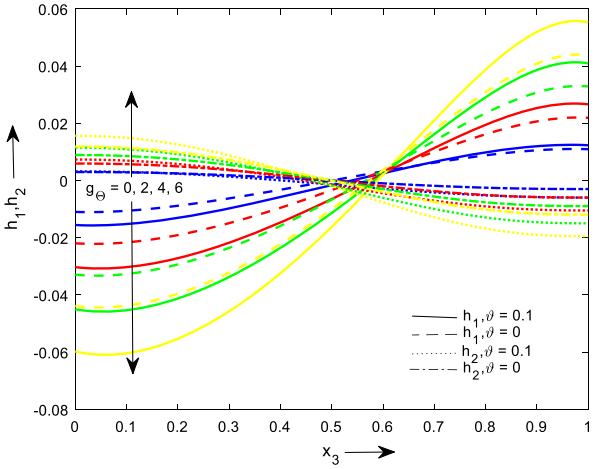

3.3 Effects on temperature field (TF)

Figure 15 displays the temperature profile for ϑ, and it reflects that on increasing the volumetric concentration of nanoparticles in the fluid, the flow-resisting force rises and it brings growth in the temperature. The effect of applied magnetic field intensity on the temperature is depicted in Figs. 16 and noted that increment in the magnetic field intensity leads to raise the temperature of the fluid due to magnetic drag force. The impacts of gyration of the system and Hall effect on the temperature are illustrated in Figs. 17 and 18. On incrementing the angular velocity of gyration and Hall current, the temperature of the nanofluid gets reduced, while the temperature of the purely base fluid falls down, attains a minimum value and again rises. This may be due to the flow-inducing nature of rotation and Hall current in the direction normal to the main flow. As can be easily seen from Fig. 19, the thermal buoyancy force leads to grow the fluid temperature because more thermal buoyancy force corresponds to more temperature gradient. The wall conductance constants of both the walls show the

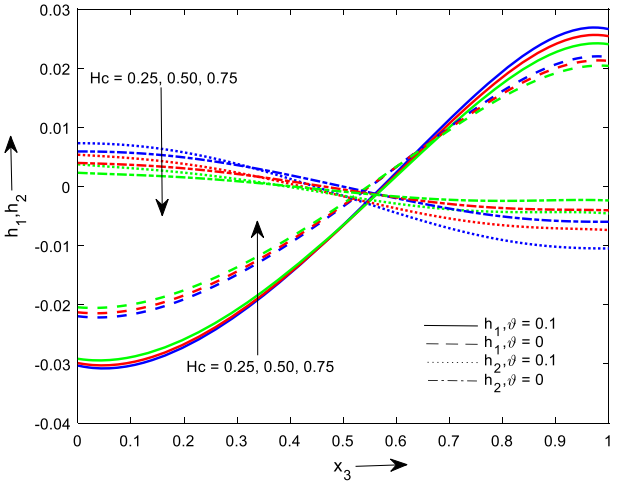

Fig. 12 Induced magnetic field (IMF) along the main and normal flow directions for various values of Hc

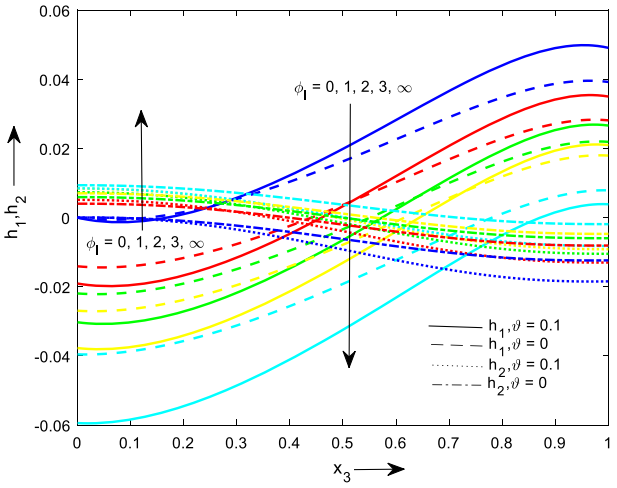

Fig. 13 Induced magnetic field (IMF) along the main and normal flow directions for various values of ϕ_l

similar temperature increasing nature as reflected in Figs. 20 and 21 because they employ the flow-resisting force. The effects of Pr and Er on the temperature are demonstrated in Figs. 22 and 23, respectively, and show that both leads to grow the fluid temperature. Pr is the ratio of the viscous and thermal diffusions, and it falls down on incrementing the thermal diffusion, and it means that thermal diffusion brings decrement in the fluid temperature. Er is the measurement of viscous dissipation, and it tends to rise the fluid temperature.

3.4 Effects on surface skin friction (SSF), mass flow rate (MFR), critical Grashof number (CGN) and heat transport rate (HTR)

The variation in nature of surface skin friction (SSF) corresponding to different flow-influencing parameters is presented in Table 2. The SSF at both the walls of the channel

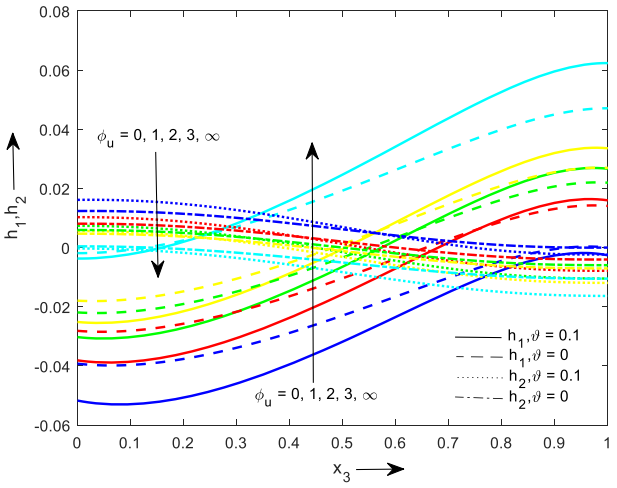

Fig. 14 Induced magnetic field (IMF) along the main and normal flow directions for various values of ϕ_u

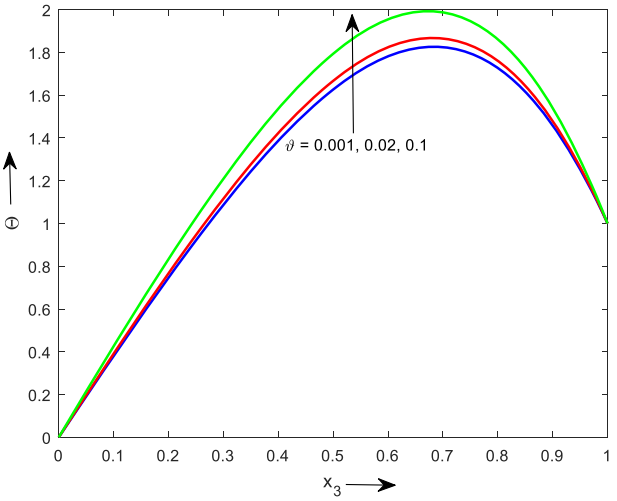

Fig. 15 Temperature field (TF) for various values of ϑ

increments for the rising values of the volume friction constant of the nanofluid and thermal buoyancy force because both tends to induce the fluid flow, while these fall down on incrementing the applied magnetic field strength and wall conductivities because these have flow retardation tendency. At both the walls of the channel, the gyration of the system and Hall current leads to reduce the SSF along main flow due to their main flow-stabilizing nature, while these leads to rise the SSF along normal flow due to their flow-inducing nature along the normal flow. Table 3 expresses the mass flow rate (MFR) within the channel. Increment in MFR is noted with rise in volume friction constant of the nanofluid, angular velocity of gyration, thermal buoyancy force and Hall current because these tends to enhance the resultant velocity. Incrementing values of magnetic field strength lead to a decrement in MFR along the main flow due to the fact that it mainly tends to retard the main flow. Thus the MFR

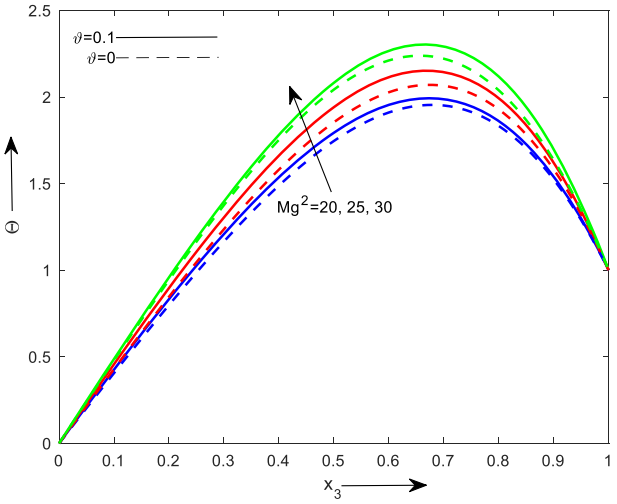

Fig. 16 Temperature field (TF) for various values of Mg^2

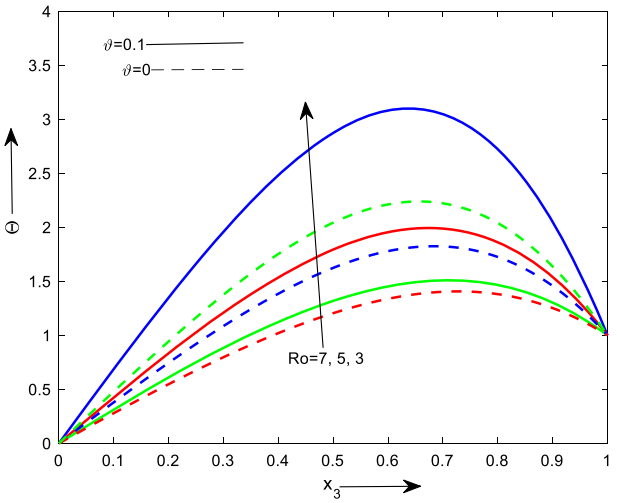

Fig. 17 Temperature field (TF) for various values of Ro

along normal flow direction increases. A strange behavior we noted that MFR falls down for the wall conductive constant range $0 \leq \phi < 1$, while MFR grows up for the wall conductive constant range $1 \leq \phi < \infty$, i.e., for lower conductive walls MFR reduces, while for higher conductive walls MFR raises. The impacts of significant flow-impacting parameters to critical Grashof number (CNG) are tabulated in Table 4. It exhibits that the volume fraction constant of nanofluid, magnetic field strength, Hall current and wall conductance have flow-stabilizing nature on the main flow at the lower wall, while the volume fraction constant of nanofluid, magnetic field strength and angular velocity of gyration exhibit flow-stabilizing nature on the normal flow at the lower wall. The volume fraction constant of nanofluid shows the destabilizing effect on the normal flow at the upper wall, while magnetic field has also a destabilizing effect on both the main and normal flows at the upper wall. The wall conduc-

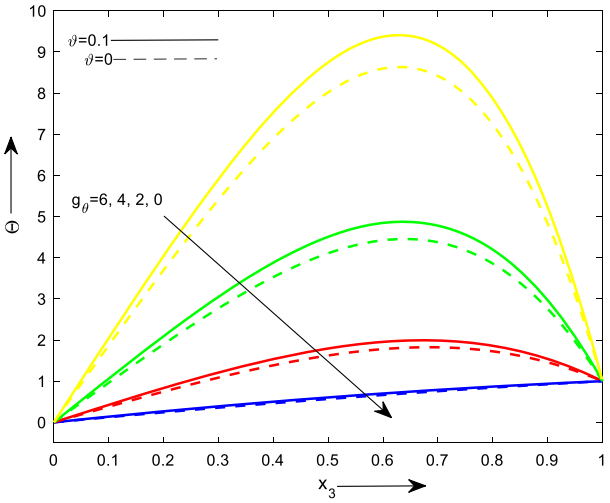

Fig. 18 Temperature field (TF) for various values of g_Θ

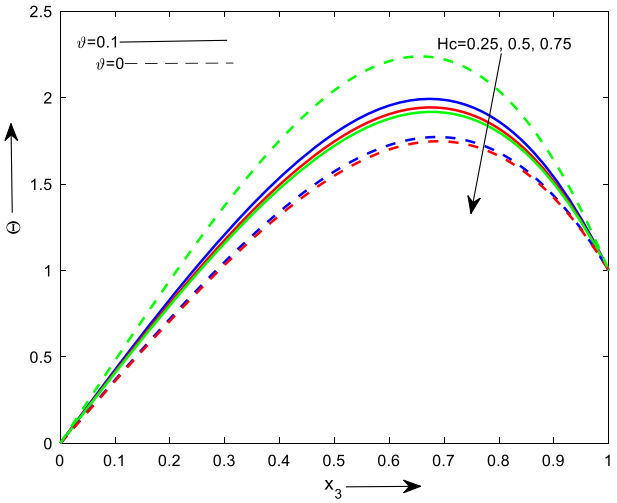

Fig. 19 Temperature field (TF) for various values of Hc

tance constants imply a stabilizing influence on both the main and normal flows at the upper wall when either both plates are non-conducting or perfectly conducting, i.e., when $\phi \neq 0$, ∞. Table 5 presents the behavior of heat transport rate (HTR) for various parameters. An increment in HTR is brought out by volume fraction constant of nanofluid, magnetic field strength, thermal buoyancy force, wall conductance constant and viscous dissipation at both the walls of the channel due to their temperature-increasing tendency. The decrement in HTR at the lower wall is brought out by angular velocity of gyration and Hall current due to their temperature-reducing tendency. The thermal diffusion brings decrement in HTR at both the walls when $0.71 \leq \mathrm{Pr} \leq 7.0$, i.e., when diffusion is high because thermal diffusion leads to reduce the fluid temperature.

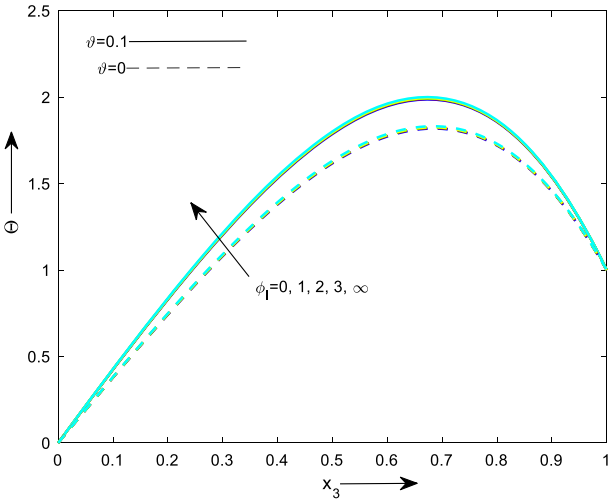

Fig. 20 Temperature field (TF) for various values of ϕ_l

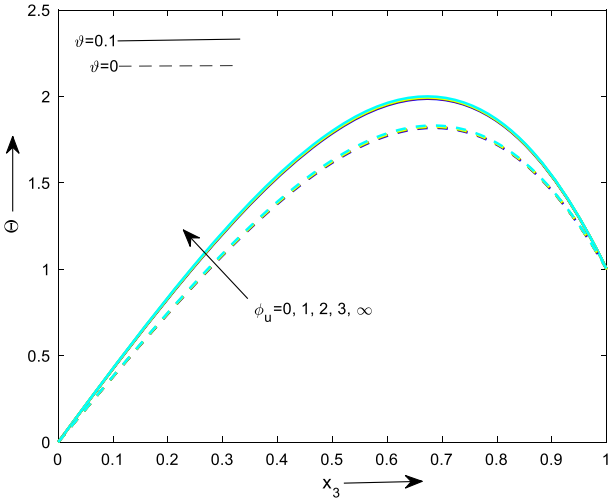

Fig. 21 Temperature field (TF) for various values of ϕ_u

3.5 Comparison of the present result with the existing result in the limiting case

In order to confirm the present results, a comparison is made between our results and the results of Singh et al. [10] which is a limiting case of our problem. The velocity field (VF) and surface skin friction (SSF) along the main and normal flow directions are computed in case of Singh et al. [10], i.e., when $\vartheta = 0$, and presented in graphical and tabular forms as Fig. 24 and Table 6, respectively. The results of Singh et al. [10] exceptionally confirm the present results.

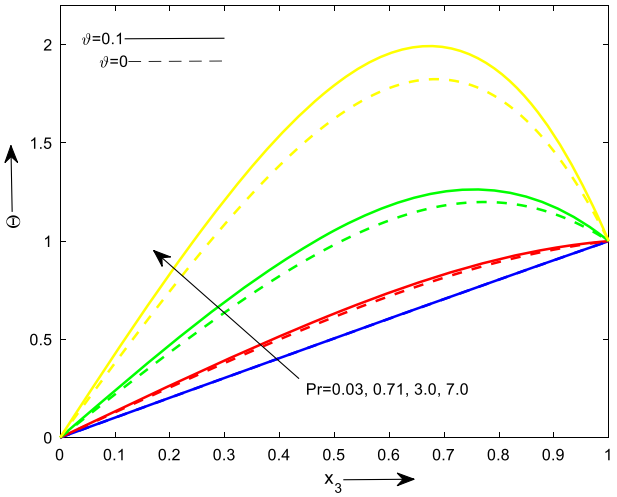

Fig. 22 Temperature field (TF) for various values of Pr

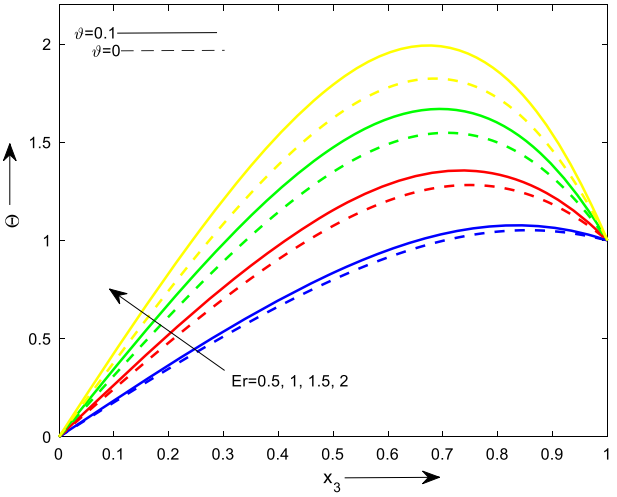

Fig. 23 Temperature field (TF) for various values of Er

4 Conclusions

In this paper we scrutinized the influences of energy dissipation, induced magnetic field and Hall current on steady mixed convective MHD flow of titanium alloy water-based nanofluid within an asymmetric channel with arbitrary wall thickness and conductance. Computational work is performed in the previous section to present and analyze the results numerically. This study is significant in analyzing the flow and heat transport nature nanofluid in the presence of strong magnetic field within the randomly conducting walls. Some important flow features of this study are:

- The volume fraction constant of nanofluid brings increment in temperature which leads to raise the thermal buoyancy force and hence fluid velocity and IMF closer to the walls. This is unique behavior which may find applications in nanoscience.

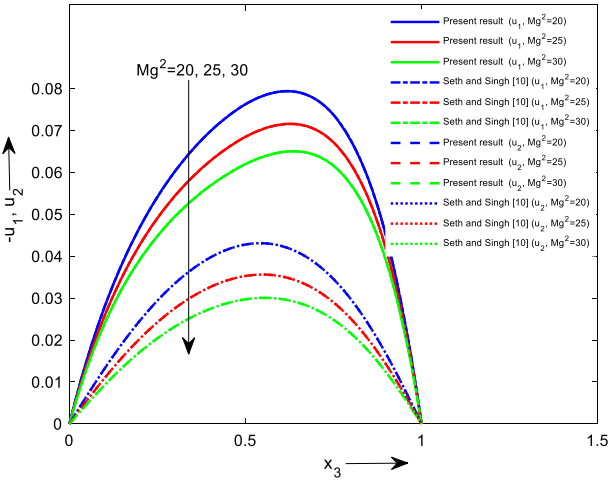

Fig. 24 Comparison of the present results of velocity field (VF) with the existing results of same in the limiting case

Table 6 Comparison of the present results of surface skin friction (SSF) with the existing results of same in the limiting case

Hc	Present results				Results of Seth and Singh [10]			
	$-\tau_{l1}$	τ_{l2}	τ_{u1}	$-\tau_{u2}$	$-\tau_{l1}$	τ_{l2}	τ_{u1}	$-\tau_{u2}$
0.25	0.3397	0.1365	0.5918	0.1742	0.3397	0.1365	0.5918	0.1742
0.50	0.3233	0.1489	0.5776	0.1977	0.3233	0.1489	0.5776	0.1977
0.75	0.3090	0.1640	0.5681	0.2214	0.3090	0.1640	0.5681	0.2214

- The gyration of the system and Hall current tends to stabilize the main flow. This feature can be applied to control the primary flow. Further these bring decrement in the induced magnetic field and temperature of nanofluid.
- On incrementing the wall electrical conductivity, the magnetic drag force enhances due to the induced magnetic field which causes the reduction in the flow velocity. This property can be used in fluid engineering to control the flow rate.

References

1. Jul. Hartmann, Hg-DYNAMICS I-Theory of the Laminar flow of an electric-ally conductive liquid in a Homogeneous magnetic field, Det Kgl. Danske Videnskabernes Selskab. Mathematisk-fysiske Meddelelser, XV, 6 (1937)
2. J.C.R. Hunt, J. Fluid Mech. **21**, 577 (1965)
3. C.C. Chang, J.T. Yen, ZAMP **13**(3), 266 (1962)
4. W.T. Snyder, J. Heat Transf. **86**(4), 552 (1964)
5. R.R. Gold, AIAA J. **5**(3), 266 (1967)
6. B.S. Mazumdar, Acta Mech. **28**(1), 85 (1977)
7. M. Tezer-Sezgin, S. Dost, Appl. Math. Model. **18**(8), 429 (1994)
8. T. Nagy, Z. Demendy, Acta Mech. **113**(1), 77 (1995)
9. M.S. Ansari, G.S. Seth, R. Nandkeolyar, Math. Comput. Model. **54**, 765 (2011)

10. G.S. Seth, J.K. Singh, Appl. Math. Model. **40**(4), 2783 (2016)
11. G.S. Seth, S. Sarkar, O.D. Makinde, J. Mech. **32**(5), 613 (2016)
12. J.K. Singh, S.G. Begum, G.S. Seth, Phys. Fluids **30**, 113602 (2018)
13. A. Borrelli, G. Giantesio, M.C. Patria, ASME J. Fluids Eng. **139**, 1 (2017)
14. G.S. Seth, J.K. Singh, N. Mahto, N. Joshi, Math. Sci. Lett. **5**, 259 (2016)
15. J.K. Singh, S. Vishwanath, Int. J. Thermofluid Sci. Technol. **7**(4), 070402 (2020)
16. J.K. Singh, G.S. Seth, S. Vishwanath, Heat Transf. **50**(2), 1812 (2021)
17. B. Kumar, G.S. Seth, R. Nandkeolyar, A.J. Chamkha, Int. J. Therm. Sci. **149**, 106101 (2019)
18. T. Hayat, J. Akram, H. Zahir, A. Alsaedi, Phys. Scr. **94**, 105201 (2019)
19. M. Rashid, K. Ansar, S. Nadeem, Phys. A Stat. Mech. Appl. **553**, 123979 (2020)
20. D. Kumar, A.K. Singh, D. Kumar, Phys. A Stat. Mech. Appl. **544**, 123562 (2020)
21. M. Raza, R. Ellahi, S.M. Sait, M.M. Sarafraz, M.S. Shadloo, I. Waheed, J. Therm. Anal. Calorim. **140**, 1277 (2020)
22. H. Sato, J. Phys. Soc. Jpn. **16**, 1427 (1961)
23. O.A. Beg, J. Zueco, H.S. Takhar, Commun. Nonlinear Sci. Numer. Simul. **14**, 1082 (2009)
24. B.K. Jha, C.A. Apere, Appl. Math. Mech. **33**, 399 (2012)
25. S. Siddiqa, M.A. Hossain, R.S.R. Int, J. Therm. Sci. **71**, 196 (2013)
26. O.D. Makinde, T. Iskander, F. Mabood, W.A. Khan, M.S. Tshehla, J. Mol. Liq. **221**, 778 (2016)
27. J.K. Singh, N. Joshi, S.G. Begum, Int. J. Heat Technol. **34**, 89 (2016)
28. R. Tripathi, G.S. Seth, M.K. Mishra, Adv. Powder Technol. **28**, 2630 (2017)
29. I. Tlili, N.N. Hamadneh, W.A. Khan, S. Atawneh, J. Therm. Anal. Calorim. **132**, 1899 (2018)
30. D. Kumar, A.K. Singh, D. Kumar, Eur. Phys. J. Plus **133**, 207 (2018)
31. B.K. Jha, P.B. Malgwi, B. Aina, Proc .IMechE Part N J. Nanomater. Nanoeng. Nanosyst. **233**, 73 (2019)
32. J.K. Singh, G.S. Seth, N. Joshi, C.T. Srinivasa, Bulg. Chem. Commun. **52**(1), 147 (2020)
33. B. Mahanthesh, B.J. Gireesha, G.T. Thammanna, T. Hayat, A. Alsaedi, In: *Proceedings of the Institution of Mechanical Engineers, Part C: Journal of Mechanical Engineering Science* **233**, 1224 (2018)
34. A.J. Chamkha, A.S. Dogonchi, D.D. Ganji, AIP Adv. **9**(2), 025103 (2019)
35. A.T. Akinshilo, BioNanoScience **9**, 740 (2019)
36. J.K. Singh, G.S. Seth, S. Vishwanath, P. Rohidas, Heat Transf. **49**(8), 4370 (2020)
37. S. Nandi, B. Kumbhakar, Therm. Sci. Eng. Progress **19**, 100561 (2020)
38. M. Shoaib, M.A.Z. Raja, M.T. Sabir, S. Islam, Z. Shah, P. Kumam, H. Alrabaiah, Sci. Rep. **10**, 18533 (2020)
39. C.-H. Chen, J. Heat Transf. **132**(6), 064503 (2010)
40. D. Gopal, N. Kishan, C.S.K. Raju, Inf. Med. Unlocked **9**, 154 (2017)
41. K. Ramesh, Propuls. Power Res. **7**, 329 (2018)
42. S.M. Atif, S. Hussain, M. Sagheer, J. Braz. Soc. Mech. Sci. Eng. **41**, 189 (2019)
43. M.D. Shamshuddin, P.V. Satya Narayana, Indian J. Phys. **94**, 1385 (2020)
44. B.K. Swain, B.C. Parida, S. Kar, N. Senapati, Heliyon **6**(10), e05338 (2020)
45. S.U.S. Choi, ASME Publ. Fed. **231**, 99 (1995)
46. S. Lee, S.U.S. Choi, S. Li, J. A. J. Heat Transfer. **121**(2), 280 (1999). https://doi.org/10.1115/1.2825978
47. C.H. Chon, K.D. Kihm, Appl. Phys. Lett. **87**, 153107 (2005)
48. A.A. Hussein, M.Z. Abdullah, M.A. Al-Nimr, Appl. Energy **164**, 733 (2016)
49. Z. Li, M. Sheikholeslami, A.J. Chamkha, Z.A. Raizah, S. Saleem, Comput. Methods Appl. Mech. Eng. **338**, 618 (2018)
50. M. Sheikholeslami, Comput. Methods Appl. Mech. Eng. **344**, 306 (2019)
51. Z.Z. Rashed, S.E. Ahmed, M.A. Sheremat, J. Mech. **35**(4), 563 (2019)
52. U. Khan, A. Zaib, I. Khan, K.S. Nisar, J. Mater. Res. Tech. **9**(1), 188 (2020)
53. M. Ramzan, H. Gul, J.D. Chung, S. Kadry, Y.M. Chu, Sci. Rep. **10**, 18342 (2020)
54. J.K. Singh, K. Suneetha, S. Vishwanath, Heat Transf. **50**, 5793 (2021)
55. S. Das, B. Tarafdar, R.N. Jana, O.D. Makinde, Spec. Top. Rev. Porous Media Int. J. **10**, 357 (2019)
56. B.K. Jha, G. Samaila, SN Appl. Sci. **2**, 1321 (2020)
57. N. Askari, H. Salmani, M.H. Taheri, M. Masoumnezhad, M.A. Kazemi, Proc. Inst. Mech. Eng. Part C J. Mech. Eng. Sci. **235**, 1966 (2021)
58. G.W. Sutton, A. Sherman, *Engineering Magnetohydrodynamics* (Dover Publications Inc., New York, 2006)
59. K.R. Cramer, S.I. Pai, *Magnetofluiddynamics for Engineers and Applied Physicists* (MacGraw-Hill, New York, 1973)
60. R. Aris, *Vectors, Tensors, and the Basic Equations of Fluid Mechanics* (Prentice Hall, Englewood Cliffs, NJ, 1962)